



ScuDo
Scuola di Dottorato ~ Doctoral School
WHAT YOU ARE, TAKES YOU FAR



Doctoral Dissertation
Doctoral Program in Aerospace Engineering (32.nd cycle)

Particle motion and gradient dynamics in turbulent flows: Theory and Numerical Simulations

Maurizio Carbone

* * * * *

Supervisor
Prof. Michele Iovieno

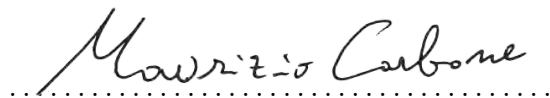
Doctoral Examination Committee:

Prof. Guido Boffetta, Università degli Studi di Torino, guido.boffetta@unito.it (Referee)
Dr. Alessandra Sabina Lanotte, CNR NANOTEC, alessandrasabina.lanotte@cnr.it (Referee)
Prof. Luca Biferale, Università degli Studi di Roma Tor Vergata, biferale@roma2.infn.it
Prof. Alain Pumir, Ecole Normale Supérieure de Lyon, Alain.Pumir@ens-lyon.fr
Dr. Michael Wilczek, Max Planck Institute (MPIDS), michael.wilczek@ds.mpg.de

Politecnico di Torino

This thesis is licensed under a Creative Commons License, Attribution - Noncommercial-NoDerivative Works 4.0 International: see www.creativecommons.org. The text may be reproduced for non-commercial purposes, provided that credit is given to the original author.

I hereby declare that, the contents and organisation of this dissertation constitute my own original work and does not compromise in any way the rights of third parties, including those relating to the security of personal data.

A handwritten signature in black ink that reads "Maurizio Carbone". The signature is written in a cursive style with a dotted line underneath it.

Maurizio Carbone
Turin,

Summary

The dynamics of fluid and inertial particles in turbulence is the main topic of this thesis. The work is divided in two parts. The first part deals with the theoretical investigation of turbulent flows, which constitute a major open problem in classical mechanics. We begin with the analysis of the turbulent energy cascade across the scales of statistically steady and isotropic turbulence. The energy cascade is a signature of time-irreversibility of turbulence and it has important implications on the motion of fluid and inertial particles in turbulent flows. An expression for the average cascade is derived in terms of coarse-grained Vortex Stretching and Strain Self Amplification, starting from the two-point energy balance and taking to account compressibility issues by introducing an incompressible filtered velocity increment. The role of Vortex Stretching and Strain Self Amplification mechanisms is examined in detail by studying the Lagrangian dynamics of the velocity gradient in the strain-rate eigenframe. The equations for the velocity gradient dynamics along the fluid particle trajectory are unclosed due to the non-locality of the pressure Hessian contribution and viscous stress. The non-local part of the pressure Hessian plays a key role in preventing singularities of the gradients but its statistical relation to local velocity gradients is not yet fully understood. A symmetry for the non-local pressure Hessian is proposed, which allows for a reduction of its dimensionality and complexity. The proposed gauge symmetry allows to transform the three-dimensional pressure Hessian into a two-dimensional tensor leaving the one-point dynamics of the velocity gradient invariants unchanged. The aim of this part is to provide a little insight into the turbulent dynamics relying on geometry and statistical analysis of results from Direct Numerical Simulations of Navier-Stokes turbulence. In the second part the dynamics of inertial particles in turbulence is considered, with focus on momentum, heat and mass transfer in particle-laden flows. The Nonuniform Fast Fourier Transform (NUFFT) is proposed as an efficient tool to perform numerical simulations of two-way coupled particle-laden flows. The NUFFT has been employed in various research areas but not yet in the field of particles in turbulence. Here it is shown that the NUFFT algorithm suits very well to the point-particle model. Details on the accuracy and parallel scaling of a pseudo-spectral code equipped with the NUFFT algorithm for the Direct Numerical Simulation of two-way coupled flows are presented. Then,

numerical experiments of two-way coupled particle-laden flows are carried out with focus on the thermal coupling. Several results are presented to characterize the fluid and particle temperature statistics, focus is put on the scale scale-dependence of two-particle statistics and thermal caustics is observed. A novel characterization of the interaction between the temperature gradients and inertial particles is also introduced. Finally, the condensational growth of water droplets in atmospheric clouds is studied, with focus on the effect of the droplet thermal inertia and on the influence of the large-scale forcing scheme. It is shown that temperature fluctuations can enhance the droplet condensational growth and that the details of the external forcing can play a relevant role, despite the broad scale separation between the droplet size and the forced scale. A more detailed overview of the Fortran-MPI code employed for the Direct Numerical Simulations of two-way coupled particle-laden flows, developed by the candidate during the PhD period, is in the Appendix. The most relevant modules of the parallel code are reported and described.

Acknowledgements

I would like to acknowledge my supervisor, Prof. Michele Iovieno, for his guidance, advices and for taking me on as his PhD student. I'm very grateful to him for this positive and constructive period. I acknowledge Dr. Andrew Bragg for his constant interest in our work, for continuously proposing new stimulating work and challenges. I'm thankful to him for his hospitality during the periods spent in his group at Duke University. I would like to acknowledge my family for the constant support offered. A very special thank to Daniela, for improving things all the times.

The computer resources necessary for the presented works have been provided by CINECA (<http://www.hpc.cineca.it/services/iscra>) under the ISCRA initiative and by LaPalma Supercomputer at the Instituto de Astrofísica de Canarias through the Red Española de Supercomputación (<https://www.res.es/>). This work also used the Extreme Science and Engineering Discovery Environment (XSEDE), supported by National Science Foundation grant ACI-1548562 [149]. Additional resources were provided by HPC@POLITO (<http://www.hpc.polito.it>).

Contents

1	Introduction	1
1.1	The Navier-Stokes equations	1
1.2	Geometric setup	4
1.3	Non-linearity	5
1.4	Cartesian tensors and the statistics of random fields	7
1.4.1	Velocity increments and the coarse-grained gradient	12
1.5	Equations for particle motion in fluids	12
1.5.1	Saffman lift	17
1.6	Features and numerical simulation of inertial particles in turbulence	17
I	Velocity gradient dynamics in isotropic turbulence	21
2	Turbulent Energy Cascade	23
2.1	Introduction	23
2.2	Theoretical background	24
2.3	The Incompressible Filtered Velocity Increment	25
2.4	Average energy cascade	27
2.4.1	Asymptotics of the average energy cascade	28
2.4.2	Roles of SSA and VS in the energy cascade	30
2.4.3	Paradoxical role of vortex stretching	31
2.5	Results & Discussion	32
2.5.1	Results for the velocity gradient invariants	36
2.6	Conclusions	36
3	Rank-reduced anisotropic pressure Hessian	43
3.1	Introduction	44
3.2	Theory	46
3.2.1	Equations for the fluid velocity gradient in the strain-rate eigenframe	47
3.2.2	A new symmetry for the dynamics of the velocity gradient invariants	48

3.2.3	Gauge symmetry for the anisotropic pressure Hessian	49
3.2.4	Using the gauge symmetry for dimensionality reduction	50
3.3	Rank-reduced anisotropic pressure Hessian	54
3.3.1	Pressure Hessian rank reduction	54
3.3.2	Rank-reduced anisotropic pressure Hessian eigenvalue	56
3.4	Statistical geometry	60
3.5	Conditioned statistical geometry	63
3.5.1	Rank-reduced anisotropic pressure Hessian–strain-rate alignment	63
3.5.2	Rank-reduced anisotropic pressure Hessian–vorticity alignment	68
3.6	Conclusions	70
II Inertial particle dynamics in isotropic turbulence		73
4	The NUFFT and its applications to DNS	75
4.1	Overview of numerical schemes for the simulation of two-way coupled particle-laden flows	76
4.2	Physical model	78
4.3	Numerical method	79
4.3.1	The B-spline polynomial basis	80
4.3.2	Interpolation: backward NUFFT	80
4.3.3	Reverse interpolation: forward NUFFT	81
4.3.4	Parallel implementation	82
4.4	Results	84
4.4.1	Validation of the NUFFT algorithm	84
4.4.2	Fluid phase-particle phase coupling	87
4.4.3	Smoothness of the coupling field	88
4.4.4	Spectral representation of the particle phase	90
4.4.5	Particle number density equivalent field	91
4.4.6	Particle momentum and temperature equivalent fields	93
4.4.7	Scale by scale analysis	95
4.5	Conclusions	97
5	Fluid–particle thermal interaction	99
5.1	Introduction	100
5.2	The physical model	103
5.2.1	Fluid phase	103
5.2.2	Particle phase	104
5.2.3	Thermal coupling	106
5.2.4	Validity and limitations of the model	106
5.2.5	Numerical method	109

5.3	Characterization of the thermal dissipation rate	110
5.3.1	Thermal dissipation due to the carrier temperature gradients	111
5.3.2	Thermal dissipation due to the particle dynamics	112
5.4	Characterization of the temperature fluctuations	116
5.4.1	Fluctuations of the carrier temperature field	116
5.4.2	Particle temperature fluctuations	118
5.5	Statistics conditioned on the local carrier flow temperature gradients	120
5.5.1	Particle clustering on the temperature fronts	120
5.5.2	Particle motion across the temperature fronts	122
5.5.3	Heat flux due to the particle motion across the fronts	123
5.6	Temperature structure functions	125
5.6.1	Structure functions of the carrier temperature field	125
5.6.2	Particle temperature structure functions	126
5.6.3	Mixed structure functions	130
5.7	Distribution of the temperature fluxes	132
5.8	Influence of momentum coupling and elastic collisions	133
5.8.1	Momentum coupling	133
5.8.2	Elastic collisions	134
5.9	Estimating the actual temperature field	136
5.9.1	Moments of the actual temperature gradient	137
5.9.2	Actual temperature field Probability Density Function	141
5.9.3	Structure functions	142
5.10	Conclusions	143
6	Condensational droplet growth in turbulence	145
6.1	Introduction	145
6.2	Model equations	148
6.2.1	Momentum	151
6.2.2	Droplet growth	152
6.2.3	Fluid flow equations	155
6.3	Setup of the numerical simulations	156
6.4	Results	158
6.4.1	Droplet size distribution	158
6.4.2	Droplet temperature distribution	162
6.4.3	Droplet–scalar gradients interaction	163
6.5	Conclusions	167
A	The numerical code	169
A.1	Setup for Fourier Transforms	169
A.2	Domain parallelization	170
A.3	Navier-Stokes equations pseudo-spectral solver	171
A.3.1	Time integration	171

A.3.2	Convective terms	172
A.3.3	Forcing methods	177
A.4	Flow fields Input/Output	179
A.5	Particle data structure	180
A.6	Particles distribution among MPI processes	181
A.7	Exchange of fields ghost regions between neighbouring MPI processes	186
A.8	Flow fields interpolation at the particle position and particle back- reaction	191
A.9	Particles collision detection	197
A.9.1	Interpolation of the particle path	200
A.10	Particles sorting	205
A.11	Particles Input/Output	208
	Bibliography	213

Chapter 1

Introduction

In this Chapter the framework and theoretical background of the work is introduced. The Navier-Stokes equations are briefly presented, by discussing some of the basic features of the convective term and its non-linearity. Fundamentals of tensor calculus are recalled, together with the application of Cartesian tensors to the study of statistically isotropic turbulence from an Eulerian perspective. Those concepts will be employed in the first part of the thesis, that deals with basic turbulence theory from a geometric perspective. Then, we consider the Lagrangian dynamics of fluid and inertial particles in turbulence, which constitutes an alternative to the Eulerian viewpoint of turbulence, and is often of practical interest. The expression for the force acting on a small inertial particle suspended in a turbulent flow is recalled and the assumptions under the point-particle model are discussed. Finally, basic features of the dynamics of point-particles in turbulence is presented. Those concepts will be employed in the second part of the thesis, that deals with the numerical simulation of inertial particles in turbulence in the two-way coupling regime.

1.1 The Navier-Stokes equations

The dynamics of a Newtonian and incompressible fluid is described by the incompressible Navier-Stokes equations

$$\nabla \cdot \mathbf{u} = 0 \tag{1.1a}$$

$$\frac{\partial \mathbf{u}}{\partial t} + \mathbf{u} \cdot \nabla \mathbf{u} = -\frac{1}{\rho_f} \nabla p + \nu \nabla^2 \mathbf{u}, \tag{1.1b}$$

where $\mathbf{u}(\mathbf{x}, t)$ is the velocity field, $p(\mathbf{x}, t)$ is the pressure field, ρ_f is the constant fluid density and ν is the fluid kinematic viscosity. At least two aspects make equation (1.1) interesting and difficult to tackle [105]: non-linearity and non-locality, which are closely connected. Indeed, equation (1.1) is actually an integro-differential

equation, since the pressure is a non-local functional of the velocity gradient,

$$\frac{p}{\rho_f}(\mathbf{x}, t) = \frac{1}{4\pi} \int d\mathbf{y} \frac{\mathbf{A}(\mathbf{y}, t) : \mathbf{A}(\mathbf{y}, t)}{\|\mathbf{x} - \mathbf{y}\|}, \quad (1.2)$$

where $\mathbf{A} = \nabla \mathbf{u}$ is the velocity gradient and the symbol $:$ indicates double contraction, $A_{ij}A_{ji}$ in Cartesian components. Due to incompressibility the pressure at a given point is instantaneously influenced by the velocity gradients at points which are far away from the point considered.

The other, and maybe most-important, feature of equation (1.1) is the quadratic non-linearity of the convective term which renders the solution of the equation impractical. An immediate consequence is that, if the solution \mathbf{u} is expressed as superposition of certain basis functions, the coefficients of those basis functions will not evolve independently but they will interact. In particular, if the Fourier representation of \mathbf{u} is employed,

$$\mathbf{u}(\mathbf{x}, t) = \int \hat{\mathbf{u}}(\mathbf{k}, t) \exp(i\mathbf{k} \cdot \mathbf{x}) d\mathbf{k} \quad (1.3)$$

modes with larger and lower wavenumber components are generated by convection through the products $\hat{\mathbf{u}}(\mathbf{k}_1, t)\hat{\mathbf{u}}(\mathbf{k}_2, t) \exp(i(\mathbf{k}_1 + \mathbf{k}_2) \cdot \mathbf{x})$. It is often the case that non-linearity depends on the coordinates adopted to describe the space-time, for example the ordinary differential equation $dx/dt = -x^2$ is linear if time is redefined to be $\tau = tx$. Therefore, non-linearity is not an invariant property of any differential equation while a definition based on the coordinates follows immediately from the definition of linear application [3]. We will return to this point later.

The convective term describes the variation in time due to the motion of the fluid particle through the velocity gradient field. By using incompressibility and the relation for differentiable vector fields \mathbf{v} and \mathbf{w}

$$\nabla(\mathbf{v} \cdot \mathbf{w}) = (\mathbf{v} \cdot \nabla)\mathbf{w} + (\mathbf{w} \cdot \nabla)\mathbf{v} + \mathbf{v} \times (\nabla \times \mathbf{w}) + \mathbf{w} \times (\nabla \times \mathbf{v}), \quad (1.4)$$

which is readily obtained by decomposing $\nabla \mathbf{v}$ and $\nabla \mathbf{w}$ into their symmetric and anti-symmetric parts, the convective term can be written as

$$\mathbf{u} \cdot \nabla \mathbf{u} = \frac{1}{2} \nabla \|\mathbf{u}\|^2 + \boldsymbol{\omega} \times \mathbf{u} \quad (1.5)$$

where $\boldsymbol{\omega} = \nabla \times \mathbf{u}$ is the vorticity. The convective variation of the velocity is due to the gradient of the kinetic energy and to a Coriolis-like contribution arising from rotation of the fluid element. The gradient term does not depend on the velocity orientation, what matters is instead the orientation of the velocity with respect to the vorticity. Of course, there is no actual Coriolis force, since the reference frame chosen to write equation (1.1) is inertial. The cross product in equation (1.5) arises because of the interaction between translation and rotation of the fluid

at a point fixed in space, while the interaction between translation and strain-rate produces convective and gradient terms. However, it is incorrect to think about the gradient term as a conservative force, since employing equation (1.5) requires that the dynamics of the fluid is analyzed at a point fixed in space, while force and acceleration are defined following the fluid element along its path. In contrast, the pressure gradient in equation (1.1b) actually produces a conservative force.

When the fluid flow is irrotational things are strongly simplified. In the case of a potential velocity field, equations (1.1a) and (1.1b) reduce to

$$\nabla^2\phi = 0 \tag{1.6}$$

$$\nabla \left[\rho \frac{\partial\phi}{\partial t} + p + \frac{1}{2} \|\nabla\phi\|^2 \right] = \mathbf{0} \tag{1.7}$$

where ϕ is a scalar potential such that $\mathbf{u} = \nabla\phi$. Therefore, potential flows can be tackled quite easily. However, the interesting features of the resulting velocity field derive only from the boundary conditions and turbulence does not exist in this framework.

Even when the irrotational field \mathbf{v} is not solenoidal, that is, we are dealing with the multidimensional Burgers equation

$$\frac{\partial\mathbf{v}}{\partial t} + \frac{1}{2} \nabla \|\mathbf{v}\|^2 = \nu \nabla^2 \mathbf{v}, \tag{1.8}$$

the convective term can still be eliminated by means of the Hopf-Cole transform [78, 36], that is reported here for a multidimensional case. Considering the diffusion equation for a scalar $q(\mathbf{x}, t)$,

$$\frac{\partial q}{\partial t} = \nu \nabla^2 q, \tag{1.9}$$

multiplying the diffusion equation by $f(q) = dF/dq$ and taking its gradient, the following equation is obtained

$$\frac{\partial}{\partial t} \nabla F = \nu \nabla^2 \nabla F - \nu \nabla \left(\frac{d^2 F}{dq^2} \|\nabla q\|^2 \right). \tag{1.10}$$

This suggests to set $\mathbf{v} = \nabla F$, which is possible only if the right-hand side of equation (1.10) can be expressed in terms of \mathbf{v} only. This implies $d^2 F/dq^2 = a (dF/dq)^2$ for some constant a . In particular, for $2a\nu = 1$, the potential field $\mathbf{v} = -2\nu \nabla \ln |B - q/(2\nu)|$ satisfies the Burgers equation (1.8) for any constant B . Notice that there are gauge terms that can be added to equation (1.9) which vanish under the transformation operated to obtain the Burgers equation.

The discussion above shows that the gradient part of the convective term, $\nabla \|\mathbf{u}\|^2$, can be tackled using basic tools. The key difficulty due to convection goes back to rotationality or, a little bit more generally, to the misalignment between $\boldsymbol{\omega}$ and \mathbf{u} . Of course, rotationality is a key feature of turbulence.

1.2 Geometric setup

Equations (1.1) are written for the vector components by defining a set of spatial coordinates $Z = \{Z^i\}_{i=1,\dots,d}$ in the d -dimensional space. Time is usually treated as a separate independent coordinate and, in this thesis, three-dimensional turbulence is considered. The covariant basis is determined from the position vector \mathbf{x} ,

$$\mathbf{z}_i = \frac{\partial \mathbf{x}}{\partial Z^i}, \quad (1.11)$$

which is associated with the corresponding covariant metric tensor $z_{ij} = \mathbf{z}_i \cdot \mathbf{z}_j$. The contravariant metric tensor is $z^{ij} = \mathbf{z}^i \cdot \mathbf{z}^j$, associated to the contravariant coordinates $\mathbf{z}^i = \nabla Z^i$, and it is the matrix inverse of covariant metric tensor. Tensors satisfy the tensor property, that is, contravariant and covariant tensors transform respectively according to

$$t^{i_1, \dots, i_n} = t^{i_1, \dots, i_n} J_{i_1}^{i'_1} \dots J_{i_n}^{i'_n}, \quad t_{i'_1, \dots, i'_n} = t_{i_1, \dots, i_n} J_{i_1}^{i'_1} \dots J_{i_n}^{i'_n}, \quad (1.12)$$

under a change of coordinates from Z to Z' defined by the Jacobian $J_i^{i'} = \partial Z^{i'} / \partial Z^i$. Here $J_i^i J_j^{j'} = \delta_j^i$, where δ_j^i is the Kronecker delta, and repeated covariant and contravariant indexes in a product imply summation. With these definitions the Navier-Stokes equations for the velocity components read

$$\nabla_k u^k = 0 \quad (1.13a)$$

$$\frac{\partial u^i}{\partial t} + \nabla_k (u^i u^k) = -\frac{1}{\rho_f} z^{ij} \nabla_j p + \nu \left[z^{jk} \nabla_j \nabla_k u^i + z^{ij} (\nabla_j \nabla_k - \nabla_k \nabla_j) u^k \right] \quad (1.13b)$$

where ∇_i is the covariant derivative which ensures the tensor property under derivation,

$$\frac{\partial \mathbf{u}}{\partial Z^i} = \left[\frac{\partial u^j}{\partial Z^i} + u^k \Gamma_{ik}^j \right] \mathbf{z}_j = \nabla_i u^j \mathbf{z}_j, \quad (1.14)$$

with the Christoffel symbol $\Gamma_{ij}^k = \mathbf{z}^k \cdot \partial \mathbf{z}_i / \partial Z^j$. In three dimension the vorticity is expressed as

$$\omega^i = \varepsilon^{ijk} z_{km} \nabla_j u^m \quad (1.15)$$

where $\varepsilon^{ijk} = \epsilon^{ijk} / \sqrt{\mathcal{Z}}$ is the Levi-Civita symbol, ϵ^{ijk} is the permutation symbol and \mathcal{Z} is the determinant of the covariant metric tensor. Both ϵ^{ijk} and $\sqrt{\mathcal{Z}}$ are relative tensors. Indeed, by definition of determinant, it is easily verified that they transform according to

$$\epsilon^{i'_1 i'_2 i'_3} = J \epsilon^{i_1 i_2 i_3} \quad \mathcal{Z}' = J^2 \mathcal{Z} \quad (1.16)$$

where $J = \det J$, is the determinant of the Jacobian describing the change of coordinates. However, the ratio between ϵ^{ijk} and $\sqrt{\mathcal{Z}}$ results into the Levi-Civita

tensor ε^{ijk} , which satisfies the tensor property (1.12), with respect to orientation-preserving change of coordinates. The fact that the vorticity, as defined in (1.15) is actually a tensor only with respect to orientation-preserving change of coordinates is usually referred to as handedness [121], and it should be taken into account when performing change of coordinates which do not preserve orientation, such as reflections.

The viscous term in equation (1.13) includes the contribution from the Ricci tensor, since covariant derivatives do not commute in general. However, if the space where the flow takes place is flat, then covariant derivatives commute. Indeed, a Cartesian basis can be defined in a flat space and the covariant derivatives reduce to partial derivatives which commute for smooth functions according to the Schwarz theorem, producing an identically zero Ricci tensor. Therefore, because of the tensor property, the Ricci tensor is zero in a flat space for all the possible coordinates.

We will consider flat spaces so that Cartesian coordinates x , which induce a right-oriented orthonormal basis, can be defined. In this Cartesian framework the metric tensor is the identity matrix and all the indexes can be lowered. Moreover, the transformation between oriented Cartesian coordinates are limited to proper rotations and the inversion of the Jacobian J reduces to transposition. An example of Navier-Stokes flow on a curved surface can be found in [58].

1.3 Non-linearity

The statement “the convective term in the Navier-Stokes equations is non-linear” is ubiquitous in fluid mechanics. But what does that really mean? Having heard the classification “non-linear” many times in various research areas, it comes naturally to ask for an intrinsic and purely geometric definition of “non-linearity”. Here we collect a few thoughts trying to interpret non-linearity for the dynamical system

$$\frac{d\mathbf{R}}{dt} = \mathbf{N}, \quad (1.17)$$

where \mathbf{R} and \mathbf{N} are the position and field vectors in the extended phase-space, constituted by the union of phase-space and time. For partial differential equations \mathbf{N} is a functional and things are more complicated. In order to write equation (1.17) we need to define a time coordinate t . However, once we have written the equation in the coordinates we prefer, any coordinate set can be defined in the extended phase-space. In the coordinates Z equation (1.17) reads

$$\frac{dZ^i}{dZ^0} = \frac{N^i}{N^0} \text{ for } i = 1, \dots, d$$

where d is the dimension of the phase-space, $N^i = \mathbf{Z}^i \cdot \mathbf{N}$ are the contravariant components of the field \mathbf{N} and $dZ^0/dt = N^0$. An equivalent formulation of (1.17)

involves functions of the extended phase-space position vector which are constant along the solution path, that is, $F^i(\mathbf{R})$ such that

$$\frac{dF^i}{dt} = \mathbf{N} \cdot \nabla F^i = 0 \text{ for } i = 1, \dots, d. \quad (1.18)$$

The initial conditions of the system are functions of F^i and d linearly independent ∇F^i exist. The contravariant basis $\mathbf{F}^i = \nabla F^i$ is a basis on the phase-space, where the phase-space is defined as the hyper-surface at constant time coordinate F^0 . The function F^0 describes the way in which we parameterize time and, to have a basis of the extended phase-space, its gradient shouldn't be a linear combination of the others \mathbf{F}^i . The geometric interpretation of equation (1.18) is that there exist coordinates F on the extended phase-space such that $\mathbf{N} = N^0 \mathbf{F}_0$ and $N^i = 0$ for $i \geq 1$. This is referred to as solution coordinates, since a particular solution is defined by $(F^0, \bar{F}^1, \dots, \bar{F}^d)$ with \bar{F}^i fixed, that is a straight line.

In order to define non-linearity we should recall the linearity property, that is superposition of effects. Superposition of effects can be expressed with the property that at fixed time coordinate the solution is a linear combination of the phase-space coordinates, so that linear combinations of solutions are still solutions. Again, here the phase-space is defined as the space at fixed time coordinate. This linearity requirement over the phase-space is expressed as

$$F^i(Z) = \sum_{j=1}^d a_j^i(Z^0) Z^j, \text{ for } i = 1, \dots, d. \quad (1.19)$$

Coordinates Z such that the solution has the functional form in equation (1.19) will be referred to as linearity coordinates. Based on equation (1.19), we can state that all integrable ordinary differential equations admit a coordinate system in the extended phase-space such that the equation for the coordinates is linear. In particular, for all time coordinates there exists a corresponding phase-space metric such that superposition of effects holds on the phase-space. Moreover, the differential equation in linearity coordinates is autonomous for appropriate choice of a_j^i . The proof is straightforward referring the solution and linearity coordinates to the Cartesian space-time coordinates x and t . Define a function $Z^0(x, t)$, construct a $d \times d$ invertible matrix \mathbf{a} , whose elements are functions of Z^0 , and its inverse \mathbf{b} . Then the phase-space linearity coordinates corresponding to the linearity time coordinate Z^0 are obtained inverting equation (1.19), $Z^i(x, t) = \sum_{j=1}^d b_j^i(Z^0) F^j(x, t)$ for $i = 1, \dots, d$. Notice that \mathbf{b} should be such that ∇Z^0 is not a linear combination of the others ∇Z^i . By choosing $d\mathbf{a}/dZ^0 = \mathbf{c}\mathbf{a}$, with \mathbf{c} a $d \times d$ constant matrix, the resulting dynamical system (1.17) is also autonomous.

The discussion above shows that “non-linearity” by itself is not a meaningful concept, it should be specified that non-linearity is observed in certain extended phase-space coordinates. If space and time are assumed to be absolute and also

described by means of a Cartesian basis, then non-linear differential equations naturally arise. This amounts to define the phase-space as hyperplanes $t = \text{const}$ and to define a Cartesian basis on the phase-space. On the other hand, if space and time are assumed to be just measure of change, the form of the solution (a linear combination in our case) can be prescribed and corresponding space-time coordinates can be defined accordingly. This amounts to define the phase-space as hyper-surfaces $Z^0 = \text{const}$ in the space-time, together with a general basis defined on the phase-space. The former approach is more intuitive, since we use coordinates which are natural for us. The latter approach is more complicated but in principle more general, since we can require the property of the solution. Both approaches encounter the same practical problems, since determining the linearity coordinates seems as difficult as solving the non-linear differential equation formulated in absolute t and x . In practice, a differential equation is easy to treat if there exists a set of coordinates in which it takes the form of a solvable equation and the transformation from absolute to linearity coordinates can be analytically derived, which seems the most difficult part. However, as observed above, there is a degree of arbitrariness in defining Z^0 and the corresponding $\mathbf{a}(Z^0)$, which may be used to determine the linearity coordinates more easily.

1.4 Cartesian tensors and the statistics of random fields

Turbulent solutions of equation (1.1) look extremely complicated in space and time and display chaotic behaviour. Therefore, Navier-Stokes turbulence is simulated numerically and the statistics of the realizations are employed to characterize turbulence under a statistical viewpoint. Of course, numerical Navier-Stokes turbulence is supposed to be reasonably close to experimental realizations of turbulent flows. The archetypal model of statistically isotropic turbulence is considered in this work. Cartesian tensors are key to study the statistics of homogeneous/isotropic turbulence, since they often constitute a convenient choice to write simple and fundamental kinematic relations.

Multi-point and multi-time correlations are basic instruments for the statistical analysis of random fields. The correlation between the Cartesian velocity components at times t_1, \dots, t_n and points $\mathbf{x}_1, \dots, \mathbf{x}_n$ is

$$\mathcal{C}_{i_1, \dots, i_n} = \langle u_{i_1}(\mathbf{x}_1, t_1) u_{i_2}(\mathbf{x}_2, t_2) \dots u_{i_n}(\mathbf{x}_n, t_n) \rangle \quad (1.20)$$

where $\langle \cdot \rangle$ represents the ensemble average. The complexity of the correlation tensor rapidly increases with the spatial dimensionality, d , and the number of times and points, n , at which the average is evaluated. If the random field \mathbf{u} is statistically isotropic the correlation tensor is strongly simplified. Isotropy means invariance under arbitrary rotation

$$\mathcal{C}_{j_1, \dots, j_n} = \mathcal{C}_{i_1, \dots, i_n} V_{i_1 j_1} V_{i_2 j_2} \dots V_{i_n j_n} \quad (1.21)$$

where rotation is expressed by means of the orthogonal matrix \mathbf{V} .

For single-point statistics, $\mathbf{x}_1 = \mathbf{x}_2 = \dots = \mathbf{x}_n$, the isotropy constraint can be applied relatively easily, since there is no dependence on the separation vectors $\mathbf{x}_i - \mathbf{x}_j$. A key result in classical group theory is that all the isotropic tensors can be expressed in terms of linearly independent fundamental isotropic tensors [85, 163]. Every invariant is isotropic, since it is a tensor of order zero. An isotropic tensor of order one, such that $\mathcal{C}_j = \mathcal{C}_i V_{ij}$, is identically zero because of the arbitrariness of the rotation axis (i.e. the eigenvector of \mathbf{V} with unitary eigenvalue). For small rotations $\Delta\varphi$ about a generic axis \mathbf{w} , the rotation matrix can be expanded at first order as $V_{ij} \sim \delta_{ij} + \Delta\varphi \epsilon_{ikj} w_k$. Using the arbitrariness of w_k and the properties of the permutation symbol, for a second order isotropic tensor, $\mathcal{C}_{j_1 j_2} = \mathcal{C}_{i_1 i_2} V_{i_1 j_1} V_{i_2 j_2}$ implies $\mathcal{C}_{i_1 i_2} = \lambda \delta_{i_1 i_2}$. Therefore an isotropic tensor of order two should be proportional to the Kronecker delta. The methodology extends to higher order isotropic tensors which are expressed as linear combinations of products of the Kronecker delta and the permutation symbol. For example, fourth order isotropic Cartesian tensors $\mathcal{C}_{i_1 i_2 i_3 i_4}$ can be expressed as linear combinations of

$$\delta_{i_1 i_2} \delta_{i_3 i_4}, \quad \delta_{i_1 i_3} \delta_{i_2 i_4}, \quad \delta_{i_1 i_4} \delta_{i_2 i_3},$$

so that isotropic tensors representation is reduced to counting and index contractions. However, dimensionality plays a key role and the basic derivation reported above does not provide appropriate results in dimension five or higher for odd-order tensors and in dimension eight or higher for even-order tensors. In particular, some of the products of Kronecker deltas may be linearly dependent of the others and the basis of high-dimensional isotropic tensors spaces is determined by means of the Capelli's identity [163, 88]. Isotropic tensors of order up to six will be used in the thesis.

For two-point statistics, $\mathbf{x}_1 = \mathbf{x}$ and $\mathbf{x}_2 = \mathbf{x}'$, things are more complicated due to the dependence of the statistics itself on the centroid $\mathbf{y} \equiv (\mathbf{x} + \mathbf{x}')/2$ and separation vector $\mathbf{r} \equiv \mathbf{x} - \mathbf{x}'$. An important two-point statistics, employed throughout the thesis, is the structure function of order n , which is defined as

$$\mathcal{S}_{i_1, \dots, i_n} = \langle (u_{i_1} - u'_{i_1})(u_{i_2} - u'_{i_2}) \dots (u_{i_n} - u'_{i_n}) \rangle, \quad (1.22)$$

where $\mathbf{u} = \mathbf{u}(\mathbf{x}, t)$ and $\mathbf{u}' = \mathbf{u}(\mathbf{x}', t)$. If the random field under consideration is statistically homogeneous its statistics do not depend on \mathbf{y} . If the random field is also statistically isotropic its statistics depend only on the separation length $r \equiv \|\mathbf{r}\|$ and the moments of its Cartesian components take a particular form. This is again a consequence of the Weyl theorem, extended including the dependence of the two-point statistics upon \mathbf{r} [126]. An isotropic linear form applied to the vector \mathbf{v} , $L(\mathbf{r}; \mathbf{v})$ can be expressed in terms of the invariants formed using \mathbf{r} and \mathbf{v} , namely $\mathbf{r} \cdot \mathbf{r}$, $\mathbf{r} \cdot \mathbf{v}$ and $\mathbf{v} \cdot \mathbf{v}$. Linearity in \mathbf{v} implies $L(\mathbf{r}; \mathbf{v}) = f(r^2) r_j v_j$ so that the matrix representation of an isotropic linear form L is

$$L_i = f(r^2) r_i. \quad (1.23)$$

An isotropic bilinear form applied to the vectors \mathbf{v} and \mathbf{w} , $Q(\mathbf{r}; \mathbf{v}, \mathbf{w})$ is expressible in terms of the invariants formed using \mathbf{r} , \mathbf{v} and \mathbf{w} , namely their scalar products and the determinant $\epsilon_{ijk}r_k b_j a_i$. Linearity in \mathbf{v} and \mathbf{w} implies $Q(\mathbf{r}; \mathbf{v}, \mathbf{w}) = f(r^2)r_j r_i v_i w_j + g(r^2)a_i b_j + \epsilon_{ijk}r_k a_i b_j$ and, imposing symmetry, the matrix representation of an isotropic bilinear form Q

$$Q_{ij} = f(r^2)r_i r_j + g(r^2)\delta_{ij}. \quad (1.24)$$

A simple geometrical interpretation of the invariants that can be constructed from up to three vectors is as follows [126]. The only scalar associated with a vector is its length. The scalars associated with two vectors, other than their lengths, is the angle between the vectors. The additional invariant due to the third vector is the volume of the parallelepiped constituted by the vectors. The arguments presented above extend to higher orders, for example, the matrix representation of an isotropic trilinear form is

$$T_{ijk} = f(r^2)r_i r_j r_k + g(r^2)r_i \delta_{jk} + h(r^2)r_j \delta_{ik} + l(r^2)r_k \delta_{ij} \quad (1.25)$$

which is of special interest to study the turbulent energy cascade.

Equation (1.25) together with the incompressibility constraint, allows to determine the functional form of the velocity structure functions and how they relate to each other [121]. This results into powerful relations like the Karman-Howarth-Monin equation [111]. However, in order to apply the incompressibility constraint, it is often necessary to prove additional relations which involve mainly the divergence of the structure function with respect to the separation vector and computation of moments of the pressure gradient [74]. Those relations have been subject of positive criticism [60, 102] which was finally resolved in [74], where the implications of local homogeneity were clearly defined and actuated. In conditions of local homogeneity, at small separation r , the two-point statistics changes rapidly with respect to the separation vector \mathbf{r} and relative slowly with respect to the centroid \mathbf{y} . Therefore, when differentiation with respect to \mathbf{x} is transformed into differentiation with respect to \mathbf{r} and \mathbf{y} , the derivative with respect to the centroid is negligible compared to that with respect to the separation vector [74]. In practice, derivatives with respect to \mathbf{x} inside the average and derivatives with respect to \mathbf{r} outside the average commute. The same applies to $-\mathbf{x}'$ and \mathbf{r} . Based on the local homogeneity hypothesis and the resulting differentiation techniques, proofs that were referred to be handy and complicated in the past [111], can be performed relatively easily and often under assumptions which are weaker than global isotropy of the random field. Here we report examples involving the second and third order structure functions that constitute basic relations in turbulence theory and will be useful throughout the thesis.

For the second order structure function, it follows from incompressibility and

local homogeneity that [74]

$$\begin{aligned} \frac{\partial}{\partial r_i} \mathcal{S}_{ij} &= \left\langle (u_i - u'_i) \frac{\partial}{\partial x_i} u_j \right\rangle = \frac{\partial}{\partial r_i} \langle (u_i - u'_i) u_j \rangle = \\ &= - \left\langle \frac{\partial}{\partial x'_i} ((u_i - u'_i) u_j) \right\rangle = 0, \end{aligned} \quad (1.26)$$

where u_i is evaluated at \mathbf{x} and u'_i is evaluated at \mathbf{x}' , both at the same time. With the additional hypothesis of local isotropy, so that (1.24) applies, and using again incompressibility, the result above allows to derive the link between second order transverse and longitudinal velocity structure functions

$$\langle \Delta u_{\perp}^2 \rangle = \langle \Delta u_{\parallel}^2 \rangle + \frac{r}{2} \frac{d}{dr} \langle \Delta u_{\parallel}^2 \rangle \quad (1.27)$$

where Δu_{\parallel} and Δu_{\perp} are the velocity increments parallel and orthogonal to the separation vector respectively. From equation (1.26) it follows also that $\partial_i \partial_j \mathcal{S}_{ij} = 0$ which corresponds to the relation for the velocity gradient $\mathbf{A} = \nabla \mathbf{u}$,

$$\langle A_{ij} A_{ji} \rangle = 0. \quad (1.28)$$

Defining the symmetric and anti-symmetric parts of the velocity gradient,

$$\mathbf{S} = \frac{1}{2} (\mathbf{A} + \mathbf{A}^{\top}), \quad \mathbf{R} = \frac{1}{2} (\mathbf{A} - \mathbf{A}^{\top}), \quad (1.29)$$

the Betchov relation [10] between vorticity and strain magnitude is obtained from equation (1.28)

$$\|\boldsymbol{\omega}\|^2 = \omega_i \omega_i = 2S_{ij} S_{ij} = 2\|\mathbf{S}\|^2. \quad (1.30)$$

For the third order structure function, by using just local homogeneity and incompressibility, it follows that,

$$\begin{aligned} \frac{\partial}{\partial r_k} \frac{\partial}{\partial r_i} \frac{\partial}{\partial r_j} \mathcal{S}_{ijk} &= - \frac{\partial}{\partial r_k} \left\langle \frac{\partial}{\partial x'_i} \frac{\partial}{\partial x_j} (u_i - u'_i)(u_j - u'_j)(u_k - u'_k) \right\rangle = \\ &= - \frac{\partial}{\partial r_k} \left\langle \frac{\partial}{\partial x'_i} \frac{\partial}{\partial x_j} (u_i u_j u_k - u'_i u_j u_k - u_i u'_j u_k - u_i u_j u'_k + \right. \\ &\quad \left. + u'_i u'_j u_k + u'_i u_j u'_k + u_i u'_j u'_k - u'_i u'_j u'_k) \right\rangle = \\ &= - \frac{\partial}{\partial r_k} \left\langle \frac{\partial}{\partial x'_i} \frac{\partial}{\partial x_j} (-u_i u'_j u_k - u_i u_j u'_k + u'_i u'_j u_k + u_i u'_j u'_k) \right\rangle = \\ &= - \frac{\partial}{\partial r_i} \left\langle \frac{\partial}{\partial x'_j} \frac{\partial}{\partial x_k} (-u_i u_j u'_k + u_i u'_j u'_k) \right\rangle = \\ &= - \frac{\partial}{\partial r_j} \left\langle \frac{\partial}{\partial x'_k} \frac{\partial}{\partial x_i} (-u_i u_j u'_k + u_i u'_j u'_k) \right\rangle = 0, \end{aligned} \quad (1.31)$$

which is a purely kinematic relation for a solenoidal vector field and does not involve the Navier-Stokes momentum equation. With the additional hypothesis of local isotropy, and using again incompressibility, the result above allows to derive the link between third order mixed and longitudinal velocity structure functions

$$\langle \Delta u_{\perp}^2 \Delta u_{\parallel} \rangle = \frac{1}{6} \frac{d}{dr} \left(r \langle \Delta u_{\parallel}^3 \rangle \right). \quad (1.32)$$

The corresponding one-point relation follows from

$$\begin{aligned} \langle A_{ij} A_{jk} A_{ki} \rangle &= \left\langle \frac{\partial}{\partial x_i} (A_{ij} A_{jk}) - A_{ij} u_k \frac{\partial u_j}{\partial x_i \partial x_k} u_k \right\rangle = \\ &= \frac{\partial}{\partial x_i} \left\langle A_{ij} A_{jk} u_k - \frac{1}{2} u_i A_{jk} A_{ki} \right\rangle = 0 \end{aligned} \quad (1.33)$$

which implies the Betchov relation between strain self-amplification and vortex stretching [10]

$$\langle \text{Tr}(\mathbf{SSS}) \rangle = \langle S_{ij} S_{jk} S_{ki} \rangle = -\frac{3}{4} \langle S_{ij} \omega_i \omega_j \rangle = -\frac{3}{4} \langle \boldsymbol{\omega}^{\top} \mathbf{S} \boldsymbol{\omega} \rangle. \quad (1.34)$$

For a summary of homogeneous/isotropic statistical relations and their applicability see [74].

The hypothesis of local homogeneity, with the subsequent operational simplifications presented above, allow to derive the Karman-Howart-Monin equation from the incompressible Navier-Stokes equations

$$\frac{\partial \mathcal{S}_{ii}}{\partial t} + \frac{\partial \mathcal{S}_{ikk}}{\partial r_k} = 2\nu \frac{\partial^2 \mathcal{S}_{ii}}{\partial r_k \partial r_k} - 4\langle \varepsilon \rangle, \quad (1.35)$$

where ε is the dissipation rate. Equation (1.35) suggests the cascade picture of statistically steady and homogeneous turbulence, since $\partial_k \mathcal{S}_{ikk}$ is a transport term and $\partial_{kk}^2 \mathcal{S}_{ii}$ is a dissipation term that contributes mainly at the smallest scales. Therefore, at intermediate scales, large enough to neglect dissipation but small enough to eventually neglect large-scale inhomogeneity and energy sources, the energy of the velocity increments $\mathcal{K} = \mathcal{S}_{ii}/2 = \langle \|\Delta \mathbf{u}\|^2 \rangle / 2$ flows on average across the scales r at a rate ε . At smallest scales, dominated by viscous effects, the energy of the velocity fluctuations is dissipated. Based on that, the Kolmogorov length-scale at which the energy of the fluctuations is dissipated can be defined, $\eta = (\nu^3/\varepsilon)^{1/4}$. In three dimensional turbulence there is on average a direct energy cascade, from the largest to the smallest scales, since Δu_{\parallel} is negatively skewed. This is taken as a phenomenological evidence, a rigorous proof based on the Navier-Stokes equation is currently missing. However, models (e.g. the Eddy Damped Quasi-Normal Markovian model) which result from a perturbative Renormalization-Group approach to the Navier-Stokes equations [136] can quantitatively predict the skewness of the longitudinal velocity increments [166]. The mechanism of average energy cascade will be analyzed in Chapter 2.

1.4.1 Velocity increments and the coarse-grained gradient

Two-point and one-point statistics can be approximately related by means of coarse-graining. Reducing a two-point statistics to a one-point statistics allows to simplify the computations removing the dependence of the statistics upon the separation vector and the classical Weyl theorem can be applied. However, the order of the tensors usually increases. Coarse-graining consists of smoothing the field under consideration up to a scale ℓ , by means of convolution with a kernel filtering function,

$$\tilde{\mathbf{u}}(\mathbf{x}, t) = \int d\mathbf{x}' G_\ell(\mathbf{x}' - \mathbf{x}) \mathbf{u}(\mathbf{x}', t) \quad (1.36)$$

where $G_\ell(-\mathbf{x}) = G_\ell(\mathbf{x})$ and $\int G_\ell = 1$. The filtered field $\tilde{\mathbf{u}}$ differs from the full field \mathbf{u} due to a sub-grid contribution, which consists of fluctuations that take place on scale smaller than ℓ . The coarse-grained field $\tilde{\mathbf{u}}$ is smooth up to scale ℓ and therefore $\Delta\tilde{\mathbf{u}} \simeq \tilde{\mathbf{A}} \cdot \mathbf{r}$ for $r \lesssim \ell$, which allows to approximate the moments of the velocity increments. For example, neglecting the sub-grid contribution, the second order Eulerian structure function can be expressed as

$$\langle \|\Delta\mathbf{u}\|^2 \rangle \simeq \langle \tilde{A}_{ji} \tilde{A}_{ik} \rangle r_j r_k, \quad (1.37)$$

where the gradients are smoothed up to scale $\ell \simeq r$. Then, the one-point isotropic tensor of order two $\langle \tilde{A}_{ji} \tilde{A}_{ik} \rangle$ can be analyzed according to the classical isotropic tensors representation [85], resulting into

$$\langle \|\Delta\mathbf{u}\|^2 \rangle \simeq \frac{1}{3} \langle \tilde{\mathbf{A}}^\top : \tilde{\mathbf{A}} \rangle r^2. \quad (1.38)$$

1.5 Equations for particle motion in fluids

The viewpoint presented above is mainly Eulerian, that is, turbulence is analyzed at a certain point fixed in space. An alternative approach is the Lagrangian viewpoint in which the features of the turbulent motion are studied by following fluid particles along their path. This corresponds to introducing the Lagrangian derivative $D/Dt = \partial_t + \mathbf{u} \cdot \nabla$ in the Navier-Stokes equations (1.1),

$$\nabla \cdot \mathbf{u} = 0 \quad (1.39a)$$

$$\frac{D\mathbf{x}}{Dt} = \mathbf{u} \quad (1.39b)$$

$$\frac{D\mathbf{u}}{Dt} = -\frac{1}{\rho_f} \nabla p + \nu \nabla^2 \mathbf{u}. \quad (1.39c)$$

Equations (1.39) describe the motion of fluid particles which are uniquely identified by the the initial position vector $\mathbf{X} = \mathbf{x}(0)$. However, the equations for the

motion of a single fluid particle is not in closed form since the pressure gradient ∇p and viscous stress $\nu \nabla^2 \mathbf{u}$ involve information at points other than the fluid particle considered. This non-locality is a key problem in the Lagrangian description of turbulence. Nevertheless, Lagrangian modelling of single-particle motion can provide insight into the turbulent dynamics and currently available models can produce statistical results which are in good agreement with the outcome of Direct Numerical Simulations of Navier-Stokes turbulence [108]. In Chapter 3 equations (1.39) will be employed to study the Lagrangian dynamics of the velocity gradient and investigate the non-local part of the pressure contribution to the gradient dynamics.

Lagrangian dynamics of particles in turbulence is of wide practical interest when inertial particles or bubbles are considered [147, 81, 104]. In order to study the motion of objects suspended in turbulent flows the expression of the force acting on the object itself should be determined. The thesis treats particles which are inertial, rigid, spherical and small with respect to the flow scales. Since the particle is small with respect to the smallest scale of the flow, and the relative velocity of the particle with respect to the fluid is also supposed to be small, the Reynolds number based on the particle size and relative velocity is small. Therefore, the flow in the proximity of the particle can be approximated as laminar, dominated mainly by the boundary condition at the particle surface. The expression of the forces exerted on an inertial, rigid, spherical particle, immersed in a low Reynolds number flow has generated debates in the literature [144, 37, 21, 5]. A satisfactory expression for the force acting on the particle, widely used in subsequent works, has been derived in [107]. However, as remarked in [107], due to the vanishing Reynolds number hypothesis the differences between the various expressions proposed for the force exerted on the particle are negligible, that is, the differences between the various expressions for the force are of the order of the contributions neglected in approximating the equations.

An inertial and rigid sphere suspended in a fluid flow perturbs the undisturbed velocity field \mathbf{u} , generating a modified flow field \mathbf{v} . It is convenient to describe the motion of the fluid around the particle from the viewpoint of the particle, defining the relative position $\mathbf{z} = \mathbf{x} - \mathbf{x}_p$ and relative velocity $\mathbf{w} = \mathbf{v} - \mathbf{v}_p$, where $\mathbf{x}_p(t)$ and $\mathbf{v}_p(t)$ are the particle position and velocity. The relative velocity field is described by the Navier-Stokes equations together with the no-slip boundary condition at the particle surface

$$\nabla \cdot \mathbf{w} = 0 \quad (1.40a)$$

$$\frac{D\mathbf{w}}{Dt} = -\frac{1}{\rho_f} \nabla p + \nu \nabla^2 \mathbf{w} + \mathbf{g} - \frac{d\mathbf{v}_p}{dt} \quad (1.40b)$$

$$\mathbf{w} = \boldsymbol{\omega}_p \times \mathbf{z} \text{ on } \|\mathbf{z}\| = r_p \quad (1.40c)$$

$$\mathbf{w} = \mathbf{u} - \mathbf{v}_p \text{ for } \|\mathbf{z}\| \rightarrow \infty, \quad (1.40d)$$

where $\boldsymbol{\omega}_p$ is the particle angular velocity, \mathbf{g} is the gravitational acceleration and r_p

is the particle radius, which serves to physically define the limit of infinite distance. Here the total derivative d/dt denotes derivation along the inertial particle path. In order to allow for a perturbative approach, the relative velocity field \mathbf{w} is separated into the undisturbed relative velocity field $\mathbf{w}^0 = \mathbf{u} - \mathbf{v}_p$ and the disturbance generated by the particle $\mathbf{w}^1 = \mathbf{w}^0 - \mathbf{w}$. The undisturbed relative velocity is governed by the Navier-Stokes equations and it does not explicitly include small-scale variations due to the presence of the particle

$$\nabla \cdot \mathbf{w}^0 = 0 \quad (1.41a)$$

$$\frac{\partial}{\partial t} \mathbf{w}^0 + \mathbf{w}^0 \cdot \nabla \mathbf{w}^0 = -\frac{1}{\rho_f} \nabla p^0 + \nu \nabla^2 \mathbf{w}^0 + \mathbf{g} - \frac{d\mathbf{v}_p}{dt}. \quad (1.41b)$$

The small-scale variations due to the particle are instead key in the equations for \mathbf{w}^1 . Under the small particle Reynolds number assumption, based on the particle radius and relative velocity with respect to the flow, the convective term can be neglected and the disturbance flow is approximately described by the equations for the unsteady Stokes problem

$$\nabla \cdot \mathbf{w}^1 = 0 \quad (1.42a)$$

$$\partial_t \mathbf{w}^1 = -\frac{1}{\rho_f} \nabla p^1 + \nu \nabla^2 \mathbf{w}^1 \quad (1.42b)$$

$$\mathbf{w}^1 = \mathbf{v}_p - \mathbf{u} + \boldsymbol{\omega}_p \times \mathbf{z} \text{ on } \|\mathbf{z}\| = r_p \quad (1.42c)$$

$$\mathbf{w}^1 \rightarrow 0 \text{ for } \|\mathbf{z}\| \rightarrow \infty \quad (1.42d)$$

For a particle relative velocity scale w' , a flow length scale L and fluid velocity scale U equations (1.42) requires that

$$\frac{r_p w'}{\nu} \ll 1, \quad \frac{r_p^2 U}{\nu L} \ll 1. \quad (1.43)$$

A key observation to derive a consistent expression for the equation of the force exerted on the particle [107] is that the order of Taylor expansion with respect to the coordinate z of the pressure and relative velocity fields should generate contributions of the same order to the stress tensor

$$\boldsymbol{\sigma} = -p\mathbf{I} + \mu (\nabla \mathbf{w} + \nabla \mathbf{w}^\top) \quad (1.44)$$

where $\mu = \rho_f \nu$ is the fluid dynamic viscosity. In particular, the stress due to the disturbance induced by the particle is assumed to be linear in z , therefore p is linear while \mathbf{w} is quadratic. The force exerted on the sphere from the undisturbed flow can be approximated as

$$\mathbf{F}^0 = \int_S \boldsymbol{\sigma}^0 \cdot \mathbf{n} dS \simeq \frac{4}{3} \pi r_p^3 [-\nabla p^0 + \mu \nabla^2 \mathbf{w}^0] = -m_f \mathbf{g} + m_f \left. \frac{D\mathbf{u}}{Dt} \right|_{x_p}, \quad (1.45)$$

under the hypothesis $r_p/L \ll 1$, that is, the undisturbed gradients vary on scales much larger than the particle size. Here $m_f = 4/3\pi\rho_f r_p^3$ is the mass of the fluid displaced by the particle. The contribution of the disturbance field is computed by solving the unsteady Stokes problem. The result is [107]

$$\begin{aligned}
 m_p \frac{d\mathbf{v}_p}{dt} = & 6\pi\mu r_p \left\{ \left[\mathbf{u}_p - \mathbf{v}_p + \frac{r_p^2}{6} \nabla^2 \mathbf{u}_p \right] + \right. \\
 & \left. + r_p \int_0^t d\tau \frac{d/d\tau \left[\mathbf{u}_p(\tau) - \mathbf{v}_p(\tau) + r_p^2 \nabla^2 \mathbf{u}_p(\tau)/6 \right]}{\sqrt{\pi\nu(t-\tau)}} \right\} + \\
 & + m_f \frac{D\mathbf{u}}{Dt} \Big|_{\mathbf{x}_p} + \frac{m_f}{2} \frac{d}{dt} \left[\mathbf{u}_p - \mathbf{v}_p + \frac{r_p^2}{10} \nabla^2 \mathbf{u}_p \right] + (m_p - m_f) \mathbf{g} \quad (1.46)
 \end{aligned}$$

where $\mathbf{u}_p(t) = \mathbf{u}(\mathbf{x}_p(t), t)$. Equation (1.46) includes the Stokes drag, due to the slip velocity between the particle and the undisturbed flow and the Faxén correction, due to the curvature of the velocity field. The history term, that involves a weighted time average of the force on the particle, is referred to as Basset history term. The fluid acceleration and added mass contributions are proportional to the mass of fluid displaced by the particle. Also, external mass forces may act on the particle. There is no force on the particle due to the flow shear because of the small particle Reynolds number hypothesis. Also, the particle is isolated, that is, other particles or boundaries are located at many particle radii far from the particle. This requires that the volume of the particle phase is small compared to the volume of the domain.

The fluid acceleration term derived in [107] and reported in equation (1.46), $D\mathbf{u}/Dt$, differs from the result in [21], $d\mathbf{u}/dt$. The total derivative along the inertial particle trajectory and along the fluid particle trajectory are in general different. However, it is erroneous to distinguish between the derivatives along the fluid particle trajectory and the inertial particle trajectory in the limit of vanishingly small Reynolds number. Indeed, the difference between the derivatives is $m_f(D/Dt - d/dt)\mathbf{u} = m_f \mathbf{w}^0 \cdot \nabla \mathbf{w}^0$ which is of the order of $r_p^2 U / (\nu L) \ll 1$ compared to the Stokes drag. The same discrepancy is in the literature regarding the added mass term but, again, the small Reynolds number limits the discussion about the details of the term in equation (1.46).

The relative importance of the terms in equation (1.46) can be evaluated based on the scales of the particle and the flow field. The particle inertia contribution and the Stokes drag are comparable if the relative velocity scale with respect to the large scale velocity is $W/U = O(\rho_p r_p^2 U / (\rho_f \nu L))$. If the particle is much denser than the fluid the particle inertia contribution can be relevant, even if $r_p^2 U / (\nu L) \ll 1$ by hypothesis. The fluid acceleration term and the Stokes drag are comparable at $W/U \simeq r_p^2 U / (\nu L)$, which results into small relative velocity by assumption. The Faxén correction [59], due to the interaction between the particle and the curvature of the velocity field, produces a relative velocity $W/U \simeq r_p^2 / L^2$, which was also

assumed to be negligible. The ratio between the added mass contribution and the Stokes drag is $O(r_p^2 U / (\nu L))$ while the history term contribution is $O(\sqrt{r_p^2 U / (\nu L)})$ with respect to the Stokes drag. Therefore, the Basset history term [7] can be the most relevant among the neglected terms. The Basset, inertial and added mass terms are important when focus is put on the transient dynamics. For example, when a particle is settling from rest under the action of gravity, the particle and fluid velocity are very close at the beginning of the motion and the resulting Stokes drag is small. In that situation inertial, added mass and history forces compensate each other. Finally, the convective acceleration due to the motion of the particle across velocity gradients is $O(UW/L)$ which are generally small, except in case of very sharp gradients or mixing between flows with different kinetic energy.

Summarizing, often the most important terms are the linear Stokes drag, the particle inertial force and gravity acceleration. This results into the simplified point-particle model, which will be employed throughout the thesis

$$\frac{d\mathbf{x}_p}{dt} = \mathbf{v}_p \quad (1.47a)$$

$$\frac{d\mathbf{v}_p}{dt} = \frac{\mathbf{u}(\mathbf{x}_p, t) - \mathbf{v}_p}{\tau_p} + \mathbf{g} \quad (1.47b)$$

with the particle velocity response time

$$\tau_p = \frac{2 \rho_p r_p^2}{9 \rho_f \nu}. \quad (1.48)$$

Equations (1.47) constitute a good approximation for the motion of heavy and small particles which move with small relative velocity with respect to the fluid (i.e. the particle phase should be well mixed). Also, the average distance between particles should be large with respect to r_p to avoid particle-particle interactions and boundaries should be located far away from the particles. The same derivation and analogous hypothesis applies for the particle temperature θ_p , which is described by equations formally identical to (1.47),

$$\frac{d\theta_p}{dt} = \frac{T(\mathbf{x}_p, t) - \theta_p}{\tau_\theta} \quad (1.49)$$

with the fluid temperature T and the particle thermal response time

$$\tau_\theta = \frac{1 \rho_p r_p^2}{3 \rho_f \kappa}, \quad (1.50)$$

where κ is the thermal conductivity of the fluid. The Prandtl number is defined as $\text{Pr} = \nu/\kappa$. The Stokes number $\text{St} = \tau_p/\tau_\eta$ and thermal Stokes number $\text{St} = \tau_\theta/\tau_\eta$ can be defined based on the particle response times and the smallest time scale of the turbulent flow, that is, the Kolmogorov time-scale $\tau_\eta = \eta^2/\nu$.

1.5.1 Saffman lift

A small particle suspended in a shear-flow experiences a lift force due to the fluid inertia and, as a consequence, the particle drifts across the flow streamlines [127]. For uniform shear, not only at the particle scale but also at larger scales, the particle experiences a net lateral force and moves steadily with respect to the fluid. That force, known as Saffman lift, is not considered in equation (1.46), since it vanishes in the limit of zero particle Reynolds number [127]. Experiments by [134] showed the so called tubular pinch effect, that is, particles in a pressure driven pipe flow migrate from the centerline to about half the pipe radius. The effect takes place for neutrally buoyant and buoyant particles and the side migration force and walls influence are concurrent. In order to explain this, Saffman neglected the effect of the walls and focused on the effect of mean shear $\mathbf{\Gamma}$. In particular, Oseen convective terms, proportional to $\mathbf{\Gamma}$, were retained in the approximated Navier-Stokes equations. There are two particle velocity scales, the relative velocity W and the velocity difference induced by the shear Γr_p , that correspond to the scales ν/W and $\sqrt{\nu/\Gamma}$ at which inertial and viscous forces are of the same order. In the far field the equations can be linearized and the particle approximated by a point-particle. The momentum balance for the disturbance field \mathbf{w} is then approximated as [138]

$$(\mathbf{\Gamma} \cdot \mathbf{z}) \cdot \nabla \mathbf{w} + \mathbf{\Gamma} \cdot \mathbf{w} = -\frac{1}{\rho_f} \nabla p' + \nu \nabla^2 \mathbf{w} + 6\pi\nu r_p \mathbf{w}_p \delta(z), \quad (1.51)$$

where $\mathbf{z} = \mathbf{x} - \mathbf{x}_p$ and $z = \|\mathbf{z}\|$. The magnitude of the lift force F_L acting on the particle is obtained by perturbation methods [127]

$$F_L = 6.46\mu r_p \sqrt{\frac{\Gamma r_p^2}{\nu}} w_p. \quad (1.52)$$

The ratio between the Saffman and Stokes forces is $O\left(\sqrt{r_p^2 U / (\nu L)}\right)$ which is small by hypothesis (1.43). However, the applicability of the hypothesis (1.43) is weakened by the square root and therefore, the Saffman lift is a key feature of the motion of moderately large particles in non-uniform flows [39].

1.6 Features and numerical simulation of inertial particles in turbulence

The transport of particles suspended in turbulent flows plays a central role in many physical and engineering problems, from combustion engines to the cooling of miniaturized components [172, 124], from cloud microphysics to sediment distribution in aquatic environments [44, 130]. Recent advances in High-Performance-Computing (HPC) allowed for high accuracy Direct Numerical Simulation (DNS) of such particle-laden turbulent flows.

Most of the literature deals with the so called one-way coupling regime, that is, on the situation in which the flow drives particle dynamics, but the presence of the particles does not have any influence on the fluid phase. This modelling hypothesis is justified for diluted suspensions, with a volume fraction not exceeding 10^{-6} [54]. Even in this dilute and one-way coupled regime, inertial particles display a non-trivial behaviour, which differs from the behaviour of the underlying fluid particles. Indeed, inertial particles can sample the surrounding turbulent flow in a non-uniform and correlated manner [147]. Particle inertia in a turbulent flow is measured through the Stokes number $St \equiv \tau_p/\tau_\eta$, which compares the particle response time to the Kolmogorov time scale. A striking feature of inertial particle motion in turbulent flows is that they spontaneously cluster even in incompressible flows [106, 160, 9, 81]. This clustering can take place across a wide range of scales [9, 16, 81], and the small-scale clustering is maximum when $St = O(1)$. A variety of mechanisms has been proposed to explain this phenomena: when $St \ll 1$ the clustering is caused by particles being centrifuged out of regions of strong rotation [106, 35], while for $St \geq O(1)$, a non-local mechanism generates the clustering, whose effect is related to the particles memory of its interaction with the flow along its path-history [71, 72, 18, 17, 16]. Recent results on the clustering of settling inertial particles in turbulence have corroborated this picture, showing that strong clustering can occur even in a parameter regime where the centrifuge effect cannot be invoked as the explanation for the clustering, but is caused by a non-local mechanism [82]. Moreover, the polydispersity and gravity have non-trivial effects on the particle distribution and relative velocity [47]. Furthermore, inertial particles form caustics regions [165], in which the relative velocity of inertial particle pairs is much larger than the fluid relative velocity at the same separation. This has implications, for example, on the growth of water droplets in atmospheric clouds.

The particle mass fraction is often large enough to allow particles to strongly affect the surrounding turbulent flow. This situation is referred to as two-way coupling regime [54] and will be considered throughout the thesis. In Chapter 4 we propose a numerical method based on the Non-Uniform Fast Fourier Transform (NUFFT) to simulate two-way coupled particle-laden turbulent flows. In Chapter 5, we will analyze in detail the interaction between the particle temperature and the fluid temperature in isotropic turbulence, while in 6 the condensational growth of cloud droplets will be considered. When the mass loading is even larger, with a volume fraction exceeding 10^{-3} [54], the particle-particle interaction becomes important, which is referred to as four-way coupling regime and requires the solution of the flow around each single particle. In the model employed we neglect particle-particle interactions that include collisions, lubrication and the perturbation of the flow in the region of a particle induced by other particles. A way to capture the whole physics of the interaction of the flow with the particle would be carry out a particle resolved DNS that, at the current state of the art, can deal with a limited

number of particles and can not simulate a wide range of flows of practical interest. Moreover, only particles large with respect to the grid resolution can be simulated since the computational grid has to include the particle boundary.

Part I

Velocity gradient dynamics in isotropic turbulence

Chapter 2

Turbulent Energy Cascade

In three dimensional turbulence there is on average a cascade of kinetic energy from the largest to the smallest scales of the flow. In this Chapter a multi-scale expression for the energy flux is derived as a functional of the coarse-grained velocity gradient tensor. The expression obtained allows to observe that vortex stretching is in fact not the main contributor to the average cascade, in contrast with the dominant idea in turbulence theory. Here we show theoretically and numerically that the self-amplification of the strain-rate field is the main contributor to the average energy cascade, and we provide several arguments for why its role must not be conflated with that of vortex stretching. However, numerical results indicate that vortex stretching plays a more important role during fluctuations of the cascade about its average behavior, which can be related to the strong intermittency of the vorticity. We also comment on the paradoxical role of vortex stretching with respect to the energy cascade and the energy dissipation rate dynamics.

This piece of work has been published in the Journal of Fluid Mechanics and most of the following material can be found in [24].

2.1 Introduction

Fluid turbulence is a non-equilibrium, high-dimensional system, and in three dimensions (3D), it exhibits an average cascade of energy from the largest scales of the system, where the energy is injected, to the smallest scales, where it is dissipated [57]. While the cascade ultimately arises from inertial forces in the flow, a detailed understanding of the cascade mechanism remains elusive [6].

One of the first descriptions of the energy cascade in turbulence [125] is that cascade occurs through a hierarchical process of instabilities whereby eddies break down and pass their energy to smaller eddies. However, there is no clear connection between this mechanism and the Navier-Stokes equation (NSE) governing the flow. An alternative idea, that has become the dominant paradigm, is that vortex

stretching (VS) drives the cascade [143, 142, 145, 42, 48]. Since Vortex Stretching explicitly appears in the equations for the velocity gradients [121], it is an appealing candidate for the cascade mechanism. However, theoretical demonstrations of the direct link between Vortex Stretching and the energy cascade are limited. In [14] a closure model was used to obtain a result relating the energy cascade and Vortex Stretching. The authors considered single-point statistics and investigated the energy flux between large, resolved, scales and smaller, sub-grid, scales. An asymptotic result that connects Vortex Stretching and the energy cascade in the limit of vanishingly small scales of the flow is derived [42] based upon the well-known Betchov relations [10].

Numerical studies have reported evidence that appears consistent with the idea that Vortex Stretching drives the energy cascade [42, 48]. However, it is possible that these numerical results only reflect correlations between the quantities, not causal connections. Stating that Vortex Stretching is the cause of the energy cascade is stronger than stating a relation between Vortex Stretching and energy cascade. Also, Vortex Stretching may be part, but not the sole mechanism, contributing to the cascade. Moreover, theoretical problems with the Vortex Stretching mechanism have also been discussed in the literature. For example, in [150, 129] it is argued that Vortex Stretching hinders the fluid kinetic energy dissipation, and that this implies that Vortex Stretching hinders the energy cascade, since dissipation is supposed to be the end result of the cascade.

In this Chapter we provide a theoretical analysis of the average turbulence cascade which allows to clarify the role Vortex Stretching plays in the energy cascade. This is achieved by means of the velocity gradient coarse-grained on variable scale, under the hypothesis of isotropic turbulence and the constrain of incompressibility.

2.2 Theoretical background

The multiscale properties of turbulence are traditionally analyzed using the velocity increments

$$\Delta \mathbf{u}(\mathbf{y}, \mathbf{r}, t) \equiv \mathbf{u}(\mathbf{y} + \mathbf{r}/2, t) - \mathbf{u}(\mathbf{y} - \mathbf{r}/2, t) \quad (2.1)$$

where \mathbf{u} is the fluid velocity, and \mathbf{r} is the vector separating two points in the flow with centroid \mathbf{y} [90, 121, 60]. The average turbulent kinetic energy at scale $r \equiv \|\mathbf{r}\|$,

$$\mathcal{K}(\mathbf{y}, \mathbf{r}, t) \equiv \frac{1}{2} \langle \|\Delta \mathbf{u}(\mathbf{y}, \mathbf{r}, t)\|^2 \rangle \quad (2.2)$$

in homogeneous turbulence is governed by the Karman-Howarth-Monin equation [43, 60, 73]

$$\frac{\partial \mathcal{K}}{\partial t} = -\nabla_{\mathbf{r}} \cdot \mathbf{T} + 2\nu \nabla_{\mathbf{r}}^2 \mathcal{K} - 2\langle \epsilon \rangle + W, \quad (2.3)$$

where ν is the fluid kinematic viscosity, $\langle \epsilon \rangle$ is the average kinetic energy dissipation rate, and W is an external power input. The energy transfer term is related to the third order velocity structure function

$$\mathbf{T} \equiv \frac{1}{2} \langle \|\Delta \mathbf{u}\|^2 \Delta \mathbf{u} \rangle \quad (2.4)$$

and it arises from inertial/convective forces in the flow. When W only acts at the largest scales, in the statistically steady case $\partial_t \mathcal{K} = 0$ and at scales which are intermediate between the smallest dissipative scales η and the largest forced scales ℓ , the energy flux balances the energy dissipation rate

$$\nabla_r \cdot \mathbf{T} \simeq -2\langle \epsilon \rangle, \text{ for } \eta \ll r \ll \ell \quad (2.5)$$

That intermediate range of scales r in which equation (2.5) is valid is referred to as inertial range [121].

To examine how the energy cascade described by the convective flux is related to Vortex Stretching, we derive a result for isotropic turbulence that relates $\nabla_r \cdot \mathbf{T}$ to the dynamics of the velocity gradient filtered at scale r . The full velocity field \mathbf{u} is decomposed into a filtered part $\tilde{\mathbf{u}}$ and a sub-grid contribution \mathbf{u}' , so that

$$\mathbf{u} = \tilde{\mathbf{u}} + \mathbf{u}', \quad (2.6)$$

where $\tilde{\mathbf{u}}$ denotes \mathbf{u} filtered on scale r by means of an isotropic kernel

$$\tilde{\mathbf{u}}(\mathbf{x}, t) \equiv \int_{\mathbb{R}^3} \mathcal{G}_r(\|\mathbf{x}'\|) \mathbf{u}(\mathbf{x} - \mathbf{x}', t) d\mathbf{x}' \quad (2.7)$$

The coarse-grained velocity increment would follow immediately from those definitions $\Delta \mathbf{u} = \Delta \tilde{\mathbf{u}} + \Delta \mathbf{u}'$. However, while $\nabla_r \cdot \Delta \mathbf{u} = 0$ due to incompressibility, $\nabla_r \cdot \Delta \tilde{\mathbf{u}} \neq 0$ since the filtering length depends on the scale r . Therefore, we have to fix this compressibility issue in order to continue our coarse-graining analysis of equation (2.3).

2.3 The Incompressible Filtered Velocity Increment

In order to fix this compressibility issue we look for a filtered velocity increment defined in the solenoidal vector space. Consider the velocity field filtered at a generic length-scale ζ which is for now an independent variable $\tilde{\mathbf{u}}(\mathbf{x}, t) \equiv \int \mathcal{G}_\zeta(\|\mathbf{x}'\|) \mathbf{u}(\mathbf{x} - \mathbf{x}', t) d\mathbf{x}'$. An incompressible filtered fluid velocity increment is denoted by $\Delta^* \tilde{\mathbf{u}}(\mathbf{y}, \mathbf{r}, \zeta, t)$, which is required to be incompressible and to reduce to the usual filtered velocity increment when the filtering length does not depend on the scale

$$\nabla_r \cdot \Delta^* \tilde{\mathbf{u}}(\mathbf{y}, \mathbf{r}, \zeta, t)|_{\mathbf{y}} = 0, \quad (2.8a)$$

$$\Delta^* \tilde{\mathbf{u}}(\mathbf{y}, \mathbf{r}, \zeta, t)|_{\zeta} = \Delta \tilde{\mathbf{u}}(\mathbf{y}, \mathbf{r}, \zeta, t), \quad (2.8b)$$

where the first relation is valid at constant centroid position \mathbf{y} and the second at constant filtering length ζ . The formal solution of (2.8a) can be expressed as

$$\Delta^* \tilde{\mathbf{u}}(\mathbf{y}, \mathbf{r}, \zeta, t) = \nabla_{\mathbf{r}} \times \tilde{\mathbf{V}}^*(\mathbf{y}, \mathbf{r}, \zeta, t)|_{\mathbf{y}}, \quad (2.9)$$

where $\tilde{\mathbf{V}}^*$ is a vector potential of the incompressible increment. Substituting equation (2.9) into (2.8b) an equation for the vector potential is obtained,

$$\nabla_{\mathbf{r}} \times \tilde{\mathbf{V}}^*(\mathbf{y}, \mathbf{r}, \zeta, t)|_{\mathbf{y}, \zeta} = \Delta \tilde{\mathbf{u}}(\mathbf{y}, \mathbf{r}, \zeta, t). \quad (2.10)$$

This now clarifies the notation used in (2.8b); $\Delta^* \tilde{\mathbf{u}}(\mathbf{y}, \mathbf{r}, \zeta, t)|_{\zeta}$ means that when the curl operator $\nabla_{\mathbf{r}} \times \{\cdot\}$ acts on $\tilde{\mathbf{V}}^*$, ζ is to be held fixed, that is, $\Delta^* \tilde{\mathbf{u}} = \Delta \tilde{\mathbf{u}}$ when ζ does not depend on r . The solution of equation (2.10) can be expressed as

$$\tilde{\mathbf{V}}^*(\mathbf{y}, \mathbf{r}, \zeta, t) = 2\tilde{\mathbf{V}}(\mathbf{y} + \mathbf{r}/2, \zeta, t) + 2\tilde{\mathbf{V}}(\mathbf{y} - \mathbf{r}/2, \zeta, t) + \tilde{\mathbf{B}}(\mathbf{y}, \zeta, t) \quad (2.11)$$

where $\tilde{\mathbf{V}}$ is a vector potential of the velocity field filtered at fixed length ζ , defined through

$$\tilde{\mathbf{u}}(\mathbf{y}, \zeta, t) = \nabla_{\mathbf{y}} \times \tilde{\mathbf{V}}(\mathbf{y}, \zeta, t)|_{\zeta} \quad (2.12)$$

and $\tilde{\mathbf{B}}(\mathbf{y}, \zeta, t)$ is an integration constant, since equation (2.10) has been integrated in \mathbf{r} at fixed \mathbf{y} and ζ . That integration constant will be fixed imposing the incompressibility condition for the third order structure function in isotropic (even locally homogeneous) flows [74]. Using equation (2.11) into (2.9) we then obtain the expression for the incompressible filtered velocity increment,

$$\Delta^* \tilde{\mathbf{u}} = \nabla_{\mathbf{r}} \times \left[2\tilde{\mathbf{V}}(\mathbf{y} + \mathbf{r}/2, t) + 2\tilde{\mathbf{V}}(\mathbf{y} - \mathbf{r}/2, t) + \tilde{\mathbf{B}}(\mathbf{y}, t) \right], \quad (2.13)$$

where the dependence on the filtering length ζ is implicit in the coarse-graining symbol.

In order to relate $\Delta^* \tilde{\mathbf{u}}(\mathbf{y}, \mathbf{r}, \zeta, t)$ to the velocity gradient filtered at scale r , namely $\tilde{\mathbf{A}} \equiv \nabla \tilde{\mathbf{u}}$, we set $\zeta = r$ and Taylor expand the vector potential $\tilde{\mathbf{V}}$ in (2.13) in the variable \mathbf{r} , explicitly retaining terms up to second-order,

$$\tilde{\mathbf{V}}(\mathbf{y} + \mathbf{r}/2, r, t) + \tilde{\mathbf{V}}(\mathbf{y} - \mathbf{r}/2, r, t) = 2\tilde{\mathbf{V}}(\mathbf{y}, r, t) + \frac{1}{4} (\mathbf{r}\mathbf{r} : \nabla \nabla) \tilde{\mathbf{V}}(\mathbf{y}, r, t) + \mathbf{h}, \quad (2.14)$$

where $\mathbf{h}(\mathbf{y}, \mathbf{r}, t)$ denotes the higher order terms in the expansion, which are sub-leading due to the smoothness of $\tilde{\mathbf{V}}$ on scales $\leq \mathcal{O}(r)$. Further, $\tilde{\mathbf{V}}$ is smoother than $\tilde{\mathbf{u}}$ since it is given by the inverse curl operator acting on $\tilde{\mathbf{u}}$. Substituting (2.14) into (2.9) yields

$$\Delta^* \tilde{\mathbf{u}} = \tilde{\mathbf{A}} \cdot \mathbf{r} + \frac{\mathbf{r}}{r} \times \left[\frac{1}{2} (\mathbf{r}\mathbf{r} : \nabla \nabla) \frac{\partial \tilde{\mathbf{V}}}{\partial r} + \frac{\partial}{\partial r} (4\tilde{\mathbf{V}} + \tilde{\mathbf{B}}) \right] + 2\nabla_{\mathbf{r}} \times \mathbf{h}, \quad (2.15)$$

where $\widetilde{\mathbf{A}} = \widetilde{\mathbf{A}}(\mathbf{y}, \zeta = r, t)$, $\widetilde{\mathbf{V}} = \widetilde{\mathbf{V}}(\mathbf{y}, \zeta = r, t)$ and $\widetilde{\mathbf{B}} = \widetilde{\mathbf{B}}(\mathbf{y}, \zeta = r, t)$. The dependence upon r due to the filtering is implicitly indicated by the tilde. The cross product term in (2.15) represents the “compressible correction” that captures the effect of the variable filtering length on the velocity increment, and guarantees $\nabla_r \cdot \Delta^* \widetilde{\mathbf{u}}(\mathbf{x}, \mathbf{r}, \zeta, t) = 0$ for all smooth $\zeta(r)$. Since the compressible correction contributes to the incompressible increment only on the plane orthogonal to \mathbf{r} , the longitudinal incompressible increments are the same of the usual filtered increments, while the perpendicular increments differ,

$$\Delta^* \widetilde{u}_{\parallel} = \Delta \widetilde{u}_{\parallel}, \quad \Delta^* \widetilde{u}_{\perp} \neq \Delta \widetilde{u}_{\perp}. \quad (2.16)$$

2.4 Average energy cascade in terms of the coarse-grained velocity gradient

Once that the incompressible filtered velocity increment is defined, the nonlinear energy flux can be expressed using the incompressible decomposition $\Delta \mathbf{u} = \Delta^* \widetilde{\mathbf{u}} + \Delta^* \mathbf{u}'$, and based on local isotropy we have

$$\nabla_r \cdot \mathbf{T} = \frac{1}{2} \left(\frac{\partial}{\partial r} + \frac{2}{r} \right) \langle \|\Delta^* \widetilde{\mathbf{u}}\|^2 \Delta^* \widetilde{u}_{\parallel} \rangle + F, \quad (2.17)$$

where $F(r)$ denotes the contributions involving the sub-grid field $\Delta^* \mathbf{u}'$. Because of isotropy, the quantity $\langle \|\Delta^* \widetilde{\mathbf{u}}\|^2 \Delta^* \widetilde{u}_{\parallel} \rangle$ is physically related to the invariant $\langle (\widetilde{\mathbf{A}}^{\top} \cdot \widetilde{\mathbf{A}}) : \widetilde{\mathbf{A}} \rangle$, which is then employed to express the third order structure functions,

$$\langle \Delta^* \widetilde{u}_{\parallel}^3 \rangle = \frac{2}{35} \langle (\widetilde{\mathbf{A}}^{\top} \cdot \widetilde{\mathbf{A}}) : \widetilde{\mathbf{A}} \rangle r^3 + \mathcal{H}_{\parallel}, \quad (2.18a)$$

$$\langle \Delta^* \widetilde{u}_{\parallel} \Delta^* \widetilde{u}_{\perp}^2 \rangle = \frac{4}{105} \langle (\widetilde{\mathbf{A}}^{\top} \cdot \widetilde{\mathbf{A}}) : \widetilde{\mathbf{A}} \rangle r^3 + C + \mathcal{H}_{\perp}, \quad (2.18b)$$

where $\mathcal{H}_{\parallel}(r)$ and $\mathcal{H}_{\perp}(r)$ denote the contributions involving from the remained of the expansion, \mathbf{h} , in (2.15). $C(r)$ denotes the contribution arising from the compressibility correction term in (2.15), which is determined by incompressibility and isotropy of the flow. Indeed, due to isotropy and incompressibility, the third order longitudinal and mixed structure functions obey [74],

$$\langle \Delta u_{\parallel} \Delta u_{\perp}^2 \rangle = \frac{1}{6} \frac{d}{dr} \left(r \langle \Delta u_{\parallel}^3 \rangle \right). \quad (2.19)$$

Requiring that equation (2.19) is satisfied by the incompressible increment, using equation (2.18a) which is free of compressibility effects, gives

$$\langle \Delta^* \widetilde{u}_{\parallel} \Delta^* \widetilde{u}_{\perp}^2 \rangle = \frac{1}{105} \frac{d}{dr} \left(\langle (\widetilde{\mathbf{A}}^{\top} \cdot \widetilde{\mathbf{A}}) : \widetilde{\mathbf{A}} \rangle r^4 + r \mathcal{H}_{\parallel} \right). \quad (2.20)$$

Substituting equations (2.18a) and (2.20) into (2.17), we finally obtain the expression for the average energy flux

$$\nabla_r \cdot \mathbf{T} = \mathcal{L} \left\{ \langle (\tilde{\mathbf{S}} \cdot \tilde{\mathbf{S}}) : \tilde{\mathbf{S}} \rangle - \frac{1}{4} \langle \tilde{\boldsymbol{\omega}} \tilde{\boldsymbol{\omega}} : \tilde{\mathbf{S}} \rangle \right\} + \mathcal{F}, \quad (2.21)$$

where \mathcal{F} is the sum of the sub-grid contribution F and the higher-order terms contributions from \mathcal{H}_{\parallel} . Equation (2.21) involves the filtered strain-rate and the filtered vorticity

$$\tilde{\mathbf{S}} \equiv \frac{1}{2} (\tilde{\mathbf{A}} + \tilde{\mathbf{A}}^{\top}), \quad \tilde{\boldsymbol{\omega}} \equiv \nabla \times \tilde{\mathbf{u}}, \quad (2.22)$$

and the linear operator

$$\mathcal{L}\{\cdot\} \equiv \left(\frac{\partial}{\partial r} + \frac{2}{r} \right) \left[\frac{r^4}{105} \left(\frac{\partial}{\partial r} + \frac{7}{r} \right) \{\cdot\} \right]. \quad (2.23)$$

Equation (2.21) is the isotropic Karman-Howarth equation [60] in which the velocity increments have been consistently related to the filtered velocity increments, by taking into account incompressibility and keeping separate the role of longitudinal and orthogonal velocity increments. The fact that, due to isotropy the third order structure function $\langle \|\Delta^* \tilde{\mathbf{u}}\|^2 \Delta^* \tilde{u}_{\parallel} \rangle$ is physically related to the invariant $\langle (\tilde{\mathbf{A}}^{\top} \cdot \tilde{\mathbf{A}}) : \tilde{\mathbf{A}} \rangle$ is key to distinguish between strain self-amplification and vortex stretching contributions to the cascade and it will be further analyzed at the end of this Chapter.

2.4.1 Asymptotics of the average energy cascade

The relation between the velocity gradients and the average energy cascade is better understood in limiting cases, when the scale r lying in the dissipation and in the inertial range. In the limit $r/\eta \rightarrow 0$, we have $\mathcal{F} \rightarrow 0$ and equation (2.21) reduces to the exact result

$$\nabla_r \cdot \mathbf{T} = \frac{r^2}{3} \langle (\mathbf{S} \cdot \mathbf{S}) : \mathbf{S} \rangle - \frac{r^2}{12} \langle \boldsymbol{\omega} \boldsymbol{\omega} : \mathbf{S} \rangle, \quad (2.24)$$

where $\mathbf{S} = \lim_{r \rightarrow 0} \tilde{\mathbf{S}}$ and $\boldsymbol{\omega} = \lim_{r \rightarrow 0} \tilde{\boldsymbol{\omega}}$ are the un-filtered strain-rate and vorticity. In the inertial range, $\nabla_r \cdot \mathbf{T}$ is independent of r , which implies $\langle (\tilde{\mathbf{S}} \cdot \tilde{\mathbf{S}}) : \tilde{\mathbf{S}} \rangle \propto \langle \tilde{\boldsymbol{\omega}} \tilde{\boldsymbol{\omega}} : \tilde{\mathbf{S}} \rangle \propto r^{-2}$, and using this in (2.21) we obtain for $\eta \ll r \ll L$

$$\nabla_r \cdot \mathbf{T} = \frac{r^2}{7} \langle (\tilde{\mathbf{S}} \cdot \tilde{\mathbf{S}}) : \tilde{\mathbf{S}} \rangle - \frac{r^2}{28} \langle \tilde{\boldsymbol{\omega}} \tilde{\boldsymbol{\omega}} : \tilde{\mathbf{S}} \rangle + \mathcal{F}. \quad (2.25)$$

It is anticipated that \mathcal{F} will play a sub-leading role in equation (2.25) as it will be later confirmed by means of the numerical result. Also notice that if the prediction

(2.25) wasn't accurate one would be free to adjust the filtering length $\zeta(r)$ in order to obtain quantitatively good results.

Equation (2.25) has similarities with the result obtained by [56] under the strong ultra-violet locality assumption (UVLA) for the instantaneous one-point scale-to-scale energy flux $\Pi(\mathbf{x}, t)$, that describes the cascade of kinetic energy from $\tilde{\mathbf{u}}$ to \mathbf{u}' . In contrast to $\Pi(\mathbf{x}, t)$, however, the instantaneous form of $\nabla_r \cdot \mathbf{T}$, namely $\nabla_r \cdot (\|\Delta \mathbf{u}\|^2 \Delta \mathbf{u})$, is not in general reducible to a form such as (2.25), even under UVLA. We also note that our general result in (2.21) differs from the energy flux result in [56] since our result in general depends on gradients in r -space of the average strain and vorticity invariants. This difference arises since in [56] the multiscale properties of the turbulence are analyzed using a one-point field, whereas ours employs a two-point field representation in terms of the velocity increments. For situations where the average invariants are not scale invariant functions of r (e.g. for low Reynolds number turbulence, or at the crossover between the dissipation and inertial ranges), then according to our result in (2.21), the energy cascade will depend to leading order on gradients of the invariants in r -space, and not only on the invariants themselves.

The invariant $(\tilde{\mathbf{S}} \cdot \tilde{\mathbf{S}}) : \tilde{\mathbf{S}}$ is the strain self-amplification (SSA) term, and when $(\tilde{\mathbf{S}} \cdot \tilde{\mathbf{S}}) : \tilde{\mathbf{S}} < 0$ it contributes to the production of $\|\tilde{\mathbf{S}}\|$ through nonlinear interaction of the straining field with itself. We have $(\tilde{\mathbf{S}} \cdot \tilde{\mathbf{S}}) : \tilde{\mathbf{S}} = \sum_i \tilde{\lambda}_i^3$, where $\tilde{\lambda}_1, \tilde{\lambda}_2, \tilde{\lambda}_3$ are the eigenvalues of $\tilde{\mathbf{S}}$, satisfying $\sum_i \tilde{\lambda}_i = 0$ and $\tilde{\lambda}_1 \geq \tilde{\lambda}_2 \geq \tilde{\lambda}_3$. It is known that $\langle (\tilde{\mathbf{S}} \cdot \tilde{\mathbf{S}}) : \tilde{\mathbf{S}} \rangle < 0$ [108], and since $\tilde{\lambda}_1 \geq 0$, and $\langle \tilde{\lambda}_2^3 \rangle > 0$ (see figure (2.1)), then $\langle (\tilde{\mathbf{S}} \cdot \tilde{\mathbf{S}}) : \tilde{\mathbf{S}} \rangle < 0$ is solely due to the negativity of $\tilde{\lambda}_3$. Together with (2.25), this shows that the contribution of SSA to the energy cascade is associated with compressional straining motions.

The invariant $\tilde{\omega} \tilde{\omega} : \tilde{\mathbf{S}}$ is the Vortex Stretching (VS) term, and when $\tilde{\omega} \tilde{\omega} : \tilde{\mathbf{S}} > 0$ it contributes to the production of enstrophy $\|\tilde{\omega}\|^2$ through the stretching of (filtered) vortex lines. We have $\tilde{\omega} \tilde{\omega} : \tilde{\mathbf{S}} = \sum_i \|\tilde{\omega}\|^2 \tilde{\lambda}_i \cos^2(\tilde{\omega}, \tilde{\mathbf{e}}_i)$, where $\tilde{\mathbf{e}}_i$ is the eigenvector corresponding to $\tilde{\lambda}_i$. It is known that $\langle \tilde{\omega} \tilde{\omega} : \tilde{\mathbf{S}} \rangle > 0$ [108], whose positivity can only come from $\tilde{\lambda}_1$ or $\tilde{\lambda}_2$. A well-known feature of turbulence is the predominant alignment of $\tilde{\omega}$ with $\tilde{\mathbf{e}}_2$ [108, 40]. Nevertheless, the contribution to Vortex Stretching associated with $\tilde{\lambda}_1$ dominates [150, 48].

Since $\langle (\tilde{\mathbf{S}} \cdot \tilde{\mathbf{S}}) : \tilde{\mathbf{S}} \rangle < 0$ and $\langle \tilde{\omega} \tilde{\omega} : \tilde{\mathbf{S}} \rangle > 0$, then according to equations (2.24) and (2.25), both SSA and VS contribute to the downscale energy cascade. Note that we are simply taking $\langle (\tilde{\mathbf{S}} \cdot \tilde{\mathbf{S}}) : \tilde{\mathbf{S}} \rangle < 0$ and $\langle \tilde{\omega} \tilde{\omega} : \tilde{\mathbf{S}} \rangle > 0$ as empirical facts. A complete explanation of the physics of the turbulent energy cascade would of course require an explanation for why these average invariants have the sign that they do. Several arguments have previously been given, however, all of them appear to be at best incomplete (e.g. [150]), and we do not attempt to provide new arguments. Nevertheless, independent of the explanation for why $\langle (\tilde{\mathbf{S}} \cdot \tilde{\mathbf{S}}) : \tilde{\mathbf{S}} \rangle < 0$ and $\langle \tilde{\omega} \tilde{\omega} : \tilde{\mathbf{S}} \rangle > 0$, the interpretation of these empirical facts is unambiguous, namely, that nonlinearity in the NSE leads to the spontaneous production of strain

and vorticity across the scales of the turbulent flow. Our goal is to understand how these processes relate to the turbulent energy cascade.

Note that equation (2.21) does not assume the cascade is dynamically local. Indeed, the filtered fields $\tilde{\mathbf{S}}$ and $\tilde{\boldsymbol{\omega}}$ involve contributions from all scales in the flow that are greater than or equal to the filter scale r , while the effects of the sub-grid scales are fully contained within \mathcal{F} . As a result, terms such as $\tilde{\boldsymbol{\omega}}\tilde{\boldsymbol{\omega}} : \tilde{\mathbf{S}}$ can involve contributions from interactions between scales of different sizes. Therefore, (2.21) is consistent with recent numerical results showing that the stretching of vortices at a given scale tends to be governed by straining motions at scales that are 3 to 5 times larger [48].

2.4.2 Roles of SSA and VS in the energy cascade

For homogeneous filtering operators, Betchov's result applies [10]

$$\langle (\tilde{\mathbf{S}} \cdot \tilde{\mathbf{S}}) : \tilde{\mathbf{S}} \rangle = -(3/4)\langle \tilde{\boldsymbol{\omega}}\tilde{\boldsymbol{\omega}} : \tilde{\mathbf{S}} \rangle, \forall r. \quad (2.26)$$

It is important to stress that this result is purely kinematic/statistical; it is derived assuming only incompressibility and statistical homogeneity of the flow. Using equation (2.26) we observe that the contribution from SSA in (2.24) and (2.25) is three times larger than that from Vortex Stretching, indicating that Vortex Stretching is not the main driver of the energy cascade, and that it plays a sub-leading role. SSA is the main mechanism driving the energy cascade.

One may object to the conclusion that SSA, not Vortex Stretching, dominates the energy cascade since if we substitute equation (2.26) into (2.25) we obtain

$$\nabla_r \cdot \mathbf{T} = -(r^2/7)\langle \tilde{\boldsymbol{\omega}}\tilde{\boldsymbol{\omega}} : \tilde{\mathbf{S}} \rangle + \mathcal{F}, \quad (2.27)$$

(a similar step to this was taken in [55], namely, the Betchov relation in (2.26) was used to express the energy flux purely in terms of Vortex Stretching for a homogeneous turbulent flow) which appears to show that Vortex Stretching is the mechanism governing the downscale energy cascade, contrary to our previous statements. Indeed, equation (2.27) would explain why previous numerical studies seemed to find a strong correlation between the energy cascade and Vortex Stretching, on average [42, 48].

Nevertheless, we argue that (2.27) is fundamentally misleading with respect to the physical mechanism driving the energy cascade (and therefore so also is (32) in [55]). Namely, it invokes (2.26) which is a purely kinematic relationship that obscures the fact that SSA and VS are dynamically very different. That SSA and VS are dynamically very different, and therefore must be correctly distinguished, may be observed in at least three different ways. First is the simple fact that the dynamical equations governing the SSA and VS invariants that can be derived from the NSE are very different [150]. Second, SSA and VS can affect the evolution

of other quantities in turbulent flows in completely different ways. For example, consider the equation for $\langle \|\tilde{\mathbf{S}}\|^2 \rangle$

$$\frac{1}{2} \frac{\partial}{\partial t} \langle \|\tilde{\mathbf{S}}\|^2 \rangle = -\langle (\tilde{\mathbf{S}} \cdot \tilde{\mathbf{S}}) : \tilde{\mathbf{S}} \rangle - \frac{1}{4} \langle \tilde{\boldsymbol{\omega}} \tilde{\boldsymbol{\omega}} : \tilde{\mathbf{S}} \rangle - \nu \langle \|\nabla \tilde{\mathbf{S}}\|^2 \rangle. \quad (2.28)$$

From (2.28) it is apparent that while $\langle \tilde{\boldsymbol{\omega}} \tilde{\boldsymbol{\omega}} : \tilde{\mathbf{S}} \rangle > 0$ acts as a sink for $\langle \|\tilde{\mathbf{S}}\|^2 \rangle$, $\langle (\tilde{\mathbf{S}} \cdot \tilde{\mathbf{S}}) : \tilde{\mathbf{S}} \rangle < 0$ acts as a source for $\langle \|\tilde{\mathbf{S}}\|^2 \rangle$. Therefore, while $\langle (\tilde{\mathbf{S}} \cdot \tilde{\mathbf{S}}) : \tilde{\mathbf{S}} \rangle = -(3/4) \langle \tilde{\boldsymbol{\omega}} \tilde{\boldsymbol{\omega}} : \tilde{\mathbf{S}} \rangle$, the negativity of $\langle (\tilde{\mathbf{S}} \cdot \tilde{\mathbf{S}}) : \tilde{\mathbf{S}} \rangle$ leads to an opposite dynamical effect on $\langle \|\tilde{\mathbf{S}}\|^2 \rangle$ than the negativity of $-\langle \tilde{\boldsymbol{\omega}} \tilde{\boldsymbol{\omega}} : \tilde{\mathbf{S}} \rangle$. Third, while the average values of SSA and VS are closely related, their statistics in general differ, and joint Probability Density Functions (PDFs) of the unfiltered SSA and VS reveal that they are weakly correlated [70].

These arguments emphasize that while inserting $\langle (\tilde{\mathbf{S}} \cdot \tilde{\mathbf{S}}) : \tilde{\mathbf{S}} \rangle = -(3/4) \langle \tilde{\boldsymbol{\omega}} \tilde{\boldsymbol{\omega}} : \tilde{\mathbf{S}} \rangle$ into (2.25) is numerically legitimate, it obscures the true physics behind the energy cascade because VS and SSA are distinct dynamical processes that have distinct effects on the dynamics of turbulence. Their roles in the cascade mechanism must therefore be distinguished; the true underlying physics is reflected in equation (2.25), not (2.27).

The above arguments are analogous to the argument that even though in homogeneous turbulence, $\langle \epsilon \rangle \equiv 2\nu \langle \|\mathbf{S}\|^2 \rangle = \nu \langle \|\boldsymbol{\omega}\|^2 \rangle$, it is dynamically incorrect to refer to $\nu \langle \|\boldsymbol{\omega}\|^2 \rangle$ as the average dissipation rate, since vorticity has no direct causal relationship with dissipation [145]. Indeed, for an incompressible, Newtonian fluid, $\epsilon \equiv 2\nu \|\mathbf{S}\|^2$, by definition. The result $\langle \epsilon \rangle = \nu \langle \|\boldsymbol{\omega}\|^2 \rangle$, like $\langle (\tilde{\mathbf{S}} \cdot \tilde{\mathbf{S}}) : \tilde{\mathbf{S}} \rangle = -(3/4) \langle \tilde{\boldsymbol{\omega}} \tilde{\boldsymbol{\omega}} : \tilde{\mathbf{S}} \rangle$, is purely kinematic, and must not be interpreted as implying a dynamical relationship.

2.4.3 Paradoxical role of vortex stretching

In [150, 129] it is emphasized that according to the NSE, Vortex Stretching opposes energy dissipation in the flow, and from this they infer that Vortex Stretching must hinder the energy cascade since dissipation is supposed to be the end result of the cascade. However, our analytical results contradict this. But this appears paradoxical; how can Vortex Stretching contribute to the downscale cascade of energy, while at the same time acting to reduce the dissipation? We suggest that the argument in [150, 129] involves a confusion concerning the nature of the connection between the energy cascade and energy dissipation. The interpretation of the inertial range result $\nabla_r \cdot \mathbf{T} = -2\langle \epsilon \rangle$ is that in the stationary state, $\partial_t \mathcal{K} = 0$, there is a balance between the energy received by scale r due to $\nabla_r \cdot \mathbf{T}$, and the rate at which energy is passed down to smaller scales, which is equal to $-2\langle \epsilon \rangle$. Therefore, the result $\nabla_r \cdot \mathbf{T} = -2\langle \epsilon \rangle$ does not mean that the mechanism of $\nabla_r \cdot \mathbf{T}$ is the dynamical cause of the energy dissipation, but rather it simply reflects an energetic balance between the two processes. This point can be made clearer by

considering that for stationary, homogeneous turbulence, $\mathcal{P} = \langle \epsilon \rangle$, where \mathcal{P} is the kinetic energy production term [121]. According to this result, there is a balance between the energy injected into the flow by the production mechanism, and the energy dissipated. However, this does not imply that the production is the dynamical cause of dissipation. In view of these considerations, there is no reason why Vortex Stretching has to contribute dynamically to $\nabla_r \cdot \mathbf{T}$ and $-2\langle \epsilon \rangle$ in the same way. Therefore, there is no actual paradox in the assertion that Vortex Stretching contributes to the downscale energy cascade, while at the same time acting to reduce the dissipation rate.

2.5 Results & Discussion

We now turn to test the theoretical results using data from a Direct Numerical Simulation (DNS) of the incompressible NSE. In our DNS, the forced, incompressible NSE are solved using a pseudo-spectral code on a periodic domain of length 2π with 2048^3 grid points, generating statistically stationary, isotropic turbulence with Taylor Reynolds number $R_\lambda = 597$. Further details on the DNS code and simulations may be found in [83, 81]. A sharp-spectral filter was used to construct $\tilde{\omega}$ and $\tilde{\mathbf{S}}$ for use in (2.21), but we also compared the results to those obtained using a Gaussian filter (see [121]), and found similar results.

In figure (2.1)(a) we compare the DNS results for $\nabla_r \cdot \mathbf{T}$ with the rhs of equation (2.21). Since we do not know \mathcal{F} we set it to zero when plotting the results. In the limit $r/\eta \rightarrow 0$ this introduces no approximation since $\lim_{r/\eta \rightarrow 0} \mathcal{F} \rightarrow 0$. The DNS data confirms the accuracy of this asymptotic behavior even up to $r = \mathcal{O}(\eta)$. The results in figure (2.1)(a) imply that in the inertial range, \mathcal{F} makes a finite, but sub-leading contribution to the cascade. We also plot separately the SSA and VS contributions to (2.21). The results confirm that in both the dissipation and inertial ranges, the average energy cascade is dominated by the contribution from SSA rather than Vortex Stretching, with the contribution from SSA being three times larger than that from Vortex Stretching.

In figure (2.1)(b) we show the DNS data for the eigenframe contributions to $\mathcal{L}\langle \sum_i \tilde{\lambda}_i^3 \rangle$, where

$$(\tilde{\mathbf{S}} \cdot \tilde{\mathbf{S}}) : \tilde{\mathbf{S}} = \sum_i \tilde{\lambda}_i^3,$$

and the results show that the $i = 3$ contribution dominates and is the sole cause of the negativity of $\mathcal{L}\langle \sum_i \tilde{\lambda}_i^3 \rangle$ at all scales in the flow. This shows that the SSA process that dominates the energy cascade is itself governed by compressional straining motions at all scales. In figure (2.1)(c) we plot the eigenframe contributions to $\mathcal{L}\langle \sum_i \tilde{\mathcal{W}}_i \rangle$, where

$$\tilde{\omega} \tilde{\omega} : \tilde{\mathbf{S}} = \sum_i \|\tilde{\omega}\|^2 \tilde{\lambda}_i \cos^2(\tilde{\omega}, \tilde{\mathbf{e}}_i) \equiv \sum_i \tilde{\mathcal{W}}_i,$$

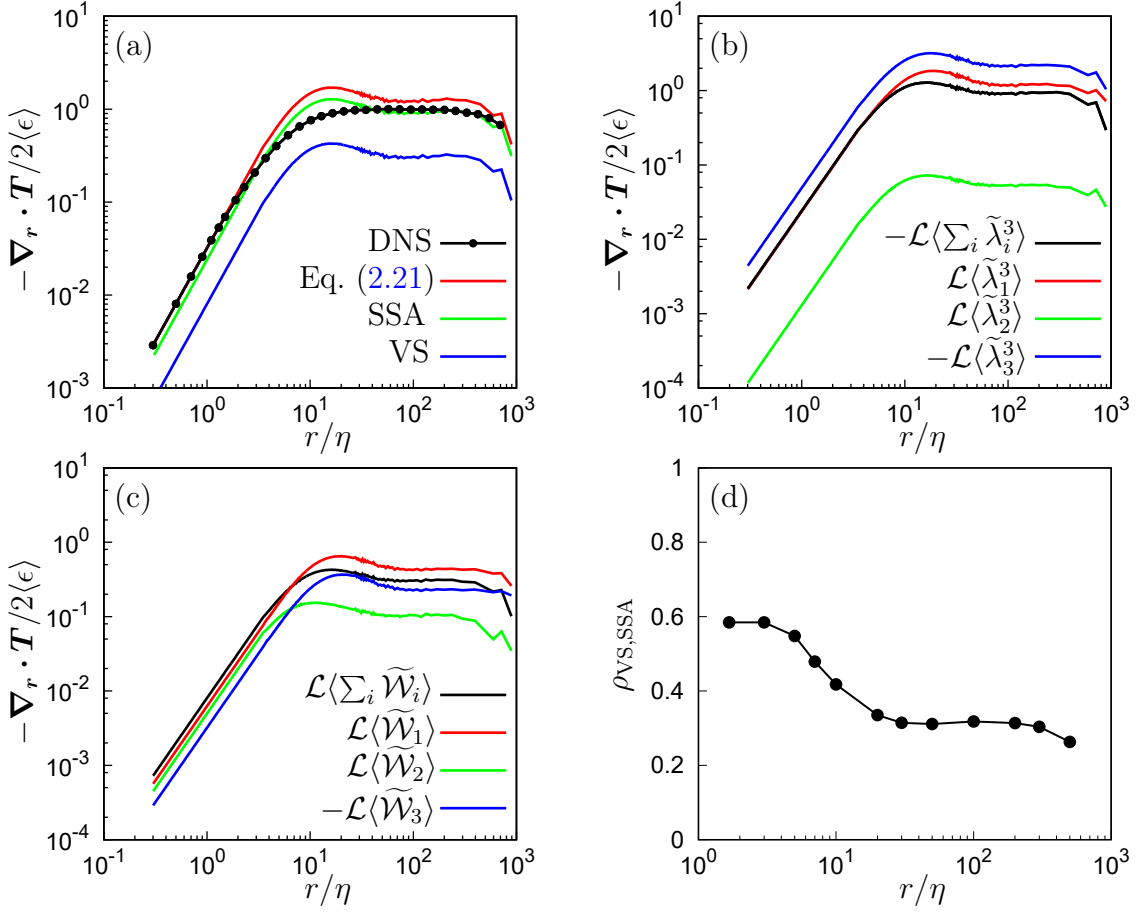


Figure 2.1: (a) Comparison of DNS data (black line with circles) for $\nabla_r \cdot \mathbf{T}$ with (2.21) (red line). Also shown are the SSA (green line) and Vortex Stretching (blue line) contributions to (2.21). Plots (b) and (c) are the eigenframe contributions from (b) SSA and (c) Vortex Stretching to (2.21). Plot (d) shows the correlation coefficient of VS and SSA, $\rho_{\text{VS,SSA}}$, as a function of the filter length scale.

and the results show that the contribution from $i = 1$ is the most positive at all scales. This is consistent with the results in [48] that show that at all scales in the flow, Vortex Stretching is dominated by the contribution from the extensional eigenvalue. Interestingly, while our results show $\langle \tilde{\mathcal{W}}_1 \rangle > \langle \tilde{\mathcal{W}}_2 \rangle$ in the dissipation range (as observed in [70]), $\langle \tilde{\mathcal{W}}_1 \rangle \gg \langle \tilde{\mathcal{W}}_2 \rangle$ in the inertial range. While $\tilde{\mathcal{W}}_1$ and $\tilde{\mathcal{W}}_3$ have fixed signs, the sign of $\tilde{\mathcal{W}}_2$ fluctuates, and as a result, the contribution to $\sum_i \langle \tilde{\mathcal{W}}_i \rangle$ from $\langle \tilde{\mathcal{W}}_2 \rangle$ may be smaller than that from $\langle \tilde{\mathcal{W}}_1 \rangle$ due to partial cancellation of positive and negative $\tilde{\mathcal{W}}_2$ in its average. To explore this, we computed $\langle |\tilde{\mathcal{W}}_2| \rangle$ and found that at all scales, $\langle \tilde{\mathcal{W}}_2 \rangle < \langle |\tilde{\mathcal{W}}_2| \rangle < \langle \tilde{\mathcal{W}}_1 \rangle$, such that the dominance of the $i = 1$ contribution to $\sum_i \langle \tilde{\mathcal{W}}_i \rangle$ is not simply caused by the fluctuating sign of $\tilde{\mathcal{W}}_2$. It is mainly because λ_1 tends to be larger than $|\lambda_2|$, so that $\langle \tilde{\mathcal{W}}_1 \rangle$ dominates

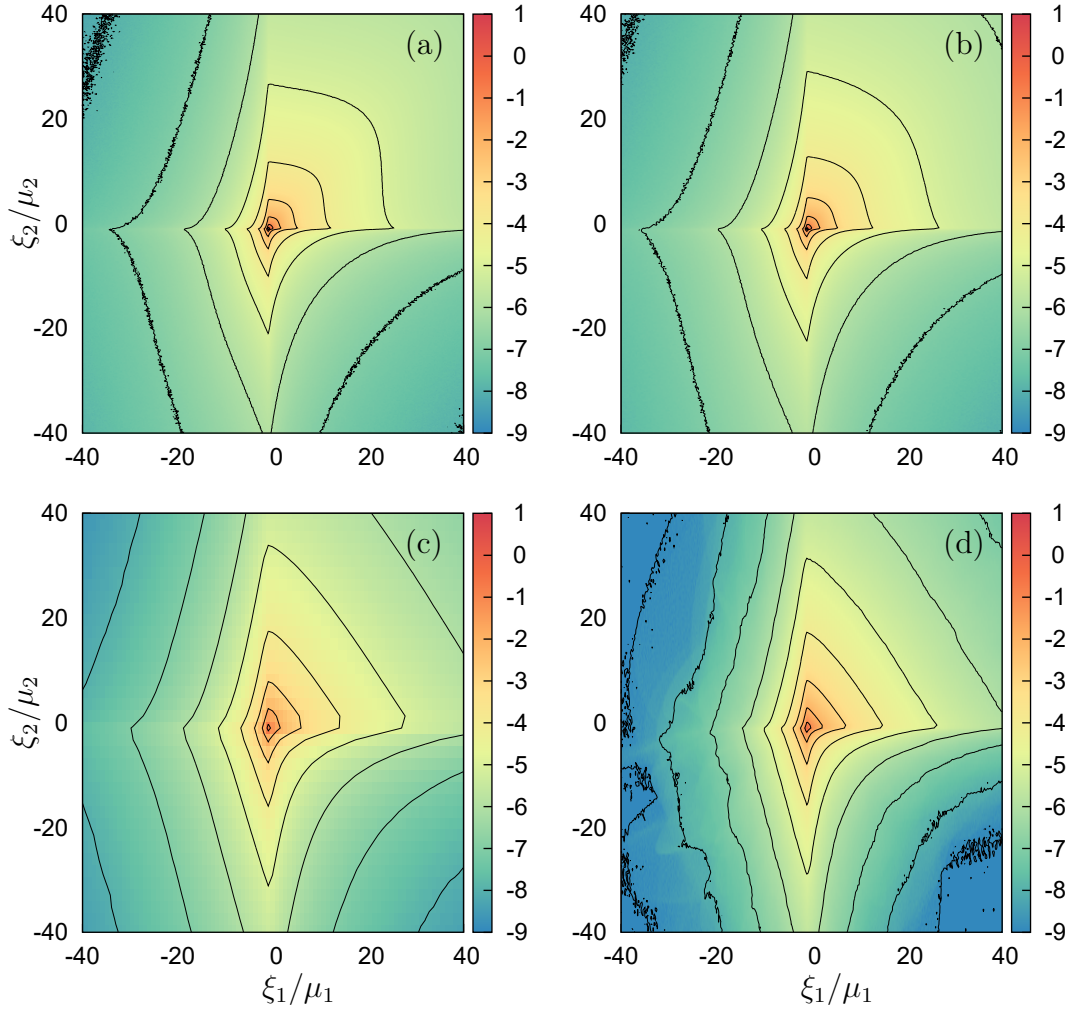


Figure 2.2: DNS results for the joint PDF of SSA and VS at filter scales (a) $r/\eta = 0$, (b) $r/\eta = 30$, (c) $r/\eta = 50$ and (d) $r/\eta = 200$. The quantity on the horizontal axis corresponds to SSA divided by its mean, $\xi_1 = (\mathbf{S}\mathbf{S}) : \mathbf{S}$ and the vertical axis corresponds to VS divided by its mean, $\xi_2 = (\boldsymbol{\omega}\boldsymbol{\omega}) : \mathbf{S}$.

$\sum_i \langle \tilde{\mathcal{W}}_i \rangle$, despite the fact that $\tilde{\boldsymbol{\omega}}$ preferentially aligns with $\tilde{\mathbf{e}}_2$ at all scales in the flow [40].

The statistics of SSA and VS are significantly different, despite the fact that their mean values are closely related through (2.26). Figure (2.1)(d) shows the correlation coefficient of VS and SSA, $\rho_{\text{VS,SSA}}$. While $\rho_{\text{VS,SSA}}$ is moderate in the dissipation range, in the inertial range $\rho_{\text{VS,SSA}}$ approaches 0.3, indicating a weak correlation. In figure (2.2) we show results for the joint PDF of VS and SSA at different filtering scales. The shape of the PDF contours are similar to those in the experimental work of [70] (they only considered the unfiltered case), showing the distinctive ‘‘corners’’ of the contour lines along $\xi_1/\mu_1 = 0$ and $\xi_2/\mu_2 = 0$.

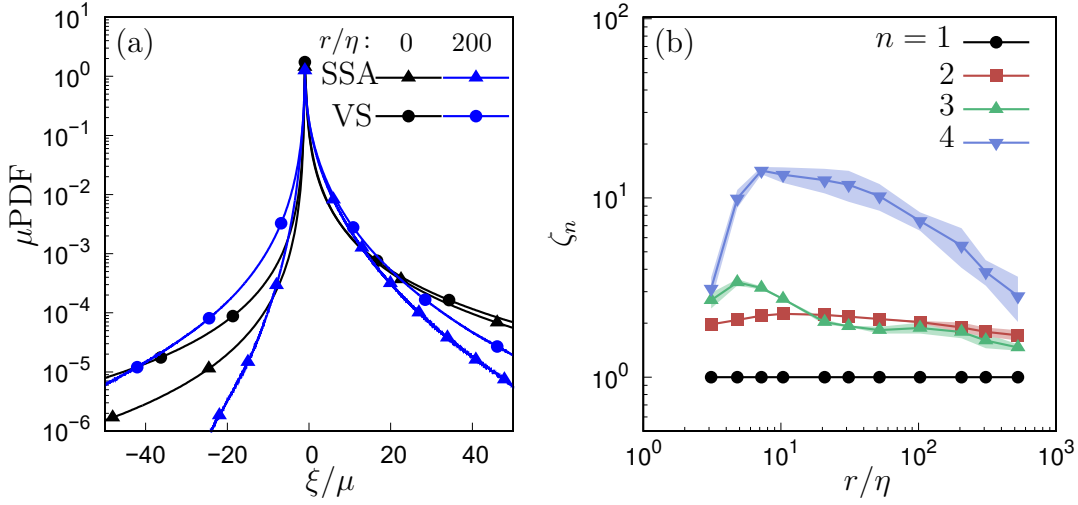


Figure 2.3: DNS results for (a) the PDF of the variable ξ (either SSA - lines with squares, or Vortex Stretching - lines with circles), normalized by the mean value μ , and at different filter scales r/η , and Plot (c) are results for $\zeta_n \equiv \langle [(-3/4)\tilde{\omega}\tilde{\omega} : \tilde{\mathbf{S}}]^n \rangle / \langle [(\tilde{\mathbf{S}} \cdot \tilde{\mathbf{S}}) : \tilde{\mathbf{S}}]^n \rangle$ for varying r/η .

Figure (2.3)(a) shows results for the PDFs of SSA and VS at different filtering scales. Concerning the $r/\eta = 0$ results, in agreement with [70] we find that for $\xi/\mu > 0$ the PDFs are similar, however in disagreement with their results, we find that the PDFs for $\xi/\mu < 0$ are quite different. The difference between the PDFs becomes larger for the filtered case $r/\eta = 200$, for both $\xi/\mu < 0$ and $\xi/\mu > 0$. These results provide further support for our earlier assertions that the roles of SSA and VS must not be conflated. Not only are they dynamically very different, but furthermore, as figure (2.3)(a) shows, the general statistics of the two processes are significantly different, despite the fact that their mean values are closely related through (2.26).

Finally, we have argued that concerning the average energy cascade, the contribution from SSA is much larger than that from Vortex Stretching. However, it is important to consider whether the same holds true for fluctuations of the energy cascade about its average behavior. To gain insight into this we consider the quantity $\zeta_n \equiv \langle [(-3/4)\tilde{\omega}\tilde{\omega} : \tilde{\mathbf{S}}]^n \rangle / \langle [(\tilde{\mathbf{S}} \cdot \tilde{\mathbf{S}}) : \tilde{\mathbf{S}}]^n \rangle$. The results for ζ_n are shown in figure (2.3)(b) for different n and filtering scales r/η . For $n = 1$, equation (2.26) gives $\zeta_1 = 1$, as observed in our numerical results for each r/η . However, for $n > 1$, $\zeta_n > 1$ at each scale, and reaches values $O(10)$ for $n = 4$, implying that Vortex Stretching may play a leading order role during strong fluctuations of the energy cascade about its average value. This increasingly important role of Vortex Stretching compared with SSA during large fluctuations of the energy cascade about the average behavior may in part be associated with the known fact that the vorticity field is more intermittent than the strain-rate field in turbulent flows [49, 31, 20].

2.5.1 Results for the velocity gradient invariants

We report the joint PDFs of the velocity gradient invariants, which are usually employed to describe the velocity gradient dynamics, that play a fundamental role in the energy cascade process. The joint PDF of the two principal invariants $\tilde{Q} = -\tilde{A}_{ij}\tilde{A}_{ji}/2$ and $\tilde{R} = -\tilde{A}_{ij}\tilde{A}_{jk}\tilde{A}_{ki}/3$, normalized with their standard deviation, is shown in figure 2.4. The characteristic sheared drop shape is observed at all the scales [108]. As the filtering length is increased the joint PDF becomes more symmetric with respect to the $\tilde{R} = 0$ axis on the $\tilde{Q} > 0$ half-plane. Dissipation and irreversibility are expected to be weaker at the largest scales so that the dynamics tends to approach time-reversibility. The $R-Q$ joint PDF is exactly time reversible if dissipation is removed and the solution remains smooth, as observed in a stochastic one-point closure for inviscid flows [164]. However, asymmetry persists in the $\tilde{Q} < 0$ half-plane in which strain dominates and most of the dissipation is expected to occur. Therefore, even when the smallest scales are removed, the signature of the average energy flux towards the smallest scales persists.

The joint PDF of the principal invariant \tilde{Q} and the invariant which acts for the energy transfer $\tilde{R}^* = \tilde{A}_{ji}\tilde{A}_{jk}\tilde{A}_{ki}$, normalized with their standard deviation, is shown in figure 2.5. The PDF is skewed towards positive $R^* > 0$ [14]. This indicates a tendency for the energy to flow towards smaller scales, especially in the strain-dominated regions, where $Q < 0$. The asymmetry of the joint PDF with respect to the $\tilde{R}^* = 0$ axis is weaker in the $Q > 0$ plane. Symmetry is not recovered at large scales, energy flows from the largest to the smallest scales ($R^* > 0$) even when the small-scale dynamics is filtered out.

2.6 Conclusions

In this Chapter the energy cascade was examined by means of two-point velocity statistics, which have been related to the coarse-grained velocity gradient. In order to remove compressibility effects due to coarse-graining an incompressible filtered velocity increment has been defined. We have also presented theoretical and numerical results showing that vortex stretching is not the main mechanism driving the average energy cascade in isotropic turbulence. Instead, the main mechanism driving the average cascade is the strain self-amplification process, which is a fundamentally distinct dynamical process from that of vortex stretching. However, our numerical results imply that vortex stretching may play a stronger role during fluctuations of the cascade about its average behavior, which may be associated with the known fact that the vorticity field is more intermittent than the strain-rate field in turbulence.

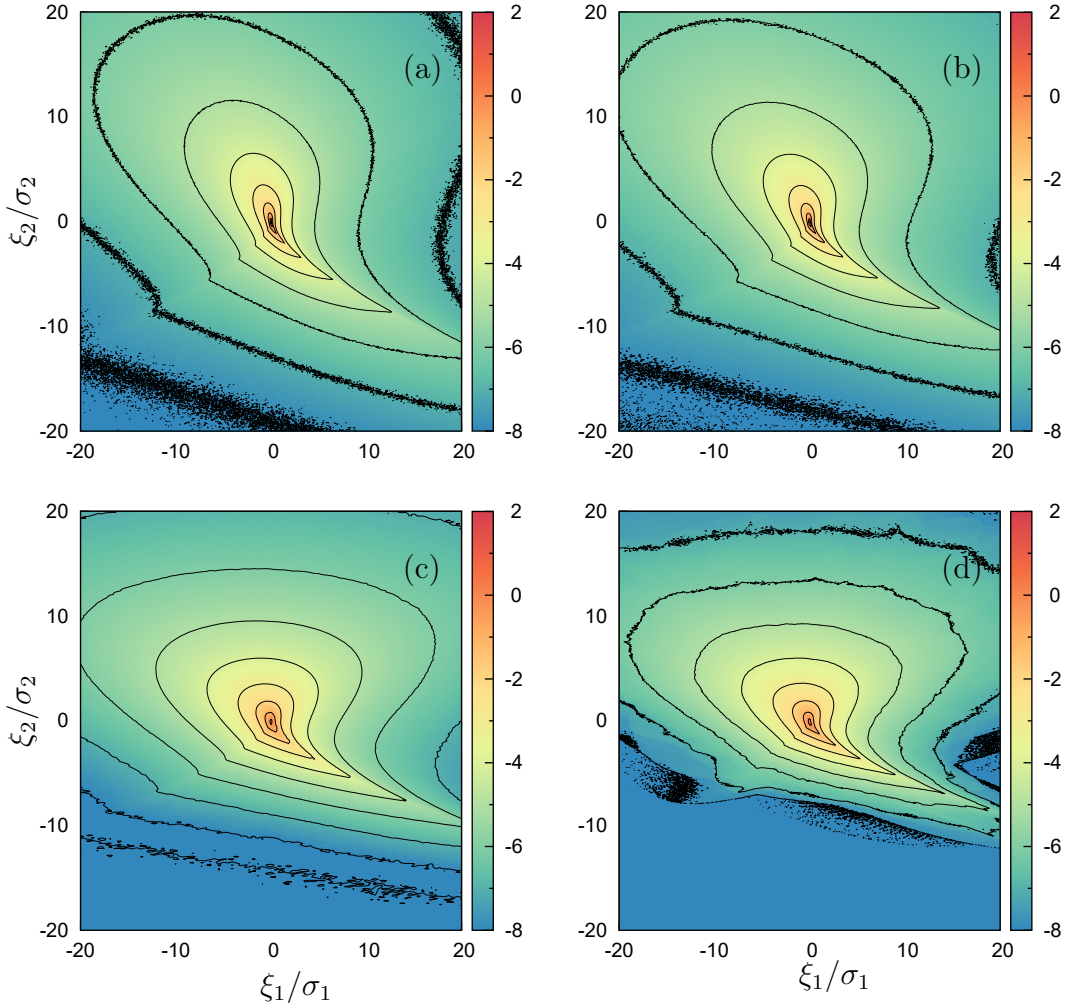


Figure 2.4: DNS results for the joint PDF of the principal invariants R and Q at filter scales (a) $r/\eta = 0$, (b) $r/\eta = 10$, (c) $r/\eta = 50$ and (d) $r/\eta = 200$. The quantity on the horizontal axis corresponds to R divided by its standard deviation while the vertical axis corresponds to Q divided by its standard deviation.

Expression for the mixed third order structure function

In this section we derive an expression for the mixed third order structure function $\langle \Delta u^2 \Delta u_{\parallel} \rangle$ in terms of the velocity gradients, based on isotropic tensor analysis, neglecting the sub-grid and higher order contributions. The analysis will show that when that structure function is expressed in terms of the related invariant $\tilde{R}^* = \tilde{A}_{ji} \tilde{A}_{jk} \tilde{A}_{ki}$ the remaining part which cannot be expressed in terms of \tilde{R}^* and its derivatives vanishes.

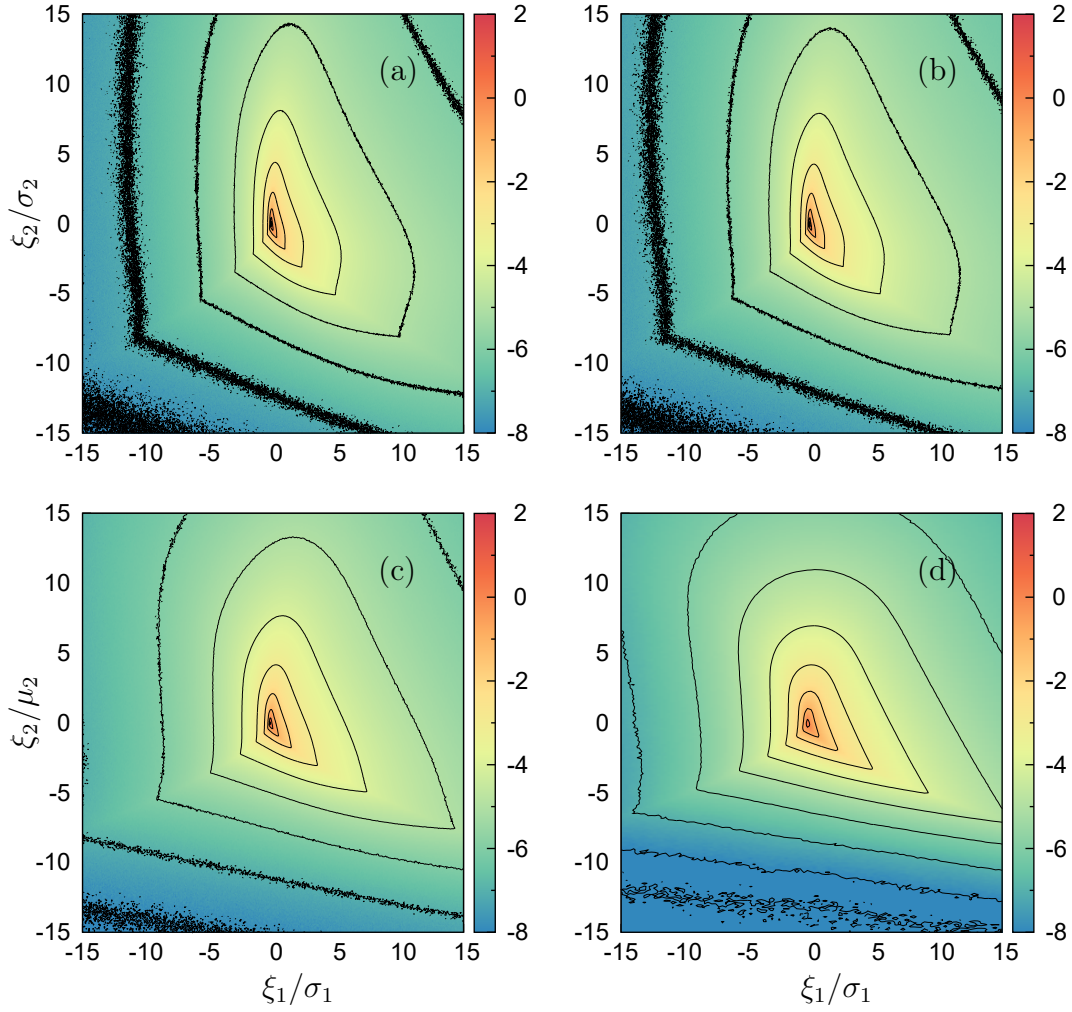


Figure 2.5: DNS results for the joint PDF of the invariants R^* and Q at filter scales (a) $r/\eta = 0$, (b) $r/\eta = 10$, (c) $r/\eta = 50$ and (d) $r/\eta = 200$. The quantity on the horizontal axis corresponds to R^* divided by its standard deviation while the vertical axis corresponds to Q divided by its standard deviation.

We start from the expression of the incompressible coarse-grained velocity increment filtered at scale $\zeta(r)$,

$$\Delta^* \tilde{u}_i(\mathbf{r}, \mathbf{y}; \zeta) = \tilde{A}_{iq}(\mathbf{y}, \zeta) r_q + \epsilon_{ijk} \left(\frac{1}{2} \frac{\partial^3 \tilde{V}_k}{\partial \zeta \partial x_p \partial x_q}(\mathbf{y}; \zeta) r_p r_q + \frac{\partial G_k}{\partial \zeta}(\mathbf{y}, \zeta) \right) \frac{d\zeta}{dr} \hat{r}_j \quad (2.29)$$

where the integration constants, which are functions of r only, have been grouped

into the term \mathbf{G} . The norm of the incompressible increment is

$$\begin{aligned} \Delta^* \tilde{u}_a \Delta^* \tilde{u}_a &= \tilde{A}_{ap} \tilde{A}_{aq} r_p r_q + \tilde{A}_{ak} \epsilon_{amb} \frac{\partial^3 \tilde{\mathcal{V}}_b}{\partial \zeta \partial x_p \partial x_q} \zeta' r_k \hat{r}_m r_p r_q + \tilde{A}_{ak} \epsilon_{amb} \frac{\partial G_b}{\partial \zeta} \zeta' r_k \hat{r}_m + \\ &+ (\delta_{kq} \delta_{bc} - \delta_{kc} \delta_{bq}) \left(\frac{1}{4} \frac{\partial^3 \tilde{\mathcal{V}}_b}{\partial \zeta \partial x_m \partial x_p} \frac{\partial^3 \tilde{\mathcal{V}}_c}{\partial \zeta \partial x_r \partial x_s} r_r r_s + \frac{\partial^3 \tilde{\mathcal{V}}_b}{\partial \zeta \partial x_m \partial x_p} \frac{\partial G_c}{\partial \zeta} \right) \zeta'^2 \hat{r}_k r_m r_p \hat{r}_q + \\ &+ (\delta_{km} \delta_{bc} - \delta_{kc} \delta_{bm}) \frac{\partial G_b}{\partial \zeta} \frac{\partial G_c}{\partial \zeta} \zeta'^2 \hat{r}_k \hat{r}_m \end{aligned} \quad (2.30)$$

Taking the product of the norm with the longitudinal component, that is, the tensor product of the terms in equation (2.30) with \tilde{S}_{ij} , and averaging gives

$$\langle \Delta^* \tilde{u}_{\parallel} \Delta^* \tilde{u}_a \Delta^* \tilde{u}_a \rangle = \langle \Delta^* \tilde{u}_{\parallel} \Delta^* \tilde{u}_{\parallel}^2 \rangle + 2 \langle \Delta^* \tilde{u}_{\parallel} \Delta^* \tilde{u}_{\perp}^2 \rangle = \langle \tilde{S}_{ij} \Delta^* \tilde{u}_a \Delta^* \tilde{u}_a \rangle \hat{r}_i r_j. \quad (2.31)$$

Compressibility is not introduced since Δu_{\parallel} is free of compressibility effects as observed above. Only the contribution from the first and the second terms in equation (2.30) can be expressed as functions of the coarse grained velocity gradient and its first derivative with respect to r . Indeed, the third term depends on the integration constant, the fourth and fifth involve products of derivatives with respect to ζ and thus they cannot be expressed in terms of the invariants of \tilde{A} . As observed above, the degree of freedom provided by the integration constant \mathbf{G} is essential to tune the incompressible increment in such a way that the isotropic and incompressible relation for the third order structure function [74] holds. Indeed, \mathbf{G} depends on \mathbf{x} and r , and the compressibility correction term, $\hat{\mathbf{r}} \times \mathbf{G}'$, has arbitrary norm and orientation on the plane orthogonal to \mathbf{r} . The resulting perpendicular increment also spans all the plane orthogonal to \mathbf{r} while the longitudinal increment is independent of \mathbf{G} . Therefore we can choose, among all the possibilities, the perpendicular increment such that equation (2.19) is satisfied. This provides the definition of \mathbf{G} in equation (2.29).

The contribution to $\langle \Delta^* \tilde{u}_{\parallel} \Delta^* \tilde{u}_a \Delta^* \tilde{u}_a \rangle$, from the first term in equation (2.30) is expressed by isotropic tensor analysis in terms of the averaged invariants of the coarse-grained velocity gradient, $\tilde{I}_1 = \langle \tilde{S}_{ij} \tilde{S}_{jk} \tilde{S}_{ki} \rangle$ and $\tilde{I}_2 = \langle \tilde{S}_{ij} \tilde{\omega}_i \tilde{\omega}_j \rangle$,

$$\langle \tilde{S}_{ij} \tilde{A}_{ap} \tilde{A}_{aq} \rangle \hat{r}_i r_j r_p r_q = \langle \Delta \tilde{u}_{\parallel}^3 \rangle + 2 \langle \Delta \tilde{u}_{\parallel} \Delta \tilde{u}_{\perp}^2 \rangle = \frac{8}{105} \tilde{I}_1 r^3 + 2 \left(\frac{1}{35} \tilde{I}_1 r^3 - \frac{1}{60} \tilde{I}_2 r^3 \right) \quad (2.32)$$

The longitudinal increment is not affected by compressibility correction and therefore

$$\langle \Delta^* \tilde{u}_{\parallel}^3 \rangle = \frac{8}{105} \tilde{I}_1 r^3 \quad (2.33)$$

Part of the contribution to $\langle \Delta^* \tilde{u}_{\parallel} \Delta^* \tilde{u}_a \Delta^* \tilde{u}_a \rangle$, from the second term in equation (2.30) can be expressed by isotropic tensor analysis in terms of the invariants of

the coarse-grained velocity gradient. The tensor resulting from the contribution to the third order structure function from the second term in equation (2.30) reads

$$\left\langle \tilde{S}_{ij} \tilde{A}_{ak} \epsilon_{amb} \frac{\partial^3 \tilde{\mathcal{V}}_b}{\partial \zeta \partial x_p \partial x_q} \right\rangle = 2 \left\langle \tilde{S}_{ij} \frac{\partial}{\partial x_k} \left(\text{asymm} \left(\frac{\partial \tilde{A}_b}{\partial x_m} \right) \right) \frac{\partial^3 \tilde{\mathcal{V}}_b}{\partial \zeta \partial x_p \partial x_q} \right\rangle \quad (2.34)$$

This Cartesian tensor has the following non zero invariants:

- contraction ik, jm, pq of (2.34), using the transverse gauge $\partial_i \tilde{A}_i = 0$:

$$J_1 = \left\langle \tilde{S}_{ij} \tilde{A}_{ai} \epsilon_{ajb} \frac{\partial^3 \tilde{\mathcal{V}}_b}{\partial \zeta \partial x_p \partial x_p} \right\rangle = 2 \left\langle \tilde{S}_{ij} \tilde{R}_{ai} \frac{\partial \tilde{R}_{aj}}{\partial \zeta} \right\rangle$$

- contraction ik, jq, mp of (2.34), using the definition of the potential:

$$J_2 = \left\langle \tilde{S}_{ij} \tilde{A}_{ai} \epsilon_{amb} \frac{\partial^3 \tilde{\mathcal{V}}_b}{\partial \zeta \partial x_m \partial x_j} \right\rangle = \left\langle \tilde{S}_{ij} \tilde{A}_{ai} \frac{\partial \tilde{A}_{aj}}{\partial \zeta} \right\rangle$$

- contraction im, jp, kq of (2.34), using the inverse definition of the potential:

$$J_3 = \left\langle \tilde{S}_{ij} \tilde{A}_{ak} \epsilon_{aib} \frac{\partial^3 \tilde{\mathcal{V}}_b}{\partial \zeta \partial x_j \partial x_k} \right\rangle = \frac{1}{2} \left\langle \tilde{S}_{ij} \tilde{A}_{ai} \frac{\partial \tilde{A}_{aj}}{\partial \zeta} \right\rangle + \left\langle \tilde{S}_{ij} \tilde{A}_{ak} \epsilon_{aib} \frac{\partial^2 \tilde{B}_{bj}}{\partial \zeta \partial x_k} \right\rangle$$

with B symmetric and traceless.

- contraction ip, jq, km of (2.34), using the definition of the potential:

$$J_4 = \left\langle \tilde{S}_{ij} \tilde{A}_{ak} \epsilon_{akb} \frac{\partial^3 \tilde{\mathcal{V}}_b}{\partial \zeta \partial x_i \partial x_j} \right\rangle = \left\langle \tilde{S}_{ij} \tilde{R}_{cj} \frac{\partial \tilde{A}_{ci}}{\partial \zeta} \right\rangle - \left\langle \tilde{S}_{ij} \tilde{\omega}_b \frac{\partial^2 \tilde{B}_{bj}}{\partial \zeta \partial x_i} \right\rangle$$

with B symmetric and traceless.

By sixth order isotropic tensor analysis, using the invariants listed above, we obtain

$$\left\langle \tilde{S}_{ij} \tilde{A}_{ak} \epsilon_{amb} \frac{\partial^3 \tilde{\mathcal{V}}_b}{\partial \zeta \partial x_p \partial x_q} \right\rangle \hat{r}_i \hat{r}_j \hat{r}_k \hat{r}_m \hat{r}_p \hat{r}_q = \frac{2}{105} (J_1 + 2J_2 + 2J_3 + J_4) r^4 \quad (2.35)$$

and the term proportional to the principal invariant $\tilde{R}^* = \tilde{I}_1 - \tilde{I}_2/4$ is separated out,

$$\begin{aligned} & \left\langle \tilde{S}_{ij} \tilde{A}_{ak} \epsilon_{amb} \frac{\partial^3 \tilde{\mathcal{V}}_b}{\partial \zeta \partial x_p \partial x_q} \right\rangle \hat{r}_i \hat{r}_j \hat{r}_k \hat{r}_m \hat{r}_p \hat{r}_q = \frac{2}{105} \frac{d}{d\zeta} \left\langle \tilde{A}_{ij} \tilde{A}_{ai} \tilde{A}_{aj} \right\rangle r^4 + \\ & + \frac{2}{105} \left(2 \left\langle \tilde{S}_{ij} \frac{\partial}{\partial \zeta} (\tilde{R}_{ai} \tilde{R}_{aj}) \right\rangle - \left\langle \frac{\partial \tilde{S}_{ij}}{\partial \zeta} \tilde{R}_{ai} \tilde{R}_{aj} \right\rangle \right) r^4 + \\ & + \frac{2}{105} \left(2 \left\langle \tilde{S}_{ij} \tilde{A}_{ak} \epsilon_{aib} \frac{\partial^2 \tilde{B}_{bj}}{\partial \zeta \partial x_k} \right\rangle - \left\langle \tilde{S}_{ij} \tilde{\omega}_b \frac{\partial^2 \tilde{B}_{bj}}{\partial \zeta \partial x_i} \right\rangle \right) r^4 \end{aligned} \quad (2.36)$$

where the coefficient $2/105$ of the first term is uniquely determined by the terms in equation (2.35) which are proportional to $\partial_\zeta \tilde{S}$. Using equations (2.30), (2.32), (2.33) and (5.41), the mixed third order structure function,

$$\langle \Delta^* \tilde{u}_\parallel \Delta^* \tilde{u}_\perp^2 \rangle = \frac{1}{2} \left(\langle \Delta^* \tilde{u}_\parallel \Delta^* \tilde{u}_a \Delta^* \tilde{u}_a \rangle - \langle \Delta^* \tilde{u}_\parallel^3 \rangle \right) \quad (2.37)$$

can be written as:

$$\langle \Delta^* \tilde{u}_\parallel \Delta^* \tilde{u}_\perp^2 \rangle = \frac{1}{35} \tilde{I}_1 r^3 - \frac{1}{60} \tilde{I}_2 r^3 + \frac{1}{105} \frac{d}{d\zeta} \langle \tilde{A}_{ij} \tilde{A}_{ai} \tilde{A}_{aj} \rangle \zeta' r^4 + \mathcal{R}[\mathbf{r}, \mathbf{A}, \mathbf{G}] \quad (2.38)$$

The term \mathcal{R} is a functional of the separation \mathbf{r} , the vector potential \mathbf{V} and the arbitrary constant of integration \mathbf{G} . \mathcal{R} is due to the compressibility correction and involves all the terms in $\langle \Delta^* \tilde{u}_\parallel \Delta^* \tilde{u}_a \Delta^* \tilde{u}_a \rangle$ that cannot be written as functions of $\tilde{R}^* = \tilde{S} - \tilde{I}_2/4$. \mathcal{R} is tuned by means of \mathbf{G} in such a way that equation (2.19) holds for the incompressible coarse-grained increment:

$$\frac{1}{35} \tilde{I}_1 r^3 - \frac{1}{60} \tilde{I}_2 r^3 + \frac{4}{315} \tilde{I}_1' r^4 + \mathcal{R} = \frac{16}{315} \tilde{I}_1 r^3 + \frac{4}{315} \tilde{I}_1' r^4$$

that is, using again Betchov relation:

$$\mathcal{R}[\mathbf{r}, \mathbf{A}, \mathbf{G}] = 0. \quad (2.39)$$

This shows that the quantity of interest for the energy flux, $\langle \Delta^* \tilde{u}_\parallel \Delta^* \tilde{u}_\perp^2 \rangle$, is consistently expressed in terms of the principal invariant $\tilde{R}^* = \tilde{I}_1 - \tilde{I}_2/4$.

Chapter 3

Dimensional reduction of the anisotropic pressure Hessian

Analyzing the fluid velocity gradients in a Lagrangian reference frame provides an insightful way to study the small-scale dynamics of turbulent flows, and further insight is provided by considering the equations in the eigenframe of the strain-rate tensor. The dynamics of the velocity gradient tensor is governed in part by the anisotropic pressure Hessian, which is a non-local functional of the velocity gradient field. This anisotropic pressure Hessian plays a key role in the velocity gradient dynamics, for example in preventing finite-time singularities, but it is difficult to understand and model due to its non-locality and complexity. In this work a gauge symmetry for the pressure Hessian is introduced to the eigenframe equations of the velocity gradient, such that when the gauge is added to the original pressure Hessian, the single-point dynamics of the velocity gradient invariants remain unchanged. We then exploit this gauge symmetry to perform a rank reduction on the three-dimensional anisotropic pressure Hessian, which, remarkably, is possible everywhere in the flow. The dynamical activity of the newly introduced rank-reduced anisotropic pressure Hessian is confined to two dimensional manifolds in the three dimensional flow, and exhibits striking alignment properties with respect to the strain-rate eigenframe and the vorticity vector. The dimensionality reduction, together with the strong preferential alignment properties, leads to new dynamical insights for understanding and modelling the role of the anisotropic pressure Hessian in three-dimensional flows.

This piece of work is under revision for the Journal of Fluid Mechanics and most of the following material can be found in the manuscript [29].

3.1 Introduction

The small-scale dynamics of turbulent flows is governed by highly non-linear and non-local dynamical processes, whose statistics are strongly intermittent in space and time [167, 20]. Such small-scale dynamics is effectively characterized by the velocity gradient field, rather than the velocity field itself [150]. Consequently, understanding and modelling the velocity gradient dynamics is of singular importance in the study of turbulence and has been the subject of many works in the literature. In particular, the Lagrangian description of the velocity gradient dynamics has proven to be especially fruitful for understanding and modeling [108].

The equation governing the velocity gradient tensor dynamics along a fluid particle trajectory is easily derived from the Navier-Stokes equation (NSE) but, the equation is unclosed because of the anisotropic/non-local pressure Hessian and viscous terms. Developing closure models for these complex terms requires insight, and this work concentrates on the properties of the anisotropic pressure Hessian.

The pressure field can be expressed as a linear, non-local, functional of the second invariant of the velocity gradient tensor. Therefore, a strategy to infer the statistical properties of the pressure field consists in analyzing how the velocity gradient organizes in space. A quantitative investigation of the correlation length of the velocity gradient magnitude shows that, in rotation-dominated regions, the pressure field is governed by a dissipation-scale neighbourhood while, in strain-dominated regions, the pressure is determined by an inertial-scale neighbourhood [157]. However, many works in the literature have shown that the pressure statistics can be described reasonably well by quasi-local approximations [34, 100]. Indeed, the long-range effects to the pressure field are much smaller than expected due to partial cancellation of the competing contributions of the strain-rate and vorticity magnitude to the second invariant of the velocity gradient [157].

The information about the statistics of the pressure field can then be employed to develop closure models for the Lagrangian dynamics of the velocity gradient in turbulence. In the inviscid case, an early closure model by [156] has been derived neglecting the non-local/anisotropic part of the pressure Hessian, while retaining its local/isotropic part. This model is usually referred to as the Restricted Euler (RE) model. This model led to important insights, showing the tendency for the intermediate eigenvalue of the strain-rate to be positive, and also the preferred alignment of the vorticity with the intermediate strain-rate eigenvector [22] as observed in Direct Numerical Simulation (DNS) of isotropic turbulence and homogeneous shear flows [4]. However, the RE flow exhibits a finite-time singularity for almost all initial conditions, indicating that a realistic model for the velocity gradient should take into account the anisotropic pressure Hessian, in addition to viscous contributions. Indeed, the anisotropic pressure Hessian is considered to play a major role in preventing such finite-time singularities, even for ideal fluids, and it has been analyzed in detail in several works [114, 113, 34, 157].

In an early work, the anisotropic pressure Hessian has been modelled as a stochastic process, independent of the gradient dynamics, and the stochastic differential equations for the velocity gradient have been constructed to satisfy isotropy constraints and empirical constraints as the log-normality of the dissipation rate [61]. A more advanced phenomenological and stochastic model was constructed in [32] by analyzing the Lagrangian dynamics using four tracer trajectories, forming a tetrad. The tetrad can be used to construct a scale-dependent filtered velocity gradient [112] and the closure of the model involves a direct relation between the local pressure and the velocity gradient on the tetrad. The tetrad model provided a phenomenological basis for understanding how the anisotropic pressure Hessian acts to reduce non-linearity in the flow, a property that also emerges in more systematic closures for the pressure Hessian based on Gaussian random fields [164].

The deformation history of a fluid particle in the flow has been employed to model the anisotropic pressure Hessian and viscous terms using Lagrangian coordinate closures [33]. In this model, only information on the recent fluid deformation (RFD) is retained, that is, the dynamics is affected by times up to the Kolmogorov timescale, τ_η , in the past. A phenomenological closure is then constructed assuming that at a time τ_η in the past, the Lagrangian pressure Hessian was isotropic. This model does not exhibit the singularity associated with the RE, and was shown to capture many of the non-trivial features of the velocity gradient dynamics that are observed in experiments and Direct Numerical Simulations of the NSE. However, it displays unphysical behaviour for flows at large Reynolds number. A critical comparison with DNS data [34] showed that while the closure model presented in [33] can reproduce some of the non-trivial velocity gradient dynamics, it misses some important features of the pressure Hessian dynamics and statistical geometry in the flow.

[164] proposed a closure for the Lagrangian velocity gradient equation by assuming that the velocity is a random field with Gaussian statistics. Closed expressions for the pressure Hessian and viscous terms conditioned on the velocity gradient are obtained by means of the characteristic functional of the Gaussian velocity field. The model produces qualitatively good results but, owing to the Gaussian assumption, it leads to quantitative predictions that are not in full agreement with DNS data. Therefore, to correct this aspect, the authors modified the closure such that the mathematical structure was retained, but the coefficients appearing in the model were prescribed using DNS data. This led to significant improvements, since the model provides interesting insights into the role of the anisotropic pressure Hessian in preventing the singularities arising in the RE. However, the enhanced model did not satisfy the kinematic relations for incompressible and isotropic flows [10].

Another model has been developed by [86], who combined the closure modeling ideas by both [33] and [164]. This model leads to improvements compared with the two models on which it is based, and it is formulated in such a way that by construction the model satisfies the kinematic relations of [10]. However, a quantitative

comparison with DNS data revealed some shortcomings in the ability of the model to properly capture the intermittency of the flow. Moreover, it runs into difficulties for high Reynolds number flows, like that of [33] from which it has been partly derived. The capability to reproduce intermittency and high-Reynolds number flow features is a major challenge for velocity gradient models. A recent development of velocity gradient models, based on a multiscale refined self-similarity hypothesis, proposed by [87], seems to remove the Reynolds number limitations (at least in the sense that the model does not break down at high Reynolds numbers).

In summary, while significant progress has been made since the initial modelling efforts of [156, 155], much remains to be done. A major difficulty in developing accurate closure approximations for the Lagrangian velocity gradient equation is that the dynamical effects of the anisotropic/non-local pressure Hessian on the flow are not yet fully understood and are difficult to approximate using simple closure ideas. This fact is the motivation behind the present work which aims to improve the understanding of the anisotropic pressure Hessian, and in particular, its statistical geometry relative to the strain-rate and vorticity fields. In the following, we present what appears to be a previously unrecognized gauge symmetry for the pressure Hessian, such that when this gauge is added to the pressure Hessian, the invariant dynamics of the velocity gradient tensor remains unchanged. We then exploit this gauge symmetry to perform a rank reduction on the anisotropic pressure Hessian. Remarkably, this rank reduction can be performed everywhere in the turbulent flow, and produces the newly introduced rank-reduced anisotropic pressure Hessian which lives on a two-dimensional manifold and exhibits striking alignment properties with respect to the strain-rate eigenframe and the vorticity vector. This dimensionality reduction, together with evident preferential alignments of the rank-reduced anisotropic pressure Hessian has implications in the understanding and modelling of turbulent flows.

3.2 Theory

In this Section the gauge symmetry for the invariants dynamics is derived from the equations for the velocity gradient written in the strain-rate eigenframe. The gauge is then exploited to reduce the rank of the anisotropic pressure Hessian obtaining a rank-reduced anisotropic pressure Hessian which is a two-dimensional object embedded in a three-dimensional space.

3.2.1 Equations for the fluid velocity gradient in the strain-rate eigenframe

The three-dimensional flow of a Newtonian and incompressible fluid with unitary density is described by the Navier-Stokes equations

$$\nabla \cdot \mathbf{u} = 0, \quad \frac{D\mathbf{u}}{Dt} \equiv \frac{\partial \mathbf{u}}{\partial t} + (\mathbf{u} \cdot \nabla)\mathbf{u} = -\nabla P + \nu \nabla^2 \mathbf{u}, \quad (3.1)$$

where $\mathbf{u}(\mathbf{x}, t)$, $P(\mathbf{x}, t)$ are the fluid velocity and pressure fields and ν is the kinematic viscosity. By taking the gradient of (3.1), the following equation for the velocity gradient tensor is obtained

$$\text{Tr}(\mathbf{A}) = 0, \quad \frac{D}{Dt} \mathbf{A} = -\mathbf{A} \cdot \mathbf{A} - \mathbf{H} + \nu \nabla^2 \mathbf{A}, \quad (3.2)$$

where $\mathbf{A} \equiv \nabla \mathbf{u}$ is the velocity gradient, and $\mathbf{H} \equiv \nabla \nabla P$ is the pressure Hessian. The pressure and viscous terms in equation (3.2) are not in closed form, since they cannot be expressed in terms of the velocity gradient along the fluid particle trajectory, $\mathbf{A}(\mathbf{x}(t), t)$. Models are necessary to define those terms and reliable modelling of them requires an understanding of their dynamical and statistical properties [108].

The tensor \mathbf{A} is decomposed into its symmetric and anti-symmetric part, namely the strain-rate $\mathbf{S} \equiv (\mathbf{A} + \mathbf{A}^\top)/2$, and the rate-of-rotation $\mathbf{R} \equiv (\mathbf{A} - \mathbf{A}^\top)/2$, whose components are related to the vorticity $\boldsymbol{\omega} \equiv \nabla \times \mathbf{u}$ as $R_{ij} = \epsilon_{ikj}\omega_k/2$. Using equation (3.2) the equations for \mathbf{S} and $\boldsymbol{\omega}$ are obtained, and it is insightful to write these in the eigenframe of \mathbf{S} . The eigenvectors \mathbf{v}_i of the strain-rate satisfy $\mathbf{v}_i \cdot \mathbf{v}_j = \delta_{ij}$, where δ_{ij} is the Kronecker delta, and thus define an orthonormal basis. The strain-rate eigenvectors remain orthogonal so that the strain-rate basis undergoes rigid body rotation only, with rotation rate $\boldsymbol{\omega}$,

$$\frac{D\mathbf{v}_i}{Dt} = \boldsymbol{\omega} \times \mathbf{v}_i. \quad (3.3)$$

The equations for the velocity gradient in the strain-rate eigenframe read

$$\sum_{j=1}^3 \lambda_j = 0 \quad (3.4)$$

$$\frac{D\lambda_i}{Dt} = -\lambda_i^2 + \frac{1}{4}(\omega^2 - \bar{\omega}_i^2) - \bar{H}_{i(i)} + \overline{\nu \nabla^2 S_{i(i)}}, \quad (3.5)$$

$$\bar{W}_{ij}(\lambda_{(j)} - \lambda_{(i)}) = -\frac{1}{4}\bar{\omega}_i\bar{\omega}_j - \bar{H}_{ij} + \overline{\nu \nabla^2 S_{ij}}, \quad j \neq i, \quad (3.6)$$

$$\frac{D\bar{\omega}_i}{Dt} = \lambda_{(i)}\bar{\omega}_i - \bar{W}_{ij}\bar{\omega}_j + \overline{\nu \nabla^2 \omega_i}, \quad \text{for } i = 1, 2, 3 \quad (3.7)$$

where λ_i are the strain-rate eigenvalues, the overline indicates tensors components in the strain-rate eigenframe, so that $\bar{\omega}_i = \mathbf{v}_i \cdot \boldsymbol{\omega}$ and $\bar{H}_{ij} = \mathbf{v}_i \cdot \mathbf{H} \cdot \mathbf{v}_j$ and $\omega^2 \equiv \bar{\omega}_i \bar{\omega}_i$. In these equations, the indexes in parenthesis are not contracted. The anti-symmetric tensor \mathbf{W} is related to the eigenframe angular velocity $\boldsymbol{\omega}$ through

$$W_{ij} = \epsilon_{ikj} \omega_k \quad (3.8)$$

and \bar{W}_{ij} are the components of \mathbf{W} in the strain-rate eigenframe. The eigenframe equations (3.4), (3.5), (3.6), (3.7) allow to sort out the interaction between local strain and vorticity and have been studied in detail [156, 50, 113].

3.2.2 A new symmetry for the dynamics of the velocity gradient invariants

The eigenframe equations satisfy basic symmetries. They are naturally invariant under the transformation $\bar{\omega}_i \rightarrow -\bar{\omega}_i$, since the eigenvectors are only defined up to an arbitrary sign. The inviscid equations are also invariant under time reversal $t \rightarrow -t$. However, the equations also possess another kind of symmetry that does not appear to have been previously recognized. That new symmetry arises from the fact that in the equation governing $\bar{\omega}_i$, the strain-rate eigenframe rotation rate $\boldsymbol{\omega}$ only enters through the cross product $\bar{W}_{ij} \bar{\omega}_j$ and therefore its component along the vorticity direction, $\boldsymbol{\omega} \cdot \boldsymbol{\omega}$, does not affect in any way the time evolution of the velocity gradient invariants. In order to show this fact we first define the transformation

$$\mathbf{W} \rightarrow \mathbf{W} + \gamma \mathbf{R}, \quad (3.9)$$

that corresponds to adding to the rotation-rate of the strain-rate eigenframe an additional rotation about the vorticity axis at rate $\gamma\omega/2$, where $\gamma(\mathbf{x}, t)$ is a non-dimensional scalar field. If we introduce the transformation (3.9) into the eigenframe equations, the equation governing the strain-rate eigenvalues (3.5) and the vorticity components in the strain-rate eigenframe (3.7) remain unchanged. Indeed the equation for λ_i is not affected by the transformation (3.9) since it does not contain \mathbf{W} . The equation for $\bar{\omega}_i$ is also unaffected since by definition $\mathbf{R} \cdot \boldsymbol{\omega} = \mathbf{0}$ and, therefore,

$$\frac{D\bar{\omega}_i}{Dt} = \lambda_{(i)} \bar{\omega}_i - [\bar{W}_{ij} + \gamma \bar{R}_{ij}] \bar{\omega}_j + \overline{\nu \nabla^2 \omega_i} = \lambda_{(i)} \bar{\omega}_i - \bar{W}_{ij} \bar{\omega}_j + \overline{\nu \nabla^2 \omega_i}. \quad (3.10)$$

On the other hand, the off-diagonal algebraic equation (3.6) becomes

$$\bar{W}_{ij} (\lambda_{(j)} - \lambda_{(i)}) = -\frac{1}{4} \bar{\omega}_i \bar{\omega}_j - \bar{H}_{ij} - \gamma \bar{R}_{ij} (\lambda_{(j)} - \lambda_{(i)}) + \overline{\nu \nabla^2 S_{ij}}, \quad j \neq i. \quad (3.11)$$

This equation is not invariant under the transformation (3.9). However, while this changes the orientation of the strain-rate eigenframe with respect to a fixed,

arbitrary, reference frame, it does not affect either λ_i or $\bar{\omega}_i$. Therefore, the transformation $\mathbf{W} \rightarrow \mathbf{W} + \gamma \mathbf{R}$ corresponds to a symmetry for the invariants of the velocity gradient tensor, that can be expressed in terms of λ_i or $\bar{\omega}_i$. For example, the second and third invariants of the velocity gradient tensor can be written as

$$Q = -\sum_i \lambda_i^2/2 + \sum_i \bar{\omega}_i^2/4, \quad R = -\sum_i \lambda_i^3/3 - \sum_i \lambda_i \bar{\omega}_i^2/4. \quad (3.12)$$

It is important to note, however, that multi-time or multi-point invariants of the velocity gradients are not in general invariant under the gauge transformation. For example, $\mathbf{S}(\mathbf{x}(t), t) : \mathbf{S}(\mathbf{x}(t'), t')$ is affected by the gauge transformation since the transformation arbitrarily modifies the relative orientations of the eigenframes of $\mathbf{S}(\mathbf{x}(t), t)$ and $\mathbf{S}(t', \mathbf{x}(t'))$. Nevertheless, multi-time or multi-point products of λ_i or $\bar{\omega}_i$ are invariant under the gauge transformation. In this Chapter we focus on single-point and single-time quantities.

3.2.3 Gauge symmetry for the anisotropic pressure Hessian

The anisotropic/non-local pressure Hessian is defined as

$$\mathcal{H} \equiv \mathbf{H} - \frac{1}{3} \mathbf{I} \text{Tr}(\mathbf{H}) = \mathbf{H} + \frac{1}{3} \mathbf{I}(\mathbf{A} : \mathbf{A}), \quad (3.13)$$

where \mathbf{I} is the three-dimensional identity matrix. This anisotropic pressure Hessian satisfies $\text{Tr}(\mathcal{H}) = 0$ and contains all of the non-local part of \mathbf{H} . It is also important to notice that its non-local dependence on the flow field is only through the second invariant of the velocity gradient Q [105]. The invariance of the eigenframe dynamics under the transformation $\mathbf{W} \rightarrow \mathbf{W} + \gamma \mathbf{R}$ is interpreted as a gauge symmetry for \mathcal{H} . That is, the term $\gamma \bar{R}_{ij} (\lambda_{(j)} - \lambda_{(i)})$ in equation (3.11) is added to $\bar{\mathcal{H}}_{ij}$ defining $\mathcal{H}_\gamma = \mathcal{H} + \delta \mathcal{H}$, without affecting the eigenframe dynamics, which is described through λ_i and $\bar{\omega}_j$. In particular, the gauge term

$$\delta \mathcal{H} = \gamma \sum_{i,j} \bar{R}_{ij} (\lambda_j - \lambda_i) \mathbf{v}_i \mathbf{v}_j^\top \quad (3.14)$$

is the commutator of anti-symmetric and symmetric part of the velocity gradient

$$\delta \mathcal{H} = \gamma [\mathbf{R}, \mathbf{S}], \quad (3.15)$$

where $[\mathbf{R}, \mathbf{S}] \equiv \mathbf{R} \cdot \mathbf{S} - \mathbf{S} \cdot \mathbf{R}$. Then, the gauge symmetry consists in the fact that the single-point and single-time Lagrangian dynamics of the velocity gradient invariants is identical when \mathcal{H} is replaced by

$$\mathcal{H}_\gamma = \mathcal{H} + \gamma [\mathbf{R}, \mathbf{S}]. \quad (3.16)$$

The gauge symmetry holds for all real and finite multiplier $\gamma(\mathbf{x}, t)$, which at this stage is still undetermined.

It is interesting to note that a term identical to that in equation (3.15) also arises from a closure of the pressure Hessian assuming a random velocity field with Gaussian statistics [164]. In the framework of the Gaussian closure, the coefficient of $[\mathbf{R}, \mathbf{S}]$ is the only one that requires specific knowledge of the spatial structure of the flow and must be prescribed by phenomenological closure hypothesis, while all other coefficients of the model can be determined exactly. However, our analysis implies that the ability of the Gaussian closure to predict the invariants of the velocity gradient tensor will not be impacted by the phenomenological closure hypothesis, since its contribution in the dynamics corresponds to the gauge term in equation (3.15) that does not affect the velocity gradient invariants.

3.2.4 Using the gauge symmetry for dimensionality reduction

While any finite and real γ provides a suitable \mathcal{H}_γ , there may exist certain choices of γ that generate representations of \mathcal{H}_γ that live on a lower dimensional manifold in the system (in the sense that some of its eigenvalues are zero). If such configurations exist and are common, this could significantly aid the understanding and modelling of the anisotropic pressure Hessian in the turbulence dynamics. To seek for such lower dimensional configurations is equivalent to seek for configurations in which a rank-reduction on \mathcal{H}_γ can be performed. We denote such rank-reduced forms of \mathcal{H}_γ by \mathcal{H}_γ^* . Notice that $\text{rk}(\mathcal{H}_\gamma^*) = 1$ is not possible since $\text{Tr}(\mathcal{H}_\gamma) = 0$, and therefore either $\text{rk}(\mathcal{H}_\gamma^*) = 2$ or $\mathcal{H}_\gamma^* = \mathbf{0}$.

In seeking for lower dimensional representations, when \mathcal{H} is singular the gauge term is not needed as \mathcal{H} already lives on a lower dimensional manifold and we take $\mathcal{H}_\gamma^* = \mathcal{H}$, corresponding to the choice $\gamma = 0$. On the other hand, when \mathcal{H} is not singular we seek for a non-zero vector \mathbf{z}_2 such that $\mathcal{H}_\gamma^* \cdot \mathbf{z}_2 = \mathbf{0}$, where \mathbf{z}_2 corresponds to the eigenvector of \mathcal{H}_γ^* associated with its zero (and intermediate) eigenvalue. This is equivalent to the generalized eigenvalue problem $\det(\mathcal{H}_\gamma^*) = 0$, that is,

$$\det(\mathbf{I} + \gamma \mathcal{H}^{-1}[\mathbf{R}, \mathbf{S}]) = 0. \quad (3.17)$$

Notice that \mathcal{H} can be safely inverted in equation (3.17), since the case of singular \mathcal{H} has been already taken into account and corresponds to $\gamma = 0$. If there exist finite and real values for γ that solve equation (3.17), then those values of γ generate a rank-two \mathcal{H}_γ^* . Defining $\mathcal{E} \equiv \mathcal{H}^{-1}[\mathbf{R}, \mathbf{S}]$, the characteristic equation governing $\xi \equiv -1/\gamma$ reads

$$\xi^3 - c\xi^2 - b\xi - a = 0, \quad (3.18)$$

with coefficients $a, b, c \in \mathbb{R}$ given by

$$a \equiv \det(\boldsymbol{\mathcal{E}}), \quad b \equiv \frac{1}{2}(\boldsymbol{\mathcal{E}} : \boldsymbol{\mathcal{E}} - \text{Tr}(\boldsymbol{\mathcal{E}}) \text{Tr}(\boldsymbol{\mathcal{E}})), \quad c \equiv \text{Tr}(\boldsymbol{\mathcal{E}}). \quad (3.19)$$

The properties of the roots of (3.18) are determined by the discriminant of the polynomial

$$\mu \equiv b^2 c^2 + 4b^3 - 4c^3 a - 27a^2 - 18abc. \quad (3.20)$$

When $\mu = 0$, all of the roots of (3.18) are real and at least two are equal, when $\mu > 0$ there are three distinct real roots, and when $\mu < 0$ there is one real root and two complex conjugate roots. In every case, there is at least one real root since all the coefficients are real and the degree of the characteristic polynomial is odd. Provided that $a \neq 0$, a real and finite $\gamma \equiv -1/\xi$ exists. When $a = 0$, a real and finite γ may or may not exist according to the value of the discriminant μ . This shows that configurations where a rank-two $\boldsymbol{\mathcal{H}}_\gamma$ does not exist, that is, the pressure Hessian is intrinsically three-dimensional, may only occur when $a = 0$. Interestingly, $a \equiv \det \boldsymbol{\mathcal{H}} \det[\boldsymbol{R}, \boldsymbol{S}]$ and, since by hypothesis $\det \boldsymbol{\mathcal{H}} \neq 0$ the rank reduction of the anisotropic pressure Hessian may not be performed where $\det[\boldsymbol{R}, \boldsymbol{S}] = 0$. The determinant of the commutator is

$$\det[\boldsymbol{R}, \boldsymbol{S}] = \frac{1}{4}(\lambda_2 - \lambda_1)(\lambda_3 - \lambda_2)(\lambda_1 - \lambda_3)\bar{\omega}_1\bar{\omega}_2\bar{\omega}_3, \quad (3.21)$$

so that, when either one or more of the vorticity components in the strain-rate eigenframe is zero, and/or the straining-rate configuration is axisymmetric, a singular $\boldsymbol{\mathcal{H}}_\gamma$ may not exist. However, since \boldsymbol{S} and $\boldsymbol{\omega}$ have continuous probability distributions, then the probability that $\det[\boldsymbol{R}, \boldsymbol{S}] = 0$ is in fact zero. Therefore, the rank reduction of $\boldsymbol{\mathcal{H}}_\gamma$ should be possible everywhere in the flow.

Configurations in which multiple rank-reduced anisotropic pressure Hessian can be defined at the same point, that is, there exist more than a single real and finite multiplier γ , admit an additional discrete symmetry which allows different $\boldsymbol{\mathcal{H}}_\gamma^*$ to generate the same dynamics of the velocity gradient invariants. We fix this additional gauge by choosing γ that provides the maximum alignment between the intermediate eigenvector of the rank-reduced anisotropic pressure Hessian and the vorticity. As it will be shown in §3.3, this is justified on the basis of the numerical results, which indicate a marked preferential alignment of the intermediate eigenvector of the rank-reduced anisotropic pressure Hessian with the vorticity.

The rank reduction of the anisotropic pressure Hessian, defined through equation (3.17), allows for a noticeable reduction of the complexity of the anisotropic pressure Hessian leading to a better understanding of its dynamical effects. Indeed, the fully three-dimensional anisotropic pressure Hessian is specified by five real numbers, being a square matrix of size three. In particular, it takes two numbers

to specify the normalized eigenvector \mathbf{y}_1 , one additional number for \mathbf{y}_2 (then \mathbf{y}_3 is automatically determined) and two more numbers for the independent eigenvalues φ_1 and φ_3 (since $\sum_i \varphi_i = 0$). Therefore, the anisotropic pressure Hessian can be written as

$$\mathcal{H} = \sum_{i=1}^3 \varphi_i \mathbf{y}_i \mathbf{y}_i^\top. \quad (3.22)$$

We keep the standard convention $\varphi_1 \geq \varphi_2 \geq \varphi_3$. On the other hand, the rank-reduced anisotropic pressure Hessian is specified by only four real numbers. Indeed it is a traceless and singular square matrix of size three. In particular, it takes two numbers to specify the plane orthogonal to the normalized eigenvector \mathbf{z}_2 an additional number to specify the orientation of \mathbf{z}_1 on the plane orthogonal to \mathbf{z}_2 (then \mathbf{z}_3 is determined) and a number for the single independent eigenvalue ψ . Therefore, the rank-reduced anisotropic pressure Hessian can be written as

$$\mathcal{H}_\gamma^* = \psi (\mathbf{z}_1 \mathbf{z}_1^\top - \mathbf{z}_3 \mathbf{z}_3^\top) \quad (3.23)$$

since the intermediate eigenvector is identically zero and the others satisfy $\psi_1 = -\psi_3 = \psi$ and $\psi \geq 0$. The pressure Hessian lives locally on the plane Π_2 orthogonal to \mathbf{z}_2 , which is the tangent space to a more complex manifold. The tensor \mathcal{H}_γ^* acts on a generic vector \mathbf{q} amplifying its component along \mathbf{z}_1 , cancelling its component along \mathbf{z}_2 and amplifying and flipping its component along \mathbf{z}_3 . The rank-reduced anisotropic pressure Hessian is effective only on the plane Π_2 . The eigenvalue of the rank-reduced anisotropic pressure Hessian can be related to the full anisotropic pressure Hessian and the vorticity since $\boldsymbol{\omega}^\top \cdot \mathcal{H} \cdot \boldsymbol{\omega} = \boldsymbol{\omega}^\top \cdot \mathcal{H}_\gamma \cdot \boldsymbol{\omega}$ which implies

$$\psi = \frac{\sum_i \varphi_i (\boldsymbol{\omega} \cdot \mathbf{y}_i)^2}{(\boldsymbol{\omega} \cdot \mathbf{z}_1)^2 - (\boldsymbol{\omega} \cdot \mathbf{z}_3)^2}. \quad (3.24)$$

Moreover, the tensors \mathcal{H} and \mathcal{H}_γ satisfy the relation $\boldsymbol{\omega}^\top \cdot \mathbf{S} \cdot \mathcal{H} \cdot \boldsymbol{\omega} = \boldsymbol{\omega}^\top \cdot \mathbf{S} \cdot \mathcal{H}_\gamma \cdot \boldsymbol{\omega}$ which yields another equation for the eigenvalue ψ ,

$$\psi = \frac{\sum_i \varphi_i \boldsymbol{\omega} \cdot \mathbf{y}_i (\mathbf{S} \cdot \boldsymbol{\omega}) \cdot \mathbf{y}_i}{\boldsymbol{\omega} \cdot [\mathbf{z}_1 (\mathbf{S} \cdot \boldsymbol{\omega}) \cdot \mathbf{z}_1 - \mathbf{z}_3 (\mathbf{S} \cdot \boldsymbol{\omega}) \cdot \mathbf{z}_3]}. \quad (3.25)$$

Equation (3.24) shows that a perfect alignment between \mathbf{z}_2 and $\boldsymbol{\omega}$ would result in an infinitely large ψ , unless the anisotropic pressure Hessian fulfills the condition $\boldsymbol{\omega}^\top \cdot \mathcal{H} \cdot \boldsymbol{\omega} = 0$. For example, such a peculiar configuration occurs when the flow is exactly two-dimensional, for which $\mathcal{H}_\gamma^* = \mathcal{H}$. In general, a large eigenvalue ψ corresponds to strong alignment between \mathbf{z}_2 and $\boldsymbol{\omega}$, as it will be discussed in §3.3.

This rank-reduction brings two-dimensional features into three-dimensional flows, and it is interesting to note that the equations for the velocity gradient already contain another two-dimensional flow feature. In particular, in equation (3.5) the term $(\omega^2 - \bar{\omega}_i^2)/4$ arises from the eigenframe representation of $\mathbf{R} \cdot \mathbf{R} = -\omega^2 \mathbf{P}_\omega/4$ where

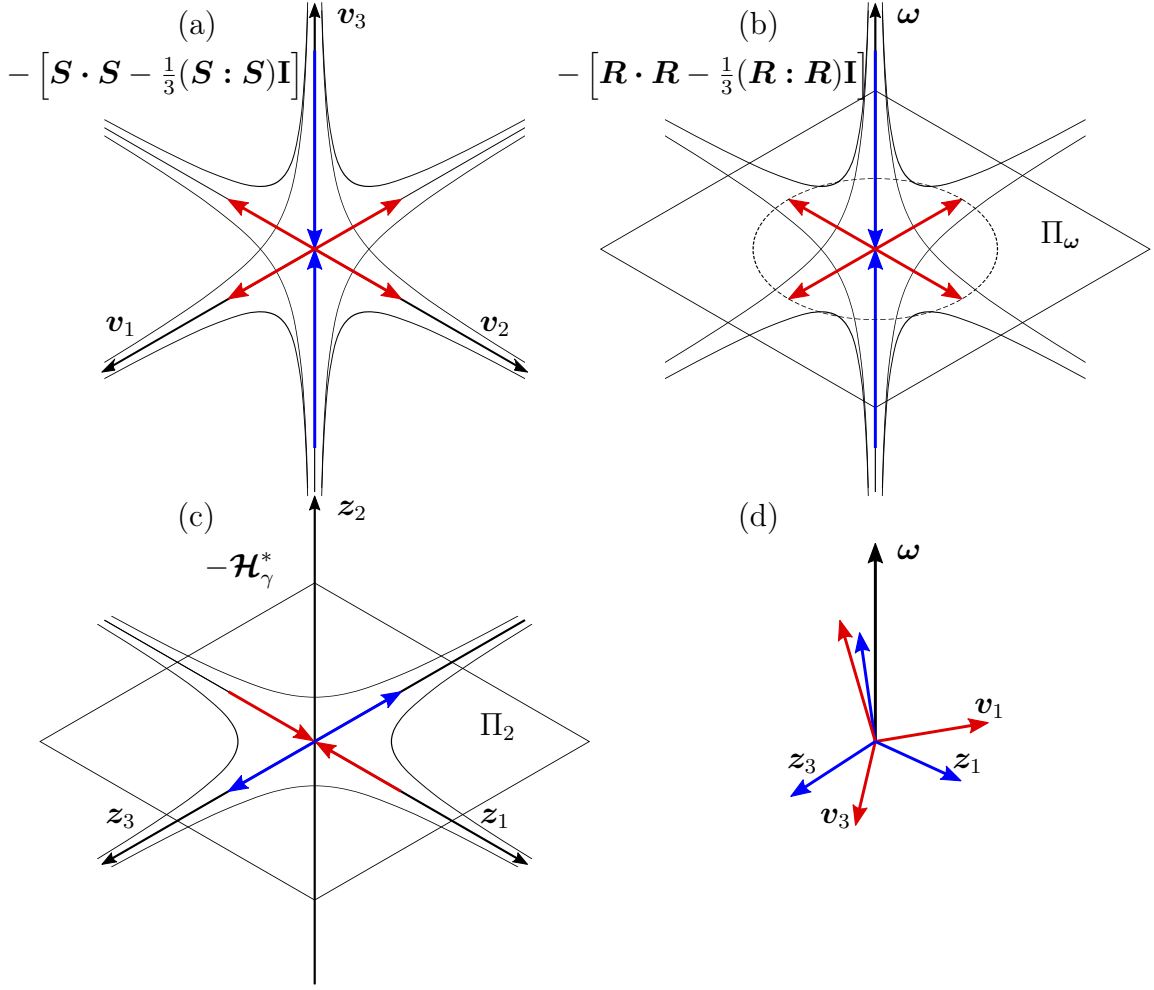


Figure 3.1: Schematic representation of contribution of the terms on the right hand side of equation (3.26). (a) Strain term $-\left[\mathbf{S} \cdot \mathbf{S} - \frac{1}{3}(\mathbf{S} : \mathbf{S})\mathbf{I}\right]$ for the typical configuration $\lambda_1 = \lambda_2 = -\lambda_3/2$. (b) Rotation term $-\left[\mathbf{R} \cdot \mathbf{R} - \frac{1}{3}(\mathbf{R} : \mathbf{R})\mathbf{I}\right]$ which isotropically produces stretching rate along the plane orthogonal to ω and a compression parallel to ω . (c) Rank-reduced anisotropic pressure Hessian $-\mathcal{H}_\gamma^*$ which produces straining along the z_3 direction, and hinders it along the z_1 direction. (d) Typical configuration for the relative orientation of strain-rate eigenframe, vorticity and rank-reduced anisotropic pressure Hessian eigenframe.

\mathbf{P}_ω is the projection tensor on the plane Π_ω orthogonal to the vorticity vector ω . This term describes the straining motion in the plane orthogonal to ω that is associated with the centrifugal force produced by the spinning of the fluid particle about its vorticity axis. As we will discuss later, this two-dimensional effect can be compared with the two-dimensional effect of \mathcal{H}_γ^* on the velocity gradient evolution, leading to interesting insights into their respective dynamical roles. Moreover, \mathcal{H}_γ^*

is a two dimensional object in a three-dimensional space which opens the possibility to effectively compare pressure Hessian statistics between two-dimensional and three-dimensional flows. However, the tangent space to the manifold defined by \mathcal{H}_γ^* varies in space and time, therefore the flow on Π_2 can not be directly compared with Euclidean two-dimensional turbulence but with flows in more complex geometries [58].

Using the dynamical equivalence of \mathcal{H} and \mathcal{H}_γ^* , we may re-write the equation governing λ_i as (ignoring the viscous term)

$$\frac{D\lambda_i}{Dt} = - \left(\lambda_i^2 - \frac{1}{3} \sum_j \lambda_j^2 \right) - \frac{1}{4} \left(\bar{\omega}_i^2 - \frac{1}{3} \sum_j \bar{\omega}_j^2 \right) - \bar{\mathcal{H}}_{\gamma,i(i)}, \quad (3.26)$$

and in figure 3.1 we provide a schematic to illustrate the role of each of the terms on the right hand side of (3.26).

3.3 Rank-reduced anisotropic pressure Hessian

We now turn to assess the properties of \mathcal{H}_γ^* . We do this using data from a Direct Numerical Simulation (DNS) of statistically stationary, isotropic turbulence. The DNS data used are those by [81, 82], at a Taylor micro-scale Reynolds number $R_\lambda = 597$. The data have been obtained through a pseudo-spectral method to solve the incompressible NSE on a three-dimensional, triperiodic cube discretized with 2048^3 grid points. A deterministic forcing method that preserves the kinetic energy in the flow has been employed. A detailed description of the numerical method used can be found in [83].

3.3.1 Pressure Hessian rank reduction

We first consider the properties of γ as determined by the numerical solution of equation (3.18) with $\gamma \equiv -1/\xi_{RF}$ real and finite. At each grid point we solve the generalized eigenvalue problem (3.17) to determine real and finite multipliers γ for which \mathcal{H}_γ^* is singular. The numerical solution of equation (3.18) is ill-conditioned when $\det[\mathbf{R}, \mathbf{S}]$ is very small. Therefore, we skip the grid points at which $\det[\mathbf{R}, \mathbf{S}]$ is less than a predefined numerical tolerance. We confirmed, however, that the results are only weakly sensitive to this small tolerance value. Figure 3.2 shows the probability of the multiplicity of real and finite values for γ obtained solving (3.18). The statistics are constructed by averaging the flow over space and time, a total of ten snapshots spanning six eddy turnover times have been used. The rank-reduced anisotropic pressure Hessian exists at the vast majority of the grid points, the configurations with no real and finite multipliers is observed at only about 0.1% of the grid points and corresponds to $\det[\mathbf{R}, \mathbf{S}]$ very small. The most common case ($\sim 60\%$ of the grid points) corresponds to three real and finite roots ξ_{RF} and

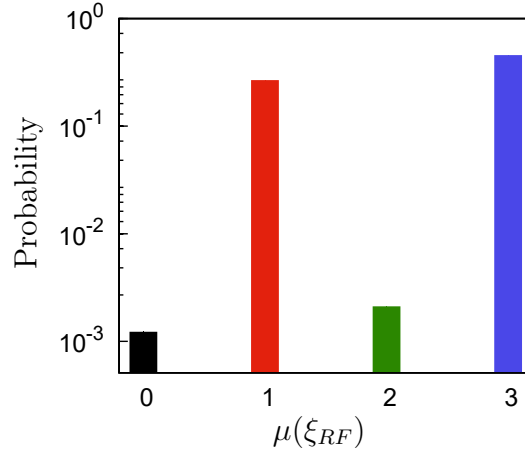


Figure 3.2: Probability of multiplicity of real and finite roots of equation (3.18).

thus three real and finite multipliers γ . Therefore, in addition to the continuous symmetry which allows to map \mathcal{H} into \mathcal{H}_γ^* there is a discrete symmetry, which allows three dynamically equivalent pressure Hessian, which generate the same dynamics of the velocity gradient invariants. The next most common case ($\sim 40\%$ of the grid points) is a single real and finite root ξ_{RF} and so a single γ and a single rank-two \mathcal{H}_γ^* . The case with two real and finite roots (and the third root asymptotically small compared with these) is rare ($\sim 0.15\%$ of the grid points) and corresponds to $\det[\mathbf{R}, \mathbf{S}]$ close to zero. In the configurations in which there exist multiple γ 's, the multiplier which gives the highest alignment between the vorticity vector and the intermediate eigenvector of the rank-reduced anisotropic pressure Hessian is selected. Indeed, that preferential alignment is a clear feature of the rank-reduced anisotropic pressure Hessian, as we will see below.

The probability density function (PDF) of the multiplier γ for which \mathcal{H}_γ has rank two is shown in figure 3.3(a). The PDF of the multiplier is highly non-Gaussian and the multiplier can be very large, even if with a small probability. This is due to the intermittency of the velocity gradient field, that is, large values of the coefficients of equation (3.18) and also due to the high probability of small $\det[\mathbf{R}, \mathbf{S}]$. In that case indeed, the matrix used for the reduction, $[\mathbf{R}, \mathbf{S}]$, spans the whole three-dimensional domain but with a very small eigenvalue in a certain eigendirection. As a consequence, the multiplier γ should be large enough to compensate the component of \mathcal{H} in that eigendirection, which can have large values. The probability density function of $\det[\mathbf{R}, \mathbf{S}]$ is shown in figure 3.3(b). The results show that $\det[\mathbf{R}, \mathbf{S}]$ is highly intermittent, being small throughout the vast majority of the flow, but exhibiting extreme fluctuations in very small regions. This can be understood in terms of the fact that according to equation (3.21), $\det[\mathbf{R}, \mathbf{S}]$ is an high-order moment of the velocity gradient field. Moreover, the tendency for small values of $\det[\mathbf{R}, \mathbf{S}]$ can also be understood in terms of the well-known fact that

$\boldsymbol{\omega}$ tends to misalign with \boldsymbol{v}_3 [108], leading to small values for $\bar{\omega}_3$ and therefore to small values of $\det[\boldsymbol{R}, \boldsymbol{S}]$ via equation (3.21).

We now turn to investigate the flow features conditioned on $\det[\boldsymbol{R}, \boldsymbol{S}]$. The high probability to observe small $\det[\boldsymbol{R}, \boldsymbol{S}]$ is consistent with the average of the strain and rotation magnitude conditioned on the local value of $\det[\boldsymbol{R}, \boldsymbol{S}]$, the results for which are shown in figure 3.3(c). The values of $\tau_\eta^2 \|\boldsymbol{S}\|^2$ and $\tau_\eta^2 \|\boldsymbol{R}\|^2$ when $\det[\boldsymbol{R}, \boldsymbol{S}] \rightarrow 0$, where τ_η is the Kolmogorov timescale, are both slightly less than $1/2$, that is the precise value of the unconditioned averages $\tau_\eta^2 \langle \|\boldsymbol{S}\|^2 \rangle = \tau_\eta^2 \langle \|\boldsymbol{R}\|^2 \rangle$ in isotropic turbulence. For larger values of $\det[\boldsymbol{R}, \boldsymbol{S}]$, $\|\boldsymbol{R}\|^2$ has a well defined power law scaling, $\|\boldsymbol{R}\|^2 \sim |\det[\boldsymbol{R}, \boldsymbol{S}]|^{1/3}$, as shown in the inset of figure 3.3(c). The power law exponent is consistent with simple dimensional analysis. On the other hand, while $\|\boldsymbol{S}\|^2$ also depends on $\det[\boldsymbol{R}, \boldsymbol{S}]$ as a power law, the exponent is less than $1/3$, and cannot be predicted by simple dimensional analysis. This is somewhat reminiscent of the results in [20] for $\langle \|\boldsymbol{R}\|^2 \|\boldsymbol{S}\|^2 \rangle$ and $\langle \|\boldsymbol{S}\|^2 \|\boldsymbol{R}\|^2 \rangle$, where they found that the former was well described by dimensional analysis (i.e. by Kolmogorov's 1941 theory, see [121]), while the latter was not. The average of the second invariant of the velocity gradient tensor Q conditioned on the local value of $\det[\boldsymbol{R}, \boldsymbol{S}]$ is shown in figure 3.3(d). Interestingly, the region where $\det[\boldsymbol{R}, \boldsymbol{S}]$ is small is slightly strain dominated (i.e. $Q < 0$). On the other hand, the regions where $|\det[\boldsymbol{R}, \boldsymbol{S}]|$ is relatively large, the dynamics is clearly rotation-dominated. When the conditioned average of Q is weighted with the PDF of $\det[\boldsymbol{R}, \boldsymbol{S}]$ it yields $\langle Q \rangle = 0$ for isotropic turbulence, which indicates the very large relative weight of regions of the flow contributing to $\langle Q | \det[\boldsymbol{R}, \boldsymbol{S}] \rangle$ being negative and very small.

3.3.2 Rank-reduced anisotropic pressure Hessian eigenvalue

The rank-reduction of the anisotropic pressure Hessian corresponds to set its intermediate eigenvalue to zero by means of the gauge term $\gamma[\boldsymbol{R}, \boldsymbol{S}]$. Since the anisotropic pressure Hessian is traceless by definition, $\text{Tr}(\boldsymbol{\mathcal{H}}) = 0$, it has in general two non-zero principal invariants. On the other hand, the rank-reduced anisotropic pressure Hessian has only one non-zero principal invariant, that is $\text{Tr}((\boldsymbol{\mathcal{H}}_\gamma^*)^2)$ since $\det(\boldsymbol{\mathcal{H}}_\gamma^*) = 0$.

Figures 3.4(a,b) show that whereas $\boldsymbol{\mathcal{H}}$ is in general a fully three-dimensional object with three non-zero eigenvalues φ_i that satisfy $\sum_{i=1}^3 \varphi_i = 0$, $\boldsymbol{\mathcal{H}}_\gamma^*$ is a two-dimensional object with only two active eigenvalues that satisfy $\psi_1 = -\psi_3 = \psi$, the intermediate eigenvalue being identically zero, $\psi_2 = 0$. Note that here and throughout, all eigenvectors are unitary, and are ordered according to their corresponding eigenvalues, such that $\varphi_1 \geq \varphi_2 \geq \varphi_3$. The distributions of the eigenvalues $\varphi_1 \geq 0$ and $\varphi_3 \leq 0$ of the anisotropic pressure Hessian display marked tails and are almost symmetric with respect to each other. On the contrary, the distribution of φ_2 has moderate tails and it is positively skewed. The eigenvalue of the rank-reduced

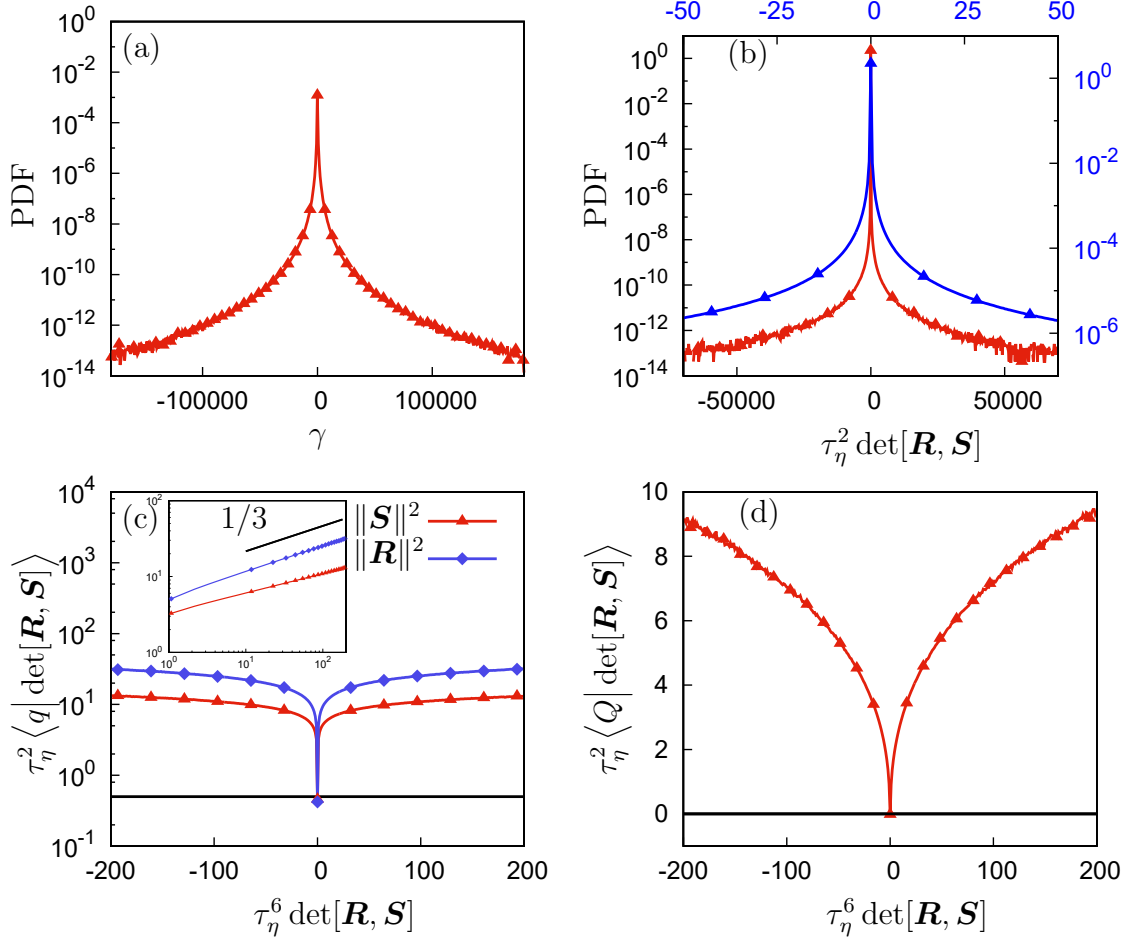


Figure 3.3: (a) Probability density function (PDF) of the real and finite multiplier $\gamma = -1/\xi_{RF}$. (b) PDF of the determinant of the commutator of anti-symmetric and symmetric part of the velocity gradient, $\det[\mathbf{R}, \mathbf{S}]$, the blue curve refers to the blue labels and represents the same PDF over a smaller range. (c) Strain magnitude $\|\mathbf{S}\|^2$ and rotation magnitude $\|\mathbf{R}\|^2$ conditioned on $\det[\mathbf{R}, \mathbf{S}]$, the same plot in logarithmic scale is in the inset. (d) Second invariant of the velocity gradient tensor Q conditioned on $\det[\mathbf{R}, \mathbf{S}]$.

anisotropic pressure Hessian, ψ , exhibits very large fluctuations. Its distribution has wide tails which show that ψ , even if with small probability, can take extremely large values. This is in part due to the large intermittency of the flow, giving rise to large values of $[\mathbf{R}, \mathbf{S}]$ and γ (although with small probability). Therefore, the geometrical simplification obtained by replacing the three-dimensional \mathcal{H} with the two-dimensional \mathcal{H}_γ^* also comes with the cost that the eigenvalue of \mathcal{H}_γ^* is far more intermittent than those of \mathcal{H} .

The large values observed for ψ are also closely related to the dimensionality

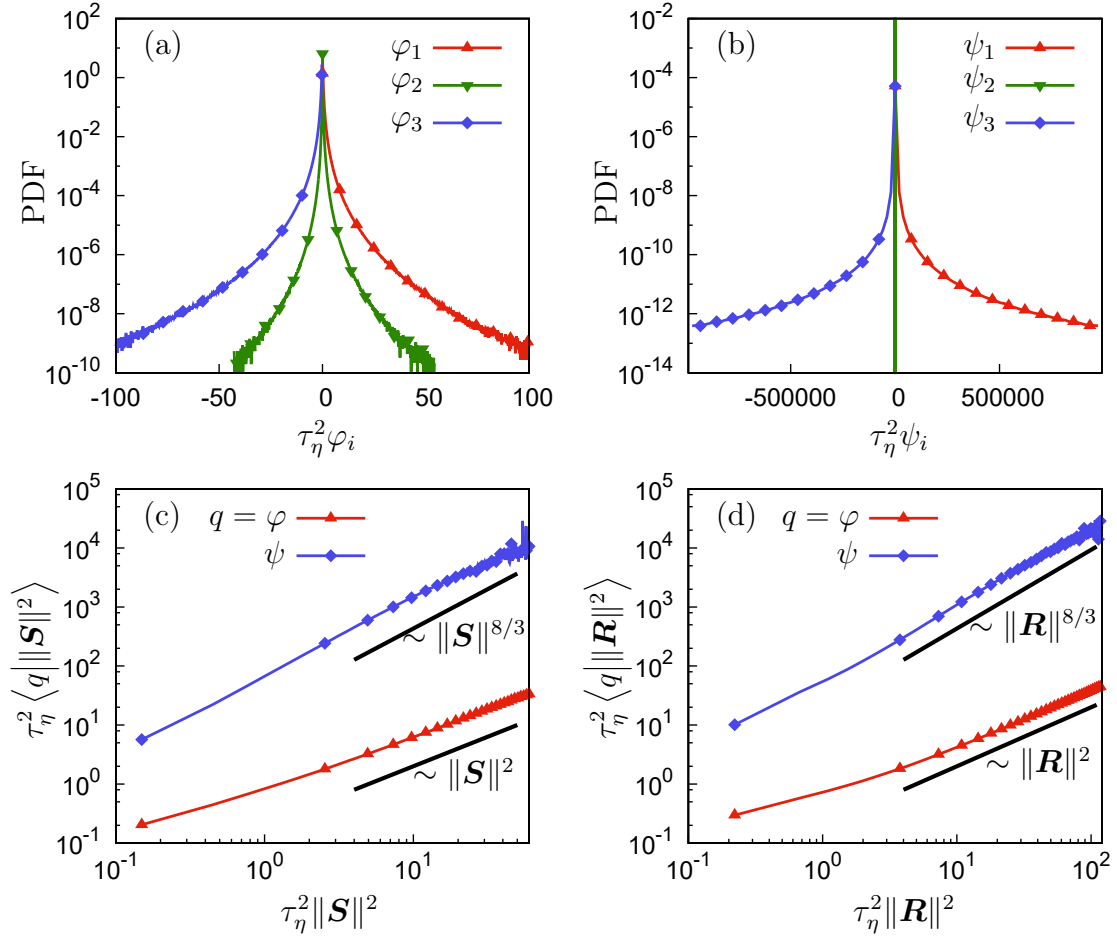


Figure 3.4: Probability density function of the eigenvalues of (a) \mathcal{H} and (b) eigenvalues of \mathcal{H}_γ^* , normalized with the Kolmogorov timescale τ_η . (c) Magnitude of the anisotropic pressure Hessian eigenvalues $\varphi = \sqrt{\sum_i \varphi_i^2}$ and anisotropic pressure Hessian eigenvalue, ψ , conditioned on the local strain-rate magnitude and (d) on the rotation-rate magnitude.

reduction. In order to investigate this point we condition the eigenvalues of \mathcal{H} and \mathcal{H}_γ^* on the magnitude of the local strain and vorticity $\| \mathbf{S} \|^2$ and $\| \mathbf{R} \|^2$. For the anisotropic pressure Hessian we define $\varphi = \sqrt{\sum_i \varphi_i^2}$ and compute the conditional averages $\langle \varphi \| \mathbf{S} \|^2 \rangle$ and $\langle \varphi \| \mathbf{R} \|^2 \rangle$. Similarly, for the rank-reduced anisotropic pressure Hessian we look at $\langle \psi \| \mathbf{S} \|^2 \rangle$ and $\langle \psi \| \mathbf{R} \|^2 \rangle$. The results from the DNS are shown in figures 3.4(c,d). The results reveal a simple scaling $\langle \varphi \| \mathbf{S} \|^2 \rangle \sim \| \mathbf{S} \|^2$, as dimensional analysis suggests. This lends supports to the model in [164], in which the pressure Hessian is a linear combination of \mathbf{S}^2 , \mathbf{R}^2 and $[\mathbf{R}, \mathbf{S}]$. The scaling $\langle \varphi \| \mathbf{S} \|^2 \rangle \sim \| \mathbf{S} \|^2$ is evident especially for large values of $\| \mathbf{S} \|^2$. This may

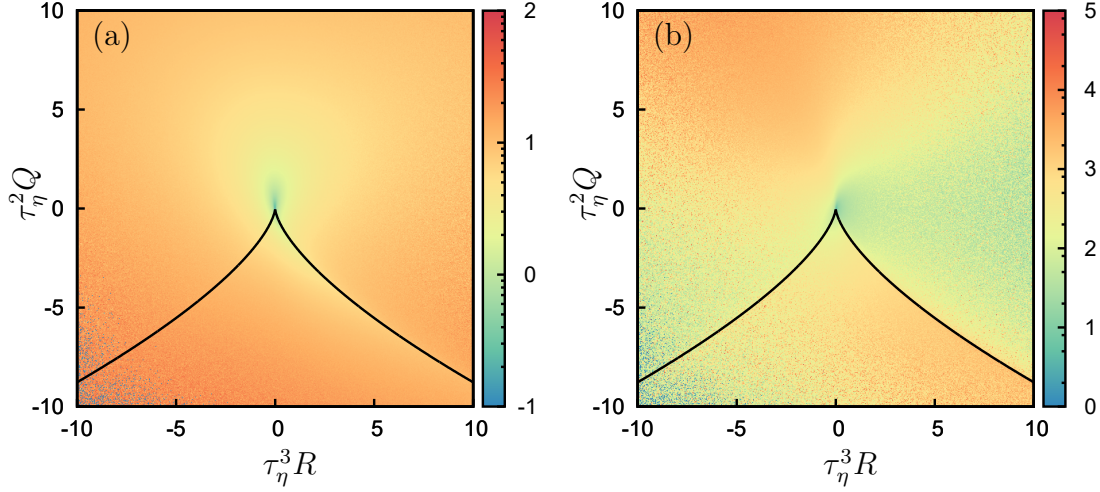


Figure 3.5: Results for (a) $\langle \varphi | R, Q \rangle$, where $\varphi = \sqrt{\sum_i \varphi_i^2}$, and (b) $\langle \psi | R, Q \rangle$ as functions of R, Q . Colors denote the magnitude of the terms, and black lines denote the Vieillefosse tails.

reflect the idea that during large fluctuations, the length-scale associated with \mathbf{S} is smaller as compared to situations where \mathbf{S} is small or moderate. If true, then the pressure Hessian is more localized during large fluctuations, giving rise to the scaling $\langle \varphi | \|\mathbf{S}\|^2 \rangle \sim \|\mathbf{S}\|^2$ that reflects a local relationship between φ and $\|\mathbf{S}\|^2$. On the other hand, for the rank-reduced anisotropic pressure Hessian eigenvalue we find $\langle \psi | \|\mathbf{S}\|^2 \rangle \sim \|\mathbf{S}\|^{2\zeta}$ with $\zeta > 1$ (in particular ζ between $4/3$ and $5/4$). Nevertheless, $\langle \psi | \|\mathbf{S}\|^2 \rangle$ maintains a well defined power law trend, which has positive implications for modelling the anisotropic pressure Hessian using information inferred by the rank-reduced anisotropic pressure Hessian. Due to the higher exponent, ψ is on average much larger than φ at fixed velocity gradient magnitude, especially when large gradients occur. The scaling of the eigenvalues magnitude conditioned on $\|\mathbf{R}\|^2$ is very similar to the scaling of the same quantity conditioned on $\|\mathbf{S}\|^2$ for both \mathcal{H} and \mathcal{H}_γ^* . The different scaling of ψ and φ with respect to the velocity gradient magnitude can be deduced from equation (3.24). Indeed, the denominator in equation (3.24) can be very small since the vorticity tends to align with \mathbf{z}_2 , which, as we will see in the next section, inducing large values of ψ . This is due to the constraint $\boldsymbol{\omega}^\top \cdot \mathcal{H} \cdot \boldsymbol{\omega} = \boldsymbol{\omega}^\top \cdot \mathcal{H}_\gamma^* \cdot \boldsymbol{\omega}$. From the viewpoint of dimensionality, the rank-reduced anisotropic pressure Hessian is a two-dimensional tensor which has to produce the same effect on the velocity gradient invariants as a fully three-dimensional tensor due to the gauge symmetry. Therefore the geometrical scaling of \mathcal{H}_γ^* is likely to differ from the scaling of \mathcal{H} , which can span the whole three-dimensional embedding space.

In figure 3.5 we plot the conditioned averages $\langle \varphi | R, Q \rangle$ and $\langle \psi | R, Q \rangle$. The

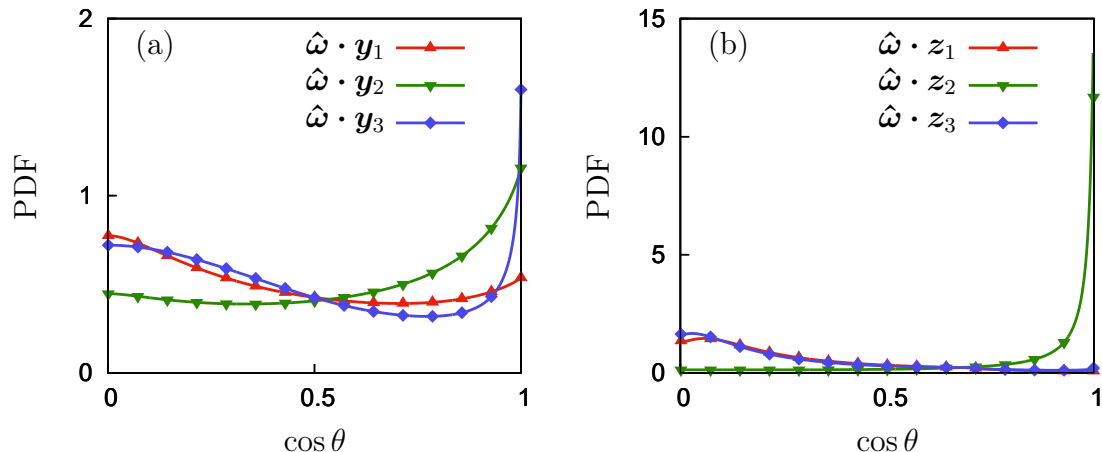


Figure 3.6: PDF of the orientation between the vorticity vector and (a) the eigenframe of the pressure Hessian, (b) the eigenframe of the rank-reduced anisotropic pressure Hessian. The alignment is expressed by inner product between the normalized vorticity $\hat{\omega} \equiv \omega / \|\omega\|$ and normalized eigenvectors of \mathcal{H} (y_i) and \mathcal{H}_γ^* (z_i).

results show that $\langle \varphi | R, Q \rangle$ is quite large everywhere except for small R, Q and its shape shares similarities with the sheared drop shape of the joint PDF of the invariants R, Q , that is in figure 3.10(d). In contrast, $\langle \psi | R, Q \rangle$ is largest in the quadrants $Q > 0, R < 0$ and $Q < 0, R > 0$ (especially below the right Vieillefosse tail) corresponding to regions of enstrophy and strain production. Therefore, it is not only that the magnitudes of \mathcal{H} and \mathcal{H}_γ^* differ significantly, but also that they are most active in different regions of the flow. Indeed, \mathcal{H}_γ^* is most active in the regions where the velocity gradients are also most active, while \mathcal{H} is active and strong in many regions where the velocity gradients display relatively little activity (e.g. the quadrant $Q < 0, R < 0$). In this sense then, one might say that \mathcal{H}_γ^* is more closely tied to the dynamics of the velocity gradients than \mathcal{H} .

3.4 Statistical geometry of the velocity gradient dynamics

We now turn to consider the statistical geometry of the system. In figure 3.6 we consider the alignment between the vorticity ω and the eigenframes of \mathcal{H} and \mathcal{H}_γ^* . While there is a strong preferential statistical alignment of the intermediate strain-rate eigenvector v_2 with ω [108], the preferential statistical alignment between ω and the pressure Hessian eigenvectors y_i is very weak. There is only a moderate tendency for alignment between $y_{2,3}$ and ω [34]. This constitutes an obstacle for understanding the role of the anisotropic pressure Hessian in turbulence.

On the other hand, the results in figure 3.6 show a striking alignment between ω and the rank-reduced anisotropic pressure Hessian eigenvectors z_i . Indeed, there is

a remarkable tendency for \mathbf{z}_2 to align with $\boldsymbol{\omega}$, that is consistent with the preferential alignment between \mathbf{v}_2 and $\boldsymbol{\omega}$ and between \mathbf{z}_2 and \mathbf{v}_2 (figure 3.7). As discussed in §3.2.4, the contribution of the vorticity and rank-reduced anisotropic pressure Hessian to the straining motion in the fluid is confined to planes. In particular, the straining associated with the centrifugal force produced by the spinning of the fluid particle about the vorticity axis acts in the plane $\Pi_{\boldsymbol{\omega}}$, orthogonal to $\boldsymbol{\omega}$, while the contribution from the rank-reduced anisotropic pressure Hessian lies on the plane Π_2 , orthogonal to its intermediate eigenvector \mathbf{z}_2 . The results shown in figure 3.6(b) indicate that these two planes tend to almost coincide. However, the effects of $\boldsymbol{\omega}$ and \mathcal{H}_γ^* on the strain-rate dynamics are radically different. The rotation of the fluid element generates a stretching rate of magnitude $\omega^2/4$ on the plane $\Pi_{\boldsymbol{\omega}}$ and its contribution is isotropic, since the eigenvalue of the projection tensor $\mathbf{P}_{\boldsymbol{\omega}}$ is the same for all the eigenvectors that belong to the plane $\Pi_{\boldsymbol{\omega}}$, as in figure 3.1(b). On the other hand, the rank-reduced anisotropic pressure Hessian causes a stretching rate of magnitude ψ in direction \mathbf{z}_3 and an equal and opposite compression in the direction \mathbf{z}_1 , orthogonal to \mathbf{z}_3 , as in figure 3.1(c). This results in a marked anisotropy of the effect of \mathcal{H}_γ^* on the plane Π_2 . Since the planes $\Pi_{\boldsymbol{\omega}}$ and Π_2 tend to be almost parallel, the anisotropic pressure Hessian can be understood as the cause of the anisotropy which is lacking in the centrifugal forces produced by the vorticity in the $\Pi_{\boldsymbol{\omega}}$ plane, and this anisotropy is a key element in the prevention of the blow-up of the system.

Interestingly, the gauge term used in defining \mathcal{H}_γ^* , equation (3.16), arises from a rotation of the strain-rate eigenframe about $\boldsymbol{\omega}$ and the results show that \mathcal{H}_γ^* lives on a two-dimensional manifold that statistically has a strong, but imperfect tendency to be orthogonal to $\boldsymbol{\omega}$. The dynamical significance of the slight misalignment is that it allows the anisotropic pressure Hessian to contribute to the eigenframe dynamics. Indeed, if \mathcal{H}_γ^* were exactly orthogonal to $\boldsymbol{\omega}$, then the anisotropic pressure Hessian would make no direct contribution to the vorticity dynamics, and its only role would be to contribute to the strain-rate dynamics, described by equation (3.5) and (3.6). It is known that in the inviscid case, the neglect of the anisotropic pressure Hessian in the eigenframe dynamics leads to a finite time singularity [156]. Therefore, assuming that the slight misalignment between \mathcal{H}_γ^* and $\boldsymbol{\omega}$ is not solely due to viscous effects, then this misalignment must also play a role in regularizing the eigenframe dynamics thus preventing the onset of singularities in the inviscid Euler system.

Figures 3.7(a-c-e) present the statistical alignment of the eigenvectors \mathbf{y}_i of \mathcal{H} , with the strain-rate eigenvectors \mathbf{v}_j . The alignments between the pressure Hessian eigenframe and the strain-rate eigenframe do not reveal any strong preferences, with weak alignment tendencies to $\mathbf{y}_1 \cdot \mathbf{v}_1 \approx 0.71$ and $\mathbf{y}_{1,3} \cdot \mathbf{v}_3 \approx 0.71$. Therefore, there is a very mild tendency for \mathbf{y}_1 to form a $\pi/4$ angle with \mathbf{v}_1 and \mathbf{v}_3 and for \mathbf{y}_3 to form a $\pi/4$ angle with \mathbf{v}_3 . These weak alignments make it difficult to model the directionality of \mathcal{H} in any simple way in terms of the eigenframe of the strain-rate

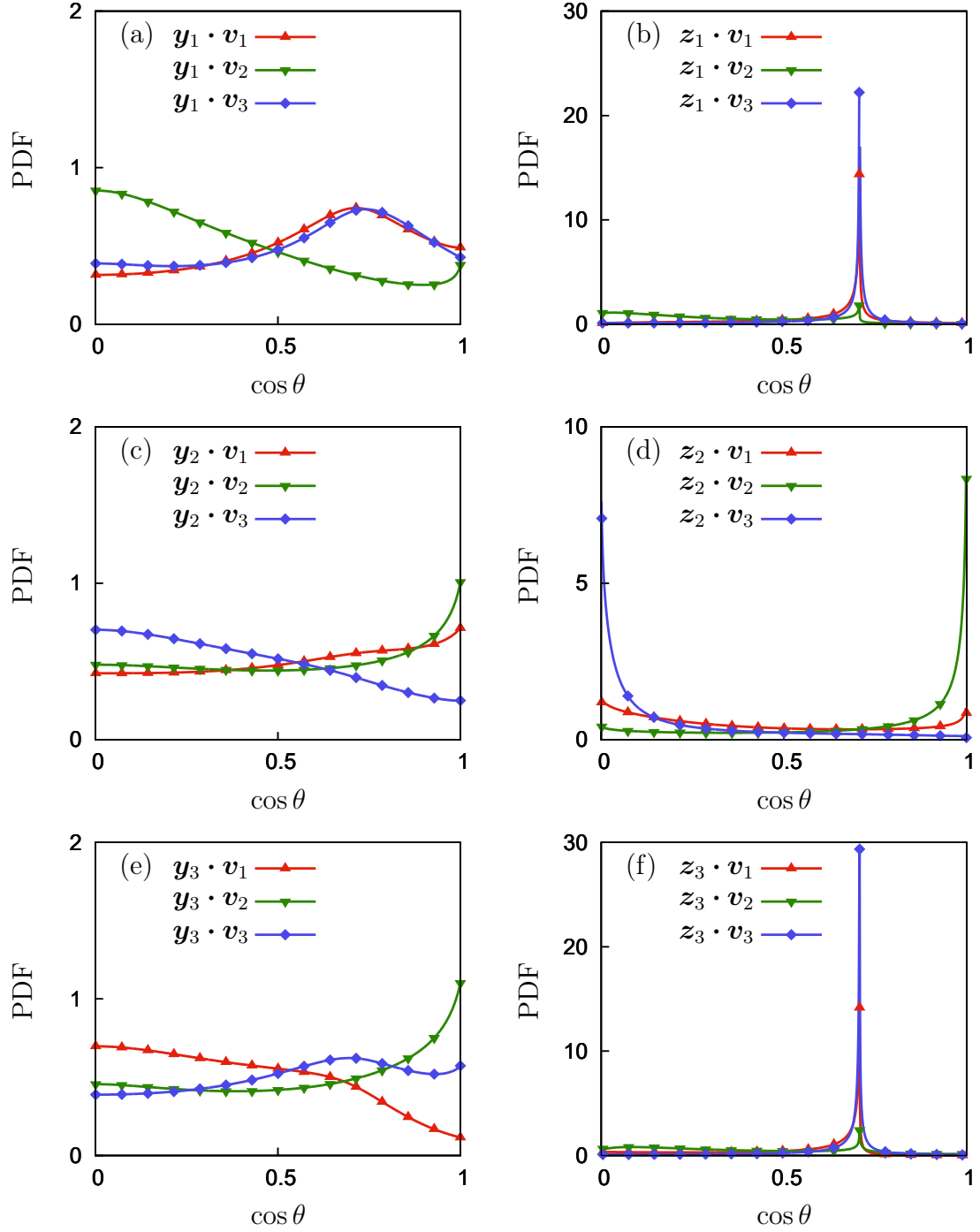


Figure 3.7: PDF of the relative orientation between the pressure Hessian eigenframe and the strain eigenframe (a-c-e) and relative orientation between the rank-reduced anisotropic pressure Hessian eigenframe and the strain eigenframe (b-d-f). The orientation is expressed by inner product of the eigenvectors of the strain-rate tensor \mathbf{v}_i with the eigenvectors of $\mathcal{H}(\mathbf{y}_i)$ and the eigenvectors of $\mathcal{H}_\gamma^*(\mathbf{z}_i)$.

tensor.

Figure 3.7(b-d-f) show the alignments between the eigenvectors \mathbf{z}_i of \mathcal{H}_γ^* , with \mathbf{v}_j . The results show, in striking contrast to the corresponding plots for the alignment of \mathcal{H} , that the eigenframe \mathcal{H}_γ^* exhibits remarkable alignment properties with a strong tendency to have $\mathbf{z}_{1,3} \cdot \mathbf{v}_{1,3} \approx 0.71$, $\mathbf{z}_2 \cdot \mathbf{v}_2 \approx 1$ and $\mathbf{z}_2 \cdot \mathbf{v}_3 \approx 0$. This means that the tangent space Π_2 to the two-dimensional manifold on which \mathcal{H}_γ^* acts tends to be orthogonal to \mathbf{v}_2 . On that plane the eigenvectors \mathbf{z}_1 and \mathbf{z}_3 of \mathcal{H}_γ^* tend to be inclined at an angle of $\pi/4$ relative to both \mathbf{v}_1 and \mathbf{v}_3 . This evidence makes the rank-reduced anisotropic pressure Hessian suitable for modelling, since there is a well defined most probable configuration for the orientation of \mathcal{H}_γ^* with respect to \mathbf{S} . Those clear preferential alignments between $\boldsymbol{\omega}$ and \mathbf{S} with \mathcal{H}_γ^* also helps understanding how the anisotropic pressure Hessian prevents blow-up, as we will discuss in the next section.

3.5 Conditioned statistical geometry

The simpler geometry of the rank-reduced anisotropic pressure Hessian together with its well-defined preferential alignments can facilitate the understanding of the pressure Hessian on the dynamics of the velocity gradient invariants. In particular, the role of the anisotropic pressure Hessian in preventing the blow-up of the Restricted Euler system can be analyzed by considering how the statistical alignment properties of \mathcal{H}_γ^* depend on \mathbf{S} and $\boldsymbol{\omega}$.

The finite-time singularity prevention mechanism can be safely tackled by using \mathcal{H}_γ^* instead of \mathcal{H} since such regularity problem is expressed in terms of invariants and is not linked with the orientation of the strain-rate eigenframe with respect to a fixed frame. The equations for the invariants dynamics, (3.5) and (3.7), show that there is a local stabilizing effect due to the reduction of the strain-rates by the centrifugal force produced by the vorticity. However, it is known that this mechanism alone is not sufficient to prevent blow-up of the system [108], and the anisotropic pressure Hessian provides the additional contribution to stabilize the dynamics. This can be understood more easily when the rank-reduced anisotropic pressure Hessian is employed instead of the full anisotropic pressure Hessian. Indeed, \mathcal{H}_γ^* is effective only on a plane and the results show a clear tendency for \mathbf{S} and $\boldsymbol{\omega}$ to preferentially align with \mathcal{H}_γ^* , which is in striking contrast with their mild preferential alignment with \mathcal{H} .

3.5.1 Rank-reduced anisotropic pressure Hessian–strain-rate alignment

The components of the rank-reduced anisotropic pressure Hessian, \mathcal{H}_γ^* , in the strain-rate eigenframe can be expressed as

$$\mathbf{V}^\top \cdot \mathcal{H}_\gamma^* \cdot \mathbf{V} = \mathbf{V}^\top \cdot \mathbf{Z} \cdot \boldsymbol{\psi} \cdot \mathbf{Z}^\top \cdot \mathbf{V} \quad (3.27)$$

where \mathbf{V} and \mathbf{Z} are the matrices which contain the strain-rate eigenvectors components and rank-reduced pressure Hessian eigenvectors components with respect to a Cartesian basis, that is, $V_{ij} \equiv \mathbf{e}_i \cdot \mathbf{v}_j$ and $Z_{ij} \equiv \mathbf{e}_i \cdot \mathbf{z}_j$. The diagonal and singular matrix ψ contains the eigenvalues of the rank-reduced anisotropic pressure Hessian, $(\psi, 0, -\psi)$. The components of \mathcal{H}_γ^* in the strain-rate eigenframe can be explicitly computed,

$$\overline{\mathcal{H}}_\gamma^* = \mathbf{V}^\top \cdot \mathcal{H}_\gamma^* \cdot \mathbf{V} = \psi \begin{bmatrix} \bar{z}_{11}^2 - \bar{z}_{13}^2 & \bar{z}_{11}\bar{z}_{21} - \bar{z}_{13}\bar{z}_{23} & \bar{z}_{11}\bar{z}_{31} - \bar{z}_{13}\bar{z}_{33} \\ \bar{z}_{11}\bar{z}_{21} - \bar{z}_{13}\bar{z}_{23} & \bar{z}_{21}^2 - \bar{z}_{23}^2 & \bar{z}_{21}\bar{z}_{31} - \bar{z}_{23}\bar{z}_{33} \\ \bar{z}_{11}\bar{z}_{31} - \bar{z}_{13}\bar{z}_{33} & \bar{z}_{21}\bar{z}_{31} - \bar{z}_{23}\bar{z}_{33} & \bar{z}_{31}^2 - \bar{z}_{33}^2 \end{bmatrix}, \quad (3.28)$$

where $\bar{z}_{ij} \equiv \mathbf{v}_i \cdot \mathbf{z}_j$ is the i -th strain-rate eigenframe component of the j -th eigenvector \mathbf{z}_j and $\sum_i \bar{z}_{ij}^2 = 1$. Since \mathcal{H}_γ^* acts only on the plane Π_2 , spanned by \mathbf{z}_1 and \mathbf{z}_3 , the expression of \mathcal{H}_γ^* in the strain-rate eigenframe is simplified. The rank-reduction allows for separation of variables between the magnitude and orientation contributions. The magnitude of the pressure Hessian is described solely by ψ while the orientation depends on the dot products \bar{z}_{ij} . The factorization into the product of a function only of the eigenvalue and a function only of the alignment of the eigenframes is a feature of two-dimensional traceless tensors, while in three dimensions such separation of variables is in general not possible [6].

The diagonal components of \mathcal{H}_γ^* in the strain-rate eigenframe cause a variation of the strain-rate eigenvalues. Using equation (3.28) in (3.5), and neglecting the viscous contribution, gives

$$\frac{D}{Dt} \lambda_i = - \left(\lambda_i^2 - \frac{1}{3} \sum_j \lambda_j^2 \right) - \frac{1}{4} \left(\bar{\omega}_i^2 - \frac{1}{3} \sum_j \bar{\omega}_j^2 \right) - \psi (\bar{z}_{i1}^2 - \bar{z}_{i3}^2). \quad (3.29)$$

It is known that the blow up of the Restricted Euler model occurs in the quadrant $R > 0, Q < 0$ where the invariants R and Q are defined in equation (3.12). In particular, the blow-up is associated with $R \rightarrow +\infty$ and $Q \sim -(27R^2/4)^{1/3} \rightarrow -\infty$ [156]. In this quadrant the straining field is in a state of bi-axial extension, with $\lambda_1 > 0, \lambda_2 > 0, \lambda_3 < 0$. Therefore, to explore how \mathcal{H}_γ^* prevents blow-up, we must consider its effects on the states where $\lambda_1 > 0, \lambda_2 > 0, \lambda_3 < 0$. From equation (3.29) we see that \mathcal{H}_γ^* will act to prevent blow-up in the quadrant $Q < 0, R > 0$ if $\bar{z}_{13}^2 - \bar{z}_{11}^2 < 0$, $\bar{z}_{23}^2 - \bar{z}_{21}^2 < 0$, and $\bar{z}_{33}^2 - \bar{z}_{31}^2 > 0$. To consider this, in figure 3.8 we show the conditioned averages $\langle \bar{z}_{i3}^2 - \bar{z}_{i1}^2 | R, Q \rangle$. The results confirm that when $Q < 0, R > 0$, $\langle \bar{z}_{23}^2 - \bar{z}_{21}^2 | R, Q \rangle < 0$, and $\langle \bar{z}_{33}^2 - \bar{z}_{31}^2 | R, Q \rangle > 0$, showing that \mathcal{H}_γ^* acts to reduce $|\lambda_2|$ and $|\lambda_3|$. However, contrary to expectation, they also show that $\langle \bar{z}_{13}^2 - \bar{z}_{11}^2 | R, Q \rangle > 0$, such that \mathcal{H}_γ^* explicitly acts to increase λ_1 when $Q < 0, R > 0$. Nevertheless, since $\sum_i \lambda_i = 0$, if \mathcal{H}_γ^* acts to reduce $|\lambda_3|$ when $Q < 0, R > 0$, then it also indirectly acts to reduce λ_1 , since $\lambda_1 \rightarrow \infty$ is not possible unless $|\lambda_3| \rightarrow \infty$ (noting $-\lambda_3 \geq \lambda_2$). Therefore, the effect of \mathcal{H}_γ^* is somewhat subtle, directly acting

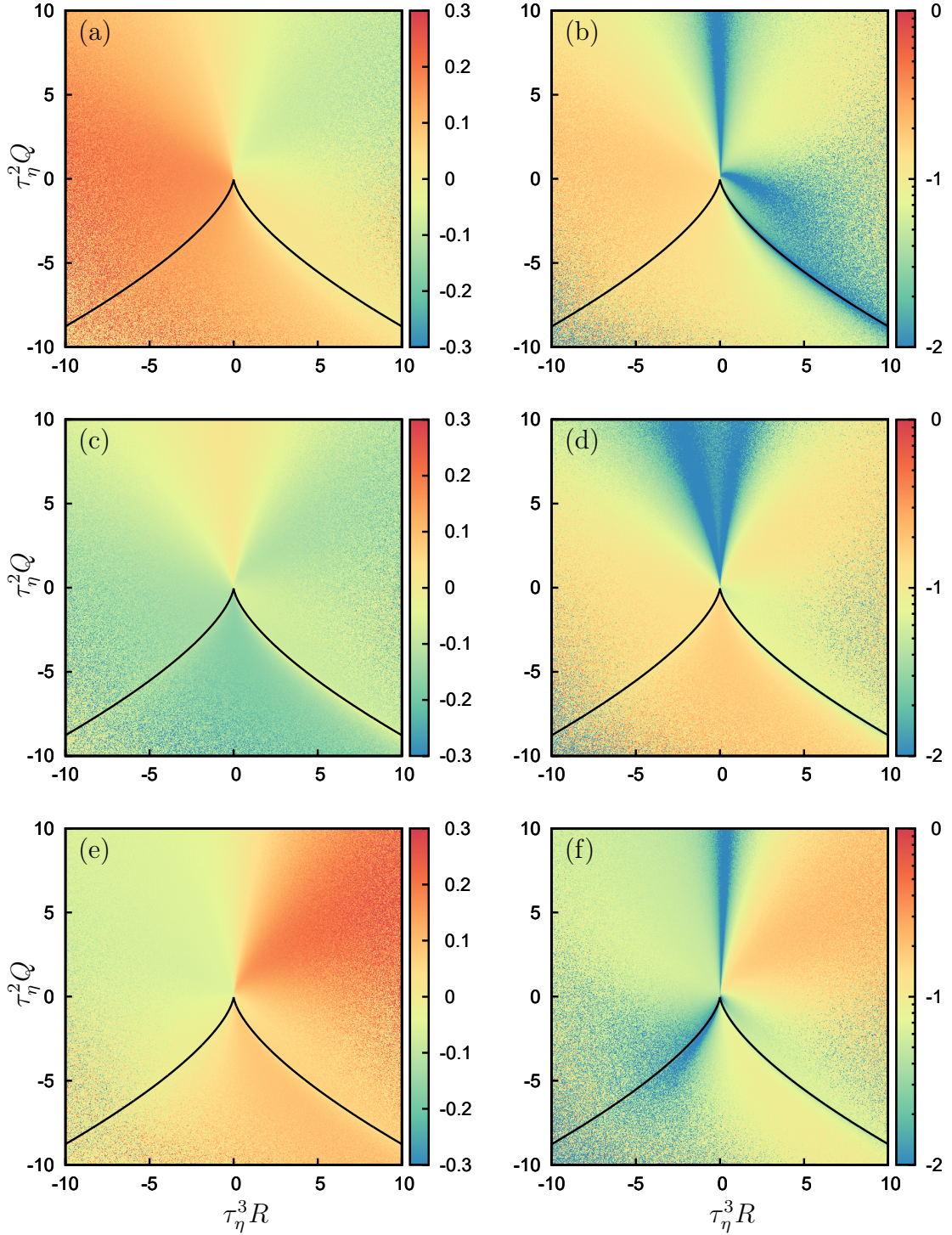


Figure 3.8: Results for $\langle \bar{z}_{i3}^2 - \bar{z}_{i1}^2 | R, Q \rangle$, (a) $i = 1$, (c) $i = 2$, (e) $i = 3$. The color range has been truncated to $[-0.3, 0.3]$ in order to highlight the trend of the variables around the most probable values. Results for $\langle |\bar{z}_{i3}^2 - \bar{z}_{i1}^2| | R, Q \rangle$ in logarithmic scale, (b) $i = 1$, (d) $i = 2$, (f) $i = 3$. Black lines denote the Vieillefosse tails.

to prevent blow-up of λ_2 and λ_3 , and only indirectly acting to prevent the blow-up of λ_1 . Interestingly, the direct amplification of λ_1 due to \mathcal{H}_γ^* becomes very small in a narrow region along the right Vieillefosse tail, as the colors in figure 3.8(b) show. Therefore, this amplification mechanism is not effective in the phase space region in which the Restricted Euler system blows up.

The scalar products \bar{z}_{ij} preferentially lie in a very narrow interval around a few well defined values, as clearly indicated by the results in figure 3.7. In particular, the eigenvectors $\mathbf{z}_{1,3}$ of \mathcal{H}_γ^* tend to form an angle of $\pi/4$ with the eigenvectors $\mathbf{v}_{1,3}$ of \mathbf{S} . Therefore a typical configuration for the relative orientation between \mathcal{H}_γ^* and \mathbf{S} is

$$\mathbf{V}^\top \cdot \mathbf{Z} = \begin{bmatrix} \cos(\pi/4 + \epsilon_{11}) & \sin(\epsilon_{12}) & \cos(\pi/4 + \epsilon_{13}) \\ \sin(\epsilon_{21}) & \cos(\epsilon_{22}) & \sin(\epsilon_{23}) \\ \cos(\pi/4 + \epsilon_{31}) & \sin(\epsilon_{32}) & \cos(\pi/4 + \epsilon_{33}) \end{bmatrix}, \quad (3.30)$$

where the quantities ϵ_{ij} represent the deviations of the angles from the idealized configuration considered, and there is a dependence of the sign on the angle between \mathbf{v}_1 and \mathbf{z}_1 , which can be $\pi/4$ or $3\pi/4$ (depending upon the sign of the eigenvalues that are chosen). That sign does not change the discussion below. Considering only small deviations from the most probable alignment, that is, considering $|\epsilon_{ij}| \ll 1$, the elements of the rotation matrix in equation (3.30) can be Taylor-expanded and, at first order in ϵ_{ij} , the expression for the rank-reduced anisotropic pressure Hessian in the strain-rate eigenframe reduces to

$$\bar{\mathcal{H}}_\gamma^* = \mathbf{V}^\top \cdot \mathcal{H}_\gamma^* \cdot \mathbf{V} \sim \psi \begin{bmatrix} -2\epsilon_{11} & \epsilon_{32} & \pm 1 \\ \epsilon_{32} & 0 & \epsilon_{12} \\ \pm 1 & \epsilon_{12} & 2\epsilon_{11} \end{bmatrix}, \quad (3.31)$$

where the orthonormality constraint, $\mathbf{V} \cdot \mathbf{V}^\top = \mathbf{I}$, has been used to relate the small perturbation angles. It is the diagonal components of \mathcal{H}_γ^* that contribute directly to the rate of change of the strain-rate eigenvalues, as in equation (3.29), and the anisotropic pressure Hessian has no direct effect on the strain-rate eigenvalues when the most probable alignments, $\epsilon_{ij} = 0$, occur. At the level of this first order approximation, the effect of \mathcal{H}_γ^* on the first and third eigenvalue always has the opposite sign, which is consistent with the stabilizing effect of the pressure Hessian. Therefore, according to this first order approximation, the pressure Hessian tends to counteract both λ_1 and λ_3 by imposing a negative rate of change of λ_1 and a positive rate of change of λ_3 , such that both the most positive and negative eigenvalues are pulled toward smaller magnitudes. The results in figure 3.8 confirm this prediction in the $Q > 0, R > 0$ quadrant, where it is seen that \mathcal{H}_γ^* acts to suppress the magnitudes of both λ_1 and λ_3 . That the linearized prediction fails in the region $Q < 0, R > 0$ is perhaps not surprising since that is the region of most intense nonlinear activity, and where \mathcal{H}_γ^* must be sufficiently large (and by implication ϵ_{ij} cannot be too small) in order to counteract the blow-up associated

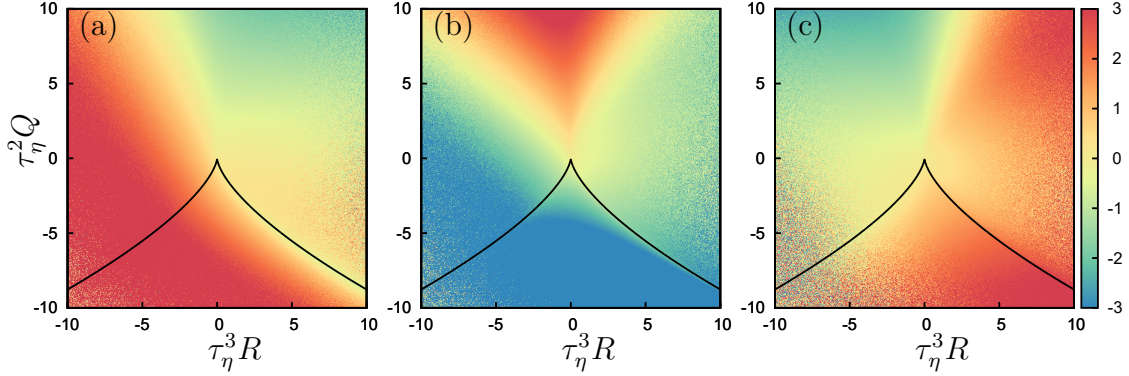


Figure 3.9: Results for $\langle -\overline{\mathcal{H}}_{\gamma,i(i)}^* | R, Q \rangle$, the average of the diagonal components of $-\mathcal{H}_\gamma^*$ in the strain-rate eigenframe conditioned on the principal invariants R, Q . (a) $i = 1$, (b) $i = 2$, (c) $i = 3$. Black lines denote the Vieillefosse tails.

with the RE dynamics. The linearization also predicts that the influence of \mathcal{H}_γ^* on λ_2 is only a second order effect when ϵ_{ij} is small. However, this prediction is in general not supported by the DNS, since the results in figure 3.8 show that in most of the Q, R plane, the rank-reduced anisotropic pressure Hessian strongly hinders the growth of positive λ_2 .

In order to fully quantify the effect of \mathcal{H}_γ^* , its magnitude should also be considered together with its orientation. The average of the diagonal components of $-\mathcal{H}_\gamma^*$ in the strain-rate eigenframe conditioned on the invariants R, Q is shown in figure 3.9. Despite the large magnitude of the rank-reduced anisotropic pressure Hessian eigenvalue, the contribution of \mathcal{H}_γ^* to the strain-rate eigenvalue dynamics is moderate on average. Figure 3.5 shows that the eigenvalue of \mathcal{H}_γ^* , namely ψ , is very large along the right Vieillefosse tail and in the quadrant $Q > 0, R < 0$. Figures 3.8(a–c) show that $\langle |\bar{z}_{i3}^2 - \bar{z}_{i1}^2| | R, Q \rangle$ is small along the right Vieillefosse tail, and these small values of $|\bar{z}_{i3} - \bar{z}_{i1}|$ compensate the large magnitude of ψ in the same region. In particular, the orientational contribution of \mathcal{H}_γ^* to the dynamics of λ_1 , namely $|\bar{z}_{13} - \bar{z}_{11}|$, is very small along the right Vieillefosse tail. This indicates how the direct amplification of λ_1 due to \mathcal{H}_γ^* does not lead to blow up, since this amplification is strong for $R < 0$, but is very weak along the right Vieillefosse tail where RE blows up, as shown in figure 3.9(a). As observed above, the rank-reduced anisotropic pressure Hessian tends to suppress positive values of λ_2 in the $R > 0, Q < 0$ quadrant, as displayed in figure 3.9(b). Interestingly, however, \mathcal{H}_γ^* contributes to the growth of positive λ_2 in the region $Q > 0, R < 0$, where ω and \mathbf{v}_2 are also strongly aligned (see figure 3.10 (b)). As such, \mathcal{H}_γ^* indirectly contributes to vortex stretching. The results in figure 3.9(c) show that, the rank-reduced anisotropic pressure Hessian strongly hinders λ_3 along the right Vieillefosse tail, contributing to its amplification only in a small region where $R < 0$ and $Q > 0$. This is a key way in which \mathcal{H}_γ^* acts to prevent blow-up in the region $R > 0, Q < 0$.

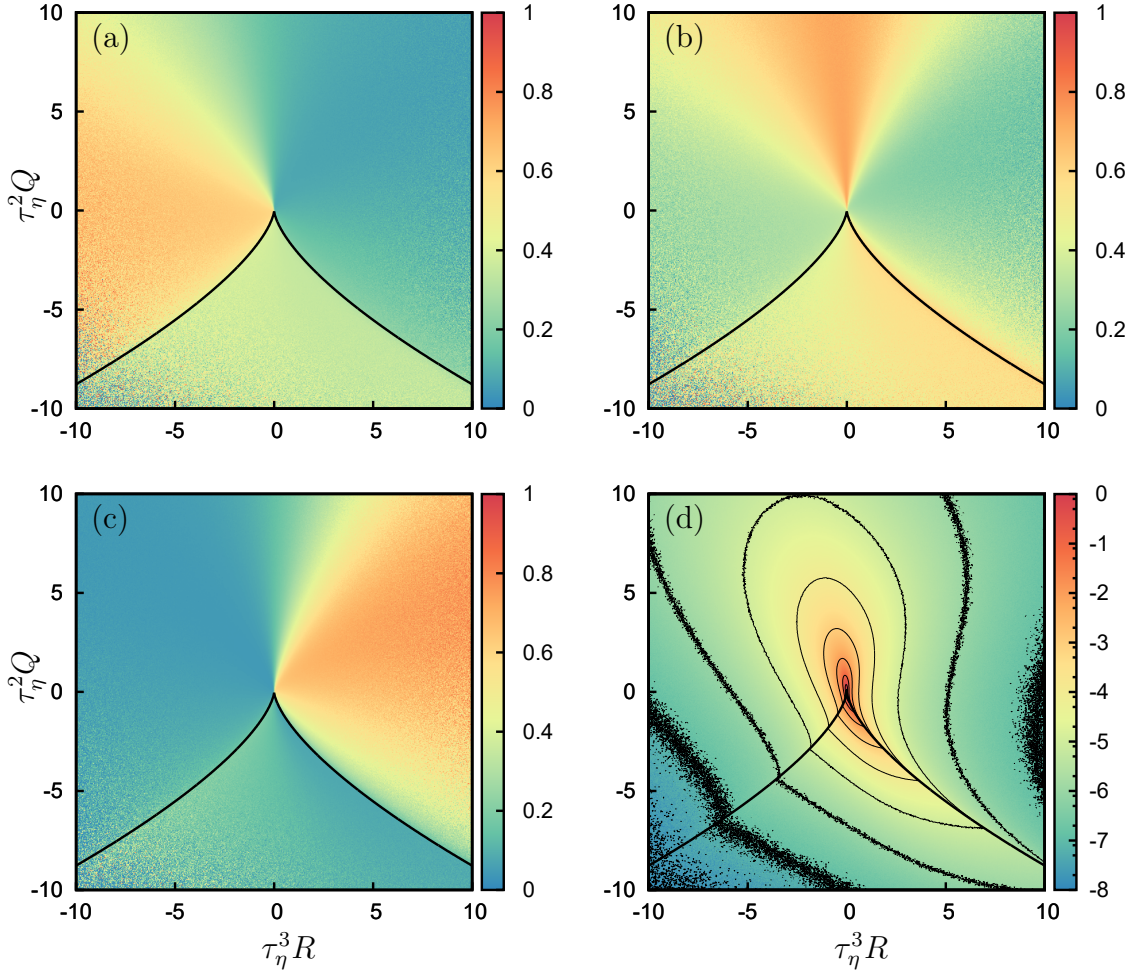


Figure 3.10: Results for $\langle (\hat{\boldsymbol{\omega}} \cdot \mathbf{v}_i)^2 | R, Q \rangle$, the statistical alignment between vorticity and eigenvectors of the strain-rate tensor, conditioned on the principal invariants R, Q . (a) $i = 1$, (b) $i = 2$, (c) $i = 3$. Plot (d) shows the joint probability density of the principal invariants R and Q . Black lines denote the Vieillefosse tails.

3.5.2 Rank-reduced anisotropic pressure Hessian–vorticity alignment

As shown earlier, \mathcal{H}_γ^* exhibits remarkable alignment properties with respect to the vorticity $\boldsymbol{\omega}$. In view of this, we now consider how this alignment impacts the way that \mathcal{H}_γ^* competes with the centrifugal term produced by vorticity to control the growth of the strain-rates. This can be explored by considering the strain-rates along the vorticity direction.

The statistical alignments of the vorticity vector with the strain-rate eigenvectors, quantified by $(\mathbf{v}_i \cdot \hat{\boldsymbol{\omega}})^2$, conditioned on the invariants R and Q , are shown in figure 3.10. The vorticity tends to align with the most extensional strain-rate

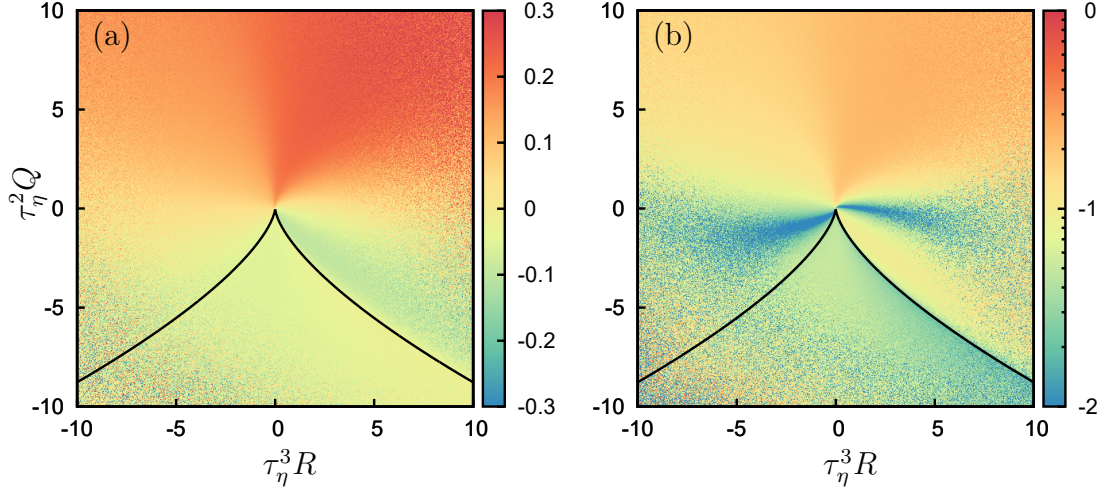


Figure 3.11: Statistical alignment between vorticity and eigenvectors of the rank-reduced anisotropic pressure Hessian, conditioned on the principal invariants R, Q . Results for (a) $\langle (\hat{\omega} \cdot \mathbf{z}_3)^2 - (\hat{\omega} \cdot \mathbf{z}_1)^2 \mid R, Q \rangle$ and (b) $\langle |(\hat{\omega} \cdot \mathbf{z}_3)^2 - (\hat{\omega} \cdot \mathbf{z}_1)^2| \mid R, Q \rangle$ in logarithmic scale. Black lines denote the Vieillefosse tails.

eigenvector in the region $R < 0$ and also, to a lesser extent, between the Vieillefosse tails. Alignment between the vorticity and the most compressional strain-rate eigenvector takes place in the region $R > 0$ only, above the right Vieillefosse tail. The vorticity vector strongly aligns with the intermediate strain-rate eigenvector in the region $Q > 0$, close to the $R = 0$ axis and along the right Vieillefosse tail. The half-plane $Q > 0$ and the vicinity of the right Vieillefosse tail correspond to the bulk of probability on the Q, R plane [108], as shown in figure 3.10(d), and therefore preferential alignment between vorticity and the intermediate strain-rate eigenvector is observed. In the phase-space region in which the alignment between vorticity and the intermediate strain-rate eigenvector is strong, the contribution of \mathcal{H}_γ^* to the dynamics of λ_2 is larger. This is observed by comparing figure 3.10(b) and figure 3.9(b).

We now turn to the combined effects of \mathcal{H}_γ^* and $\boldsymbol{\omega}$ on the strain-rate dynamics. The evolution equation for \mathbf{S} may be written as (ignoring the viscous term)

$$\frac{D\mathbf{S}}{Dt} = - \left(\mathbf{S} \cdot \mathbf{S} - \frac{\text{Tr}(\mathbf{S} \cdot \mathbf{S})}{3} \mathbf{I} \right) - \frac{1}{4} \left(\boldsymbol{\omega} \boldsymbol{\omega}^\top - \frac{\omega^2}{3} \mathbf{I} \right) - \mathcal{H}. \quad (3.32)$$

We consider the projection of this equation along the instantaneous vorticity direction $\hat{\boldsymbol{\omega}} \equiv \boldsymbol{\omega}/\omega$, and along this direction, the contribution of the last two terms is

$$\hat{\boldsymbol{\omega}} \cdot \left(-\frac{1}{4} \boldsymbol{\omega} \boldsymbol{\omega}^\top + \frac{\omega^2}{12} \mathbf{I} - \mathcal{H} \right) \cdot \hat{\boldsymbol{\omega}} = -\frac{1}{6} \omega^2 - \psi \left((\hat{\boldsymbol{\omega}} \cdot \mathbf{z}_1)^2 - (\hat{\boldsymbol{\omega}} \cdot \mathbf{z}_3)^2 \right), \quad (3.33)$$

where the properties of \mathcal{H}_γ^* have allowed us to use \mathcal{H}_γ^* instead of \mathcal{H} . Note that the term $-\omega^2/6$ comes entirely from the contribution of vorticity to the isotropic part of the pressure Hessian, since the centrifugal contribution does not act along the direction of vorticity, but only orthogonal to it. Equation (3.33) shows that (noting $\psi \geq 0$) when the vorticity is more aligned with the extensional/compressional direction of \mathcal{H}_γ^* , then \mathcal{H}_γ^* acts with/against the contribution from vorticity to oppose/aid the production of strain along the vorticity direction. In figure 3.11 we consider the DNS data for $\langle (\hat{\omega} \cdot \mathbf{z}_3)^2 - (\hat{\omega} \cdot \mathbf{z}_1)^2 | R, Q \rangle$. The results show that in $Q > 0$ regions, the vorticity vector preferentially aligns with the most compressional eigenvector of the rank-reduced anisotropic pressure Hessian, so that $\langle (\hat{\omega} \cdot \mathbf{z}_3)^2 - (\hat{\omega} \cdot \mathbf{z}_1)^2 | R, Q \rangle > 0$. On the contrary, in $Q < 0$ regions $\langle (\hat{\omega} \cdot \mathbf{z}_3)^2 - (\hat{\omega} \cdot \mathbf{z}_1)^2 | R, Q \rangle < 0$. This striking behavior means that in vorticity dominated regions, \mathcal{H}_γ^* acts to increase the strain-rate along the vorticity direction, and the opposite in strain dominated regions.

3.6 Conclusions

In this Chapter a new symmetry for the Lagrangian dynamics of the velocity gradient invariants has been presented and it has been interpreted as a gauge for the anisotropic pressure Hessian. This gauge arises because the dynamics of the strain-rate eigenvalues and vorticity components in the strain-rate eigenframe are unaffected by the angular velocity of the eigenframe along the vorticity direction. Using this symmetry, we have introduced a modified pressure Hessian, \mathcal{H}_γ^* , that is the sum of the standard pressure Hessian and the gauge term. We then sought for lower dimensional representations of the pressure Hessian by performing a rank-reduction on \mathcal{H}_γ^* , allowed by the additional degree of freedom provided by the gauge symmetry. Remarkably, this rank reduction is possible everywhere in the flow, and consequently everywhere in the flow a two-dimensional \mathcal{H}_γ^* may be defined that generates exactly the same eigenframe dynamics as the full three-dimensional pressure Hessian \mathcal{H} . We also showed that \mathcal{H}_γ^* exhibits remarkable alignment properties with respect to the strain-rate eigenframe and vorticity, that are not possessed by \mathcal{H} . In particular, the plane on which \mathcal{H}_γ^* acts tends to be almost orthogonal to the vorticity vector. Consistently, the intermediate eigenvector of \mathcal{H}_γ^* strongly aligns with the strain-rate intermediate eigenvector. Also, the most compressional/extensional eigenvectors of \mathcal{H}_γ^* preferentially form an angle of $\pi/4$ with the most compressional/extensional eigenvectors of the strain-rate tensor.

The rank-reduced anisotropic pressure Hessian offers promising applications. For example, the reduction in dimensionality, provided by replacing \mathcal{H} with \mathcal{H}_γ^* in the eigenframe equations, is a step towards more efficient modeling, since the rank-reduced anisotropic pressure Hessian can be specified by only four numbers instead of five required for the fully three-dimensional \mathcal{H} . The eigenvalues of \mathcal{H}_γ^* are also shown to be strongly related to the local strain-rate and vorticity in the

flow, suggesting relatively simple ways to model these eigenvalues in Lagrangian models for the velocity gradient tensor. This property, together with the reduction in dimensionality and the remarkable alignment properties of \mathcal{H}_γ^* , offer promising insights into ways in which the anisotropic pressure Hessian and its effects on the eigenframe dynamics can be modelled. The development of such a model will be the subject of future work.

Part II

Inertial particle dynamics in isotropic turbulence

Chapter 4

The Non-Uniform Fast Fourier Transform and its applications to the Direct Numerical Simulation of particle-laden flows

In this Chapter we describe the application of the Nonuniform Fast Fourier Transform (NUFFT) to the pseudo-spectral Eulerian-Lagrangian Direct Numerical Simulation (DNS) of particle-laden flows. In particular, the ability of the NUFFT to predict the particle feedback on the fluid flow is examined. In the two-way coupling regime, the particle back-reaction on the fluid phase can substantially modify the flow statistics across all the scales, when particle loading is significant, therefore it is critical to obtain an accurate representation of the particle phase on the Cartesian grid, which accuracy is consistent with that of the other discretization methods employed in a DNS. The mixed Eulerian-Lagrangian approach is usually employed in the numerical simulation of flows laden with particles. The flow fields (that is fluid velocity, temperature, etc.) are represented on a fixed, Eulerian, grid. The grid is structured, Cartesian and equispaced in Fourier pseudo-spectral methods, in order to allow for the use of the Fast Fourier Transform (FFT) algorithm. On the other hand, the particle dynamics is resolved by following the particles along their paths, that is with a Lagrangian approach. An effective coupling method is needed in order to interconnect those two radically different approaches for the fluid and particle phases. In particular the flow fields should be interpolated at the particle position and the particle feedback on the flow fields should be represented on the Eulerian grid. While many works in the literature focus on the direct interpolation of the fields at the particles position, only a few methods are available for the computation of particle back-reaction. For example, the B-spline interpolation is a well-established method for one-way coupled simulations, while low order schemes, such as the Particle In Cell (PIC) method, are often employed to represent the

particle phase on the Eulerian grid. That low order approach can seriously reduce the overall accuracy of the simulation.

We show how the particle momentum and temperature feedback on the flow can be computed by means of a forward NUFFT and the B-spline interpolation can be carried out as a backward NUFFT. The NUFFT is based upon the convolution theorem for the Fourier transform and consists of a convolution with a prescribed basis function followed by a Fast Fourier Transform. Since the backward and forward transformations are symmetric and the (non local) convolution computed in physical space is removed in Fourier space, this procedure satisfies all constraints for a consistent interpolation scheme, and allows an efficient implementation of high-order interpolations.

The resulting method is applied to the direct numerical simulation of a statistically steady and isotropic turbulent flow with different particle Stokes numbers in the two-way coupling regime. The inertial particle statistics show that the feedback from the particles on the flow fields is far from being analytic and therefore challenging to represent. Also, it is shown how the NUFFT can also be employed to accurately represent the particle phase in Fourier space, allowing for a spectral characterization of the particles statistics.

This piece of work has been presented at the WIT Advances in Fluid Mechanics Conference [28] and it is in press in the International Journal of Safety and Security Engineering [27].

4.1 Overview of numerical schemes for the simulation of two-way coupled particle-laden flows

In many particle-laden flows arising in nature and engineered systems the particle mass fraction is large enough to allow particles to strongly affect the surrounding turbulent flow [172, 130]. This situation is referred to as two-way coupling regime [54]. The accurate computation of the particle back-reaction is a key feature of Direct Numerical Simulations of two-way coupled particle-laden flows. The most immediate approach to compute the particle back-reaction on the fluid flow is the particle in cell (PIC) method. However, with that method, the smoothness of the resulting field is determined by the particle number density. This reduces accuracy and can lead to numerical instabilities. Moreover, the low order polynomials used have been shown to corrupt particle Lagrangian statistics [154] and we will show that the Eulerian statistics are corrupted as well when a low order method is employed. An alternative approach consists of regularizing the impulsive force exerted by the particle by means of Gaussian kernels [170]. This technique, referred to as regularization functions, guarantees stability of the computation but it introduces a high frequency damping which depends on the chosen regularization scale. The scale dependence can be eliminated by the Steady Stokeslet [117], which is however

challenging to introduce in a parallel implementation, since each particle substantially affects a large portion of the surrounding domain. More elaborate techniques, such as the fast multipole method [66] or the fast Ewald summation method [101], have been reported to cope with this wide support issue. Only recently, a reliable and efficient algorithm to compute particle back-reaction on a Cartesian grid was developed and assessed [69]. The authors exploited the closed solution of the unsteady Stokes flow around a small rigid sphere isolating analytically the singular part of the Stokes flow around each particle, which is then reintroduced in the flow, after a predefined regularization time. The Exact Regularized Point Particle method (ERPP) guarantees high accuracy and the momentum conservation, however, it requires the evaluation of the analytical solution for the unsteady Stokes flow at a previous time, at each time step.

In this thesis the Non-Uniform Fast Fourier Transform is employed to compute the particle back-reaction on the fluid flow. More generally, it is shown that inertial particle statistics, which are inherently discrete, can be characterized through Eulerian fields, which are equivalent to the particle phase and are constructed by means of the NUFFT. The NUFFT algorithm has been used in a wide range of applications, from medical imaging [52] to molecular dynamics [148, 120]. By means of a discrete convolution and Fast Fourier Transform over an oversampled grid, the NUFFT provides a representation of the Fourier transform of an irregular and non-uniformly sampled field. The number of operations required for the computation of the NUFFT with accuracy ε of a field sampled at M points is $O(M \log(M) - M \log(\varepsilon))$ [51]. The NUFFT consists of three steps: (1) a convolution in physical space of the field with a basis function to regularize the field; (2) FFT of the regularized field; (3) a deconvolution in Fourier space. Accuracy is determined by the properties of the basis function used for the convolution and by the smoothness of the field. In the point-mass approximation particle back-reaction is described by a superposition of Dirac delta functions centered on the particles. Since the B-spline interpolation performs better than other methods currently available [75], especially if employed along with pseudo-spectral methods, and it has been recognized as a valuable basis for fast gridding [11], we propose to use a B-spline basis. According to the classification by [67], a type-1 NUFFT is used to compute the coupling and a type-2 NUFFT is used to interpolate.

The interpolation and reverse interpolation methods should satisfy a few constraints. By accurate consideration on the energy balance of the coupled system, Sundaram and Collins [139] pointed out that the interpolation schemes for interpolation and reverse interpolation must be symmetric in order to guarantee the energy conservation. Furthermore, they argued that the spurious non-locality introduced by interpolation and reverse interpolation should be minimized for a consistent and convergent method. These constraints are naturally satisfied by the B-spline interpolation (regarded as a backward NUFFT) together with the forward NUFFT for the computation of the coupling. Indeed, since the backward NUFFT is the

inverse of the forward NUFFT, symmetry is implicit by definition. Moreover, the non-locality introduced in physical space is removed in Fourier space because convolution and deconvolution are carried out with respect to the same basis. Finally, the localized support of the B-spline basis allows the efficient parallelization of the NUFFT algorithm, since the particle affects only a limited region of the surrounding flow and next neighbor communications suffice [120], an important feature of any algorithms devoted to the direct numerical simulation of turbulent flows.

Most of the works in the literature separated the analysis of the algorithm from the physics of inertial particles in turbulence. However, an intriguing scenario arises when the performance of the NUFFT algorithm is analyzed as a function of particle inertia because the accuracy of the method depends on the regularity of the coupling term which in turns depends on the particle inertia.

4.2 Physical model

The Eulerian-Lagrangian model for particle-laden flows in the two-way coupling regime is considered. The point-like particles are advected by the turbulent flow and tend to thermalize with the surrounding fluid. For small pressure and temperature variations within the fluid phase, compressibility effects can be neglected and, therefore, the temperature, $T(\mathbf{x}, t)$, behaves as a passively advected scalar in a solenoidal velocity field, $\mathbf{u}(\mathbf{x}, t)$, so that the fluid flow is described by the following equations:

$$\nabla \cdot \mathbf{u} = 0, \quad (4.1a)$$

$$\partial_t \mathbf{u} + \nabla \cdot (\mathbf{u} \mathbf{u}^\top) = -\frac{1}{\rho_f} \nabla p + \nu \nabla^2 \mathbf{u} - \mathbf{C}_u + \mathbf{f}, \quad (4.1b)$$

$$\partial_t T + \nabla \cdot (\mathbf{u} T) = \kappa \nabla^2 T - C_T + f_T, \quad (4.1c)$$

where, ρ_f , ν and κ are the fluid density, kinematic viscosity and thermal conductivity respectively. The particle back-reaction on the fluid flow is in the \mathbf{C}_u and C_T terms, that we aim to compute accurately and efficiently.

The dynamics of small sub-Kolmogorov, heavy, spherical particles can be modelled by a simplified Maxey-Riley equation [107] together with an analogous equation for the particle temperature [172]:

$$\frac{d^2 \mathbf{x}_p}{dt^2} = \frac{d\mathbf{v}_p}{dt} = \frac{\mathbf{u}(\mathbf{x}_p, t) - \mathbf{v}_p}{\tau_p}, \quad (4.2a)$$

$$\frac{d\theta_p}{dt} = \frac{T(\mathbf{x}_p, t) - \theta_p}{\tau_\theta}, \quad (4.2b)$$

where $\mathbf{x}_p(t)$ is the particle position, $\mathbf{v}_p(t)$ is the particle velocity, $\theta_p(t)$ is the particle

temperature. The particle momentum and thermal response times are

$$\tau_p = \frac{2}{9} \frac{\rho_p}{\rho_f} \frac{r_p^2}{\nu}, \quad \tau_\theta = \frac{1}{3} \frac{\rho_p c_p}{\rho_f c_f} \frac{r_p^2}{\kappa}, \quad (4.3)$$

where r_p is the particle radius, ρ_p and c_p are the particle density and specific heat capacity, ρ_f and c_f are the fluid density and specific heat capacity. The ratios between the particle relaxation times and the Kolmogorov time scale, τ_η , define the Stokes and thermal Stokes numbers, $\text{St} = \tau_p/\tau_\eta$ and $\text{St}_\theta = \tau_\theta/\tau_\eta$, which parameterize the particle inertia and thermal inertia.

This model is valid when the size of the particles is smaller than the smallest dynamically significant spatial flow scale, that is the Kolmogorov scale, and the volume fraction is low to moderate (dilute suspensions) [54, 38]. Particles exert forces on the surrounding fluid which are opposite to the force the fluid exerts on the particles. Analogously, the heat flux from each particle to the fluid is opposite to the heat flux from the fluid to the particle. This results into the following form of the point-particle feedback:

$$\mathbf{C}_u(\mathbf{x}, t) = \frac{4}{3} \pi \sum_{p=1}^{N_P} \frac{\rho_p}{\rho_f} r_p^3 \frac{d\mathbf{v}_p}{dt} \delta(\mathbf{x} - \mathbf{x}_p) \quad (4.4a)$$

$$C_T(\mathbf{x}, t) = \frac{4}{3} \pi \sum_{p=1}^{N_P} \frac{\rho_p c_p}{\rho_f c_f} r_p^3 \frac{d\theta_p}{dt} \delta(\mathbf{x} - \mathbf{x}_p). \quad (4.4b)$$

The Dirac delta functions arises because of the point-particle approximation. The disturbance (force) induced by each particle has infinitesimally small support (since $r_p \ll \eta$) and infinite amplitude (that is force per unit volume), resulting into finite magnitude of the disturbance. The Dirac delta functions should be handled numerically. It is shown how the smoothness of the coupling fields relates to the scaling exponent of the particle acceleration (and particle temperature rate of change) in the dissipation range. As the particle inertia is increased the coupling field is far from being analytic.

4.3 Numerical method

In the numerical simulations presented in this thesis the backward NUFFT is used to interpolate the fluid velocity and temperature at the particle position, required for the particle dynamics, equation (4.2), while the forward NUFFT is used to compute the particle momentum and temperature back-reaction, equation (4.4). In this section the NUFFT algorithm and its parallel implementation are analyzed in detail.

4.3.1 The B-spline polynomial basis

The one dimensional B-spline polynomials are defined by the convolution

$$B_n(x) = B_{n-1}(x) * B_0(x) \quad (4.5)$$

where B_0 is the rectangular function defined on an interval of amplitude Δx , that is the grid spacing in the numerical implementation,

$$B_0(x)\Delta x = \begin{cases} 1, & \text{if } |x|/\Delta x \leq 1/2 \\ 0, & \text{otherwise} \end{cases}$$

The function B_0 numerically emulates the Dirac delta function. The Fourier representation of the B-spline basis is

$$\widehat{B}_{N_S-1}(k_x) = \frac{1}{2\pi} \left(\text{sinc} \left(k_x \frac{\Delta x}{2} \right) \right)^{N_S}. \quad (4.6)$$

The spline basis in three dimensions is obtained by separation of variables [75],

$$B(\mathbf{x}) = B(x)B(y)B(z). \quad (4.7)$$

For sake of clarity, the order subscript will be omitted. It is worth noting that the B-spline basis presents an important advantage with respect to the discrete Gaussian regularization, because the consistency constraint is exactly satisfied also over a finite number of grid points x_i ,

$$\sum_{i=1}^{n+1} B_n(x_i - x_p) = 1,$$

which guarantees that energy is conserved in the convolution of the fields with the B-spline polynomials. This constraint is only approximately satisfied by a continuous Gaussian discretized over a finite number of grid points. A most important computational feature is the localized support of the B-spline basis, since the convolutions in physical space are executed on a limited portion of the domain, thus allowing an efficient parallelization [120]. A comprehensive introduction to the B-spline basis with a view to the NUFFT is in [11].

4.3.2 Interpolation: backward NUFFT

The fields are interpolated at particle positions by means of a backward NUFFT with B-spline basis [75, 28]. The spectral representation of the field to interpolate, $\widehat{u}(\mathbf{k})$, is projected onto the B-spline basis,

$$\widetilde{\widehat{u}}(\mathbf{k}, t) = \frac{1}{(2\pi)^3} \frac{\widehat{u}(\mathbf{k}, t)}{\widehat{B}(\mathbf{k})}. \quad (4.8)$$

In a spectral DNS, due to the dealiasing, $|k_x \Delta x| \leq 2\pi/3$ so that \widehat{B} , defined in equation (4.6), is always positive. The FFT algorithm applies to $\widetilde{\mathbf{u}}(\mathbf{k}, t)$, since it is represented on an equispaced grid. Thus, the field is transformed to the physical space,

$$\widetilde{\mathbf{u}}(\mathbf{x}, t) = \mathcal{F}^{-1} [\widetilde{\mathbf{u}}(\mathbf{k}, t)] \quad (4.9)$$

and convolution with the B-spline basis yields the field at the particle position,

$$\mathbf{u}(\mathbf{x}_p, t) = \widetilde{\mathbf{u}} * B_{(p)} \quad (4.10)$$

where $B_{(p)} = B(\mathbf{x} - \mathbf{x}_p)$ is the B-spline centered at the particle position. The convolution step, equation (4.10), introduces spurious non-locality, since the field at the particle position is affected by the field at all the points within the support of the B-spline. Such non-locality is compensated through the initial spectral deconvolution, equation (4.8). Without the deconvolution in Fourier space, the interpolated field would be coarse-grained and its value at the particle position would be affected by points which are far away from the particle [139].

4.3.3 Reverse interpolation: forward NUFFT

The particle momentum and temperature back-reaction, defined by equation (4.4), are computed in Fourier space on the Cartesian grid by means of the forward NUFFT with B-spline basis. Due to the point-particle model, the particle mass is finite while the particle surface is infinitesimal, so that the stress on the particle should be infinite to result into a finite force. This gives rise to non-smooth coupling fields. The forward NUFFT allows to represent such a non-smooth field and it consists of three steps [67]. At first, a smooth field is obtained by means of the convolution of the coupling terms with the B-spline basis in physical space:

$$\widetilde{\mathbf{C}}_u(\mathbf{x}, t) = \frac{4}{3} \pi \frac{\rho_p}{\rho_f} \sum_p r_p^3 \frac{d\mathbf{v}_p}{dt}(t) B(\mathbf{x} - \mathbf{x}_p). \quad (4.11)$$

This step can also be interpreted as splitting the real particle into many smaller particles. Each particle exerts a force on the fluid which is $B(\mathbf{x} - \mathbf{x}_p)$ times the force exerted on the real particle. This highlights the non-locality introduced by the B-spline regularization: the overall force exerted by the fictitious particles equals the force exerted by the real particle, but the smaller forces are applied in many different points. The smooth coupling field,

$$\widetilde{\mathbf{C}}_u(\mathbf{x}, t) = \mathbf{C}_u * B \quad (4.12)$$

is transformed by means of FFT,

$$\widehat{\widetilde{\mathbf{C}}}_u(\mathbf{k}, t) = \mathcal{F} [\widetilde{\mathbf{C}}_u(\mathbf{x}, t)] \quad (4.13)$$

and then, the convolution is removed in Fourier space,

$$\widehat{\mathbf{C}}_u(\mathbf{k}, t) = \frac{1}{(2\pi)^3} \frac{\widehat{\mathbf{C}}_u(\mathbf{k}, t)}{\widehat{B}(\mathbf{k})} \quad (4.14)$$

This step can be interpreted as gathering together the sub-particles obtained splitting the actual particle in the first step, equation (4.11). The NUFFT only uses smearing internally, equation (4.12), and undoes it in the deconvolution step, equation (4.14). Therefore the non-locality introduced by the convolution is removed, in the limit of the discretization. The forward NUFFT strongly differs from simple regularization in this sense. Moreover, the symmetry between backward and forward NUFFT ensures consistency and energy conservation [139, 28].

4.3.4 Parallel implementation

The Eulerian-Lagrangian code is parallelized by means of the Message Passing Interface with a pencil domain decomposition. The FFTs are executed in parallel by means of the P3DFFT library [118]. Thus, the transposition of the pencils required for the three-dimensional FFT are performed by means of the MPI_Alltoall utility. Due to the Eulerian domain decomposition, the Lagrangian particles migrate through next-neighbouring processes and need to be redistributed at each time step. Accordingly, the interpolation at the position of particles which are close to the borders between processors also requires communication of the fluid fields at the borders. The same communicator is employed to exchange both particle and fields at the boundary between processors by means of the MPI_Neighbor_collectives utilities. The coexistence of global and local communications is challenging for the parallel architecture and can be optimized by accurate choice of the neighboring processors, by MPI process binding.

The convolutions in physical space require considerable amount of computational time and should be optimized. Convolutions also introduce aliasing, which is removed by padding. A 3/2 oversampling factor is employed, that is the same used to evaluate the convective terms in the DNS. As the order of the B-spline polynomials employed increases, the portion of grid points to exchange between neighbouring processors becomes larger, rendering the communications more costly. The optimum values of the degree of the basis depends on the resolution, $k_{\max}\eta$, and does not exceed 4 for usual resolutions ($k_{\max}\eta \approx 1.5$), as discussed in [154]. Due to the compact support of the employed basis, each particle contributes to the coupling field in a limited number of grid-points surrounding its position, which substantially improves the efficiency of the computation and parallelization. The discrete convolution required to carry out the NUFFTs is discretized as

$$u(\mathbf{x}_p) = \int_{\Omega_B} B(\mathbf{x} - \mathbf{x}_p) \tilde{u}(\mathbf{x}) d\mathbf{x} \approx \sum_{l,m,n} \Delta x^3 B(\mathbf{x}_{lmn} - \mathbf{x}_p) \tilde{u}_{lmn} \quad (4.15)$$

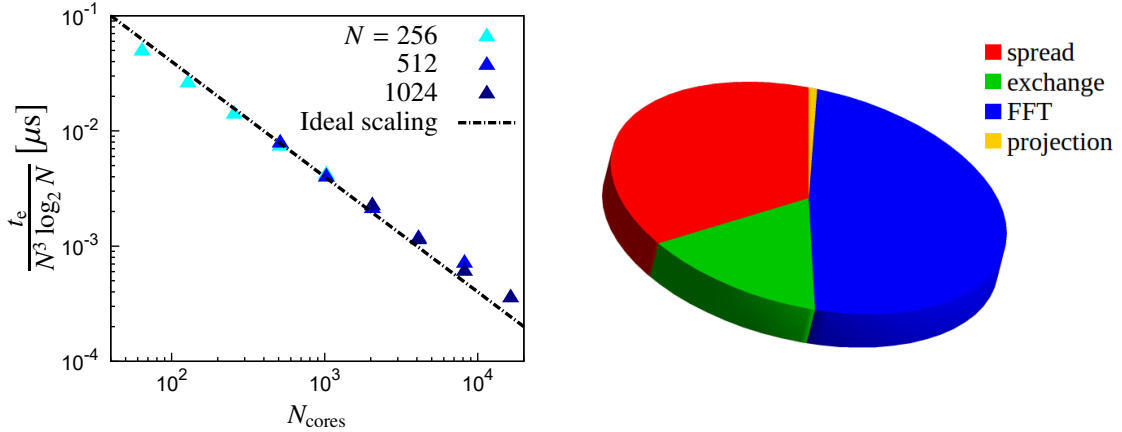


Figure 4.1: Parallel performance of the code on the Marconi-KNL cluster. (a) Parallel scaling of the DNS, the elapsed time refers to a single DNS step and N is the number of resolved Fourier modes; (b) CPU time spent on each step of the forward NUFFT algorithm for $N = 1024$ and on 16384 processors. The discrete convolutions are computed on $N_S = 4$ grid points.

where the components of the position vector \mathbf{x}_{lmn} in the Cartesian basis are $\Delta x [l, m, n]^T$, $\tilde{u}_{lmn} = \tilde{u}(\mathbf{x}_{lmn})$ and the sum is extended over the support of the B-spline. Separation of variables is exploited to reduce the number of operations, executing the contraction of the three indexes as a sequence of three contractions on each index [75]. Also, separation of variables allows to efficiently implement the discretization of equation (4.11),

$$\sum_{p,l,m,n} a_p B(\mathbf{x}_{lmn} - \mathbf{x}_p) = \sum_p a_p \sum_n B(z_n - z_p) \sum_m B(y_m - y_p) \sum_l B(x_l - x_p),$$

providing a noticeable speed-up of the computation. An additional advantage of the B-spline basis, from the implementation viewpoint, is that its Fourier transform can be pre-computed and stored, avoiding the evaluation of exponentials at each interpolation. Moreover, in three dimensions, the values of B along each coordinate can be stored separately, substantially reducing the memory requirement [28].

The scaling of the parallel computation on the Marconi-KNL cluster is shown in figure 4.1(a). The elapsed time refers to a step of the DNS, that is the computation of a time step of equations (4.1) and (4.2). The velocity and temperature fields are discretized with N^3 Fourier modes, $N_P = (3N/2)^3$ particles are dispersed in the flow and the discrete convolutions are computed on $N_S = 4$ grid points. The elapsed time is normalized by the expected computational cost of the FFT and NUFFT algorithms, that is $O(N^3 \log_2 N)$. The percentage of CPU time necessary for each step of the forward NUFFT is shown in figure 4.1(b), for 1024^3 Fourier modes, 1536^3 particles and on 16384 processors. The spreading step refers to the convolution in physical space, equation (4.12). The exchange step refers to the send/receive

Inverse Reynolds number	$\nu = \text{Re}^{-1}$	0.0025
Prandtl number	$\text{Pr} = \nu/\kappa$	1
TKE dissipation rate	ε	0.25
Temperature fluctuation dissipation rate	χ	0.1
Taylor microscale Reynolds number	Re_λ	130
Forced wavenumber	k_f	$\sqrt{2}$
Domain size	L	2π
Number of Fourier modes	N	256
Resolution	$k_{\max}\eta$	1.7
Particle/fluid density ratio	ρ_p/ρ_f	1000
Particle/fluid specific heat capacity ratio	c_p/c_f	4
Volume fraction	ϕ	0.0002
Number of particles	N_P	3343360 – 49136640
Stokes number	St	0.5, 0.75, 1, 1.5, 2, 3
Thermal Stokes number	St_θ	6 St

Table 4.1: Dimensionless parameters for the numerical simulations.

and summation of the halo regions between neighbouring MPI processes. In the highly parallel computation considered, the exchange step takes a moderate amount of time with respect to the other steps. The FFT, equation (4.13), is the most expensive part of the algorithm while the projection step, equation (4.14), is the least expensive, since it consists only of a multiplication. Further details on the numerical code can be found in Appendix A.

4.4 Results

Results of a Direct Numerical Simulation (DNS) of a forced, statistically steady, homogeneous and isotropic particle-laden turbulent flow are presented. The fluid and particle phase are two-way coupled and the parameters used in the simulations are listed in Table 4.1. The spectra of the fluid velocity and temperature fields are shown in figure 4.2, for various inertia of the suspended particles.

4.4.1 Validation of the NUFFT algorithm

As a preliminary test, the convergence of our implementation of the NUFFT for different order of the B-spline basis has been examined, varying the number of points used for the discrete convolutions, equation (4.15). To assess the accuracy of the B-spline interpolation [75], computed as a backward NUFFT, the following

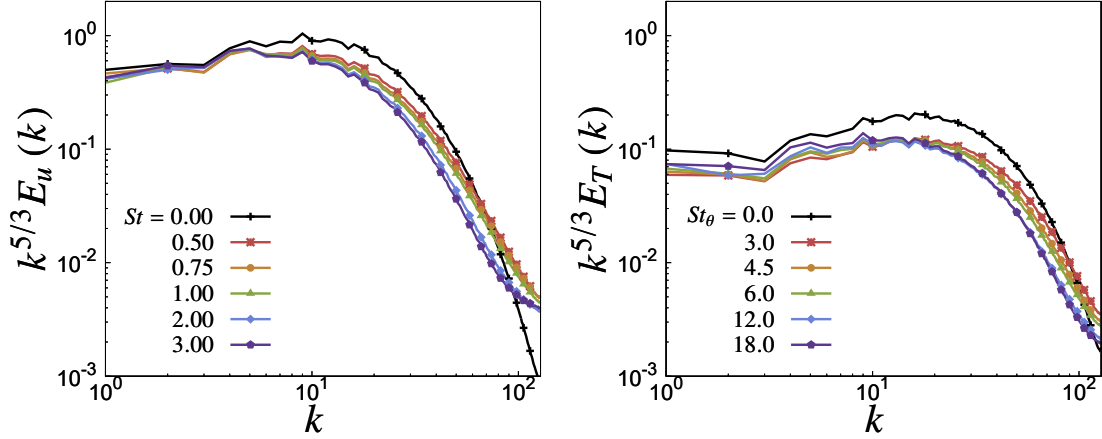


Figure 4.2: Spectra of the flow fields for different particle inertia, measured by the Stokes number. (a) Fluid velocity spectra; (b) Fluid temperature spectra.

set of three-dimensional trigonometric polynomials with unitary root mean square value in Ω has been used,

$$T_k = \left\{ \overline{f_k^j}(\mathbf{x}) = \sqrt{8} \cos(k_x x) \sin(k_y y) \cos(k_z z) : \left[k_x^2 + k_y^2 + k_z^2 \right] = k^2 \right\}_{j=1, \dots, N_{T_k}}.$$

T_k is a subset of the trigonometric polynomials with wavevector in the shell $\|\mathbf{k}\| = k$ so it contains $N_{T_k} \approx 4\pi k^2$ elements, neglecting the effect of the discretization in Fourier space. The backward NUFFT takes as input the polynomial $\overline{f_k^j}$ together with the particle position \mathbf{x}_p and returns the approximation $f_k^j(\mathbf{x}_p)$ of the value of the polynomial at the particle position. The error of the backward NUFFT can be estimated as the average of the absolute errors occurred in the interpolation of each element f_k^j of T_k , averaged over all the particles:

$$\epsilon_k^b = \frac{1}{N_p} \frac{1}{N_{T_k}} \sum_{p=1}^{N_p} \sum_{j=1}^{N_{T_k}} \left| f_k^j(\mathbf{x}_p) - \overline{f_k^j}(\mathbf{x}_p) \right|$$

The convergence and accuracy of the forward NUFFT with B-spline basis is assessed by performing the Fourier transform of a three-dimensional random field. The test signal is a superposition of Dirac delta functions with random, uniformly distributed, amplitude a_p centered at random points \mathbf{x}_p ,

$$C(\mathbf{x}) = \sum_p a_p \delta(\mathbf{x} - \mathbf{x}_p)$$

The mean amplitude of the spikes is zero, while its variance is unitary. Indeed, in order to compare the forward NUFFT with the B-spline interpolation, the trigonometric polynomials used for the interpolation and the Fourier modes of the random

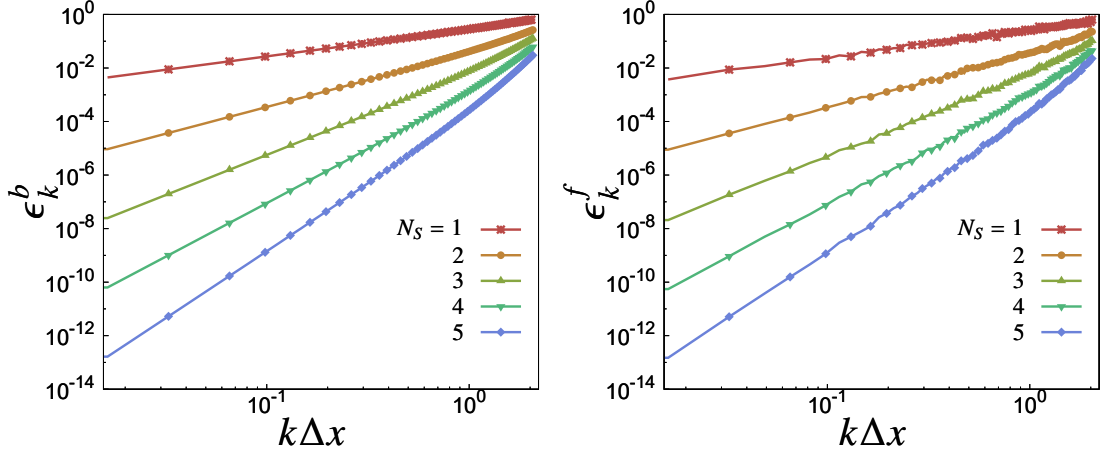


Figure 4.3: Absolute error of the NUFFT for different degrees of the polynomial basis. (a) Error in the interpolation of a trigonometric polynomial with unitary rms value and wavenumber k ; (b) Error in the Fourier transform of a random uniform field with unitary rms value at wavenumber k .

field should have the same root mean square value. In three dimensions this implies to take into account that the surface of the shells at constant wavenumber k grows as $\sim k^2$. The forward NUFFT takes as input the positions of the particles together with the amplitude of the spikes and returns the approximation $\hat{C}_{\mathbf{k}}$ of the Fourier transform of the superposition of Dirac functions. We define the error of the forward NUFFT as the average of the absolute errors occurred in the computation of each mode of the Fourier transform $\hat{C}_{\mathbf{k}}$, averaged over all the modes at constant k :

$$\epsilon_k^f = \frac{1}{N_{T_k}} \sum_{j=1}^{N_{T_k}} \left| \hat{C}_{\mathbf{k}}^j - \overline{\hat{C}_{\mathbf{k}}^j} \right|_{\|\mathbf{k}\|=k}$$

figure 4.3 shows the error of the backward NUFFT ϵ_k^b and the forward NUFFT ϵ_k^f for different degrees of the B-spline polynomial basis. The order of convergence matches the number of points used for the interpolation in each direction: $\epsilon_k^b \sim k^{-N_s}$ for $k \rightarrow 0$. It is critical to introduce a small error at low wavenumbers, since the large scales of the flow contain the largest amount of the energy in a turbulent flow, as shown in figure 4.2. The optimum value of the order of interpolation for the DNS of particle-laden turbulent flows has been discussed in [154]. Remarkably, the absolute errors of the backward and forward NUFFT are the same. This fact assesses the forward NUFFT as an accurate and efficient tool for computing the back-reaction of the particles on the flow. Indeed, the forward NUFFT shares all the advantages of the B-spline interpolation (backward NUFFT) which performs vastly better than other methods [75], especially if employed in pseudo-spectral codes.

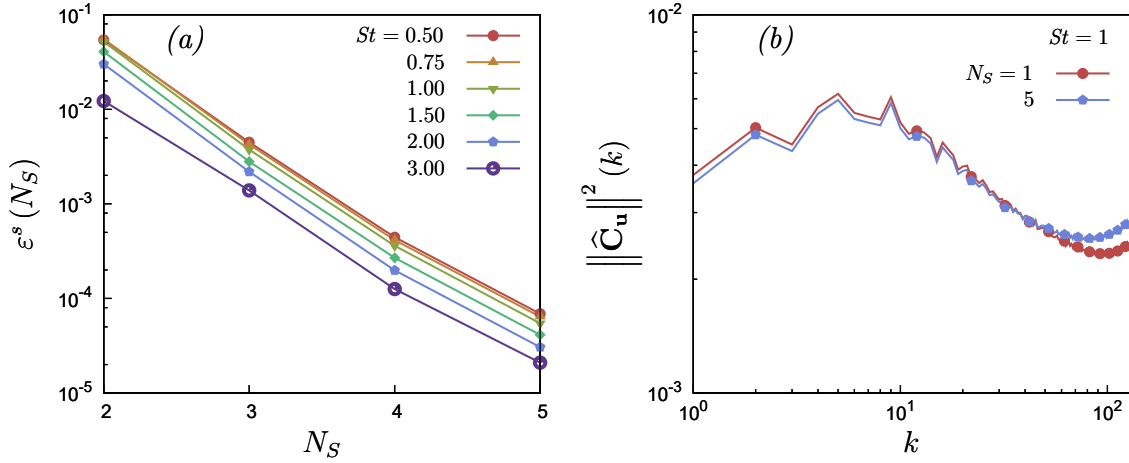


Figure 4.4: Convergence of the forward NUFFT. (a) Convergence of the spectral representation of the momentum coupling quantified by the relative error ϵ^s ; (b) Effect of the order of the basis on the momentum coupling spectrum.

4.4.2 Fluid phase-particle phase coupling

The accuracy of the NUFFT in Direct Numerical Simulations is now assessed, by analyzing the effect of the order of the B-spline basis on the spectral representation of the coupling terms. A quantitative estimation of the convergence is obtained by comparing the spectrum of the coupling terms computed with B-splines of different orders,

$$\epsilon^s(N_S) = \frac{\sum_k \left| \left| \hat{C}_k \right|_{N_S}^2 - \left| \hat{C}_k \right|_{N_S-1}^2 \right|}{\sum_k \left| \hat{C}_k \right|_{N_S}^2}, \quad (4.16)$$

where subscript N_S indicates the number of points used for the discrete convolution. figure 4.4(a) shows the relative error $\epsilon^s(N_S)$ on the momentum coupling as a function of N_S for different Stokes numbers. The error introduced by a low order basis may be too large for a DNS: N_S larger than two is required to achieve an accuracy which is at least comparable with the accuracy of the time integration and spatial discretization employed in standard DNS. Moreover, regularization functions would fail to provide an accurate representation of the coupling, since this technique would cut the large amount of energy contained in the coupling field at large wavenumbers, according to the chosen regularization scale. figure 4.4(b) compares the three dimensional spectrum of the momentum coupling for $St = 1$ computed by NUFFT with order zero ($N_S = 1$) and order four ($N_S = 5$) B-spline basis. The two spectra noticeably differ, since the low-order polynomial overestimates the coupling energy at low wavenumbers and underestimates the coupling energy at high wavenumbers.

The exact Fourier representation of a generic coupling term,

$$C(\mathbf{x}) = \sum_p a_p \delta(\mathbf{x} - \mathbf{x}_p),$$

reads

$$\widehat{C}_k = \sum_p a_p \exp(-i\mathbf{k} \cdot \mathbf{x}_p), \quad (4.17)$$

and its three-dimensional discrete spectrum is

$$\left| \widehat{C}_k \right|^2 \sim 4\pi k^2 \sum_p a_p^2 + 2 \sum_{\|\mathbf{k}\|=k} \sum_p \sum_{q>p} a_p a_q \cos(\mathbf{k} \cdot (\mathbf{x}_p - \mathbf{x}_q)), \quad (4.18)$$

where the number of grid points on a spherical shell of radius k is approximated with its continuum limit, $4\pi k^2$. The second term at right hand side of equation (4.18) is related to the correlation between the positions of the particles, so that for weakly correlated particles the first term at right hand side of equation (4.18) dominates, thus producing a $\sim k^2$ spectrum. This trend is due to the discrete nature of the coupling term, specifically, to the interaction of the particle with itself and it gives rise to an infinite amount of spectral energy. This self-interaction contribution always dominates at large k . On the other hand, when a finite correlation exists, the second term at right hand side of equation (4.18) dominates and, for a large number of particles, the spectrum of the particle feedback is determined by two-particle statistics. These behaviours can be seen in figure 4.5, which shows the spectra of the velocity and temperature coupling, computed by means of NUFFT with fourth-order B-spline basis. The coupling terms contain considerable amount of energy at large wavenumbers and, for large Stokes numbers, a k^2 trend appears in the higher simulated wavenumbers, as it has been observed in the framework of cloud microphysics [130]. The k^2 trend is evident for particles with large inertia, $St > 1$, and it extends at lower wavenumbers when St increases. Indeed, the k^2 trend is accentuated by lack of correlation between particle pairs, equation (4.18), which is the case of particles with large inertia. The next section deals with the possible removal of the particle self-interaction.

4.4.3 Smoothness of the coupling field

The statistics of the coupling term are characterized in order to gain insight into the field that the forward NUFFT has to deal with. Since the coupling term, in the limit of the point-particle model, can be treated only in the sense of distributions and we aim to represent it as a field on an Eulerian grid, then coarse-graining is required. The force exerted by the particle on the finite region of fluid Ω' , centered at \mathbf{x} is

$$\widetilde{C}_u(\mathbf{x}, t) = \frac{4}{3} \pi \frac{\rho_p}{\rho_f} \frac{r_p^3}{|\Omega'|} \sum_{\mathbf{x}_p \in \Omega'(\mathbf{x})} \frac{\mathbf{v}_p - \mathbf{u}(\mathbf{x}_p, t)}{\tau_p} \quad (4.19)$$

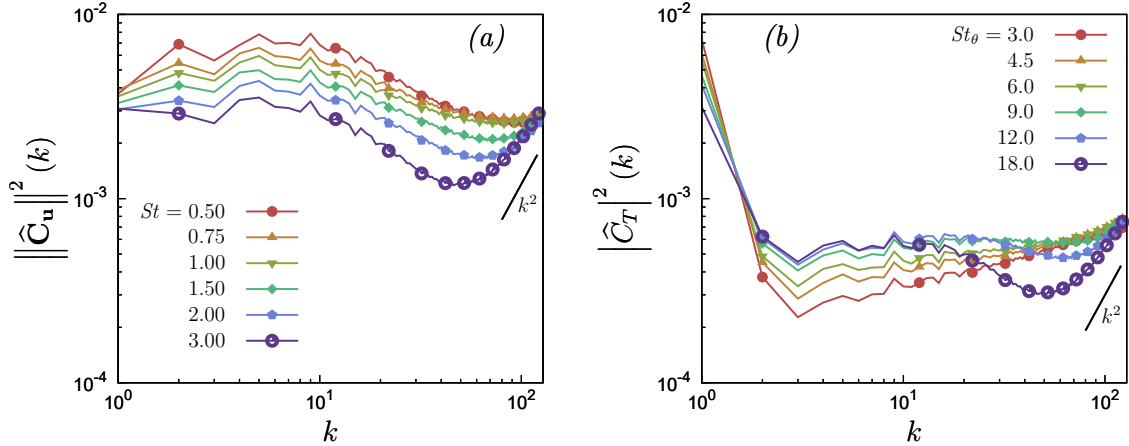


Figure 4.5: Spectra of the coupling terms, obtained by means of the forward NUFFT with $N_S = 5$. (a) Momentum coupling; (b) Temperature coupling.

The coarse grained back-reaction, equation (4.19), is exploited to analyze the regularity of the coupling terms, by characterizing its increments $\delta_r \widetilde{\mathbf{C}}_u(\mathbf{x}, t) = \widetilde{\mathbf{C}}_u(\mathbf{x} + \mathbf{r}, t) - \widetilde{\mathbf{C}}_u(\mathbf{x})$ using the Hölder condition

$$\langle \|\delta_r \mathbf{C}_u\| \rangle \leq \Lambda \|\mathbf{r}\|^{\alpha_H}, \quad \forall \mathbf{x}, \mathbf{r} \in \Omega$$

for non-negative real numbers Λ and α_H , independent of \mathbf{x} and \mathbf{r} . Here $\langle \cdot \rangle$ is the ensemble average, approximated by a spatial average for isotropic turbulence. Equation (4.19) shows that, when only the fluid exerts a force on the particle, the increments of the coarse-grained coupling field are proportional to the increments of the particle acceleration $\langle \delta_r \|\mathbf{C}_u\| \rangle \propto \langle \delta_r \|\dot{\mathbf{v}}\| \rangle$, thus the structure functions of the particle acceleration provide insight on the regularity of the coupling field. In particular, they highlight the dependence on the particle inertia of the order of Hölder-continuity α_H . At small separation, the particle acceleration structure functions show a well defined power law behaviour $\langle \delta_r \|\dot{\mathbf{v}}\| \rangle \sim r^{\alpha(\text{St})}$, as in figure 4.6, which implies

$$\langle \delta_r \|\mathbf{C}_u\| \rangle \sim r^{\alpha(\text{St})} \leq \Lambda r^{\alpha_H}$$

for $r \rightarrow 0$. Hence, the scaling exponent of the structure functions at small separation $\alpha(\text{St})$ is an upper bound for α_H . When the particle collisions are not taken to account and the ghost collision approximation is used, particles may overlap breaking the relation $\langle \delta_r \|\mathbf{C}_u\| \rangle \propto \langle \delta_r \|\dot{\mathbf{v}}\| \rangle$. However, we expect that in a steady and isotropic turbulent flow the exact overlapping of distinct particles is an event of zero probability.

The second order structure functions of the particle acceleration and the scaling exponents $\zeta_{a_{\parallel}}^n$ of the n -th order structure function of the particle acceleration are shown in figure 4.6. The second order structure functions display a well defined power law behaviour at small separation. However, the scaling exponent is much

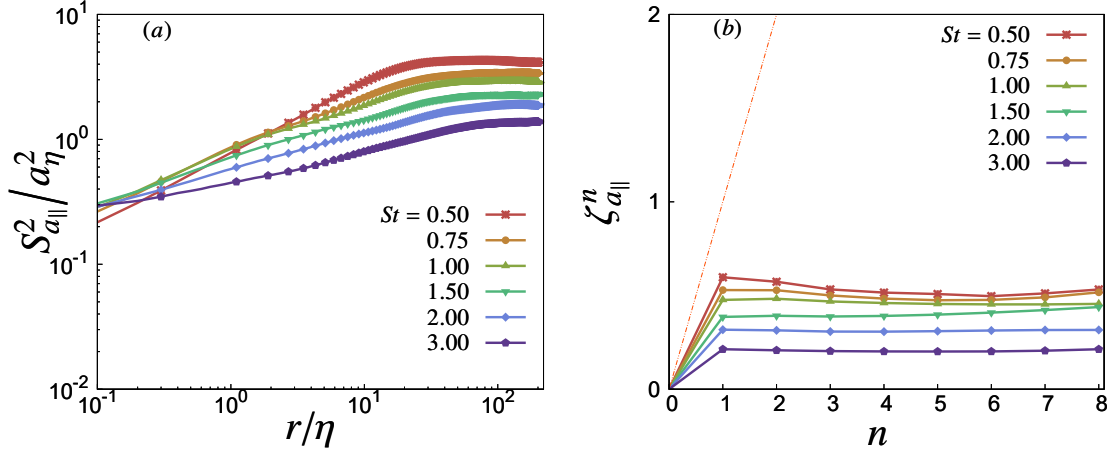


Figure 4.6: Structure functions of the particle acceleration for different particle inertia. (a) Second order structure functions of the particle acceleration; (b) Scaling exponent at small separation of the n -th order structure function of the particle acceleration. The statistics indicate the multifractal behaviour of the inertial particles.

less than the value expected for a regular field. The exponents rapidly saturate at values which decrease with the particle inertia, confirming the irregularity of the coupling at small scales. Another issue for the representation of the coupling field is the particle clustering [18]. Inertial particles tend to sample strain-dominated regions of the flow agglomerating in those regions. As a consequence, the coupling term is a superposition of spikes centered at points which are not uniformly distributed in the domain.

4.4.4 Spectral representation of the particle phase

Numerically, a set of particles can be representing on an Eulerian grid only by filtering the superposition of spikes centered at the particles on a certain length, that is the grid spacing Δx . The filtered distribution at the point \mathbf{x} , coarse-grained on a cubic box \mathcal{B} of size Δx centered at \mathbf{x} , is

$$\tilde{C}(\mathbf{x})\Delta x^3 = \sum_p a_p, \quad p : |(x_p)_i - x_i| < \Delta x/2$$

where the sum is extended only to the particles which lie in the box \mathcal{B} . The amplitude of the spikes can be thought to interpolate a (smooth) field $a(\mathbf{x})$, that is $a_p = a(\mathbf{x}_p)$. The fields C and a are non-trivially related, since a is sampled randomly and non-uniformly. Assuming that the field a is smooth, a Taylor expansion about

the point \mathbf{x} gives

$$\tilde{C}(\mathbf{x})\Delta x^3 \sim \sum_p \left[a(\mathbf{x}) + \frac{\partial a}{\partial x_j}(\mathbf{x}) ((x_p)_j - x_j) + \frac{1}{2} \frac{\partial^2 a}{\partial x_j \partial x_k}(\mathbf{x}) ((x_p)_j - x_j) ((x_p)_k - x_k) \right],$$

where $|(x_p)_i - x_i| < \Delta x/2$. Let $n(\mathbf{x})$ the number of particles in the box \mathcal{B} , then

$$C(\mathbf{x})\Delta x^3 \sim n(\mathbf{x})a(\mathbf{x}) + \sum_p \left[\frac{\partial a}{\partial x_j}(\mathbf{x}) ((x_p)_j - x_j) + \frac{1}{2} \frac{\partial^2 a}{\partial x_j \partial x_k}(\mathbf{x}) ((x_p)_j - x_j) ((x_p)_k - x_k) \right]$$

where the sum is extended only to the particles which lie in the box \mathcal{B} . A zeroth order approximation, with respect to the increment Δx , is $C(\mathbf{x}) \sim n(\mathbf{x})a(\mathbf{x})$ and therefore the equivalent field can be computed

$$a(\mathbf{x}) = \frac{C(\mathbf{x})\Delta x^3}{n(\mathbf{x})}. \quad (4.20)$$

The full distribution C , which includes the variable density of the particles, and the equivalent field a , which is understood as the smooth field that the particles interpolate, should be carefully distinguished. The expression for the equivalent field a involves approximations, in particular all the variations of the field on scale Δx have been neglected. If the number of particles in the box \mathcal{B} is large enough the odd derivatives contributions vanish by symmetry while the even derivatives have instead a relevant impact on the equivalent field representation. In particular, the curvature of the field a at \mathbf{x} gives the largest contribution.

4.4.5 Particle number density equivalent field

Two-particle statistics can be efficiently characterized in Fourier space through Non-Uniform Fast Fourier Transform, so as to determine the density, momentum and temperature fields equivalent to the particles discrete distribution. Particle mass density and velocity fields can be employed to quantify the particle clustering [12]. From the discrete particle distribution, the particle phase density is

$$\rho(\mathbf{x}, t) = \sum_p m_p \delta(\mathbf{x} - \mathbf{x}_p(t)),$$

where $m_p = 4\rho_p\pi r_p^3/3$ is the single particle mass. Since the particles are monodisperse in these simulations then $m = m_p$. The discrete particle mass distribution is smoothed by means of B-splines and represented in physical space on a Cartesian grid:

$$\tilde{\rho}(\mathbf{x}, t) = m \sum_p B(\mathbf{x} - \mathbf{x}_p(t)). \quad (4.21)$$

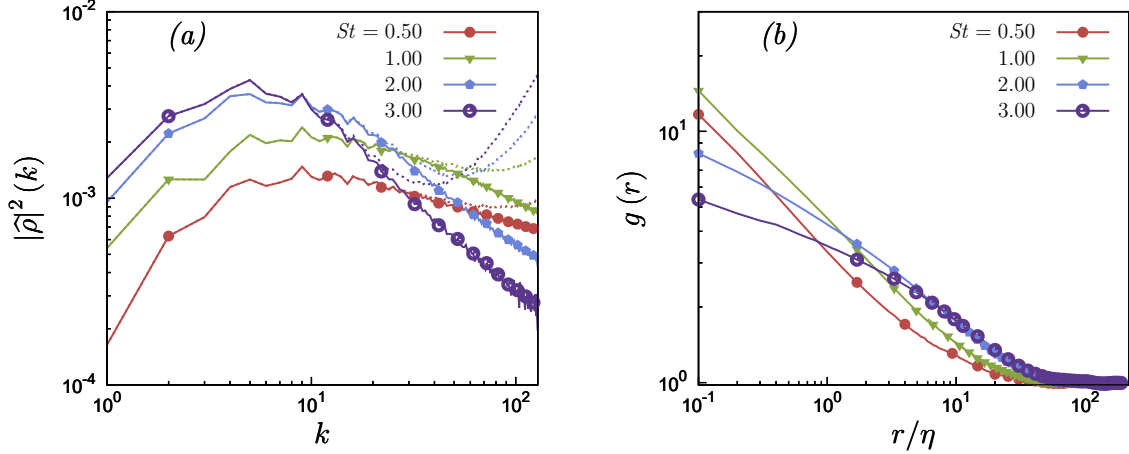


Figure 4.7: Inertial particle clustering observed in Fourier and in physical space. (a) Three dimensional corrected spectra (solid) and bare spectra (dotted line) of the particle mass distribution; (b) Radial distribution function for different particle inertia.

The smoothed field is transformed by means of FFT and the convolution is removed in Fourier space. Therefore, the spectrum of the particle density field can be obtained as

$$|\hat{\rho}(k, t)|^2 = \frac{1}{(2\pi)^6} \sum_{\|\mathbf{k}\|=k} \left| \frac{\mathcal{F}[\tilde{\rho}](\mathbf{k}, t)}{\mathcal{F}[B](\mathbf{k})} \right|^2, \quad (4.22)$$

where the denominator removes the B-spline regularization and ensures that the mean value of ρ is equal to $\rho_p \phi$, that is, $\hat{\rho}(0, t) = \rho_p \phi$. equation (4.22) provides the NUFFT approximation to the discrete reference spectrum of (4.21), which is

$$|\hat{\rho}(k, t)|_r^2 \sim \frac{m^2}{(2\pi)^6} \left[4\pi k^2 N_P + 2 \sum_{\|\mathbf{k}\|=k} \sum_p \sum_{q>p} \cos(\mathbf{k} \cdot (\mathbf{x}_q(t) - \mathbf{x}_p(t))) \right]. \quad (4.23)$$

The $\sim k^2$ trend is removed from the NUFFT approximation of the spectrum, equation (4.22), using the expression of the exact spectrum, equation (4.23),

$$|\hat{\rho}(k, t)|_c^2 = \frac{1}{(2\pi)^6} \left[\sum_{\|\mathbf{k}\|=k} \left| \frac{\mathcal{F}[\tilde{\rho}](\mathbf{k}, t)}{\mathcal{F}[B](\mathbf{k})} \right|^2 - 4\pi k^2 N_P m^2 \right], \quad (4.24)$$

to obtain a corrected spectrum.

The spectra of the particle mass distribution field, for different particle inertia, are shown in figure 4.7(a). The solid lines represent the corrected spectrum, defined by equation (4.24), while the dotted lines refer to the bare spectrum, defined in equation (4.22). In the lower wavenumber range the two spectra coincide, they

begin to differentiate as soon as particle inertia is able to decorrelate particle motions. Therefore the threshold wavenumber at which this happens reduces as the Stokes number is increased. The slope of the spectrum gives an indication of particle clustering, with lower slopes produced by the sharpening of particle concentration fronts [12], which is maximum at $St = O(1)$. The slope of the spectra at large wavenumbers is well above -3 , that is the value corresponding to square-integrable gradient of the particle density field. Thus, the particle density field displays fronts for finite particle inertia [12]. The particle density field encloses features which can be characterized in physical space by means of the radial distribution function (RDF). The radial distribution function is defined as the ratio between the number of particles N_r which lie on a spherical shell of radius r and the average number of particles expected on the shell for a uniform particle distribution [81]:

$$g(r) = \frac{|\Omega|}{N_P} \lim_{\delta r \rightarrow 0} \frac{N_r(\delta r)}{4\pi r^2 \delta r}, \quad (4.25)$$

Fluid particles, for which $St = 0$, are uniformly distributed in the domain, so that $g(r) = 1$. As the Stokes number is increased particles tend to agglomerate at small separation and this small-scale clustering is maximum at $St = O(1)$. As the Stokes number is further increased the clustering strength reduces and the particles distribution tend to be uniform again. The RDF directly provides information about clustering using physical space quantities only. Remarkably, an equivalent description of clustering can be carried out by means of the corrected spectra of the particle mass distribution equivalent field. In fact, at large wavenumber, the spectrum of the particle mass distribution increases with St up to $St = O(1)$ and then decreases. This coincides with the trend of the radial distribution functions at small separation. Notice that the information about small scale clustering is not evident from the bare spectra, since it is concealed by the k^2 trend. The spectral analysis of the particle mass distribution by means of equivalent field shows that the NUFFT can be employed to characterize two-particle statistics in a simpler manner than the challenging direct computation in physical space.

4.4.6 Particle momentum and temperature equivalent fields

Particle equivalent fields for the particle velocity and temperature allow to draw similarity between the spectral representation of the particle phase and the particle structure functions. The smoothed equivalent particle velocity and temperature fields are defined as

$$\tilde{\mathbf{v}}(\mathbf{x}, t) = \frac{\sum_p m_p \mathbf{v}_p(t) B(\mathbf{x} - \mathbf{x}_p(t))}{\sum_p m_p B(\mathbf{x} - \mathbf{x}_p(t))}, \quad (4.26)$$

$$\tilde{\theta}(\mathbf{x}, t) = \frac{\sum_p m_p c_p \theta_p(t) B(\mathbf{x} - \mathbf{x}_p(t))}{\sum_p m_p c_p B(\mathbf{x} - \mathbf{x}_p(t))}, \quad (4.27)$$

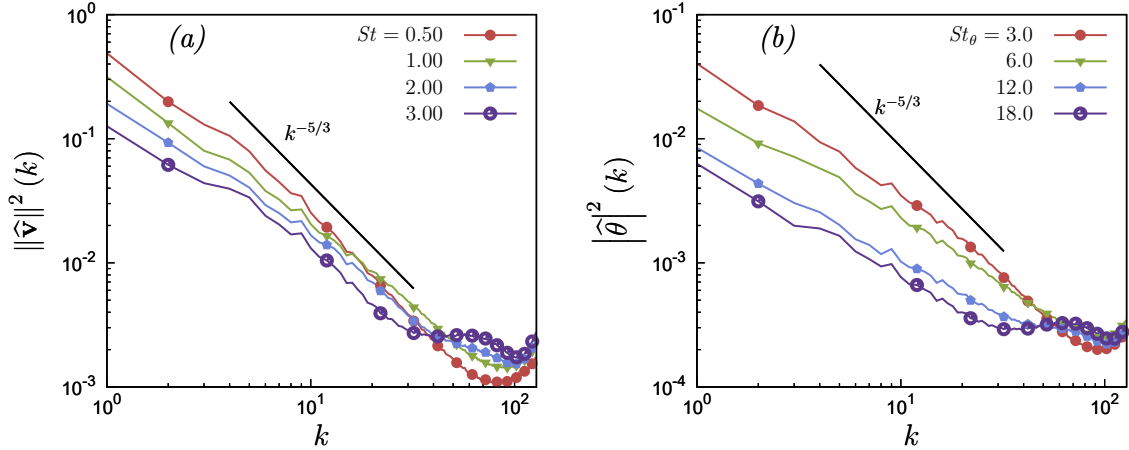


Figure 4.8: Spectra of the particle equivalent fields for different particle inertia. (a) Spectrum of the particle velocity equivalent field; (b) Spectrum of the particle temperature equivalent field.

so that particle momentum and enthalpy per unit volume are $\tilde{\rho}\tilde{\mathbf{v}}$ and $\tilde{\rho}c_p\tilde{\theta}$. The equivalent velocity and temperature field definition takes into account that several particles could be located around each grid point. For $St = 0$ and $St_\theta = 0$, these equivalent fields coincide with the fluid velocity and temperature fields because velocity and temperature are equal to the fluid velocity and temperature and particles are uniformly distributed. As for the particle density field, the particle velocity and temperature smoothed fields can be transformed by means of FFTs. Figure 4.8 shows the spectra of the particle velocity and temperature equivalent fields. An inertial range can be identified in the particle velocity and temperature equivalent fields spectra. However, this observation is only qualitative, since a higher Reynolds number would be required to observe a well developed inertial scaling. The trend of the particle velocity spectrum is close to the Kolmogorov scaling at low Stokes numbers. In fact, particles with low inertia tend to behave as the underlying fluid particles. As the Stokes number increases the slope of the spectrum in the inertial range decreases, indeed particles tend to spatially decorrelate, and the bare momentum spectrum approaches a k^2 trend as seen above. The energy of the particle velocity and temperature fluctuations decreases with the particle inertia, which is evident at the largest scales. At small scales, the k^2 trend, not removed in figure, is not as evident as for the coupling terms. The spectra of the continuum equivalent temperature presents a larger deviation from the Obukhov scaling because the thermal Stokes number is always much larger than the Stokes number in the simulations, since $St_\theta = 6St$ is chosen in order to emulate water droplets in air. Thus, even at the smallest Stokes number the behaviour of the particle temperature is much different than the underlying fluid temperature. This larger thermal Stokes number, which corresponds to a larger thermal relaxation time, produces a large

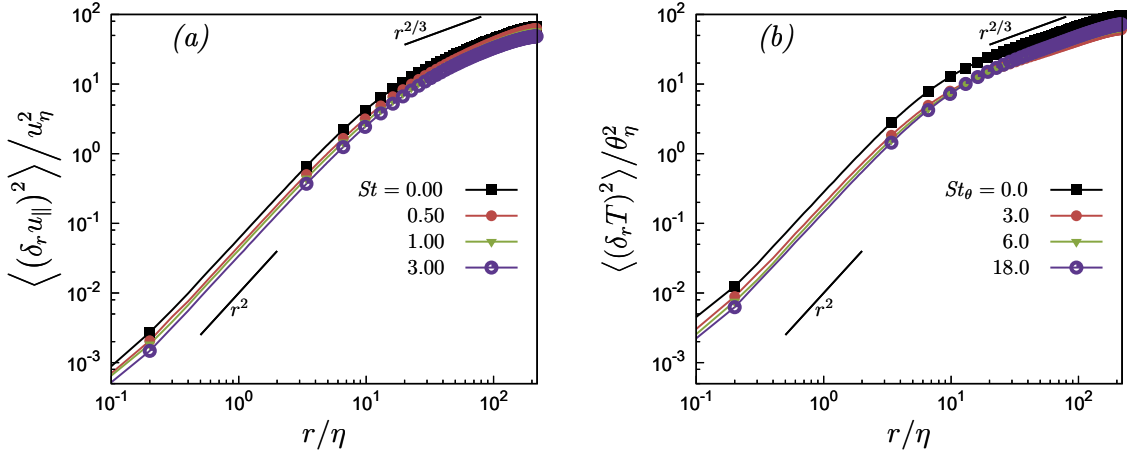


Figure 4.9: Second order structure functions of fluid velocity and temperature in the two-way coupling regime, for various inertia of the suspended particles. (a) Longitudinal fluid velocity structure functions; (b) Fluid temperature structure functions.

memory effect along particle paths, so that they are more sensible to large scale fluctuations and their statistics can be affected by the details of the large-scale forcing. Moreover, these deviations from the Obukhov scaling can also be attributed to the high intermittency of the advected passive scalars like temperature and to the tendency of particles to cluster in the regions of large temperature gradients [25]. These may be some of the reasons behind the deviation of the spectrum of the equivalent temperature field from the classical Obukhov scaling.

4.4.7 Scale by scale analysis

Inertial particles modify the fluid flow fluctuations across all the scales of the flow through the coupling terms in equation (4.1). This effect of particles on the flow can be quantified through the second order longitudinal velocity and temperature structure functions, which are defined as:

$$S_{u_{\parallel}}^2(r) = \langle (\delta_r \mathbf{u} \cdot \hat{\mathbf{r}})^2 \rangle, \quad S_T^2(r) = \langle (\delta_r T)^2 \rangle,$$

where $\langle \cdot \rangle$ indicates the ensemble average, $\delta_r \mathbf{u}$ is the velocity increment computed at separation \mathbf{r} , $r \equiv \|\mathbf{r}\|$ and $\hat{\mathbf{r}} = \mathbf{r}/r$ is the unit vector in the direction of the separation vector.

figure 4.9 shows the second order longitudinal fluid velocity structure functions and fluid temperature structure function, for different inertia of the suspended particles. The statistics are non-dimensionalized by means of a small-scale velocity fluctuation $u_{\eta} = (\varepsilon \nu)^{1/4}$ and a small-scale temperature fluctuation $\theta_{\eta} = \chi^{1/2} (\kappa/\varepsilon)^{1/4}$. The fluctuations of the fluid velocity field are modulated by the suspended inertial

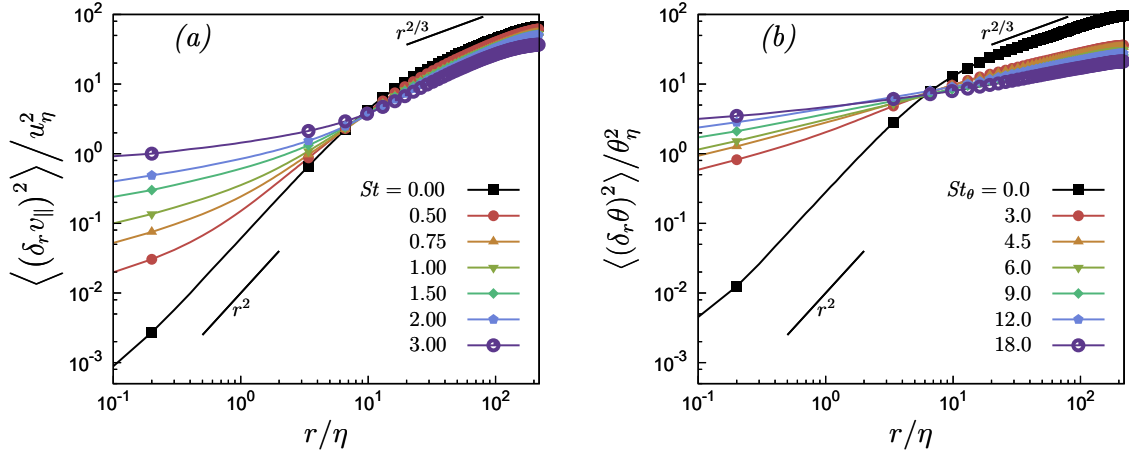


Figure 4.10: Second order structure functions of particle velocity and temperature in the two-way coupling regime, for various particle inertia. (a) Longitudinal particle velocity structure functions; (b) Particle temperature structure functions.

particles at all the scales. At the smallest scales the second order structure functions always decrease due to the presence of particles, and the reduction is more evident as the particle inertia is increased. At small separation the second order structure function is proportional to the dissipation rate of turbulent kinetic energy (TKE) due to the fluid velocity gradients, that is $S_{u_{\parallel}}^2 \propto \|\nabla \mathbf{u}\|^2$, $r \leq \eta$. Thus, the contribution to the dissipation rate by the interaction with the particles increases monotonically with particle inertia, at energy injection rate maintained constant. A qualitative similar behaviour can be observed in the fluid temperature structure function.

At a separation larger than the integral length scale ℓ , the second order structure function is proportional to the variance of the fluctuations of the velocity field, that is $S_{u_{\parallel}}^2 \propto u'^2$, $r \geq \ell$. These results show that the turbulent kinetic energy decreases as the particle inertia is increased. However, in this scale range the fluid temperature field displays a qualitatively different behaviour. In fact, the suppression of the fluid temperature fluctuations by the suspended inertial particles appears to have a maximum because particles with a relaxation time much larger than fluid time scales become less and less effective in the large-scale modulation of the fluid temperature fluctuations [25]. The most effective Stokes number for large-scale fluctuations suppression may depend on the Reynolds and Prandtl numbers and deserves further investigation.

figure 4.10 shows the second order longitudinal particle velocity structure function and particle temperature structure function, for different particle inertia. At small separation, as the Stokes number is increased, the second order particle velocity and temperature structure functions noticeably deviate from the r^2 behaviour, that is the behaviour expected for an analytic field. Pairs of particles which are

very close to each other have on average much larger relative velocity than the corresponding fluid particles [165]. At intermediate-large scales the particle velocity and temperature second order structure functions exhibits a $r^{2/3}$ trend [81] which is consistent with the inertial range scaling of the particle velocity and temperature spectra in figure 4.8. At large separation the energy of the particle velocity and temperature fluctuations always decrease increasing the particle inertia, for Stokes numbers large enough. This is consistent with the reduction of the particle velocity and temperature spectral energy, figure 4.8. However, due to the large inertia, small particle velocity and temperature fluctuations correspond to relatively large fluctuations of momentum and thermal energy. The particle velocity and temperature structure functions show qualitatively similar behaviour, even though the thermal Stokes number of the particles is quite larger than the dynamic particle Stokes number, rendering the thermal caustics and filtering more evident. A detailed examination of the temperature modulation due to inertial particles in turbulence can be found in [25].

4.5 Conclusions

The ability of the Non-Uniform Fast Fourier Transform to allow an accurate simulation of particle-laden turbulent flows has been explored. The NUFFT with B-spline basis turned out to be an effective tool for the numerical simulation of particle-laden flows in the two-way coupling regime. Also, the NUFFT allows for the spectral representation of the particle phase by means of equivalent fields, which can be employed to characterize two-particle statistics. It is shown that particle clustering can be described in detail by means of the particle mass distribution equivalent field, obtained by NUFFT. Also, analogies can be drawn between the particle second order structure functions and the spectra of the particle velocity and temperature equivalent fields. The ability to easily obtain equivalent particle fields is an interesting feature of the NUFFT which is promising to compute multiple particle statistics from Direct Numerical Simulations of particle-laden flows.

Chapter 5

Multiscale fluid–particle thermal interaction in isotropic turbulence.

In this Chapter we use direct numerical simulations to investigate the interaction between the temperature field of a fluid and the temperature of small particles suspended in the flow, employing both one and two-way thermal coupling, in a statistically stationary, isotropic turbulent flow. Using statistical analysis, we investigate this variegated interaction at the different scales of the flow. We find that the variance of the carrier flow temperature gradients decreases as the thermal response time of the suspended particles is increased. The probability density function (PDF) of the carrier flow temperature gradients scales with its variance, while the PDF of the rate of change of the particle temperature, whose variance is associated with the thermal dissipation due to the particles, does not scale in such a self-similar way. The modification of the fluid temperature field due to the particles is examined by computing the particle concentration and particle heat fluxes conditioned on the magnitude of the local fluid temperature gradient. These statistics highlight that the particles cluster on the fluid temperature fronts, and the important role played by the alignments of the particle velocity and the local fluid temperature gradient. The temperature structure functions, which characterize the temperature fluctuations across the scales of the flow, clearly show that the fluctuations of the carrier flow temperature increments are monotonically suppressed in the two-way coupled regime as the particle thermal response time is increased. Thermal caustics dominate the particle temperature increments at small scales, that is, particles that come into contact are likely to have very large differences in their temperature. This is caused by the nonlocal thermal dynamics of the particles: the scaling exponents of the inertial particle temperature structure functions in the dissipation range reveal very strong multifractal behavior. Further insight is provided by the flux of temperature increments across the scales. All together, these results reveal a number of non-trivial effects, with a number of important practical consequences.

A preliminary version of this work has been published in the proceedings of the iTi Conference [26], the full work has been published in the Journal of Fluid Mechanics and most of the following material can be found in [25].

5.1 Introduction

The interaction between inertial particles and scalar fields in turbulent flows plays a central role in many natural problems, ranging from cloud microphysics [123, 65] to the interactions between plankton and nutrients [44], and dust particle flows in accretion disks [140]. In engineered systems, applications involve chemical reactors and combustion chambers, and more recently, microdispersed colloidal fluids where the enhanced thermal conductivity due to particle aggregations can give rise to non-trivial thermal behavior [122, 110], and which can be used in cooling devices for electronic equipment exposed to large heat fluxes [41].

In this work, we focus on the heat exchange between advected inertial particles and the fluid phase in a turbulent flow, with a parametric emphasis relevant to understanding particle-scalar interactions in cloud microphysics. Understanding the droplet growth in clouds requires to characterize the interaction between water droplets and the humidity and temperature fields. A major problem is to understand how the interaction between turbulence, heat exchange, condensational processes, and collisions can produce the rapid growth of water droplets that leads to rain initiation [123, 65]. While the study of the transport of scalar fields and particles in turbulent flows are well established research areas in both theoretical and applied fluid dynamics [92, 141], the characterization of the interaction between scalars and particles in turbulent flows is a relatively new topic [8], since the problem is hard to handle analytically, requires sophisticated experimental techniques, and is computationally demanding.

When temperature differences inside the fluid are sufficiently small, the temperature field behaves almost like a passive scalar, that is, the fluid temperature is advected and diffused by the fluid motion but has negligible dynamical effect on the flow. Even in this regime, the statistical properties of the passive scalar field are significantly different from those of the underlying velocity field that advects it. Different regimes take place according to the Reynolds number and the ratio between momentum and scalar diffusivities [135, 161, 162].

Experiments, numerical simulations and analytical models show that a passive scalar field is always more intermittent than the velocity field, and passive scalars in turbulence are characterized by strong anomalous scaling [77]. This is due to the formation of ramp–cliff structures in the scalar field [30, 162]: large regions in which the scalar field is almost constant are separated by thin regions in which the scalar abruptly changes. The regions in which the scalar mildly changes are referred to as Lagrangian coherent structures. The thin regions with large scalar gradient,

where the diffusion of the scalar takes place, are referred to as fronts. It has been shown that the large scale forcing influences the passive scalar statistics at small scales [63]. In particular, a mean scalar gradient forcing preserves universality of the statistics while a large scale Gaussian forcing does not. However, the ramp-cliff structure was observed with different types of forcing, implying that this structure is universal to scalar fields in turbulence [162, 8]. Moreover, recent measurements of atmospheric turbulence have shown that external boundary conditions, such as the magnitude and sign of the sensible heat flux, have a significant impact on the fluid temperature dynamics within the inertial range, while for the same scales the fluid velocity increments are essentially independent of these large-scale conditions [173].

When a turbulent flow is seeded with inertial particles, the particles can sample the surrounding flow in a non-uniform and correlated manner [147]. Particle inertia in a turbulent flow is measured through the Stokes number $St \equiv \tau_p/\tau_\eta$, which compares the particle response time to the Kolmogorov time scale. A striking feature of inertial particle motion in turbulent flows is that they spontaneously cluster even in incompressible flows [106, 160, 9, 81]. This clustering can take place across a wide range of scales [9, 16, 81], and the small-scale clustering is maximum when $St = O(1)$. A variety of mechanisms has been proposed to explain this phenomena: when $St \ll 1$ the clustering is caused by particles being centrifuged out of regions of strong rotation [106, 35], while for $St \geq O(1)$, a non-local mechanism generates the clustering, whose effect is related to the particles memory of its interaction with the flow along its path-history [71, 72, 18, 17, 16]. Note that recent results on the clustering of settling inertial particles in turbulence have corroborated this picture, showing that strong clustering can occur even in a parameter regime where the centrifuge effect cannot be invoked as the explanation for the clustering, but is caused by a non-local mechanism [82].

When particles have finite thermal inertia, they will not be in thermal equilibrium with the fluid temperature field, and this can give rise to non-trivial thermal coupling between the fluid and particles in a turbulent flow. A thermal response time τ_θ can be defined so that the particle thermal inertia is parameterized by the thermal Stokes number $St_\theta \equiv \tau_\theta/\tau_\eta$ [169]. Since both the fluid temperature and particle phase-space dynamics depend upon the fluid velocity field, there can exist non-trivial correlations between the fluid and particle temperatures even in the absence of thermal coupling. Indeed, it was show by [8] that inertial particles preferentially cluster on the fronts of the scalar field. Associated with this is that the particles preferentially sample the fluid temperature field, and when combined with the strong intermittency of temperature fields in turbulent flows, that can cause particles to experience very large temperature fluctuations along their trajectories.

Several works have considered aspects of the fluid-particle temperature coupling using numerical simulations. For example, [172] investigated a particle-laden

channel flow, with a view to modeling the modification of heat transfer in micro-dispersed fluids. They considered both momentum and temperature two-way coupling and observed that, depending on the particle inertia, the heat flow at the wall can increase or decrease. [93] considered a similar set-up with larger dispersed particles, and they observed a stronger modification of the fluid temperature statistics due to the particles. [170, 171] considered turbulence induced by buoyancy, where the buoyancy was generated by heated particles. They observed that the resulting flow is driven by thermal plumes produced by the particles. As the particle inertia was increased, the inhomogeneity and the effect of the coupling were enhanced in agreement with the fact that inertial particles tend to cluster on the scalar fronts. [95] examined how the spatial distribution of droplets is affected by large scale inhomogeneities in the fluid temperature and supersaturation fields, considering the transition between homogeneous and inhomogeneous mixing. A similar flow configuration was also investigated by [64].

Each of these studies was primarily focused on the effect of the inertial particles on the large-scale statistics of the fluid temperature field. However, the results of [8] imply that the effects of fluid-particle thermal coupling could be strong at the small scales, owing to the fact that they cluster on the fronts of the temperature field. Moreover, there is a need to understand and characterize the multiscale thermal properties of the particles themselves. In order to address these issues, we have conducted direct numerical simulations (DNS) to investigate the interaction between the scalar temperature field and the temperature of inertial particles suspended in the fluid, with one and two-way thermal coupling, in statistically stationary, isotropic turbulence. Using statistical analysis, we probe the multiscale aspects of the problem and consider the particular ways that the inertial particles contribute to the properties of the fluid temperature field in the two-way coupled regime.

This Chapter is organized as follows. In section 5.2 we present the physical model used in the DNS, and present the parameters in the system. In section 5.3 the statistics of the fluid temperature and time derivative of the particle temperature are considered, which allow us to quantify the contributions to the thermal dissipation in the system from the fluid and particles. In section 5.4 we consider the statistics of the fluid and particle temperature. In section 5.5 we consider the heat flux due to the particle motion conditioned on the local fluid temperature gradients in order to obtain insight into the details of the thermal coupling. In section 5.6 we consider the structure functions of the fluid and particle temperature increments, along with their scaling exponents. In section 5.7 we consider the probability density functions (PDFs) of the fluxes of fluid and particle temperature increments across the scales of the flow. Finally, concluding remarks are given in section 5.10.

5.2 The physical model

In this section we present the governing equations of the physical model which will be solved numerically to simulate the thermal coupling and behavior of a particle-laden turbulent flow.

5.2.1 Fluid phase

We consider a statistically stationary, homogeneous and isotropic turbulent flow, governed by the incompressible Navier-Stokes equations. The turbulent velocity field advects the fluid temperature field (assumed a passive scalar), together with the inertial particles. In this study, we account for two-way thermal coupling between the fluid and particles, but only one-way momentum coupling. Therefore, the governing equations for the fluid phase are

$$\nabla \cdot \mathbf{u} = 0, \quad (5.1a)$$

$$\partial_t \mathbf{u} + \mathbf{u} \cdot \nabla \mathbf{u} = -\frac{1}{\rho_0} \nabla p + \nu \nabla^2 \mathbf{u} + \mathbf{f}, \quad (5.1b)$$

$$\partial_t T + \mathbf{u} \cdot \nabla T = \kappa \nabla^2 T - C_T + f_T. \quad (5.1c)$$

Here $\mathbf{u}(\mathbf{x}, t)$ is the velocity of the fluid, $p(\mathbf{x}, t)$ is the pressure, ρ_0 is the density of the fluid, ν is its kinematic viscosity, $T(\mathbf{x}, t)$ is the temperature of the fluid and κ is the thermal diffusivity. The ratio between the momentum diffusivity ν and the thermal diffusivity κ defines the Prandtl number $\text{Pr} \equiv \nu/\kappa$. In this work, we consider $\text{Pr} = 1$, leaving further exploration of its effect on the system to future work. The \mathbf{f} and f_T terms in equations (5.1b) and (5.1c) represent the external forcing, and C_T is the thermal feedback of the particles on the fluid temperature field, that is, the heat exchanged per unit time and unit volume between the fluid and particles at position \mathbf{x} .

When the forcing is confined to sufficiently large scales, it is assumed that the details of the forcing do not influence the small-scale dynamics. Previous experimental evidence seems to confirm this [137], leading to a universal behaviour of the small-scales. However, recent studies [63] pointed out that this hypothesis of universality is partially violated by the advected scalar fields, whose inertial range statistics exhibit sensitivity to the details of the imposed forcing. Since we aim to characterize temperature and temperature gradient fluctuations in the dissipation range for different inertia of the suspended particles, we employ a forcing that imposes the same total dissipation rate for all the simulations. This produces results which can be meaningfully compared for different parameters of the suspended particles, since the response of the system to the same injected thermal power can be

examined. Therefore, we employ the large scale forcing [94, 95],

$$\hat{\mathbf{f}}(\mathbf{k}, t) = \varepsilon \frac{\hat{\mathbf{u}}(\mathbf{k}, t)}{\sum_{\mathbf{k}_f \in \mathcal{K}_f} \|\hat{\mathbf{u}}(\mathbf{k}_f, t)\|_2} \delta_{\mathbf{k}, \mathbf{k}_f}, \quad \hat{f}_T(\mathbf{k}, t) = \chi \frac{\hat{T}(\mathbf{k}, t)}{\sum_{\mathbf{k}_f \in \mathcal{K}_f} |\hat{T}(\mathbf{k}_f, t)|_2} \delta_{\mathbf{k}, \mathbf{k}_f}, \quad (5.2)$$

in the wavenumber space. A hat indicates the Fourier transform and \mathbf{k}_f is the wavenumber which here belongs to the set of forced wavenumbers, $\mathcal{K}_f = \{\mathbf{k}_f : \|\mathbf{k}_f\| = k_f\}$; ε and χ are the imposed dissipation rates of velocity and temperature variance, respectively. This employed forcing scheme thus allows to control the overall dissipation rate and, therefore, to control the Stokes number.

The value of the parameters relative to the fluid flow, employed in the simulations are given in table 5.1. Time-averaged energy and temperature spectra, in absence of particle thermal feedback, are shown in figure 5.1(a).

5.2.2 Particle phase

We consider rigid, point-like particles which are heavy with respect to the fluid, and small with respect to any scale of the flow. In particular, the particle density ρ_p is much larger than the fluid density $\rho_p \gg \rho_0$, and the particle radius r_p is much smaller than the Kolmogorov length scale $r_p \ll \eta$. With these assumptions (and neglecting gravity) the particle acceleration is described by the Stokes drag law. Analogously, the rate of change of the particle temperature is described by Newton's law for the heat conduction

$$\frac{d\mathbf{x}_p}{dt} \equiv \mathbf{v}_p, \quad (5.3a)$$

$$\frac{d\mathbf{v}_p}{dt} = \frac{\mathbf{u}(\mathbf{x}_p, t) - \mathbf{v}_p}{\tau_p}, \quad (5.3b)$$

$$\frac{d\theta_p}{dt} = \frac{T(\mathbf{x}_p, t) - \theta_p}{\tau_\theta}. \quad (5.3c)$$

Here $\tau_p \equiv 2\rho_p r_p^2 / (9\rho_0 \nu)$ is the particle momentum response time, $\tau_\theta \equiv \rho_p c_p r_p^2 / (3\rho_0 c_0 \kappa)$ is the particle thermal response time, c_p is the particle heat capacity, and c_0 is the fluid heat capacity at constant pressure. The Stokes number is defined as $St \equiv \tau_p / \tau_\eta$, and the thermal Stokes number is defined as $St_\theta \equiv \tau_\theta / \tau_\eta$, where τ_η is the Kolmogorov time scale.

We consider nine values of St_θ and three values of St in order to explore the behavior of the system over a range of parameter values. Since we are accounting for thermal coupling, each combination of St_θ and St must be simulated separately, and when combined with the large number of particles in the flow domain, the set of simulations require considerable computational resources. Therefore, in the present study we restrict attention to $Re_\lambda = 88$, but future explorations should consider

Kinematic viscosity	ν	0.005
Prandtl number	Pr	1
Velocity fluctuations dissipation rate	ε	0.27
Temperature fluctuations dissipation rate	χ	0.1
Kolmogorov time scale	τ_η	0.136
Kolmogorov length scale	η	0.0261
Taylor micro-scale	λ	0.498
Integral length scale	ℓ	1.4
Root mean square velocity	u'	0.88
Kolmogorov velocity scale	u_η	0.192
Small scale temperature	T_η	0.117
Taylor Reynolds number	Re $_\lambda$	88
Integral scale Reynolds number	Re $_l$	244
Forced wavenumber	k_f	$\sqrt{2}$
Number of Fourier modes	N	128 (3/2)
Resolution	$N\eta/2$	1.67

Table 5.1: Flow parameters for the numerical simulations in this study. Dimensional parameters are non-dimensionalized into arbitrary code units. The characteristic parameters of the fluid flow are defined from its energy spectrum $E(k) \equiv \int_{\|\mathbf{k}\|=k} \|\hat{\mathbf{u}}(\mathbf{k})\|^2 d\mathbf{k}/2$. The dissipation rate of turbulent kinetic energy is: $\varepsilon \equiv 2\nu \int k^2 E(k) dk$. The Kolmogorov length $\eta \equiv (\nu^3/\varepsilon)^{1/4}$, time scale $\tau_\eta \equiv (\nu/\varepsilon)^{1/2}$ and velocity scale $u_\eta \equiv \eta/\tau_\eta$. The Taylor micro-scale is: $\lambda \equiv u'/\sqrt{\langle |\nabla \mathbf{u}|^2 \rangle}$. The root mean square velocity is $u' \equiv \sqrt{(2/3) \int E(k) dk}$ and the integral length scale $\ell \equiv \pi/(2u'^2) \int E(k)/k dk$. Similarly, the spectrum, root mean square value and dissipation rate of the scalar field are: $E_T(k) \equiv \int_{\|\mathbf{k}\|=k} |\hat{T}(\mathbf{k})|^2 d\mathbf{k}/2$, $T' \equiv \sqrt{2 \int E_T(k) dk}$, $\chi_f \equiv 2\kappa \int k^2 E_T(k) dk$. The small scale temperature is determined by the viscosity and dissipation rate: $T_\eta \equiv \sqrt{\chi \tau_\eta}$. Since the Prandtl number is unitary the small scales of the scalar and the velocity field are of the same order.

larger Re $_\lambda$ in order to explore the behavior when there exists a well-defined inertial range in the flow.

In order to obtain deeper insight into the role of the two-way thermal coupling, we perform simulations with (denoted by S1) and without (denoted by S2) the thermal coupling. The particle parameters employed in the simulations are in table 5.2. The second order longitudinal structure functions of the particle velocity are shown in figure 5.1(b), for all the Stokes numbers investigated.

Particle phase volume fraction	ϕ	0.0004
Particle to fluid density ratio	ρ_p/ρ_0	1000
Particle back reaction	C_T	S1: included; S2: neglected.
Stokes number	St	0.5; 1; 3.
Thermal Stokes number	St_θ	0.2; 0.6; 1; 1.5; 2; 3; 4; 5; 6.
Number of particles	N_P	12500992; 4419584; 847872.

Table 5.2: Particles parameters in dimensionless code units. The Stokes number is $St \equiv \tau_p/\tau_\eta$ and thermal Stokes number $St_\theta \equiv \tau_\theta/\tau_\eta$ and the particle response times are defined in the text. In the simulations, St_θ is varied by varying the particle heat capacity. The different combinations of St and St_θ are simulated including the two-way thermal thermal coupling (simulations S1) and neglecting it (simulations S2).

5.2.3 Thermal coupling

In the two-way thermal coupling regime, the thermal energy contained in the fluid is finite with respect to the thermal energy of the particles, therefore, when heat flows from the fluid to the particle the fluid loses thermal energy at the particle position. Due to the point-mass approximation, the feedback from the particles on the fluid temperature field is a superposition of Dirac delta functions, centered on the particles. Hence the coupling term in equation (5.1c) is given by

$$C_T(\mathbf{x}, t) = \frac{4}{3}\pi \frac{\rho_p}{\rho_0} \frac{c_p}{c_0} r_p^3 \sum_{p=1}^{N_P} \frac{d\theta_p}{dt} \delta(\mathbf{x} - \mathbf{x}_p). \quad (5.4)$$

5.2.4 Validity and limitations of the model

The physical model in sections 5.2.1–5.2.3, is normally referred to as point-particle model. The two-way thermal coupling regime is considered, that is, the particles can affect the fluid temperature field while the direct particle-particle thermal interaction is neglected. Previous estimations [54] have shown that particle-particle interactions become relevant at average volume fractions ϕ exceeding 10^{-3} . In this work, the volume fraction lies in the two-way coupling regime and the average distance between particles exceeds the particle diameter by an order of magnitude. In our simulations $\phi = 4 \times 10^{-4}$, which is small enough to neglect particle collisions, but large enough for two-way momentum coupling between the particles and fluid to be important [53]. Nevertheless, we ignore two-way momentum coupling in the present study. The motivation is that including both two-way momentum and two-way thermal coupling introduces too many competing effects that would compound a thorough understanding of the problem. We therefore

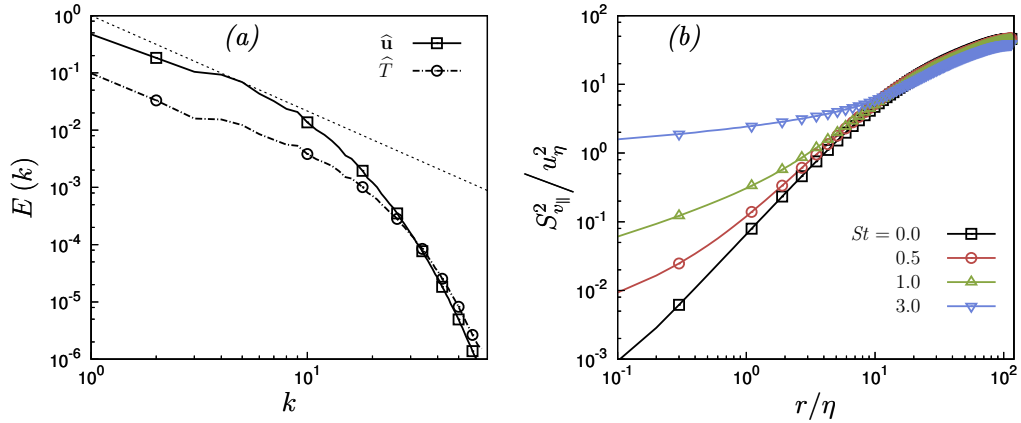


Figure 5.1: (a) Three-dimensional energy spectrum of the fluid velocity field (open squares) and temperature field (open circles). The temperature field is computed without any feedback from the particles on the fluid flow (simulations S2). (b) Second order longitudinal structure functions of the particle velocity for various Stokes numbers.

employ a reductionistic approach, seeking first to understand the role of two-way thermal coupling in the absence of momentum coupling, and then in a future study will explore their combined effects. Even aside from this methodological point, the results still have physical relevance since the thermal relaxation time is often larger than the momentum relaxation time in many particle-laden flows. For example, St_{θ}/St ranges from 2 to 6 for many liquid droplets in air (≈ 4 for water droplets in air). Therefore thermal feedback can be more relevant to the thermal balance than momentum feedback on momentum balance. This is confirmed by the analysis of the effect of momentum coupling and elastic collisions on the temperature statistics, presented in section 5.8. An additional set of simulations shows that, in the range of parameters considered in this work, both phenomena have a minimal effect.

The numerical solution of equations (5.1) and (5.3) is considered a Direct Numerical Simulation, insofar as that the Kolmogorov scale is resolved [103], even though the details of the flow near the surface of each particle are not resolved. This point-particle simplification is formally valid for particles which are smaller than the smallest active scale in the flow, the Kolmogorov microscale [147]. When the particle Reynolds number (based on the slip velocity between the particle and the local fluid) is small, the effect of the stresses on the particle can be described using a Stokes drag force [107]. Under an analogous set of conditions, the heat transfer between the particle and the fluid is a diffusive process, that has a timescale r_p^2/κ . For small point-like particles, this timescale is much smaller than the Kolmogorov time-scale, so that the heat transfer is a quasi-steady process which leads to the Newton-like equation for heat transfer in (5.4) [172, 8]. In this work, the ratio

between the particle radius r_p and the Kolmogorov scale η is well below 0.1 for $St = 0.5$ and $St = 1$ and about 0.1 at $St = 3$. Therefore finite size effects are negligible up to $St = 1$, while there may be small errors for $St = 3$. The impact of these small errors should be quantified in a future work using a more sophisticated model that resolves the flow around the particle surface. Also the fluid continuity equation should be in principle modified, due to the volume occupied by inertial particles. However, the error introduced in the continuity equation, proportional to the rate of change of the local volume fraction, is of the same order of the error introduced by other approximations in the model which are quite small.

In the point-mass Eulerian-Lagrangian here employed, the fluid temperature in equation (5.3c) should be understood as the temperature of the carrier fluid flow without the local effect of the disturbance due to the presence of the particles [13]. Neglecting this disturbance is justified for particles with a diameter much smaller than the Kolmogorov scale and much smaller than the grid spacing. In the case of two-way momentum coupling, the error introduced by neglecting the disturbance can be estimated to be less than 10% for the particle parameters we are considering [79]. A similar estimation is expected for the fluid temperature disturbance due to the particle, since the equations for the particle velocity and temperature are analogous. At the largest simulated Stokes number, $St = 3$, the same estimation indicates that an error of about 15% can be introduced. Therefore, the error is larger for this case, though certainly a sub-leading effect. Some simplified, efficient ways to compute the effect of the particle disturbance are available for the two-way momentum coupling [79], but equivalent models for the thermal coupling problem are not well developed or tested. Given this, and the fact that for our small particles the corrections due to the disturbance terms would be sub-leading, it is justified to neglect their effect as a first approximation for understanding this complex problem.

We also emphasize that the statistics of the fluid temperature field presented in this work refer to the carrier, resolved, temperature field, with the disturbance temperature field produced by the particles neglected. The actual (or total) temperature field is the superposition of the carrier temperature field and the disturbance induced by the particles. In the limit of large scale separation between the particle size and Kolmogorov scale and in the dilute regime, the disturbance field produced by the particle can be determined analytically and so the statistics of the actual temperature field can be reconstructed knowing the resolved carrier flow and the analytic solution for the particle temperature disturbance field. This aspect is discussed in section 5.9.

Summarizing, because of the marked scale separation between the particle size and the Kolmogorov scale, $r_p \ll \eta$, and low particle volume fraction, $\phi \ll 1$, which are the conditions explored in our study, the point-particle method provides a good first approximation to the complex problem under consideration. The statistics for the temperature field reported in this work refer to the carrier temperature field, in which the near-particle temperature changes are excluded, while the statistics of the

actual temperature field can be recovered a posteriori on the basis of the modelling hypothesis. Future work should explore the problem using methods where the flow around the particle is resolved, referred to as FRDNS (Fully Resolved DNS) [13, 69]. However, even with currently available High Performance Computational resources, FRDNS is limited to a small number of particles making it unfeasible at present to explore the problem of interest in this work [15].

5.2.5 Numerical method

We perform direct numerical simulation of incompressible, statistically steady and isotropic turbulence on a tri-periodic cubic domain. Equations (5.1a), (5.1b), and (5.1c) are solved by means of the pseudo-spectral Fourier method for the spatial discretization. The 3/2 rule is employed for dealiasing [23], so that the maximum resolved wavenumber is $k_{\max} = N/2$. The required Fourier transforms are executed in parallel using the P3DFFT library [118]. Forcing is applied to a single scale, that is to all wavevectors satisfying $\|\mathbf{k}\|^2 = k_f$, with $k_f = 2$, and the equations for the fluid velocity and temperature Fourier coefficients are evolved in time by means of a second order Runge-Kutta exponential integrator [76]. This method has been preferred to the standard integrating factor because of its higher accuracy and, above all, because of its consistency. Indeed, in order to obtain an accurate representation of small scale temperature fluctuations, it is critical that the numerical solution conserves thermal energy. The same time integration scheme is used to solve particle equations (5.3a), (5.3b) and (5.3c), thus providing overall consistency, since the system formed by fluid and particles is evolved in time as a whole.

The fluid velocity and temperature are interpolated at the particle position by means of fourth order B-spline interpolation. The interpolation is implemented as a backward Non-Uniform Fast Fourier Transform (NUFFT) with B-spline basis: the fluid field is projected onto the B-spline basis in Fourier space through a deconvolution, than transformed into the physical space by means of a inverse Fast Fourier Transform (FFT). A convolution provides the interpolated field at particle position [11]. Since B-splines have a compact support in physical space and deconvolution in Fourier space reduces to a division, this provide an efficient way to obtain high order interpolation. This guarantees smooth and accurate interpolation and its efficient implementation is suitable for pseudo-spectral methods [75]. The coupling term (5.4) has to be projected on the Cartesian grid used to represent the fields. This is performed by means of the forward Non-Uniform Fast Fourier Transform with B-spline basis [11]. Briefly, the algorithm works as follows [28]. The convolution of the distribution $C_T(\mathbf{x}, t)$ with the B-spline polynomial basis $B(\mathbf{x})$ is computed in physical space, so that it can be effectively represented on the Cartesian grid

$$\tilde{C}_T(\mathbf{x}, t) = C_T * B = \frac{4}{3}\pi \frac{\rho_p}{\rho_0} \frac{c_p}{c_0} r_p^3 \sum_{p=1}^{N_P} \frac{d\theta_p}{dt} B(\mathbf{x} - \mathbf{x}_p). \quad (5.5)$$

The smoothed field \tilde{C}_T is transformed by means of a FFT obtaining $\mathcal{F}[\tilde{C}_T]$ in Fourier space. Finally, the convolution with the B-spline is removed in Fourier space,

$$\hat{C}(\mathbf{k}, t) = \frac{\mathcal{F}[C_T * B]}{\mathcal{F}[B]} = \frac{\mathcal{F}[\tilde{C}_T]}{\mathcal{F}[B]}. \quad (5.6)$$

Since the convolution is removed in Fourier space, increasing the order of B-spline provides higher accuracy, without introducing non locality, even if the number of grid points influenced by each particle becomes larger in the preliminary convolution. A fourth order B-spline polynomial is employed in these simulations and a test with the same forcing, same parameters, with a larger resolution (256^3 Fourier modes) confirmed the grid-independence of the results. Also, the backward and forward transformations are symmetric, that guarantees energy conservation [139]. A detailed description and assessment of the NUFFT in the framework of particles in turbulence can be found in [28].

5.3 Characterization of the thermal dissipation rate

In the flow under consideration, the total dissipation rate of the temperature field χ is constant due to the forcing term f_T . The total dissipation has a contribution from the carrier fluid and particle phases and is given by

$$\chi = \kappa \langle \|\nabla T\|^2 \rangle + \frac{\phi}{\tau_\theta} \frac{\rho_p c_p}{\rho_0 c_0} \langle (T(\mathbf{x}_p, t) - \theta_p)^2 \rangle. \quad (5.7)$$

An analogous balance was derived for kinetic energy dissipation rate [139]. It is worth noting that, in practice, the sense of the bracket operator is not strictly the same for the two terms: one is computed as spatial and time average, while the other is computed as time average over the set of particles. We indicate with χ_f the dissipation due to the fluid temperature gradient and with χ_p the dissipation due to the particles, the two terms in the right hand side of equation (5.7), so that $\chi = \chi_f + \chi_p$. Note that both contributions to the dissipation rate are proportional to the kinematic thermal conductivity of the fluid since $\tau_\theta \propto 1/\kappa$, and hence both the dissipation mechanisms are due to molecular diffusivity. By inserting the definition of the particle thermal relaxation time into equation (5.7), it is possible to rewrite it as

$$\chi = \kappa \left[\langle \|\nabla T\|^2 \rangle + 3\phi \left\langle \left(\frac{T(\mathbf{x}_p, t) - \theta_p}{r_p} \right)^2 \right\rangle \right], \quad (5.8)$$

which evidences that the temperature disturbance induced by the particle has a lengthscale of the order of the particle radius.

The portion of temperature fluctuations dissipated by the two different mechanisms depends on the statistics of the differences between the particle and local carrier flow temperatures. In the limit $St_\theta \rightarrow 0$ we have $T(\mathbf{x}_p, t) = \theta_p$, such that all of the dissipation is associated with the fluid. In the general case, the statistics of $T(\mathbf{x}_p, t) - \theta_p$ depend not only on St_θ , but also implicitly upon St , with the statistics of $T(\mathbf{x}_p, t)$ depending on the spatial clustering of the particles. This coupling between the particle momentum and temperature dynamics can lead to non-trivial effects of particle inertia on χ_p . Physically, the overall dissipation rate of the temperature field is due to the gradients of the total temperature gradients, which is the superposition of the carrier temperature field and the near-particle temperature field, with the total temperature equal to the particle temperature at the particle surface. However, the point-particle model separates the dissipation rate due to the carrier, resolved, temperature field χ_f and the dissipation rate due to the suspended particles χ_p . This is allowed because of the marked scale separation between the smallest scale of the carrier field, that is the Kolmogorov scale η , and the scale of the gradients induced by the suspended particles, that is the particle size r_p , with $r_p \ll \eta$. This is detailed in section 5.9, in which the relation between the moments of the carrier temperature field gradient and the actual temperature field gradient is also discussed.

5.3.1 Thermal dissipation due to the carrier temperature gradients

Since the flow is isotropic, χ_f is given by

$$\chi_f = 3\kappa \langle (\partial_x T)^2 \rangle \quad (5.9)$$

We consider fixed Reynolds number and $Pr = 1$, thus κ is the same in all the presented simulations, and so $\langle (\partial_x T)^2 \rangle$ fully characterizes χ_f . Moreover, given the expected structure of the field $\partial_x T$, it is instructive to consider its full Probability Density Function (PDF), in addition to its moments in order to know how different regions of the flow contribute to the average dissipation rate χ_f .

Figure 5.2(a) shows the normalized PDFs of $\partial_x T$ for $St = 3$, for various St_θ , where the PDFs are normalized using the standard deviation of the distribution, $\sigma_{\partial_x T}$. The distribution is almost symmetric and it displays elongated exponential tails. The largest temperature gradients exceed the standard deviation by an order of magnitude [116]. Remarkably, the shape of the PDF shows a very weak dependence on St and St_θ , over all the considered range of these parameters, such that the PDF shape scales with $\sigma_{\partial_x T}$. Consistently, the kurtosis of the fluid temperature gradients distribution is approximately constant, which confirms that the fluid temperature gradient PDF is approximately self-similar.

The variance of the resolved fluid temperature gradient is proportional to the actual dissipation rate of the temperature fluctuation χ_f (the proportionality factor

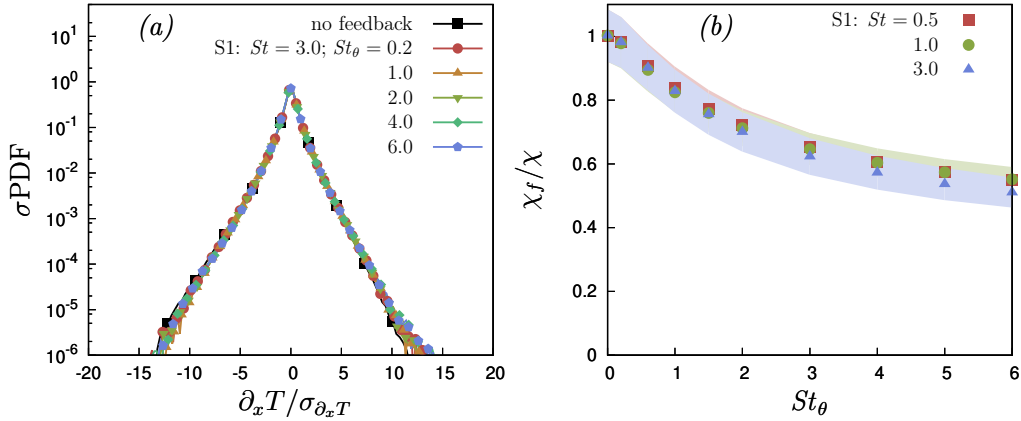


Figure 5.2: PDF of the carrier flow temperature gradient $\partial_x T$ from simulations S1, at $St = 3$, for various St_θ (a) and (b) dissipation rate, χ_f , of the fluid temperature fluctuations, for different St as a function of St_θ . The filled lines indicate the maximum deviations of the dissipation rate occurred in the time interval used to compute averages.

being 3κ , the same in all the simulations). In contrast to the PDF shape, the suspended particles have a strong impact on χ_f , as shown in figure 5.2. As St_θ is increased, χ_f decreases. However, this is mainly due to the fact that as St_θ is increased, χ_p increases, and so χ_f must decrease since $\chi = \chi_f + \chi_p$ is fixed. The influence of the Stokes number on χ_f is very small in the range of parameters considered.

5.3.2 Thermal dissipation due to the particle dynamics

The dissipation rate due to the particles, χ_p , depends on the difference between the particle temperature and the fluid temperature at the particle position,

$$\chi_p = 3\kappa\phi \left\langle \left(\frac{T(\mathbf{x}_p, t) - \theta_p}{r_p} \right)^2 \right\rangle. \quad (5.10)$$

For notational simplicity, we define $\varphi_p \equiv \sqrt{3\phi} (T(\mathbf{x}_p, t) - \theta_p) / r_p$. When φ_p is normalized by its standard deviation, we can relate this to the rate of change of the particle temperature using equation (5.3c)

$$\frac{\dot{\theta}_p}{\sigma_{\dot{\theta}_p}} = \frac{\varphi_p}{\sigma_{\varphi_p}}. \quad (5.11)$$

The normalized PDF of $\dot{\theta}_p$ for $St = 1$ and $St = 3$, and for various St_θ is shown in figure 5.3. Figure 5.3(a) shows the normalized PDF of $\dot{\theta}_p$, for $St = 1$ for the set of

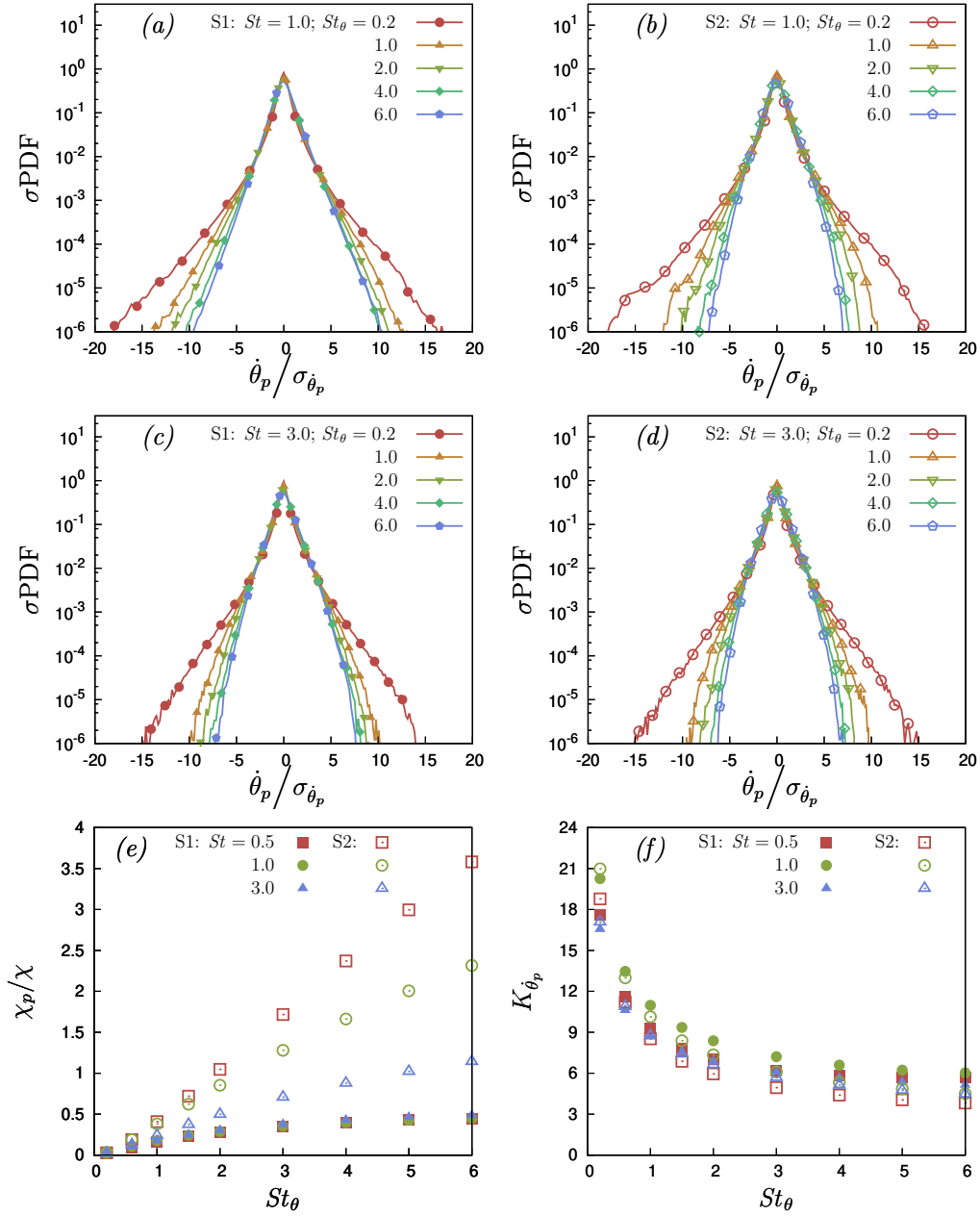


Figure 5.3: PDF of $\hat{\theta}_p$ for $St = 1$ (a-b) and $St = 3$ (c-d), and for various St_θ . Plots (a-c) are from simulations S1, in which the two-way thermal coupling is considered, while plots (b-d) are from simulations S2, in which the two-way coupling is neglected. (e) Dissipation rate χ_p of the temperature fluctuations due to the particles, for different St as a function of St_θ . (f) Kurtosis of the PDF of $\hat{\theta}_p$.

simulations S1, in which the two-way thermal coupling is taken to account. Figure 5.3(b) shows the corresponding results for simulations S2, in which the two-way

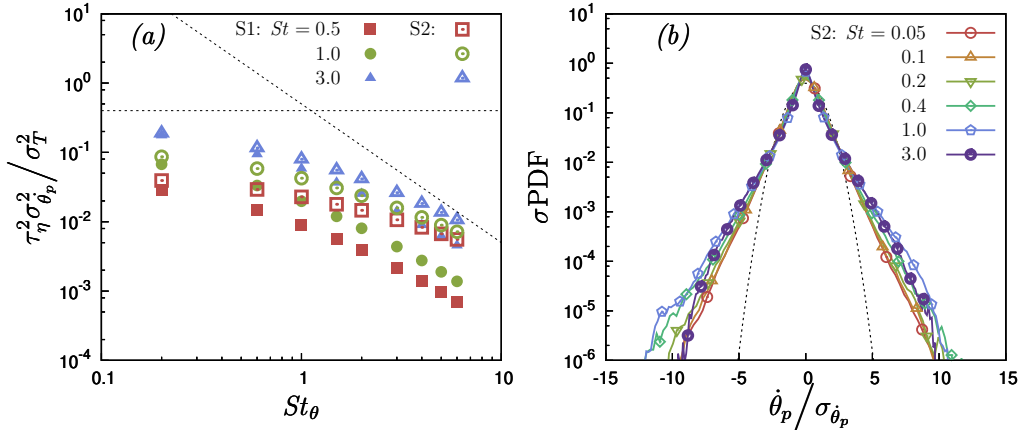


Figure 5.4: (a) Variance of the particle temperature rate of change as a function of the thermal Stokes number for different Stokes numbers. The dotted lines represent the expected asymptotic behaviour for $St_\theta \ll 1$ and $St_\theta \gg 1$. (b) Normalized PDF of the particle temperature rate of change, $\dot{\theta}_p$ at $St_\theta = 1$ for various Stokes number. The dotted line shows a Gaussian PDF for reference. Results obtained neglecting the particle thermal feedback.

thermal coupling is neglected. The normalized PDF of $\dot{\theta}_p$ for $St = 3$, with and without the two-way thermal coupling, is shown in figures 5.3(c-d).

In contrast to the fluid temperature gradient PDFs, the shape of the PDF of $\dot{\theta}_p$ is not self-similar with respect to its variance. As St_θ is increased, the normalized PDF becomes narrower. This is due to the fact that as St_θ is increased, the particles respond more slowly to changes in the fluid temperature field, analogous to the “filtering” effect for inertial particle velocities in turbulence [131, 81]. The PDF shapes are mildly affected by St , and for larger St_θ , extreme fluid temperature-particle temperature differences are suppressed when the two-way thermal coupling is neglected.

The variance of $\dot{\theta}_p$ is proportional to the particle dissipation rate χ_p ,

$$\langle \dot{\theta}_p^2 \rangle = \left\langle \frac{(T(\mathbf{x}_p, t) - \theta_p)^2}{\tau_\theta^2} \right\rangle = \frac{r_p^2 \chi_p}{3\kappa\phi\tau_\theta^2}, \quad (5.12)$$

and the results for this are shown in figure 5.3(e), for various St and St_θ , and for simulations S1 and S2. The results show that as St_θ is increased, χ_p increases. This is mainly because as St_θ is increased, the thermal time correlation of the particle increases, and the particle temperature depends strongly on its encounter with the fluid temperature field along its trajectory history for times up to $O(\tau_\theta)$ in the past. As a result, the particle temperature can differ strongly from the local carrier flow temperature. The results also show that χ_p is dramatically suppressed when two-way thermal coupling is accounted for. One reason for this is that as shown earlier,

two-way thermal coupling leads to a suppression in the fluid temperature gradients. As these gradients are suppressed, the fluid temperature along the particle trajectory history differs less from the local carrier flow temperature than it would have in the absence of two-way thermal coupling, and as a result χ_p is decreased.

The results for kurtosis of $\dot{\theta}_p$, as a function of St_θ and for various St are shown in figure 5.3(f). The results show that the kurtosis decreases with increasing St_θ . This is mainly due to the filtering effect mentioned earlier, wherein as St_θ is increased, the particles are less able to respond to rapid fluctuations in the fluid temperature along their trajectory. Further, the kurtosis is typically larger when the two-way thermal coupling is taken into account (simulations S1), and is maximum for $St = 1$. This is due to the particle clustering on the fronts of the fluid temperature field, as will be discussed in section 5.5.

Our results for the PDF of $\dot{\theta}_p$ and its moments differ somewhat from those in [8]. This is in part due to the difference in the forcing methods employed by [8] and that in our study. The solution of (5.3c) may be written as [8]

$$\langle \dot{\theta}_p^2 \rangle = \frac{1}{2\tau_\theta^3} \int_0^\infty \left\langle \left(\delta_t T_p(t) \right)^2 \right\rangle \exp\left(-\frac{t}{\tau_\theta}\right) dt, \quad (5.13)$$

where $\delta_t T_p(t) \equiv T(\mathbf{x}_p(t), t) - T(\mathbf{x}_p(0), 0)$. In the regime $St_\theta \ll 1$, the exponential in (5.13) decays very fast in time so that the main contribution to the integral comes from $\delta_t T_p$ for infinitesimal t , with $\delta_t T_p \sim t^n$ for $t \rightarrow 0$. Substituting $\delta_t T_p \sim t^n$ into (5.13) we obtain the leading order behavior

$$\langle \dot{\theta}_p^2 \rangle \sim \frac{1}{2\tau_\theta^3} \int_0^\infty t^{2n} \exp\left(-\frac{t}{\tau_\theta}\right) dt \sim St_\theta^{2n-2}, \quad St_\theta \ll 1. \quad (5.14)$$

[8] used a white in time forcing for the fluid scalar field, giving $n = 1/2$, and yielding $\langle \dot{\theta}_p^2 \rangle \sim St_\theta^{-1}$ for $St_\theta \ll 1$. However, the forcing scheme that we have employed generates a field $T(\mathbf{x}, t)$ that evolves smoothly in time, so $n = 1$ and $\langle \dot{\theta}_p^2 \rangle \sim \text{constant}$ for $St_\theta \ll 1$.

For $St_\theta \gg 1$, the integral in (5.13) is dominated by uncorrelated temperature increments, $\delta_t T \sim t^0$, such that $\langle \dot{\theta}_p^2 \rangle \sim St_\theta^{-2}$. The comparison between figure 5.4(a) and figure 5 of [8] highlights the different asymptotic behavior of $\sigma_{\dot{\theta}_p}^2 \equiv \langle \dot{\theta}_p^2 \rangle$ for $St_\theta \ll 1$, but the same behavior $\langle \dot{\theta}_p^2 \rangle \sim St_\theta^{-2}$ for $St_\theta \gg 1$. Further, as expected, our DNS data approaches these asymptotic regimes for both the cases with and without two-way thermal coupling.

Another difference is that in the results of [8], the tails of the PDFs of $\dot{\theta}_p$ for $St_\theta = 1$ become heavier as St is increased, whereas our results in figure 5.3 show that while the kurtosis of these PDFs increases from $St = 0.5$ to $St = 1$, it then decreases from $St = 1$ to $St = 3$. In order to examine this further, we performed simulations (without two-way thermal coupling) for $St_\theta = 1$ and $St \leq 0.4$. The

results are shown in figure 5.4(b), and in this regime we do in fact observe that the tails of the PDFs of $\dot{\theta}_p$ become increasingly wider as St is increased. Taken together with the results in figure 5.3, this implies that in our simulations, the tails of the PDFs of $\dot{\theta}_p$ become increasingly wider as St is increased until $St \approx 1$, where this behavior then saturates, and upon further increase of St the tails start to narrow. This non-monotonic behavior is due to the particle clustering in the fronts of the temperature field, which is strongest for $St \approx 1$ (see §5.5). While the results in [8] over the range $St \leq 3.7$ do not show the tails of the PDFs of $\dot{\theta}_p$ becoming narrower, their results clearly show that the widening of the tails saturates (see inset of figure 5 in [8]). It is possible that if they had considered larger St , they would have also began to observe a narrowing of the tails as St was further increased. Possible reasons why the widening of the tails saturates at a lower value of St in our DNS than it does in theirs include is the effect of Reynolds number ($Re_\lambda = 315$ in their DNS, whereas in our DNS $Re_\lambda = 88$), and differences in the scalar forcing method. This raises the question about Reynolds number dependency. We expect that the strong intermittency of advected passive scalars in high Reynolds number flows may affect the results quantitatively. However, two-way coupled simulations at higher Reynolds numbers are computationally demanding and are left for a future work.

5.4 Characterization of the temperature fluctuations

This section consists of a short overview of the one-point temperature statistics. Note that due to the large scale forcing used in the DNS, the one-point statistics of the flow can be affected by the forcing method employed [46]. The deterministic forcing may also generate some long standing patterns at large scales. However, the analyzed configuration allows to fix the same average dissipation rate of temperature and velocity fluctuations for all the Stokes numbers considered, which provides considerable advantages for the interpretation of the results.

The statistics of the carrier temperature field, in which the near-particle disturbances are excluded, are presented in this section. As discussed in section 5.9, the one-point statistics of the carrier temperature field are very close to the one-point statistics of the actual fluid temperature field in the dilute regime.

5.4.1 Fluctuations of the carrier temperature field

Figures 5.5(a-b) show the normalized one-point PDF of the carrier flow temperature for $St = 1$ and $St = 3$, respectively, and for various St_θ . The PDFs are normalized with the standard deviation of the distribution σ_T . The PDFs are almost Gaussian for low St_θ , while the tails become wider as St_θ is increased. However, we are unable to explain the cause of this enhanced non-Gaussianity. The temperature PDFs are also not symmetric, and display a bump in the right tail. This behavior

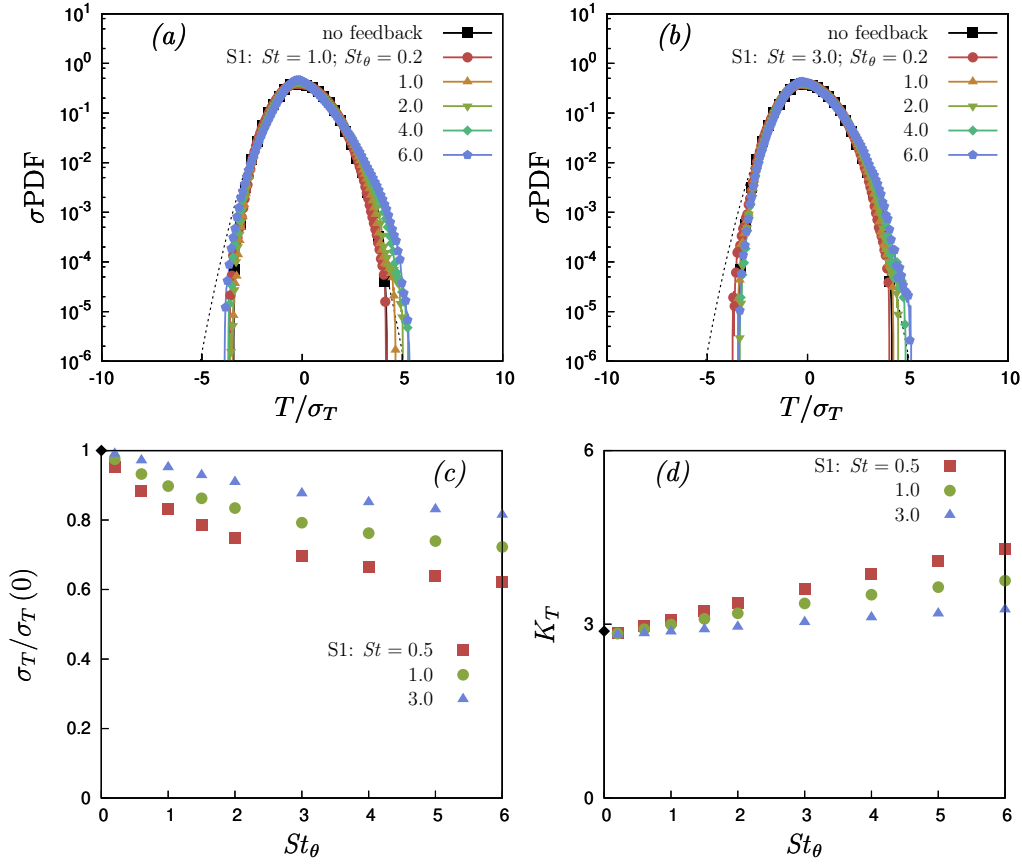


Figure 5.5: PDF of the carrier flow temperature for $St = 1$ (a) and $St = 3$ (b), and for various St_θ . (c) Variance of the carrier flow temperature fluctuations for different St as a function of St_θ . (d) Kurtosis of the carrier flow temperature PDF. These results are from simulations S1 in which the two-way thermal coupling is considered.

was also reported by [116] for the case without particles, and it appears to be a low Reynolds number effect that is also dependent on the forcing method employed.

The effect of St on σ_T is striking, whereas we saw earlier in figure 5.2(c) that χ_f only weakly depends on St . To explain the dependence upon the Stokes number we note that the energy balance (5.8) can be rewritten as

$$\chi = \kappa \left[\langle \|\nabla T\|^2 \rangle + \frac{2}{3} \frac{\phi}{\eta^2} \frac{\rho_p}{\rho_0} \frac{1}{St} \langle (T(\mathbf{x}_p, t) - \theta_p)^2 \rangle \right]. \quad (5.15)$$

The factor $\phi\rho_p/(\rho_0\eta^2)$ is constant in our simulations. Therefore, since our DNS data suggest that χ_f is a function of St_θ only (see figure 5.2(c)), from (5.15) and (5.3c) we obtain

$$\langle T(\mathbf{x}_p, t)^2 \rangle - \langle \theta_p^2 \rangle \propto St f(St_\theta). \quad (5.16)$$

The kurtosis of the fluid temperature fluctuation is shown in figure 5.5(d), as a function of St_θ and for various St . For small St_θ , the kurtosis of the fluid temperature fluctuation is close to the value for a Gaussian PDF, namely 3. However, as St_θ is increased, the kurtosis increases. Furthermore, the kurtosis decreases with increasing St for the range considered in our simulations. The explanation of these trends in the kurtosis is unclear.

5.4.2 Particle temperature fluctuations

Figures 5.6(a-b) show the normalized one-point PDF of the particle temperature with $St = 1$, for various St_θ , and for simulations S1 and S2. Figures 5.6(c-d) show the corresponding results for $St = 3$, and the PDFs are normalized by their standard deviations. When the two-way thermal coupling is accounted for, the tails of the particle temperature distribution tend to become wider as St_θ is increased. On the other hand, when the two-way coupling is neglected, the PDF of the particle temperature is very close to Gaussian, and its shape is not sensitive to either St or St_θ .

The variance of the particle temperature fluctuations monotonically decrease with increasing St_θ , as shown in figure 5.6(e). The results also show a strong dependence on St , but most interestingly, the dependence on St is the opposite for the cases with and without two-way coupling. To understand this we note that using the formal solution to the equation for $\theta_p(t)$ (ignoring initial conditions) we may construct the result

$$\langle \theta_p^2(t) \rangle = \frac{1}{\tau_\theta^2} \int_0^t \int_0^t \langle T(\mathbf{x}_p(s), s) T(\mathbf{x}_p(s'), s') \rangle e^{-(2t-s-s')/\tau_\theta} ds ds'. \quad (5.17)$$

If we now substitute into this the exponential approximation

$$\langle T(\mathbf{x}_p(s), s) T(\mathbf{x}_p(s'), s') \rangle \approx \langle T^2(\mathbf{x}_p(t), t) \rangle \exp[-|s - s'|/\tau_T],$$

where τ_T is the timescale of $T(\mathbf{x}_p(t), t)$, then we obtain

$$\langle \theta_p^2(t) \rangle = \frac{\langle T^2(\mathbf{x}_p(t), t) \rangle}{1 + \tau_\theta/\tau_T}. \quad (5.18)$$

This result reveals that the particle temperature variance is influenced by St in two ways. First, $\langle T^2(\mathbf{x}_p(t), t) \rangle$ depends upon the spatial clustering of the inertial particles, and this depends essentially upon St . Second, the timescale τ_T is the timescale of the fluid temperature field measured along the inertial particle trajectories, and hence depends upon St . For isotropic turbulence, this timescale is expected to decrease as St is increased, which would lead to $\langle \theta_p^2(t) \rangle$ decreasing as St increases, which is the behavior observed in figure 5.6(e). In the presence of

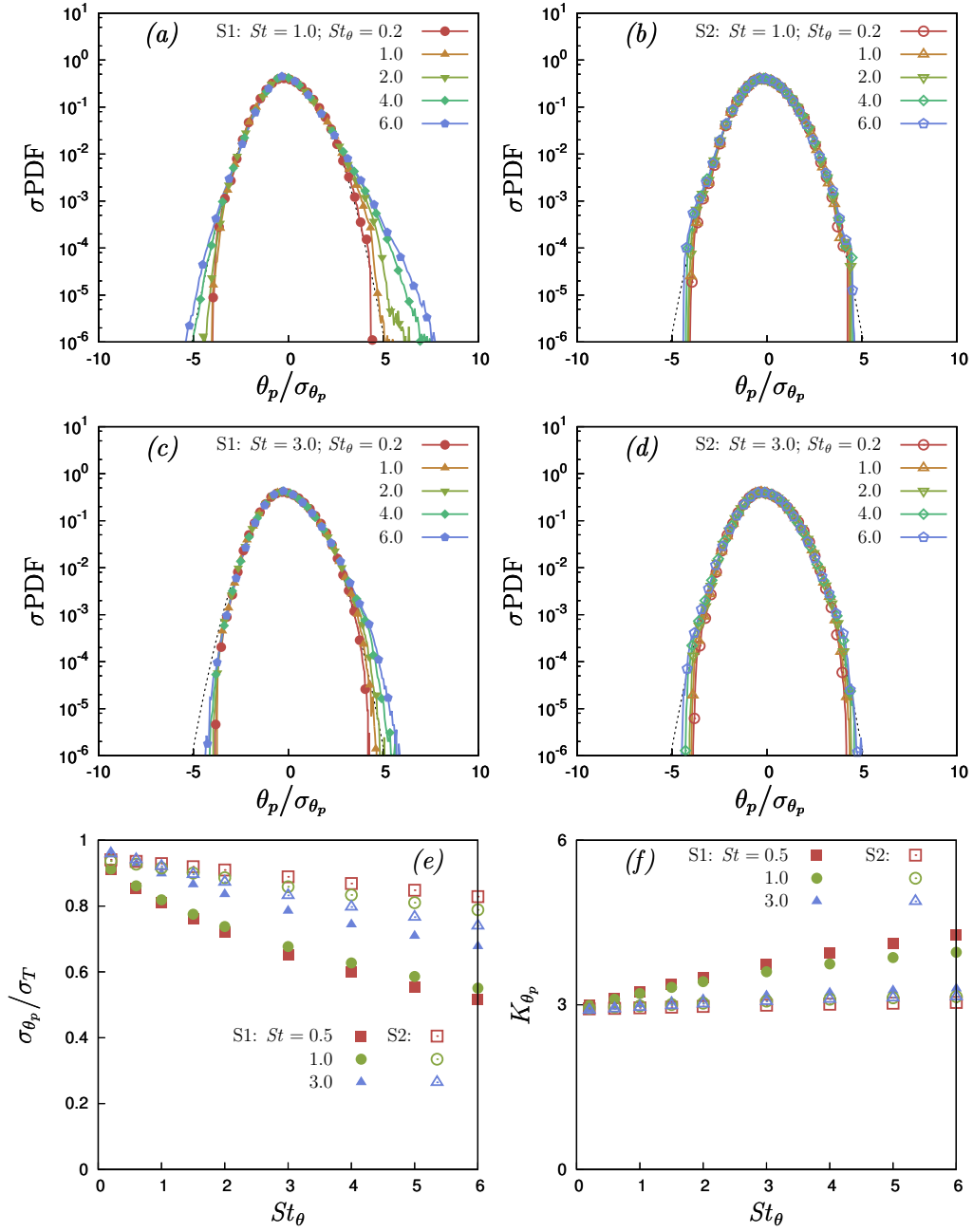


Figure 5.6: PDF of the particle temperature for $St = 1$ (a-b) and $St = 3$ (c-d), for various St_θ . Plots (a-c) are from simulations S1, in which the two-way thermal coupling is considered, while plots (b-d) are from simulations S2, in which the two-way coupling is neglected. (e) Variance of the particle temperature fluctuations for different St numbers as a function of St_θ . (f) Kurtosis of the particle temperature distribution.

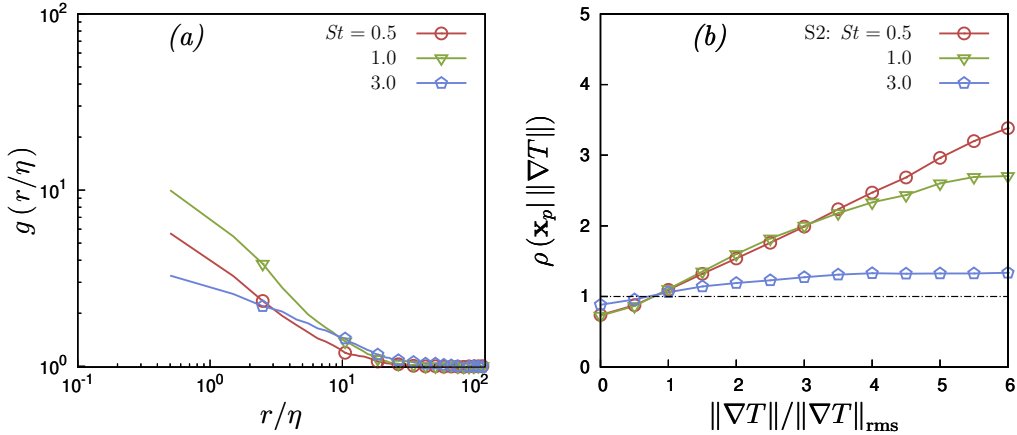


Figure 5.7: (a) Radial distribution function (RDF) as a function of the separation r/η for various St . (b) Particle number density conditioned on the magnitude of the fluid temperature gradient at the particle position, for various St . These results are from simulations S2, in which the two-way thermal coupling is neglected.

two-way coupling, however, $\langle T^2(\mathbf{x}, t) \rangle$ increases with increasing St , as shown earlier. In the two-way coupled regime this increase in $\langle T^2(\mathbf{x}, t) \rangle$ leads to an increase in $\langle T^2(\mathbf{x}_p(t), t) \rangle$ that dominates over the decrease of τ_T with increasing St , and as a result $\langle \theta_p^2(t) \rangle$ increases with increasing St .

The kurtosis of the particle temperature increases with increasing St_θ when the two-way thermal coupling is accounted for, as shown in figure 5.6(f) (simulations S1, filled symbols). Conversely, the kurtosis of the particle temperature remains constant as St_θ is increased when the two-way thermal coupling is ignored (simulations S2, open symbols).

5.5 Statistics conditioned on the local carrier flow temperature gradients

In this section we consider additional quantities to obtain deeper insight into the one-point particle to fluid heat flux. In particular, we explore the relationship between this heat flux and the local carrier flow temperature gradients.

5.5.1 Particle clustering on the temperature fronts

It is well known that inertial particles in turbulence form clusters [9], which may be quantified using the radial distribution function (RDF). As shown in figure 5.7(a), the particle number density in our simulations at small separations is an order of magnitude larger than the mean density when $St = O(1)$. [8] showed that inertial particles also exhibit a tendency to preferentially cluster in the fluid temperature

fronts where the temperature gradients are large. To demonstrate this, they measured the temperature dissipation rate at the particle positions and showed that this was higher than the Eulerian dissipation rate of the fluid temperature fluctuations. Note that previous works ([68, 69]) have shown that the radial distribution function can be reduced by momentum coupling, which we are neglecting. A future work that includes two-way momentum coupling should consider how this affects the way inertial particles sample high temperature gradients in the flow.

We quantify the tendency for inertial particles to cluster in the fluid temperature fronts by computing the single particle position probability density, conditioned upon the norm of the fluid temperature gradient:

$$\rho(\mathbf{x}_p | \|\nabla T\|) = \frac{\rho(\|\nabla T\|(\mathbf{x}_p))}{\rho(\|\nabla T\|)} \quad (5.19)$$

This conditioned probability can also be understood as the ratio between the fraction of inertial particles $n_p(\text{St}; \|\nabla T\|)$ located in a region of a given temperature gradient magnitude $\|\nabla T\|$ and the number of particles $n_p(0; \|\nabla T\|)$ which would be located in the same region for $\text{St} \rightarrow 0$, that is, when particles follow fluid trajectories:

$$\rho(\mathbf{x}_p | \|\nabla T\|) = \frac{n_p(\text{St}; \|\nabla T\|)}{n_p(0; \|\nabla T\|)}. \quad (5.20)$$

By defining $\|\nabla T\|_{\text{rms}}$ as the rms value of $\|\nabla T\|$, small values of $\|\nabla T\|/\|\nabla T\|_{\text{rms}}$ may be interpreted as corresponding to the large scales, and are associated with the Lagrangian coherent structures in which the temperature field is almost constant. Large values of $\|\nabla T\|/\|\nabla T\|_{\text{rms}}$ may be interpreted as corresponding to the small scales, and are associated with fronts in the fluid temperature field. The results for $\rho(\mathbf{x}_p | \|\nabla T\|)$ are shown in figure 5.7(b), for the simulations without two-way thermal coupling (the results show only a weak dependence on St_θ when the two-way coupling is included). Due to the clustering on the temperature fronts, $\rho(\mathbf{x}_p | \|\nabla T\|)$ is an increasing function of $\|\nabla T\|$ and it is larger than unity in the region of large temperature gradient. The probability to observe a gradient of a certain magnitude (which is proportional to $n_p(0; \|\nabla T\|)$) decays almost exponentially with increasing $\|\nabla T\|$, as in figure 5.2(a). For values of St at which the maximum particle clustering takes place, $n_p(\text{St}; \|\nabla T\|)$ is up to four times larger than $n_p(0; \|\nabla T\|)$ in regions of strong temperature gradients. We expect even higher values at the largest $\|\nabla T\|$, however it is difficult to obtain statistically relevant results in correspondence of such extreme events. These results therefore support the conclusions of [8] that inertial particles preferentially cluster in the fronts of the fluid temperature field where $\|\nabla T\|/\|\nabla T\|_{\text{rms}}$ is large.

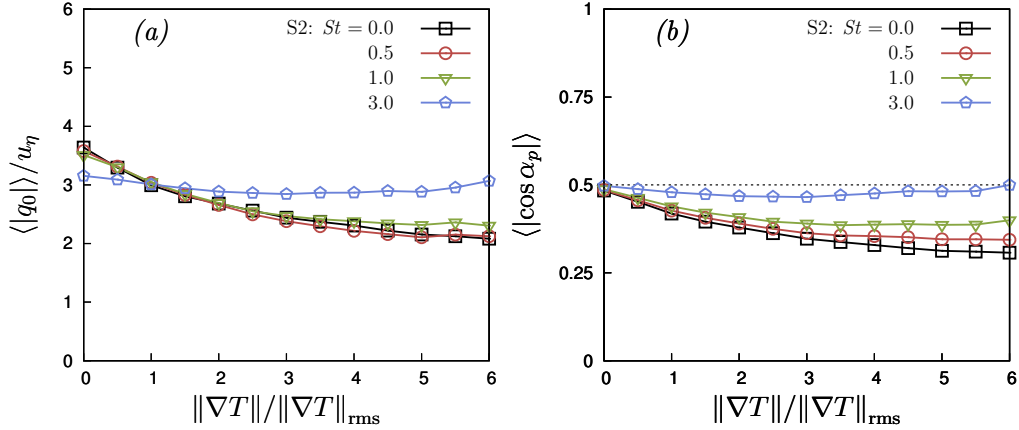


Figure 5.8: (a) Results for $\langle |q_0(\|\nabla T\|) \rangle / u_\eta$, for various St . (b) Results for $\langle |\cos \alpha_p| \rangle$ as a function of $\|\nabla T\|$, for various St . These results are from simulations S2, in which the two-way thermal coupling is neglected.

5.5.2 Particle motion across the temperature fronts

To obtain further insight into the thermal coupling between the particles and fluid we consider the properties of the particle heat flux conditioned on $\|\nabla T\|$. In particular, we consider the following quantity

$$q_n(\|\nabla T\|) \equiv (T(\mathbf{x}_p) - \theta_p)^n \mathbf{v}_p \cdot \mathbf{n}_T(\mathbf{x}_p) \Big|_{\|\nabla T\|}, \quad (5.21)$$

where \mathbf{n}_T is the normalized, resolved, temperature gradient

$$\mathbf{n}_T(\mathbf{x}_p) \equiv \frac{\nabla T(\mathbf{x}_p)}{\|\nabla T(\mathbf{x}_p)\|}. \quad (5.22)$$

The statistics of q_n provide a way to quantify the relationship between the particle heat flux and the local carrier temperature gradients in the fluid. Understanding this relationship is key to understanding how the particles modify the properties of the fluid temperature and temperature gradient fields. It is justified to investigate the interaction between the resolved temperature field, in which the near-particle disturbances are not represented, since, in the dilute regime, particles are statistically far enough that a particle rarely finds itself in the disturbance region of another particle. As discussed in section 5.9, the norm of the gradient of the perturbation field induced by the particle is proportional to r_p^{-2} and, therefore, it is usually large.

The efficiency with which the particles cross the fronts in the carrier flow temperature field is quantified by $\langle |q_0| \rangle$, and our results for this quantity in one-way coupled simulations are shown in figure 5.8(a). The curves are normalized with the Kolmogorov velocity scale u_η . At moderate Stokes number, particles tend to

accumulate near the front, therefore they cross the front with a small velocity. On the other hand, particles with large inertia slowly respond to a change of the local velocity/temperature and therefore they are less affected by the local value of the temperature gradient, carrying large temperature increments across the temperature field. Accordingly, the velocity magnitude becomes nearly independent of the local value of the temperature gradient as the particle inertia is increased, as shown in figure 5.8.

It is also important to consider whether the reduction of $\langle |q_0| \rangle$ as $\|\nabla T\|$ increases is due to the reduction of the norm of the particle velocity or to the lack of alignment between the particle velocity and the fluid temperature gradient at the particle position. Figure 5.8(b) displays the average of the absolute value of the cosine of the angle between the particle velocity and temperature gradient

$$\cos \alpha_p \equiv \frac{\mathbf{v}_p}{\|\mathbf{v}_p\|} \cdot \frac{\nabla T(\mathbf{x}_p)}{\|\nabla T(\mathbf{x}_p)\|}, \quad (5.23)$$

conditioned on $\|\nabla T\|$. The results show that as $\|\nabla T\|$ is increased, the particle motion becomes misaligned with the local carrier flow temperature gradient. This then shows that the reduction of $\langle |q_0| \rangle$ as $\|\nabla T\|$ increases is due to non-trivial statistical geometry in the system. The results also show that as St is increased, the cosine of the angle between the fluid temperature gradient and the particle velocity becomes almost independent of $\|\nabla T\|$, and $\langle |\cos \alpha_p| \rangle \approx 1/2$, the value corresponding to $\cos \alpha_p$ being a uniform random variable. This shows that as St is increased, the correlation between the direction of the particle velocity and the local carrier fluid velocity gradient vanishes.

5.5.3 Heat flux due to the particle motion across the fronts

We now turn to consider the quantity $\langle q_1 \rangle$. When the particle moves from a cold to a warm region of the fluid, the component of the particle velocity along the temperature gradient is positive, $\mathbf{v}_p \cdot \mathbf{n}_T(\mathbf{x}_p) > 0$. If the particle is also cooler than the local fluid so that $T(\mathbf{x}_p) - \theta_p > 0$, then as it moves into the region where the fluid is warmer, $q_1 > 0$ meaning that the particle will absorb heat from the fluid, and will therefore tend to reduce the local fluid temperature gradient. When the particle moves from a warm to a cold region of the flow, if $T(\mathbf{x}_p) - \theta_p < 0$ then q_1 is also positive, so that again the particle will act to reduce the local temperature gradient in the fluid. Therefore, $q_1 > 0$ indicates that the action of the inertial particles is to smooth out the fluid temperature field, reducing the magnitude of its temperature gradients, and $q_1 < 0$ implies the particles enhance the temperature gradients.

The results for $\langle q_1 \rangle$ are shown in figure 5.9 for various St and St_θ , including (simulations S1) and neglecting (simulations S2) the two-way thermal coupling. On average we observe $\langle q_1 \rangle \geq 0$, such that the particles tend to make the fluid temperature

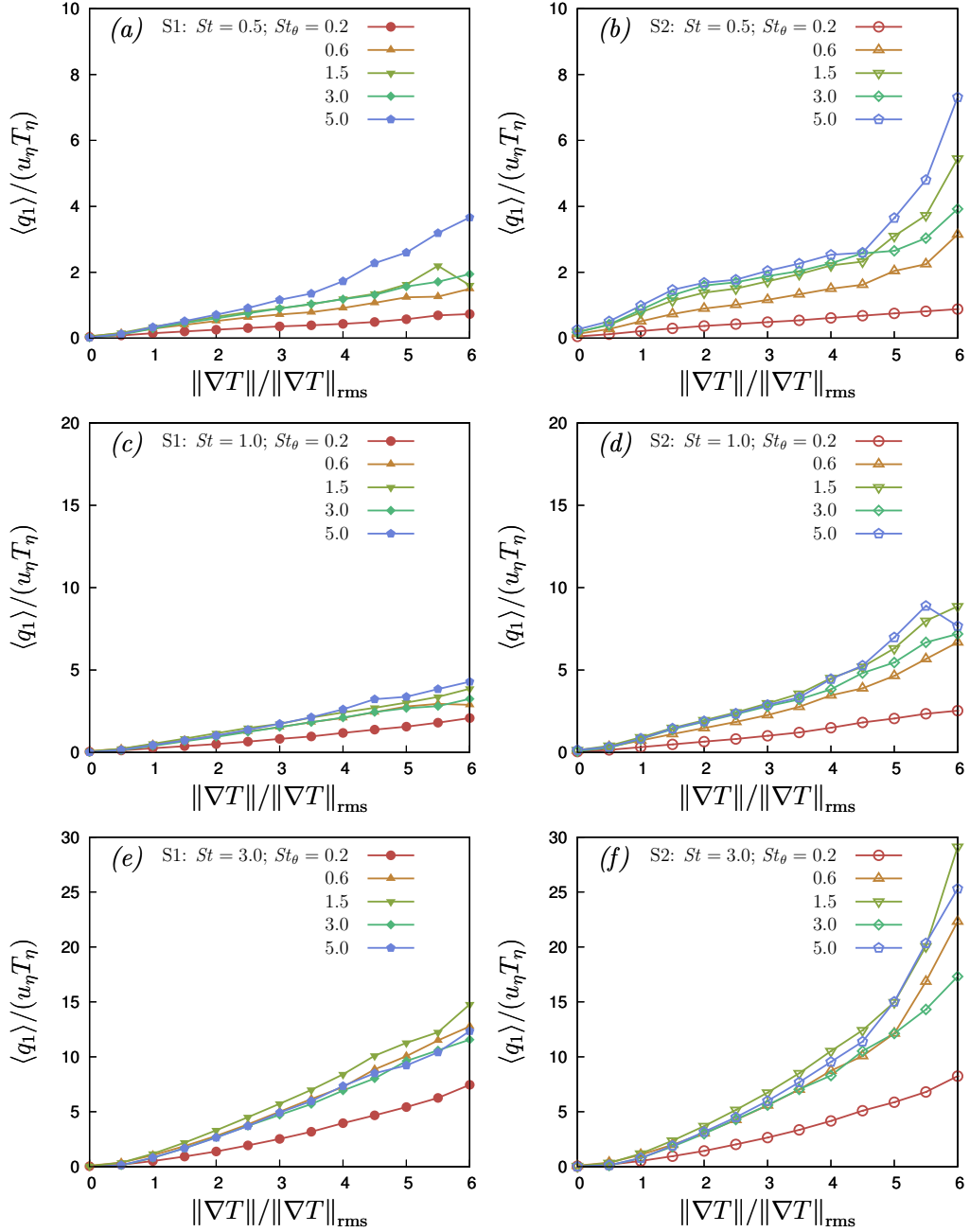


Figure 5.9: Results for $\langle q_1(\|\nabla T\|) \rangle / (u_\eta T_\eta)$ for $St = 0.5$ (a-b), $St = 1$ (c-d) and $St = 3$ (e-f), and for various St_θ . Plots (a-c-e) are from simulations S1, in which the two-way thermal coupling is considered, while plots (b-d-f) are from simulations S2, in which the two-way coupling is neglected.

field more uniform. The results show that $\langle q_1 \rangle$ tends to zero as $\|\nabla T\| \rightarrow 0$. This

indicates that the particles spend enough time in the Lagrangian coherent structures to adjust to the temperature of the fluid. However, $\langle q_1 \rangle$ increases significantly as $\|\nabla T\|$ increases, suggesting that inertial particles can carry large temperature differences across the fronts. In the limit $St_\theta \rightarrow 0$, $\langle q_1 \rangle \rightarrow 0$ reflecting the thermal equilibrium between the particles and the fluid. As St_θ is increased, the heat-flux becomes finite, however, if St_θ is too large, the particle temperature decorrelates from the fluid temperature and the heat exchange is not effective. Hence, $\langle q_1 \rangle$ can saturate with increasing St_θ . The results show that $\langle q_1 \rangle$ increases with increasing St , associated with the decoupling of \mathbf{v}_p and $\mathbf{n}_T(\mathbf{x}_p)$ discussed earlier. Finally, the results also show that two-way thermal coupling reduces $\langle q_1 \rangle$. This is simply a reflection of the fact that since the particles tend to smooth out the fluid temperature gradients, the disequilibrium between the particle and local fluid temperature is reduced, which in turn reduces the heat flux due to the particles.

5.6 Temperature structure functions

We now turn to consider two-point quantities in order to understand how the two-way thermal coupling affects the system at the small scales.

5.6.1 Structure functions of the carrier temperature field

The n -th order structure function of the resolved fluid temperature field is defined as

$$S_T^n(r) \equiv \langle |\Delta T(r, t)|^n \rangle \quad (5.24)$$

where $\Delta T(r, t)$ is the difference in the carrier temperature field at two points separated by the distance r (the “temperature increment”). The results for S_T^2 , with different St and St_θ are shown in figure 5.10. The structure functions of the actual temperature field differ from the structure functions of the carrier temperature field, due to the near-particle temperature disturbances. As discussed in section 5.9, the impact of the local near-particle perturbation is marked at small separation and the carrier flow temperature field can be understood as the actual temperature field filtered at the grid resolution scale. In order to emphasize this fact, the carrier flow temperature structure functions are reported only down to the Kolmogorov scale, which is comparable to the grid spacing.

The results show that S_T^2 decreases monotonically with increasing St_θ at all scales when the two-way thermal coupling is taken to account. In the dissipation range, S_T^2 is directly connected to the dissipation rate, and is suppressed in the same way for the three different St considered. Conversely, the suppression of the large scale fluctuations is stronger as St is reduced, at least for the range of St considered here.

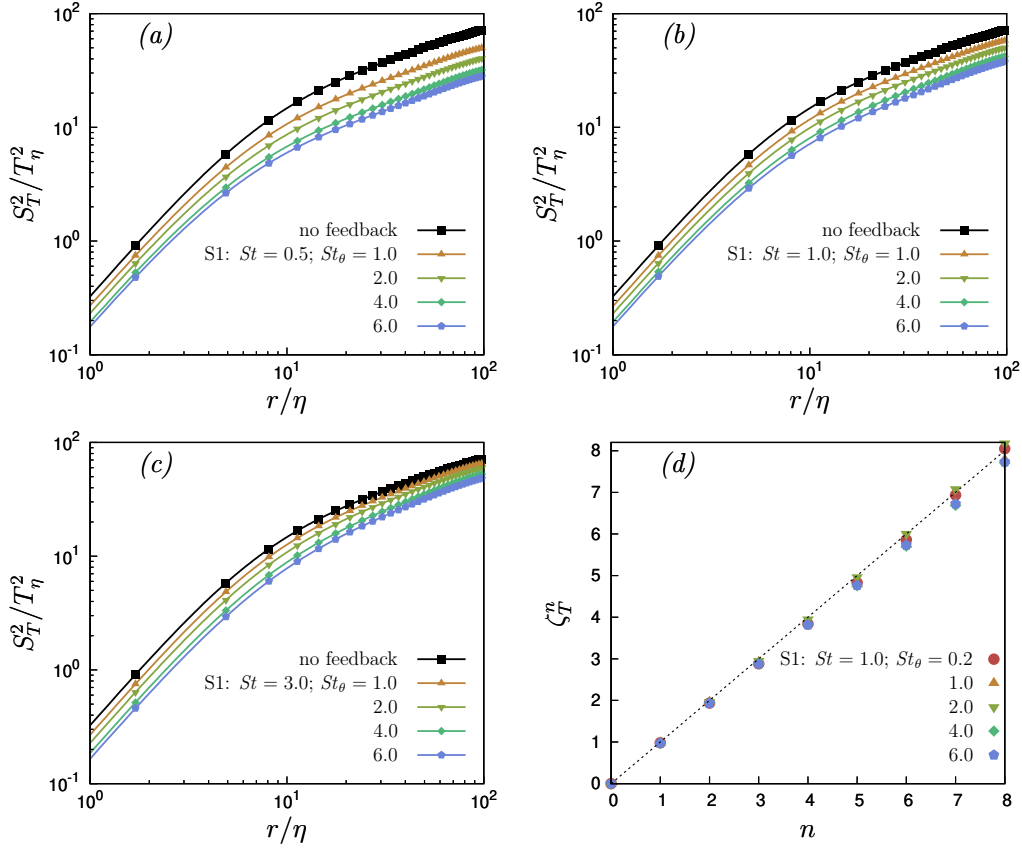


Figure 5.10: Results for S_T^2 for different St_θ , for $St = 0.5$ (a), $St = 1$ (b) and $St = 3$ (c). (d) Scaling exponents of the fluid temperature structure functions at small separation, $r \leq 2\eta$, at $St = 1$. The data is from simulations S1 in which the two-way thermal coupling is considered.

The scaling exponents of the structure functions of the carrier temperature field

$$\zeta_T^n \equiv \frac{d \log S_T^n(r)}{d \log r} \quad (5.25)$$

are shown in figure 5.10(d) for $r \leq 2\eta$. The results show that the resolved fluid temperature field remains smooth (to within numerical uncertainty) even when inertial particles are suspended in the flow.

5.6.2 Particle temperature structure functions

The n -th order structure function of the particle temperature $\theta_p(t)$ is defined as

$$S_\theta^n(r) \equiv \langle |\Delta \theta_p|^n \rangle_r \quad (5.26)$$

where $\Delta\theta_p(t)$ is the difference in the temperature of the two particles, and the brackets denote an ensemble average, conditioned on the two particles having separation r . The results for S_θ^2 for different St and St_θ , with and without two-way thermal coupling, are shown in figure 5.11.

The results show that S_θ^2 depends on St_θ in much the same way as the inertial particle relative velocity structure functions depend on St [81]. This is not surprising since the equation governing $\dot{\theta}_p$ is structurally identical to the equation governing the particle acceleration. However, important differences are that $\dot{\theta}_p$ depends on both St and St_θ , and also that the fluid temperature field is structurally different from the fluid velocity field, with the temperature field exhibiting the well-known ramp-cliff structure.

To obtain further insight into the behavior of S_θ^2 and S_θ^n in general, we note that the formal solution for $\Delta\theta_p(t)$ is given by (ignoring initial conditions)

$$\Delta\theta_p(t) = \frac{1}{\tau_\theta} \int_0^t \Delta T(\mathbf{x}_p(s), \mathbf{r}_p(s), s) \exp\left(-\frac{t-s}{\tau_\theta}\right) ds, \quad (5.27)$$

where $\Delta T(\mathbf{x}_p(s), \mathbf{r}_p(s), s)$ is the difference in the fluid temperature at the two particle positions $\mathbf{x}_p(s)$ and $\mathbf{x}_p(s) + \mathbf{r}_p(s)$. Equation (5.27) shows that $\Delta\theta_p(t)$ depends upon ΔT along the path-history of the particles, and $\Delta\theta_p(t)$ is therefore a non-local quantity. The role of the path-history increases as St_θ is increased since the exponential kernel in the convolution integral decays more slowly as τ_θ is increased. Since the statistics of ΔT increase with increasing separation, particle-pairs at small separations are able to be influenced by larger values of ΔT along their path-history, such that $\Delta\theta_p(t)$ can significantly exceed the local fluid temperature increment $\Delta T(\mathbf{x}_p(t), \mathbf{r}_p(t), t)$. This then causes S_θ^2 to increase with increasing St_θ , as shown in figure 5.11. This effect is directly analogous to the phenomena of caustics that occur in the relative velocity distributions of inertial particles at the small scales of turbulence [165], and which occur because the inertial particle relative velocities depend non-locally on the fluid velocity increments experienced along their trajectory history [19]. In analogy, we may therefore refer to the effect as “thermal caustics”, and they may be of particular importance for particle-laden turbulent flows where particles in close proximity thermally interact.

The results in figure 5.11 also reveal a strong effect of St , and one way that St affects these results is through the spatial clustering and preferential sampling of the fluid temperature field by the inertial particles. There is, however, another mechanism through which St can affect S_θ^2 . In particular, since, due to caustics, the relative velocity of the particles increases with increasing St at the small scales, then the values of $\Delta T(\mathbf{x}_p(s), \mathbf{r}_p(s), s)$ that may contribute to $\Delta\theta_p(t)$ become larger. This follows since if their relative velocities are larger, then over the time span $t-s \leq O(\tau_\eta)$ the particle-pair can come from even larger scales where (statistically) $\Delta T(\mathbf{x}_p(s), \mathbf{r}_p(s), s)$ is bigger. This effect would cause S_θ^2 to increase with St for a given St_θ , further enhancing the thermal caustics, which is exactly what is observed

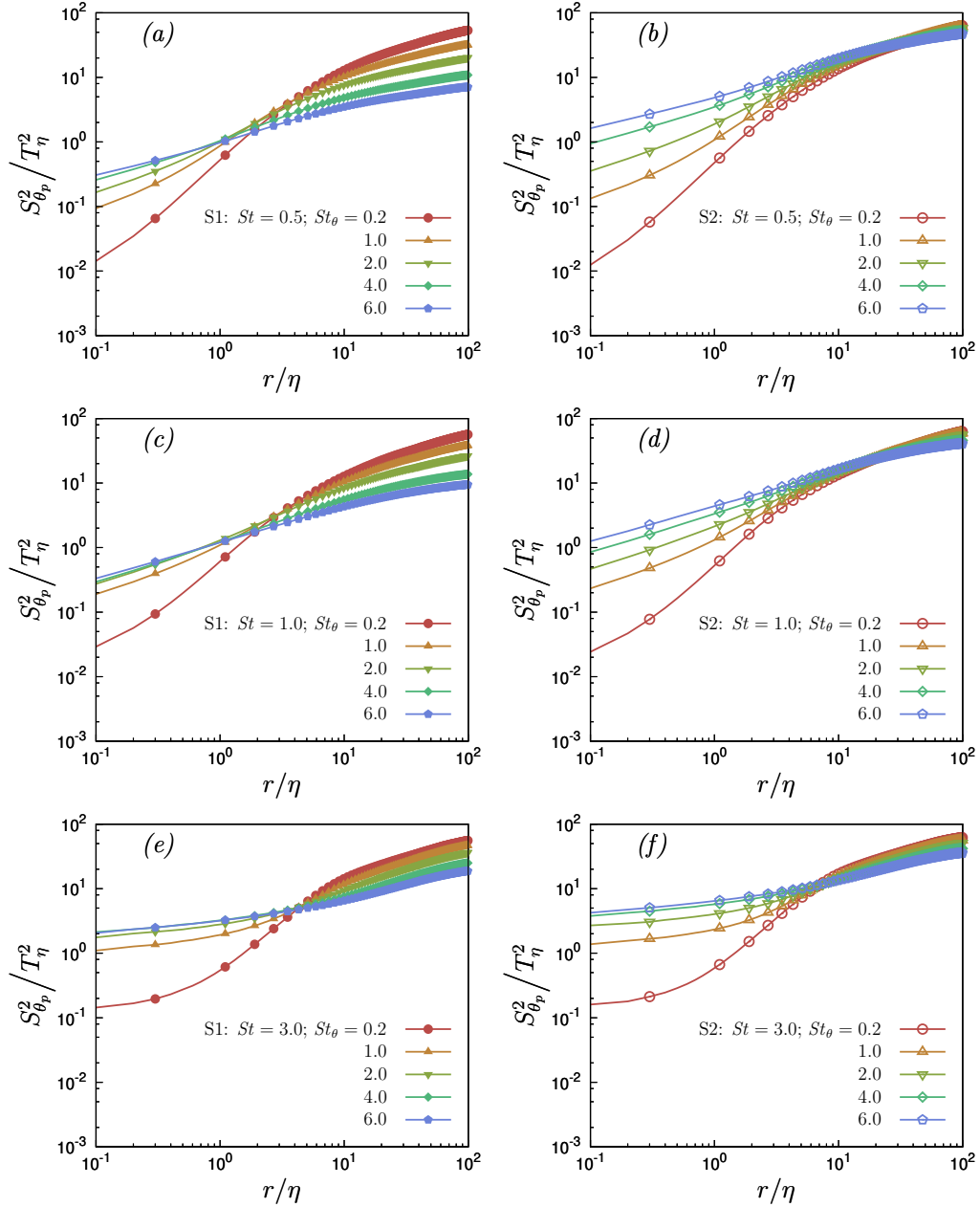


Figure 5.11: Results for S_{θ}^2 for different St_{θ} , for $St = 0.5$ (a-b), $St = 1$ (c-d) and $St = 3$ (e-f). Plots (a-c-e) are from simulations S1, in which the two-way thermal coupling is considered, while plots (b-d-f) are from simulations S2, in which the two-way coupling is neglected.

in figure 5.11. The results also show that the thermal caustics are stronger for $St_{\theta} \geq O(1)$ when the two-way thermal coupling is ignored. This is mainly due to the reduction in the fluid temperature gradients due to the two-way thermal

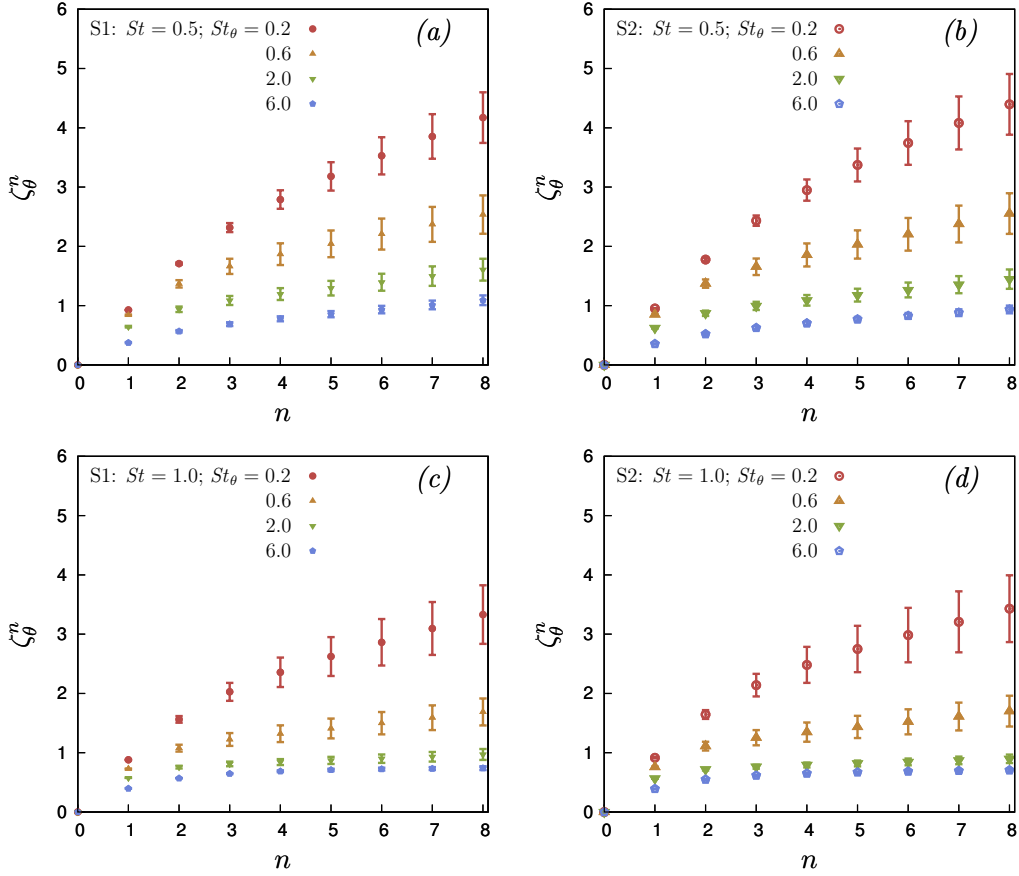


Figure 5.12: Scaling exponent of the structure functions of the particle temperature at small separation, $0.2\eta \leq r \leq 2\eta$, for various thermal Stokes numbers St_θ , at fixed Stokes number $St = 0.5$ (a-b) and $St = 1$ (c-d). Plots (a-c) are from simulations S1, in which the two-way thermal coupling is considered, while plots (b-d) are from simulations S2, in which the two-way coupling is neglected.

coupling described earlier, noting that in the limit of vanishing fluid temperature gradients, the thermal caustics necessarily disappear.

At larger scales where the statistics of ΔT vary more weakly with r , the non-local effect weakens, the thermal caustics disappear, and a filtering mechanism takes over which causes S_θ^2 to decrease with increasing St_θ . This filtering effect is directly analogous to that dominating the large-scale velocities of inertial particles in isotropic turbulence, and is associated with the sluggish response of the particles to the large scale flow fluctuations due to their inertia [81].

The particle temperature structure functions S_θ^n behave as power laws at small separation, $\log S_\theta^n(r) \approx \zeta_\theta^n \log r + a^n$, and the associated scaling exponents ζ_θ^n are shown in figure 5.12. The exponents are obtained by fitting the logarithm of the structure function in the dissipation range according to ordinary least squares. To

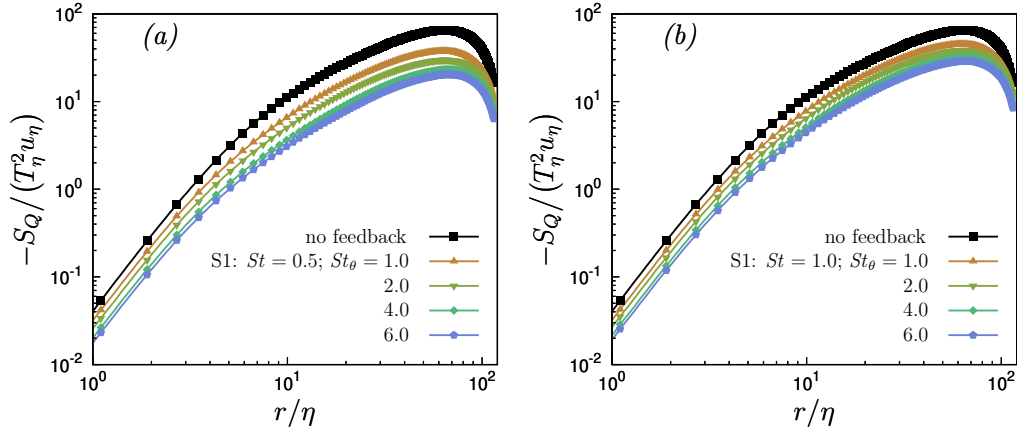


Figure 5.13: Second order mixed structure functions of the carrier flow temperature field, for different thermal Stokes numbers of the suspended particles, at $St = 0.5$ (a) and $St = 1$ (b). The data refer to the set of simulations S1, with thermal particle back-reaction included.

reduce statistical noise, we estimate ζ_θ^n by fitting the data for S_θ^n over the range $0.2\eta \leq r \leq 2\eta$. Over this range, S_θ^n do not strictly behave as power laws, and hence the exponents measured are understood as average exponents. The error bars indicate the largest deviations from the mean exponent observed in the considered range. The results in figure 5.12 reveal that particle temperature increments exhibit a strong multifractal behaviour. This multifractality is due to the non-local thermal dynamics of the particles and the formation of thermal caustics, described earlier. In particular, there exists a finite probability to find inertial particle-pairs that are very close but have large temperature differences because they experienced very different fluid temperatures along their trajectory histories. As with the thermal caustics, the multifractality is enhanced as St is increased. Most interestingly, the results for ζ_θ^n are only weakly affected by the two-way thermal coupling, despite the fact that we observed a significant effect of the coupling on S_θ^2 . This suggests that the two-way coupling affects the strength of the thermal caustics, but only weakly affects the scaling of the structure functions in the dissipation range.

5.6.3 Mixed structure functions

We turn to consider the behaviour of the flux of the temperature increments across the scales of the flow, which is associated with the mixed structure functions

$$S_Q(r) \equiv \langle (\Delta T(r, t))^2 \Delta u_\parallel(r, t) \rangle \quad (5.28)$$

where Δu_\parallel is the longitudinal relative velocity difference. The results for S_Q , for different St and St_θ are shown in figure 5.13. Just as we observed for the fluid

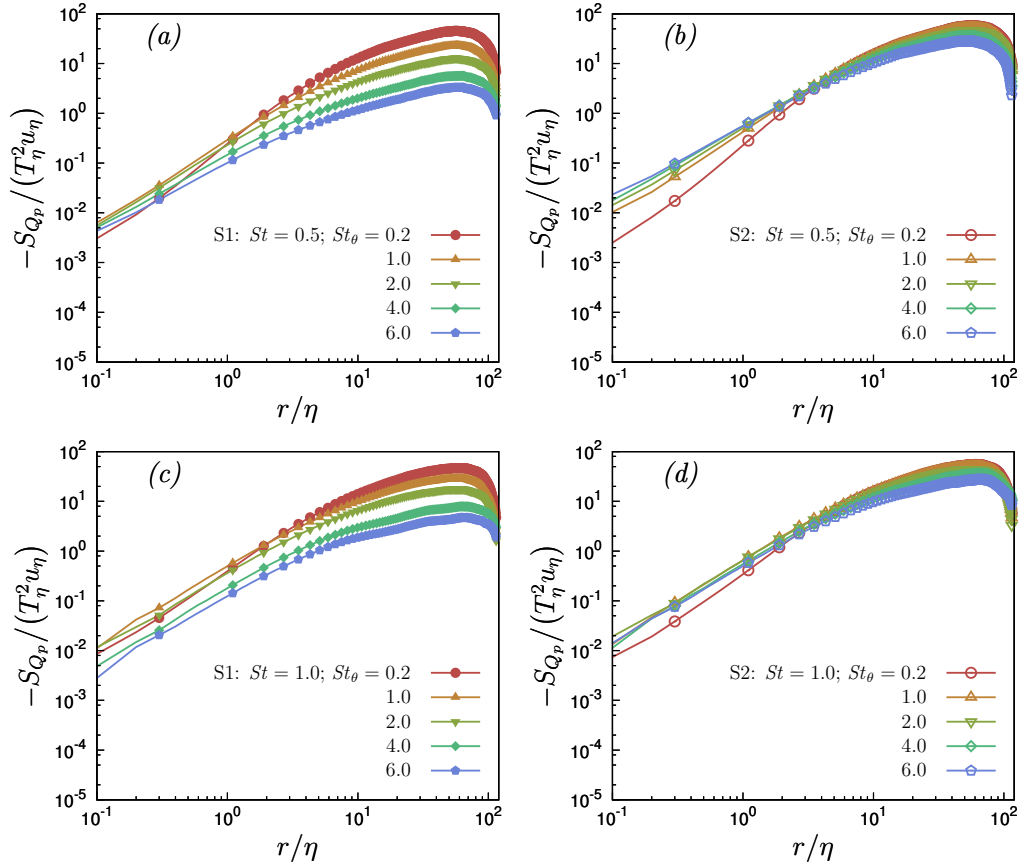


Figure 5.14: Second order mixed structure functions of the particle temperature, for different thermal Stokes numbers, at $St = 0.5$ (a-b) and $St = 1$ (c-d). The plots on the left (a-c) refer to the set of simulations S1, in which the thermal particle back-reaction is included. The plots on the right (b-d) refer to the set of simulations S2, in which the thermal particle back-reaction is neglected.

temperature structure functions, $-S_Q$ decreases monotonically with increasing St_θ , as was also observed for the fluid temperature dissipation rate χ_f . The mixed structure functions of the carrier temperature field are reported to separation down to the Kolmogorov scale, that is the scale at which the carrier temperature field is resolved, as discussed in section 5.9.

To consider the flux of the particle temperature increments, we begin by considering the exact equation that can be constructed for S_θ^n using PDF transport equations. In particular, if we introduce the PDF $\mathcal{P}(\mathbf{r}, \Delta\theta, t) \equiv \langle \delta(\mathbf{r}_p(t) - \mathbf{r})\delta(\Delta\theta_p(t) - \Delta\theta) \rangle$ and the associated marginal PDF $\varrho(\mathbf{r}, t) \equiv \int \mathcal{P} d\Delta\theta$, where \mathbf{r} and $\Delta\theta$ are time-independent phase-space coordinates, then we may derive for a statistically

stationary system the result (see [18, 17] for details on how to derive such results)

$$\left\langle [\Delta\theta_p(t)]^2 \right\rangle_r = \left\langle \Delta T(\mathbf{x}_p(t), \mathbf{r}_p(t), t) \Delta\theta_p(t) \right\rangle_r - \frac{\tau_\theta}{2\rho} \frac{\partial}{\partial \mathbf{r}} \cdot \varrho \left\langle [\Delta\theta_p(t)]^2 \mathbf{w}_p(t) \right\rangle_r, \quad (5.29)$$

where $\mathbf{w}_p(t) \equiv \partial_t \mathbf{r}_p(t)$. The first term on the right-hand side is the local contribution that remains when there exist no fluxes across the scales, and this term determines the behavior of $\langle [\Delta\theta_p(t)]^2 \rangle_r$ at the large scales of homogeneous turbulence where the statistics are independent of \mathbf{r} . The second term on the right-hand side is the non-local contribution that arises for $\text{St}_\theta > 0$, and it is this term that is responsible for the thermal caustics discussed earlier. It depends on the spatial clustering of the particles through ϱ (which is proportional to the RDF), and the flux $\langle [\Delta\theta_p(t)]^2 \mathbf{w}_p(t) \rangle_r$ which, for an isotropic system, is determined by the longitudinal component

$$S_{Q_p}(r) \equiv \frac{\mathbf{r}}{r} \cdot \left\langle [\Delta\theta_p(t)]^2 \mathbf{w}_p(t) \right\rangle_r. \quad (5.30)$$

The results for S_{Q_p} from our simulations are shown in figure 5.14, and they show that without two-way coupling, $-S_{Q_p}$ monotonically increases with increasing St_θ at the smallest scales. However, with two-way coupling, $-S_{Q_p}$ is maximum for intermediate values of St_θ , and this occurs because as shown earlier, as St_θ is increased, the fluid temperature fluctuations are suppressed across the scales.

5.7 Distribution of the temperature fluxes

We finally look at the distribution of temperature flux across the scales, in the dissipation range. We consider the PDFs of the carrier flow temperature flux $Q = (\Delta T(r, t))^2 \Delta u_{\parallel}(r, t)$ and particle temperature flux $Q = [\Delta\theta_p(t)]^2 w_{\parallel}(t)$, where $w_{\parallel}(t)$ is the parallel component of the particle-pair relative velocity.

The PDF of the carrier flow temperature flux, which does not include the contribution of the near-particle field changes, is plotted in normal form for $r \leq 2\eta$ in figure 5.15. These normalized PDFs collapse onto each other for all St and St_θ values considered. Thus, the distribution of the resolved temperature increments flux simply scales with its variance in the dissipation range, and the variance of the flux is modulated by the particles but the shape of the distribution is not affected by the particle dynamics. The PDF are strongly negatively skewed and have a negative mean value, associated with the mean flux of thermal fluctuations from large to small scales in the flow.

The PDF of the particle temperature flux is plotted in normal form for $r \leq 2\eta$ in figure 5.16. The PDF of the particle temperature flux across the scales is not self-similar with respect to its variance. Furthermore, the PDF becomes more symmetric as St_θ is increased. This is associated with the increasingly non-local thermal dynamics of the particles, which allows the particle-pairs to traverse many scales of the flow with minimal changes in their temperature difference.

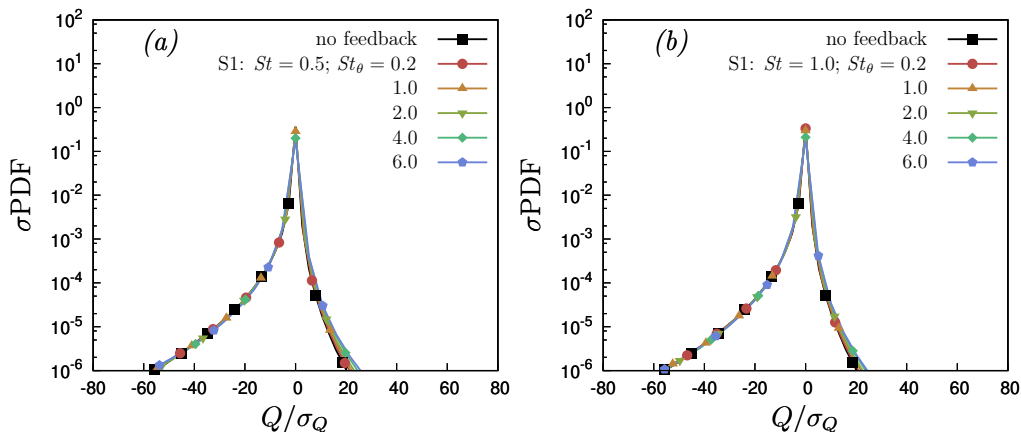


Figure 5.15: Probability density function in normal form of the flux of carrier flow temperature increments at small separations, $r \leq 2\eta$, at $St = 0.5$ (a) and $St = 1$ (b). The data refer to the set of simulations S1, with thermal feedback included.

5.8 Influence of momentum coupling and elastic collisions

In this section we quantify the effects of two-way momentum coupling and elastic collisions, which have been neglected in our simulations.

5.8.1 Momentum coupling

Concerning the momentum coupling, we have carried out few numerical simulations in which both momentum and temperature coupling are taken to account. The results show that the small scale statistics are only weakly affected by the momentum coupling. The thermal dissipation rate at different Stokes and thermal Stokes numbers, with and without momentum coupling, is shown in Figure 5.17(a), which shows that the impact of two-way momentum coupling is quite small. As expected, the effect of the momentum coupling is more evident for large Stokes numbers ($St = 3$), but even then the effect is quite small. A small reduction of the thermal dissipation due to the particles is observed since the large heat flux towards the particles is mainly a consequence of the concentration of particles in the regions of large temperature gradients, yet we expect a smoothing of the velocity field by momentum two-way coupling, which mitigates the particle preferential concentration in the vicinity of the temperature fronts. The second order structure functions of the carrier temperature field at $St = 3$ are shown in figure 5.17(b). Small quantitative modifications of the fluid temperature occur due to the momentum coupling, especially at large separation but, more importantly, the overall picture is not modified. Moreover, it should be noted that the actual Stokes number is modified by the two-way momentum coupling, since the fluid dissipation rate is no more equal to the energy injection rate in equation (5.2), resulting in a longer Kolmogorov timescale.

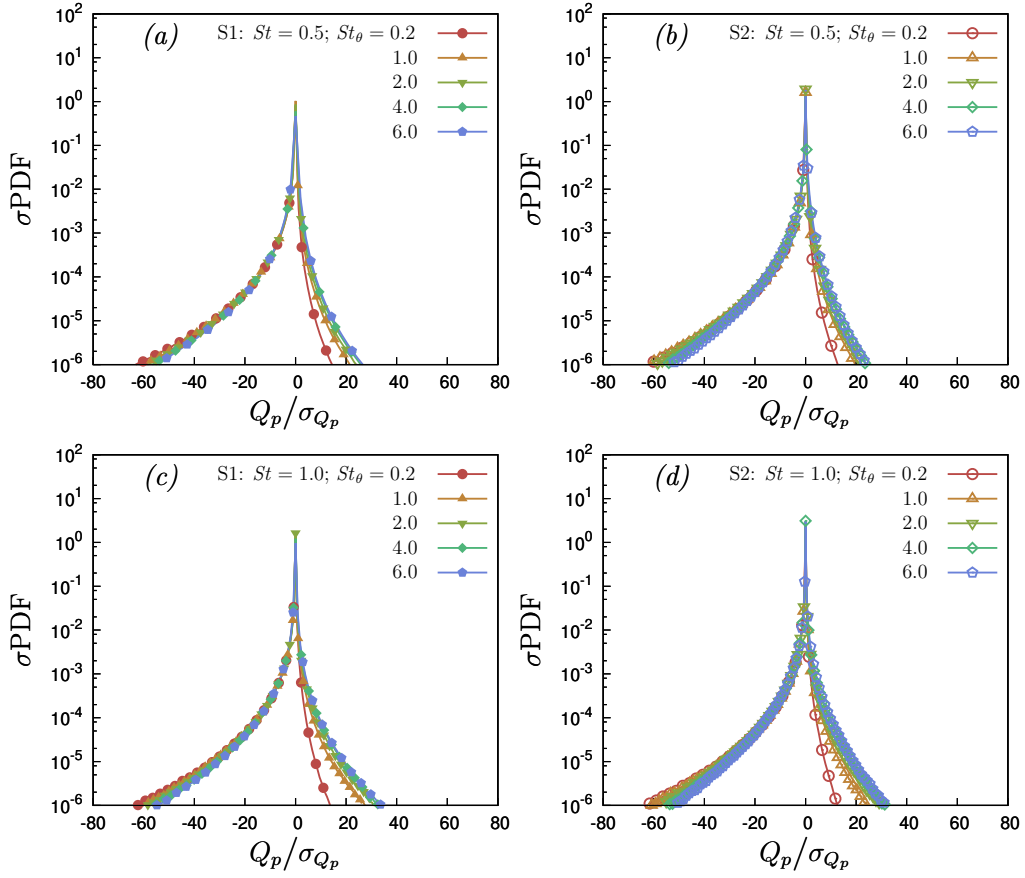


Figure 5.16: Probability density function in normal form of the flux of particle temperature increments at small separations, $r \leq 2\eta$, at $St = 0.5$ (a-b), $St = 1$ (c-d). The plots on the left (a-c) refer to the set of simulations S1, in which the thermal particle back-reaction is included. The plots on the right (b-d) refer to the set of simulations S2, in which the thermal particle back-reaction is neglected.

Data in figure 5.17 are presented using the nominal Kolmogorov timescale obtained by using overall dissipation rate, that is, the same scale of simulations without particle momentum feedback. These results justify our neglect of two-way momentum coupling in the current study as a first approximation.

5.8.2 Elastic collisions

According to the criterion by [53], the upper limit of the volume fraction for the validity of the two-way coupling is $\phi = 10^{-3}$. Above this threshold particle-particle interactions become frequent. Since in our work $\phi = 4 \times 10^{-4}$ and the Stokes number can be of order one, we have re-run some of the simulations taking into account particle-particle interactions assuming elastic collisions. Apart of collisions,

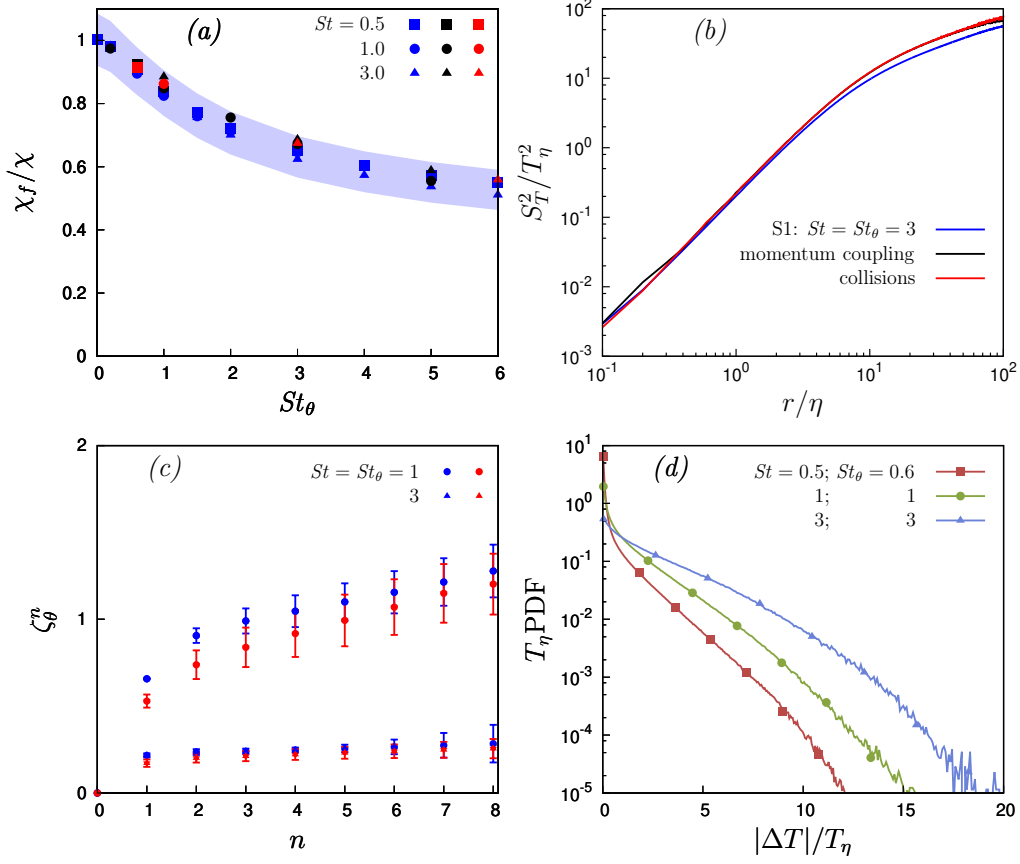


Figure 5.17: (a) Dissipation rate χ_f of the fluid temperature fluctuations, for different St as a function of St_θ and (b) second order fluid temperature structure function, at $St = St_\theta = 3$, with and without momentum coupling and elastic collisions. (c) Scaling exponents of the particle temperature structure functions at small-separation, with and without elastic collisions and momentum two-way coupling. Blue color indicates one-way momentum coupling and two-way temperature coupling, black color indicates two-way momentum and temperature coupling and red color indicates two-way momentum and temperature coupling with elastic collisions between particles. (d) PDF of the temperature difference between colliding particles. The Kolmogorov scale quantities are computed by using the overall dissipation rate.

any direct small-scale hydrodynamic interaction [115] is not taken into account.

The particle path is reconstructed at first order between time t_n and $t_{n+1} = t_n + \Delta t$, where Δt is the time step employed in the simulations. This yields the following second order equation for the relative distance between the p -th and q -th particle,

$$\|(1 - \tilde{t})(\mathbf{x}_p(t_n) - \mathbf{x}_q(t_n)) + \tilde{t}(\mathbf{x}_p(t_{n+1}) - \mathbf{x}_q(t_{n+1}))\| = 2r_p. \quad (5.31)$$

where $\tilde{t} = (t - t_n)/\Delta t$. If a real solution $\tilde{t} \in [0,1)$ exists, a collision is detected and the colliding particles p and q are evolved according to the equations for elastic collisions between rigid spheres. No heat exchange occurs during the instantaneous collision. Numerically, the direct search for collisions would be impractical, since it would require $O(N_p^2)$ operations. In our simulations, the search for collisions is performed by grouping the particles inside small boxes and searching inside each box [115]. The spurious effect of the box boundaries is removed translating the boxes and repeating the search.

The results show that, in the parameter range we are considering, the collisions only mildly affect the heat exchange between the carrier fluid and the particles. As shown in Figure 5.17(a), the change in the thermal dissipation rate due to the carrier temperature gradient is very moderate when elastic collisions are taken to account. The effect of elastic collisions on the carrier flow temperature structure functions is negligible, as in Figure 5.17(b). The effect of elastic collisions on the scaling exponents of the particle temperature structure functions at small separation is shown Figure 5.17(c). The impact of elastic collisions on those statistics at $St = 1$ is more noticeable but still moderate. The temperature difference between colliding particles is shown in Figure 5.17(c), for $St = 0.5, 1$ and 3 and corresponding $St_\theta = 0.6, 1$ and 3 . Due to the intermittency of the carrier flow temperature gradient and to the path-history effect, the relative temperature between colliding particles can be large with respect to the small-scale temperature increment T_η . However, such large temperature rarely occur and the majority of the temperature increments is concentrated in $|\Delta T| < T_\eta$, a behaviour similar to the one of relative velocity distribution between colliding particles [158]. The relative temperature between colliding particles increases with the particle inertia, as expected.

5.9 Estimating the actual temperature field

This Chapter presented the statistics of the carrier temperature field $T(\mathbf{x}, t)$, which can be resolved on the computational grid, within the limits of the point-particle model. In that model, both the particle size and the region perturbed by the particle are assumed to be much smaller than the Kolmogorov scale. The near-particle field changes are excluded in the carrier resolved fluid temperature field, which is an approximation of the actual temperature field far from particles. On the other hand, the actual temperature field includes the near-particle field perturbations, which varies on scales smaller than the Kolmogorov scale, down to the particle size, and it is such that the actual fluid temperature matches the particle temperature at the particle surface (that is, there is no thermal slip). The carrier temperature field can be understood as the actual temperature field filtered at the computational grid resolution scale, that is comparable with the Kolmogorov length scale and much larger than the particle size. Since large temperature gradients can

be expected in the perturbed regions, which are not explicitly accounted for by the carrier temperature field, in this section we analyze how the statistics of the actual temperature field relate to the particle temperature and resolved temperature field statistics.

5.9.1 Moments of the actual temperature gradient

Let us call T_* the actual temperature field, which is given by the sum of the carrier field $T(\mathbf{x}, t)$ (that is the one considered throughout the Chapter) and by the perturbations, $\tilde{T}_p(\mathbf{x}, t)$, induced by the particles. The carrier field has variations on a spatial and temporal scale from the integral scale down to the Kolmogorov microscale, while the perturbation variations are all concentrated around the particles, in a volume with a size proportional to their radius r_p . In the dilute regime we are considering, the perturbation fields induced by each particle do not overlap. Also, the suspended particles are small enough so that the Reynolds number of the relative motion with respect to the carrier fluid is small. Therefore the enthalpy equation around each particle reduces to the Fourier equation,

$$\frac{\partial T_*}{\partial t} = \kappa \nabla^2 T_*, \quad (5.32)$$

with the following boundary conditions,

$$\begin{aligned} \|\mathbf{x} - \mathbf{x}_p\| = r_p &\Rightarrow T_* = \theta_p \\ \|\mathbf{x} - \mathbf{x}_p\| \rightarrow +\infty &\Rightarrow T_* \rightarrow T. \end{aligned} \quad (5.33)$$

Equation (5.32) gives the perturbed temperature field around the particle in a particle-centered frame. Since particles have sub-Kolmogorov size, $r_p \ll \eta$, and the Prandtl number is unitary in our simulations, T can be considered uniform on the particle scale. The timescale of heat diffusion τ_d is much shorter than the timescale of the fastest fluctuations of the carrier temperature field T , which is of the order of the Kolmogorov timescale τ_η and $\tau_d/\tau_\eta \sim (r_p/\eta)^2 \ll 1$. Therefore, the solution of equation (5.32) with boundary conditions (5.33) around each particle can be approximated by its quasi-steady solution so that the actual temperature field is

$$T_*(\mathbf{x}, t) = T(\mathbf{x}, t) + \sum_{p=1}^{N_P} (\theta_p - T(\mathbf{x}_p, t)) \frac{r_p}{\|\mathbf{x} - \mathbf{x}_p\|} \quad (5.34)$$

and its gradient reads

$$\nabla T_* = \nabla T - \sum_{p=1}^{N_P} (\theta_p - T(\mathbf{x}_p)) \frac{r_p}{\|\mathbf{x} - \mathbf{x}_p\|^3} (\mathbf{x} - \mathbf{x}_p). \quad (5.35)$$

Equation (5.35) is the basis to derive the point-particle closure of the the particle heat flux, equation (5.3c) and, as we will show, it also allows to recover the single-point moments of the actual temperature gradient, which is the superposition of the carrier temperature gradient and the disturbance induced by the particles. Since the flow is statistically homogeneous, we may replace statistical averages with spatial averages. Let us indicate with Ω the overall domain, with Ω_p the region occupied by the p -th particle and $\Omega_f = \Omega - \cup_p \Omega_p$ the region occupied by the fluid. The volume of the region occupied by the fluid is $|\Omega_f| = |\Omega|(1 - \phi)$ where $\phi = \sum_p |\Omega_p|/|\Omega|$ is the particle volume fraction. Since particles are very small with respect to the scale of spatial variation of the carrier temperature field, the disturbance induced by the particle is non-negligible only in a small region surrounding the particle. Let us indicate the perturbed volume around each particle by $\tilde{\Omega}_p$, a ball of radius αr_p , where r_p is the particle radius and $\alpha > 1$ indicates to how many radii far from the particle the disturbance on the temperature gradient becomes negligible. A one-dimensional sketch of the point-particle model under consideration is in figure 5.18(a). In the undisturbed fluid volume $\tilde{\Omega}_f = \Omega - \cup_p \tilde{\Omega}_p$ the particle perturbations are negligible and the actual temperature is given only by the carrier temperature field. On the other hand, in the perturbed region, the actual temperature is the sum of the resolved and disturbance temperature. Therefore we have,

$$T_*(\mathbf{x}, t) = T(\mathbf{x}, t), \quad \mathbf{x} \in \tilde{\Omega}_f \quad T_*(\mathbf{x}, t) = T(\mathbf{x}, t) + \tilde{T}_p(\mathbf{x}, t), \quad \mathbf{x} \in \tilde{\Omega}_p \quad (5.36)$$

where $\tilde{T}_p = (\theta_p - T(\mathbf{x}_p, t)) r_p / \|\mathbf{x} - \mathbf{x}_p\|$ according to equation (5.34). The n -th order moment of the actual temperature gradient may be then evaluated by spatial average,

$$\langle \|\nabla T_*\|^n \rangle = \frac{1}{|\Omega|} \int_{\tilde{\Omega}_f} (\|\nabla T\|^2)^{n/2} d\mathbf{x} + \frac{1}{|\Omega|} \sum_p \int_{\tilde{\Omega}_p} (\|\nabla T_*\|^2)^{n/2} d\mathbf{x}. \quad (5.37)$$

In the region perturbed by the particle, the gradient of the disturbance field is larger than the gradient of the carrier field, since the disturbance decays fast in a region which is tiny with respect to the Kolmogorov scale. Therefore, using $\|\nabla T\| \ll \|\nabla \tilde{T}_p\|$, the temperature field can be Taylor-expanded in the perturbed regions, retaining terms up to $(\|\nabla T\|/\|\nabla \tilde{T}_p\|)^2$,

$$\|\nabla T_*\|^n \sim \|\nabla \tilde{T}_p\|^n \left[1 + n \frac{\nabla T \cdot \nabla \tilde{T}_p}{\|\nabla \tilde{T}_p\|^2} + \frac{n}{2} \frac{\|\nabla T\|^2}{\|\nabla \tilde{T}_p\|^2} + \frac{n(n-2)}{2} \frac{(\nabla T \cdot \nabla \tilde{T}_p)^2}{\|\nabla \tilde{T}_p\|^4} \right]. \quad (5.38)$$

The last term on the right hand side of equation (5.38) can be estimated by using the Schwarz inequality to obtain

$$\|\nabla T_*\|^n \lesssim \|\nabla \tilde{T}_p\|^n + n \|\nabla T \cdot \nabla \tilde{T}_p\| \|\nabla \tilde{T}_p\|^{n-2} + \frac{n(n-1)}{2} \|\nabla T\|^2 \|\nabla \tilde{T}_p\|^{n-2}. \quad (5.39)$$

Equation (5.39) provides a local upper bound for powers of the actual temperature gradient in the perturbed region (while $\nabla T_* = \nabla T$ in the unperturbed region), which allows to compute an upper bound for the moments of the actual temperature gradient. Using equation (5.39) into (5.37) leads to

$$\begin{aligned} \langle \|\nabla T_*\|^n \rangle &\lesssim \frac{1}{|\Omega|} \int_{\tilde{\Omega}_f} \|\nabla T\|^n d\mathbf{y} + \frac{1}{|\Omega|} \sum_p \int_{\tilde{\Omega}_p} \left[n \nabla T \cdot \nabla \tilde{T}_p \|\nabla \tilde{T}_p\|^{n-2} + \right. \\ &\quad \left. + \|\nabla \tilde{T}_p\|^n + \frac{n(n-1)}{2} \|\nabla T\|^2 \|\nabla \tilde{T}_p\|^{n-2} \right] d\mathbf{y}_p. \end{aligned} \quad (5.40)$$

The average of the product of the carrier field and the disturbance is negligible, since the carrier field varies on scale η and can be considered constant on scale $\alpha r_p \ll \eta$, except in small regions of the domain in which extreme field temperature gradients take place,

$$\begin{aligned} &\int_{\tilde{\Omega}_p} \nabla T \cdot \nabla \tilde{T}_p \|\nabla \tilde{T}_p\|^{n-2} d\mathbf{y}_p \simeq \\ &\simeq (T(\mathbf{x}_p, t) - \theta_p) |T(\mathbf{x}_p, t) - \theta_p|^{n-2} r_p^{n-1} \nabla T(\mathbf{x}_p, t) \cdot \int_{\tilde{\Omega}_p} \mathbf{y}_p \|\mathbf{y}_p\|^{1-2n} d\mathbf{y}_p = 0, \end{aligned} \quad (5.41)$$

where $\mathbf{y}_p = \mathbf{x} - \mathbf{x}_p$ and the spherical symmetry of the perturbation has been used. Computing the integrals involving \tilde{T}_p in equation (5.40), an upper bound for the n -th order moment of the actual fluid temperature gradient is obtained

$$\begin{aligned} \langle \|\nabla T_*\|^n \rangle &\lesssim (1 - \alpha^3 \phi) \langle \|\nabla T\|^n \rangle + \phi \frac{3}{2n-3} (1 - \alpha^{3-2n}) \left\langle \left| \frac{\theta_p - T(\mathbf{x}_p, t)}{r_p} \right|^n \right\rangle + \\ &\quad + \phi \frac{3n(n-1)}{4n-14} (1 - \alpha^{7-2n}) \left\langle \|\nabla T(\mathbf{x}_p, t)\|^2 \left| \frac{\theta_p - T(\mathbf{x}_p, t)}{r_p} \right|^{n-2} \right\rangle. \end{aligned} \quad (5.42)$$

Regarding the corrections due to α , equation (5.35) shows that the disturbance temperature gradient decays within a few radii from the particle. We may assume α large but still $\alpha r_p \ll \eta$ because of the marked scale separation hypothesis between the particle size and the Kolmogorov length scale, $r_p \ll \eta$. By hypothesis $\alpha^3 \phi \ll 1$ and, therefore, also $\alpha^{7-2n} \phi \ll 1$ for $n \geq 2$.

The first term on the right hand side of equation (5.42) is the contribution of the carrier flow, the other two terms are the contribution of the local perturbation due to the particles. The inequality in equation (5.42) is only due to the last term, which has been overestimated by the Schwarz inequality. The relative importance of the terms in equation (5.42) is now estimated in order to obtain a direct estimation instead of an upper bound for the moments of the actual temperature gradient. We exploit the fact that the disturbance gradient is much larger and more intermittent than the resolved gradient, therefore the second term in equation (5.42), which

behaves as $|(\theta_p - T(\mathbf{x}_p, t))/r_p|^n$, is dominant with respect the third term in the same equation, that behaves only as $|(\theta_p - T(\mathbf{x}_p, t))/r_p|^{n-2}$. An estimation of the ratio between the order of magnitude of the third and second terms on the right hand side of equation (5.42), that is,

$$\mathcal{C}_n = \frac{n(n-1)(2n-3)}{4n-14} \frac{1 - \alpha^{7-2n}}{1 - \alpha^{3-2n}} \frac{\langle \|\nabla T(\mathbf{x}_p, t)\|^2 |\theta_p - T(\mathbf{x}_p, t)|^{n-2} \rangle}{\langle |\theta_p - T(\mathbf{x}_p, t)|^n \rangle} r_p^2, \quad (5.43)$$

can be obtained neglecting the coupling between the resolved and perturbation gradient, which is justified due to the wide scale separation of those two fields, and using the results in [8], where it is shown that the average dissipation rate evaluated at the particle position is not larger than two times the overall dissipation rate. Therefore, the ratio between the order of magnitude of the third and second terms on the right hand side of equation (5.42) can be estimated as

$$\mathcal{C}_n \lesssim \frac{6}{K_n} \frac{\chi_f}{\chi_p} \left| \frac{n(n-1)(2n-3)}{4n-14} \right| \max(1, \alpha^{7-2n}) \phi, \quad (5.44)$$

where

$$K_n = \frac{\langle |\theta_p - T(\mathbf{x}_p, t)|^n \rangle}{\langle |\theta_p - T(\mathbf{x}_p, t)|^{n-2} \rangle \langle |\theta_p - T(\mathbf{x}_p, t)|^2 \rangle} \quad (5.45)$$

and χ_f/χ_p depends on St_θ and weakly on St , as in figure 5.2(b). Since $\alpha^3\phi \ll 1$, as required by the two-way coupled point-particle model, and K_n is expected to be large for $n > 2$ due to the high intermittency of the disturbance gradient (e.g. $K_4 = \text{O}(10)$ from figure 5.3(f)), we expect that $\mathcal{C}_n \ll 1$ for moderate n (e.g. $n \leq 4$) and St_θ not too small (so that χ_f/χ_p not very large). The estimation in equation (5.44) can be rewritten using equations (5.43), (5.9) and (5.10) together with the definition of Kolmogorov scales, $\langle \|\nabla T\|^2 \rangle = T_\eta^2/\eta^2$, which gives

$$\mathcal{C}_n \lesssim \frac{2}{K_n} \left| \frac{n(n-1)(2n-3)}{4n-14} \right| \max(1, \alpha^{7-2n}) \frac{T_\eta^2}{\langle |\theta_p - T(\mathbf{x}_p, t)|^2 \rangle} \left(\frac{r_p}{\eta} \right)^2. \quad (5.46)$$

Therefore $\mathcal{C}_n \ll 1$ for small particles, moderate n and St_θ reasonably large (that is, $|\theta_p - T(\mathbf{x}_p, t)|/T_\eta$ not very small). Both estimations, equations (5.44) and (5.46), show that the second term on the right hand side of equation (5.42) is the leading term of the contribution of the particle perturbation to the actual temperature gradient moments, while third term on the right hand side of equation (5.42) is sub-leading, for moderate n (e.g. $n \leq 4$), $\phi \ll 1$ and $r_p/\eta \ll 1$, which are basic hypothesis of the point-particle model. Therefore, the following simplified estimation for the moments of the actual temperature field is obtained:

$$\langle \|\nabla T_*\|^n \rangle \sim \langle \|\nabla T\|^n \rangle + \frac{3\phi}{2n-3} \left\langle \left| \frac{\theta_p - T(\mathbf{x}_p, t)}{r_p} \right|^n \right\rangle, \quad n \geq 2. \quad (5.47)$$

Equation (5.47) with $n = 2$ is the balance of thermal dissipation rate, that is equation (5.8), derived from the carrier flow temperature field equation (5.1c), which includes the particle thermal feedback. The only hypothesis necessary to obtain equation (5.47) are those that are also assumed for the validity of the point-particle model, without the need of any ad-hoc assumption. It is worth noting that the contribution of the particle perturbation to the actual temperature gradient moments can become dominant with respect to the carrier temperature field contribution. Indeed, the ratio between the second and first term on right hand side of equation (5.47) can be roughly estimated to be proportional to $\phi(\eta/r_p)^n$, which shows that the particle perturbation contribution dominates for large n , since in the point-particle model hypothesis $\phi \ll 1$ but $\eta/r_p \gg 1$. This is a signature of the intermittency introduced by the perturbation due to the particles. The quantity

$$R_n = \left(\frac{\langle \|\nabla T_*\|^n \rangle}{\langle \|\nabla T\|^n \rangle} \right)^{1/n} \quad (5.48)$$

can be used to measure the overall contribution of the perturbed regions to the temperature gradient moments, and it is shown in Figure 5.18(b) as a function of the thermal Stokes number, for $n \leq 4$ and $St = 1$. As expected, for small particle thermal inertia $R_n \sim 1$ and the difference between the actual temperature gradient distribution and the resolved temperature gradient distribution increases with St_θ . The actual temperature gradient ∇T_* is more intermittent than the carrier flow temperature gradient ∇T (which does not include the particle disturbance). The high order moments of the actual temperature gradient might be even larger than the prediction in equation (5.47), since the weight of the term neglected in equation (5.42) is proportional to the order of the moment, n . The enhanced fluid flow intermittency due to the suspended particles is consistent with the results from particle-resolved direct numerical simulations of turbulent flows laden with small fixed spheres [159].

5.9.2 Actual temperature field Probability Density Function

The PDF of the actual temperature field T_* can be obtained from the PDF of the carrier temperature field T and the PDF of the particle temperature through equation (5.34). A simple estimation, which overestimates the difference between the PDFs of T and T_* , can be obtained by assuming that T_* is equal to the particle temperature θ_p within $\tilde{\Omega}_p$,

$$T_*(\mathbf{x}, t) = T(\mathbf{x}, t), \quad \mathbf{x} \in \tilde{\Omega}_f \quad T_*(\mathbf{x}, t) \approx \theta_p, \quad \mathbf{x} \in \tilde{\Omega}_p. \quad (5.49)$$

The PDF of the actual temperature field is given by,

$$\rho_{T_*}(T') = \rho(T' \text{ and } \mathbf{x} \in \tilde{\Omega}_f) + \rho(T' \text{ and } \mathbf{x} \in \cup_p \tilde{\Omega}_p), \quad (5.50)$$

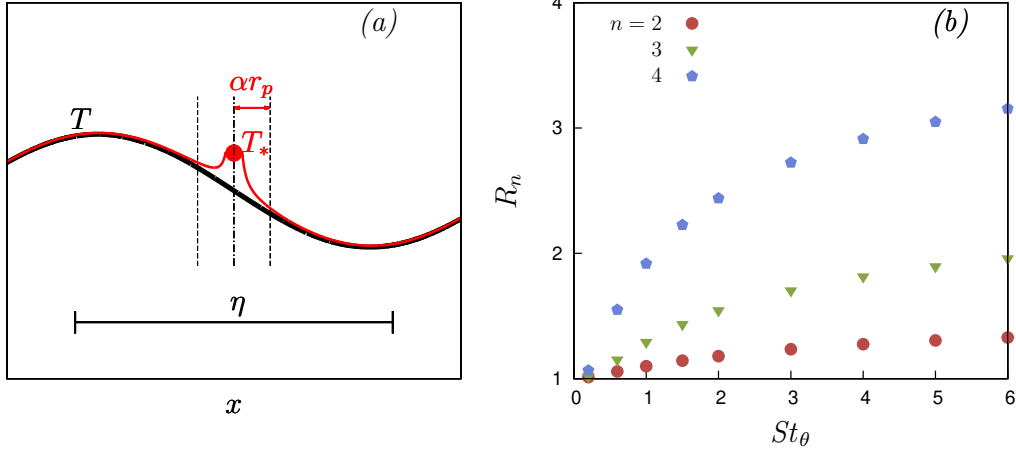


Figure 5.18: (a) Sketch of the particle model. The size of the particle and of the perturbed region is out of proportion for sake of clarity. (b) Ratio between the n -th order moment of the actual temperature gradient and the resolved carrier temperature gradient, $R_n = (\langle \|\nabla T_*\|^n \rangle / \langle \|\nabla T\|^n \rangle)^{1/n}$, as a function of the particle thermal inertia at $St = 1$.

and, through equation (5.49), it reduces to

$$\begin{aligned} \rho_{T_*}(T') &= (1 - \alpha^3 \phi) \rho_T(T') + \alpha^3 \phi \rho_\theta(T') \\ &= \rho_T(T') + \alpha^3 \phi (\rho_\theta(T') - \rho_T(T')). \end{aligned} \quad (5.51)$$

Since $\alpha^3 \phi \ll 1$ and the difference between the distribution of θ_p and T is moderate (see Figures 5.5 and 5.6), the difference between the the carrier temperature distribution T and the actual temperature distribution T_* is negligible and $\rho_T \sim \rho_{T_*}$.

5.9.3 Structure functions

The moments of the actual temperature gradient provide information about the temperature structure functions at small separation. Indeed, $\Delta T_*(r) \sim \nabla T_* \cdot \mathbf{r}$ for $r \rightarrow 0$ and the overall thermal dissipation rate χ , which is imposed by the forcing, is due to the gradients of the actual fluid temperature field,

$$\chi = \kappa \langle \|\nabla T_*\|^2 \rangle. \quad (5.52)$$

Therefore, invoking isotropy, the actual temperature field second order structure function at small separation is

$$S_{T_*}^2(r) \sim \left\langle \frac{\partial T_*}{\partial x_i} \frac{\partial T_*}{\partial x_j} \right\rangle r_i r_j = \langle \|\nabla T_*\|^2 \rangle \frac{r^2}{3} = \frac{r^2 \chi}{3\kappa}, \quad r \rightarrow 0, \quad (5.53)$$

while the second order structure function of the carrier temperature field is $\sim r^2 \chi_f / (3\kappa)$ at small separation. Small deviations from this limit may occur due to

lack of isotropy in the immediate vicinity of the particle. The structure function of the actual temperature field at small separation is proportional to the overall thermal dissipation rate. This again reflects the fact that physically all the dissipation rate derives from the actual fluid temperature gradient, the thermal slip $|\theta_p - T(\mathbf{x}_p, t)|$ being only an artifact of the point-particle model. In this work, the overall thermal dissipation rate χ is the same for all the simulations, therefore the structure function of the actual temperature field at small separation is the same for each St and St_θ . On the other hand at large separation,

$$S_{T_*}^2(r) \sim 2 \langle T_*^2 \rangle, \quad r \gg \ell_* \quad (5.54)$$

where ℓ_* is the correlation length of the actual temperature field. Information about the structure function can be then extrapolated by analyzing the single-point actual temperature field statistics. For these one-point statistics, however, the modification due to the particles is expected to be small, as in section 5.9.2. In conclusion, the variation of the fluid temperature structure function S_T at small separation due to the near-particle field changes is expected to be pronounced, while the effect of the near-particle field on the fluid temperature structure functions at large separation is expected to be very moderate in the dilute regime.

5.10 Conclusions

Using direct numerical simulations, we have investigated the interaction between the scalar temperature field and the temperature of inertial particles suspended in the fluid, with one and two-way thermal coupling, in statistically stationary, isotropic turbulence.

We found that the shape of the probability density function (PDF) of the carrier flow temperature gradients is not affected by the presence of the particles when two-way thermal coupling is considered, and scales with its variance. On the other hand, the variance of the fluid temperature gradients decreases with increasing St_θ , while St plays a negligible role. The PDF of the rate of change of the particle temperature, whose variance is associated with the thermal dissipation due to the particles, does not scale in a self-similar way with respect to its variance, and its kurtosis decreases with increasing St_θ . The particle temperature PDFs and their moments exhibit qualitatively different dependencies on St for the case with and without two-way thermal coupling.

To obtain further insight into the fluid-particle thermal coupling, we computed the number density of particles conditioned on the magnitude of the local fluid temperature gradient. In agreement with [8], we observed that the particles cluster in the fronts of the temperature field. We also computed quantities related to moments of the particle heat flux conditioned on the magnitude of the local carrier flow temperature gradient. These results showed how the particles tend to decrease the

fluid temperature gradients, and that it is associated with the statistical alignments of the particle velocity and the local carrier flow temperature gradient field.

The two-point temperature statistics were then examined to understand the properties of the temperature fluctuations across the scales of the flow. By computing the structure functions, we observed that the fluctuations of the carrier flow temperature increments are monotonically suppressed as St_θ increases in the two-way coupled regime. The structure functions of the particle temperatures revealed the dominance of thermal caustics at the small scales, wherein the particle temperature differences at small separations rapidly increase as St_θ and St are increased. This allows particles to come into contact with very large temperature differences, which has a number of important practical implications. The scaling exponents of the inertial particle temperature structure functions in the dissipation range revealed strongly multifractal behavior.

The flux of carrier flow temperature increments across the scales was found to decrease monotonically with increasing St_θ . The PDFs of this flux are strongly negatively skewed and have a negative mean value, indicating that the flux is predominately from the large to the smallest scales of the flow. In the two-way coupled regime, the presence of the inertial particles does not change the shape of the PDF. The PDF of the flux of particle temperature increments in the dissipation range becomes more and more symmetric as St_θ is increased, associated with the increasingly non-local thermal dynamics of the particles.

Finally, the effect of elastic collisions and two-way momentum coupling was analyzed. We also provided a way to recover the actual temperature field, which matches the particle temperature at the boundary of each particle, starting from point-particle model results.

The results presented have revealed a number of non-trivial effects and behavior of the particle temperature statistics. In a future work it will be important to consider the role of gravitation settling and coupling with water vapor fields, both of which are important for the cloud droplet problem. Moreover, it will be interesting to include the two-way momentum coupling and to consider the non-dilute regime.

Chapter 6

Role of the thermal inertia and forcing scheme in numerical simulations of condensational droplet growth in turbulence.

In this Chapter the role of thermal inertia of cloud droplets in the modulation of small-scale turbulence and in the broadening of the droplet size distribution is analyzed. A model for the condensational growth of a water droplet, which takes into account the finite thermal relaxation time of droplets is discussed and a full two-way coupling between the dispersed droplet and the air phase, to be used in the Direct Numerical Simulation (DNS) of turbulent warm clouds is presented. We also analyze the role of the large-scale forcing methods in the DNS of statistically isotropic turbulence laden with particles. It is shown that the droplet thermal inertia enhances the broadening of the droplet size distribution and its role can be important when the flow displays relatively large temperature gradients. Moreover, it is shown that a large-scale Gaussian forcing helps the droplet statistics to approach Gaussianity while a deterministic forcing produces droplet statistics which approach Gaussianity only after relatively long times. The effects of the large-scale forcing should be quantified and distinguished from the spontaneous formation of Gaussian droplet statistics.

A preliminary version of this work has been published in the Proceedings of the iTi Conference [80].

6.1 Introduction

The increase of computational power in the last decades has made the Direct Numerical Simulation a method of outmost importance for the investigation of all

physical problems where fluid turbulence plays a major role. In fact, even if up to now and in the foreseeable future a Direct Numerical Simulation of a complex flow or a high Reynolds number flow will not be possible, significant insight into turbulence physics can be obtained from the investigation of simple and idealized archetypal flow configurations which often cannot be reproduced or measured in laboratory experiments [109, 1]. In the wake of these progresses, it has been quite natural that DNS has been used to study the small-scale microphysical processes and turbulent transport inside a cloud from a more fundamental point of view, numerically simulating the interplay of turbulent motions with phase transition processes, to which most atmospheric motions of different spatial scales as well as precipitations are closely related [89, 45]. In fact, one of the most complex aspects of atmospheric dynamics problems is the importance of processes occurring at extremely smaller scales with respect to cloud scales in determining the overall behaviour of clouds, including their lifetime, size, ability to generate precipitation and their optical and radiative properties. Cloud droplets play a fundamental role in all these phenomena, since the release or absorption of latent heat due to water vapour condensation or evaporation is one of the main sources of energy which drive the turbulent motions in a cloud. However, the associated microscale processes are far beyond the resolution of cloud-resolving models.

Since the seminal papers [152, 153], many numerical studies have been carried out to investigate the evolution of a small portion of droplet containing turbulent cloud. In this studies the Eulerian description of the turbulent flow is coupled with the Lagrangian description of each individual droplet in order to simulate the growth by condensation and/or collision inside the bulk of the cloud due to humidity fluctuations [153, 84, 2, 98, 132, 62]. [132] showed the continuous growth of the size variance due to supersaturation fluctuations even in an homogeneous and steady state flow and built a stochastic model for that. The aim of those works is to enlighten the extent to which particle inertia and turbulent fluctuations broaden the droplet size distribution and increase the growth rate. By simulating the evolution of droplets in a homogeneous and isotropic turbulent flow which resembles the homogeneous, well-mixed interior of a cloud, where droplet spatial distribution is influenced by small-scale turbulence only, the main aim of these studies is to assess how the local non-uniformity in the flow and in the droplet distribution can contribute to the broadening of the droplet size distribution and to the enhancement of their growth. Forcing is often applied as a way to reproduce the energy input coming from larger scale phenomena that cannot be reproduced within the computational domain and to obtain a statistically steady fluid flow within the observed time, while in other cases the turbulence is sustained only by the evaporative/-condensational processes and associated buoyancy forces. A different large-scale modulation of the flow has been introduced by [62], who, instead of simulating the cloud evolution in a small cubic volume fixed in space, assumed to follow a small

cubic volume moving inside a cumulus cloud, subject to the updraft velocity resulting from mean buoyancy of the volume with respect to the surrounding mean conditions.

More recently, other studies have applied the same methodology to analyze inter-facial phenomena at the lateral cloud border. The entrainment of clear air at a simple cloud border model, that is, the mixing between a supersaturated and a under-saturated air region in a uniform turbulent flow was considered in [97, 94, 95], while the rise of a plume in an unforced, initially quiescent air region has been simulated in [119]. The entrainment and mixing of an isothermal plume in a forced homogeneous turbulence which mimics the driving force due to buoyancy was considered in [96], and the possibility to have a turbulent kinetic energy gradient at the cloud interface, as suggested by several measurements [45], was added in [64]. However, in this case the computational resources pose a limitation to cloud-edge DNS, since the evolution of a mixing layer is more sensitive to large-scales than small-scales and the computational domain often cannot be large enough to represent the very-large-scale turbulent motions. As observed in [98], Direct Numerical Simulations are actually reproducing a very small cloud rather than a small portion of a large cloud, because all interactions with these large-scale flow structures are not represented at all.

Most of these studies used the formalism introduced by [152], who adapted the classical models for the condensational growth of a single droplet in quiescent, uniform environment [123] to the motion of a droplet to a turbulent flow, while few works (e.g. [98, 132]) employed the simpler Twomey model [151]. In both cases, particles are inertial points which move subject to the Stokes drag and weight, while their size can grow or shrink according to the above mentioned models but allowing the air temperature, water vapour density (and hence relative humidity) to vary according to the prediction of the Eulerian fluid equations. In particular, thermal equilibrium between the droplet and the surrounding air is always assumed because the timescale associated to heat conduction and droplet temperature variation are much smaller than the timescale associated to the size growth. Therefore, the droplet temperature is determined by the instantaneous equilibrium between the heat released by condensation (or absorbed by the evaporating mass) and the heat transfer with air. This is valid in a uniform environment because the thermal relaxation time of a small droplet is much faster than the overall timescale of its growth by condensation. When the flow is turbulent, however, the surrounding ambient seen by the particle has changing conditions, with timescales dictated by turbulent eddies. Therefore, the fluctuations of temperature and humidity can occur on timescales of the same order of the particle thermal relaxation time. Since the thermal relaxation time for a water droplet in air is about four times the momentum relaxation time of the Stokes drag, the timescale of fluctuations of temperature and humidity can be of the same order of the thermal response time even if the Stokes number is smaller than unity.

It has been shown that the thermal inertia of particles suspended in a turbulent flow plays an important role in modulating the heat transfer across the flow [172]. The impact of the particles on the fluid flow is enhanced by particle clustering and caustics, that is, inertial particles in turbulence can agglomerate and come together from different regions of the flow with large relative velocities [81]. Particle clustering takes place on the fronts of the scalar field, i.e. finite-size particles concentrate in the regions where the passively advected scalar displays sharp gradients [8] and, as a consequence, particles can experience extreme temperature variations along their path. Most works published in literature [8, 81] considered a one-way coupling between fluid and particles, that is, fluid applies a force and heat flow on the particles but there is no feedback effect on the fluid. However, the average volume fraction of water droplets in clouds can be beyond the limits of validity of one-way coupling regime [53] and their feedback on the flow can be significant. On the other hand, inertial particles are effective for heat exchange within the fluid flow since they can easily exit the Lagrangian coherent structures [25], so that they would be strongly out of thermal equilibrium with the surrounding fluid and large heat fluxes between fluid and particles would take place. The modulation of temperature and vapour density, induced by droplets modifies the supersaturation distribution and, therefore, can influence the nucleation rate. The role of the particles is enhanced by strong local inhomogeneity, which is particularly evident at the cloud border.

In this Chapter the point mass model for Eulerian-Lagrangian Direct Numerical Simulations of cloud processes is critically reconsidered, in order to account for the lack of thermal equilibrium between the droplet and the surrounding air. Two-way coupling effects are considered and the impact of the droplet back-reaction on the moist air dynamics is examined. Moreover, the modification of the droplet statistics due to different large-scale forcing schemes is analyzed showing that, despite the wide scale separation between the droplet scale and the forced scale, the droplet statistics can be qualitatively modified by the forcing scheme.

6.2 Model equations

Cloud droplets originate from heterogeneous nucleation then they grow by vapour condensation while they are advected by the fluid flow, which consists of moist air. When the droplet size becomes large enough, the growth is dominated by collisions and subsequent coalescence. In this Section, we discuss the model for the evolution of individual cloud droplets by vapour diffusion. In order to assess the validity of model hypothesis, we begin with a review of the time scales associated with the main physical processes which affect the motion of a small droplet.

In their motion, droplets can find themselves in regions with a different temperature and can be heated (cooled) by the latent heat released (absorbed) by condensation (evaporation) at its surface. The timescale of heat diffusion in the

droplet and in the air over distances of size of the order of its radius r_d , are $\tau_{d,d} = r_d^2/(\pi\kappa)$ and $\tau_{d,a} = r_d^2/(\pi\kappa)$, where $\kappa = \lambda/(\rho c_p)$ is the thermal diffusivity in air and $\kappa = \lambda_L/(\rho_L c_L)$ is the thermal diffusivity in liquid water [133] (ρ and ρ_L are air and liquid water density, λ and λ_L are air and liquid water conductivity). Analogously, the timescales of water vapour diffusion is $\tau_{d,v} = r_d^2/\kappa_v$ where κ_v is the mass diffusion of vapour in air.

As a consequence of the diffusive momentum and heat exchanged with the surrounding air, a droplet tends to relax to the fluid velocity and temperature. If the Reynolds number of the relative motion of the droplet with respect to the fluid is small (i.e. $\text{Re}_d \ll 1$), then the timescales of velocity variations can be estimated from the balance between droplet momentum and Stokes drag, that is

$$\tau_p = \frac{2}{9} \frac{\rho_L}{\mu} r_d^2 = \frac{2}{9} \frac{\rho_L}{\rho} \frac{r_d^2}{\nu}. \quad (6.1)$$

where μ and $\nu = \mu/\rho$ are the dynamic viscosity and kinematic viscosity of air with density ρ . At the same time, since convection around the droplet is negligible, the heat transfer timescale is determined by heat diffusion only and its timescale is [133, 172]

$$\tau_\theta = \frac{1}{3} \frac{\rho_L c_L}{\lambda} r_d^2 = \frac{1}{3} \frac{\rho_L}{\rho} \frac{c_L}{c_p} \frac{r_d^2}{\kappa}. \quad (6.2)$$

For a water droplet in air $\tau_\theta \sim 4\tau_p$, therefore a droplets adjusts its temperature to the fluid temperature much slower than it does with its velocity. If the droplet is in a uniform and constant ambient, then the timescale of its growth by condensation is normally estimated as [97]

$$\tau_R = \frac{r_d^2 \rho_L}{2\kappa_v^* \rho_{vs}(T)}, \quad \kappa_v^* = \kappa_v \left(1 + \frac{L \rho_{vs}(T)}{R_v T^2} \frac{L \kappa_v}{\lambda} \right)^{-1}$$

where $\rho_{vs}(T)$, is the saturated vapour density in the surrounding ambient, L is the latent heat of condensation, R_v is the water vapour gas constant, and κ_v^* is a modified diffusivity, to account for the limiting effects of latent heat release. Since the air Prandtl number is $\text{Pr} = \nu/\kappa \sim 0.7$ and the vapour Schmidt number is $\text{Sc} = \nu/\kappa_v \sim 0.6$, then $\kappa \sim \kappa_v \sim \nu$ and, as a consequence

$$\tau_R \gg \tau_p, \tau_\theta, \tau_p \gg \tau_{d,d}, \tau_{d,a}, \tau_{d,v},$$

and the droplet growth is much slower than diffusion and its temperature/momentum relaxation. Therefore, the droplet growth can be seen as a quasi-steady process, where temperature and vapour density distributions instantaneously adjust to the much more slowly varying external conditions and droplet radius. In presence of many droplets, the heat released and water vapour absorbed gradually change the

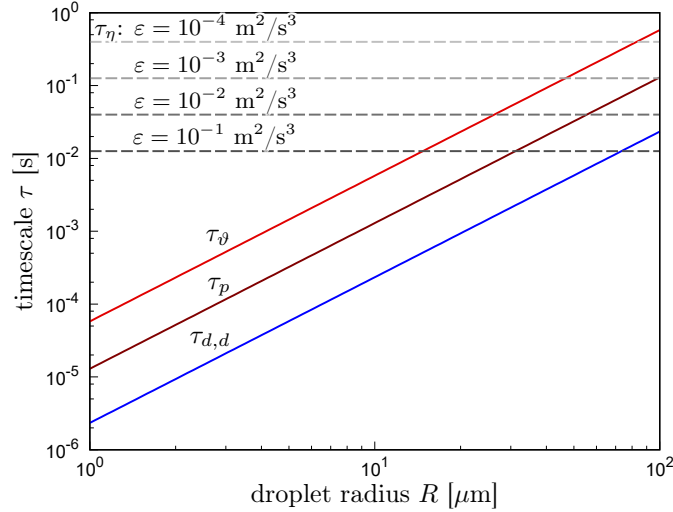


Figure 6.1: Typical timescale of the key microphysical processes affecting the evolution of a small water droplet in air as a function of the droplet radius r_d : $\tau_{d,d}$ heat diffusion timescale in the droplet; τ_p droplet momentum relaxation timescale; τ_θ droplet temperature relaxation timescale. The droplet timescales is compared with the smallest timescale of surrounding turbulence τ_η for different dissipation rates ε .

environment conditions. The timescale of this process can be evaluated, assuming a local heat balance [91, 97]

$$\tau_{\text{phase}} = \frac{1}{4\pi\kappa_v^*n_dR}$$

where n_d is the droplet number density. Since $\tau_{\text{phase}}/\tau_R = S/(2\pi n_d r_d^3) \gg 1$, with a typical supersaturation in the surrounding ambient $S = \varphi - 1$ and $\varphi = \rho_v/\rho_{vs}(T)$, the timescale of the change in the environment conditions due to the droplet phase change is much longer than the single droplet condensation timescale.

Since the flow surrounding the droplet is turbulent, there is a range of relevant external timescales, the ambient conditions change with the time scale of all the turbulent eddies. Large-scale eddies with size of order of the integral length scale ℓ , evolve with a timescale $\tau_\ell = \ell/u_{\text{rms}}$, where u_{rms} is the root mean square of velocity fluctuations. The fastest eddies have size comparable with the Kolomogorov length scale $\eta = (\nu^3/\varepsilon)^{1/4}$ and timescale $\tau_\eta = (\nu/\varepsilon)^{1/2}$. The interplay between turbulence and droplet dynamics has been discussed by [94] through the Damköhler number, defined as the ratio between the turbulent motion timescale and the phase change timescale τ_{phase} , that is, $\text{Da}_\ell = \tau_\ell/\tau_{\text{phase}}$ with reference to the large-scale motions and $\text{Da}_\eta = \tau_\eta/\tau_{\text{phase}}$ with reference to the Kolmogorov scale. However, τ_{phase} is the timescale associated to the phase change in the air due to the whole droplet ensemble, not the timescale of temperature and humidity experienced by the droplet,

the Dahmkohler number only compares the timescale of temperature and humidity changes due to local phase change and turbulent fluctuations, and it does not describe the timescales of fluctuations experienced by particles. Since single droplets are simulated in an Eulerian-Lagrangian DNS, as regards the single droplet, it is more significant to compare τ_p and τ_θ with the Kolmogorov timescale τ_η , that is, the Stokes number $St = \tau_p/\tau_\eta$ and the thermal Stokes number $St_\theta = \tau_\theta/\tau_\eta$ are the relevant dimensionless parameters. A sketch of the various timescales is shown in figure 6.1. Particles larger than $10 \div 15\mu\text{m}$ cannot be considered in thermal equilibrium with the surrounding air, since $\tau_\theta \sim \tau_\eta$ and the heat transport by droplets can have a significant impact on the fluid flow and droplets dynamics.

The timescale for the coalescence growth is determined by the average time between collisions. Its estimation is much more complex because it is the result of the interaction between the motion of all droplets and turbulence (resulting in caustics regions and clustering). Following the classical analysis by [128, 168], the collision timescale can be estimated from the droplet number density n_d and the collision rate N_c , that is the average number of collisions per unit time and volume, as

$$\tau_c = \frac{n}{N_c} \sim \frac{1}{n_d r_d^3 \sqrt{\varepsilon \nu}} = \frac{\tau_\eta}{n_d r_d^3}$$

for small, non-settling particles. Moreover, in numerical simulations, the ghost-collision approximation (in which particles can compenetrates each other) leads to overestimation of the collision rate [158] and therefore, numerical simulations which aim to analyze collision statistics should include a physical model for the outcome of droplets collision.

6.2.1 Momentum

Let us consider a droplet as an inertial point mass with variable mass $m(t)$. The equation of motion for such a system is (e.g. [146])

$$m \frac{d\mathbf{v}_d}{dt} = \mathbf{F} + \frac{dm}{dt} \mathbf{v}_r \quad (6.3)$$

where \mathbf{v}_d is the droplet velocity, \mathbf{v}_r is the relative velocity (with respect to the droplet) of the mass which condensate or evaporate and \mathbf{F} is the force on droplet. Since non-precipitating droplets are much smaller than the smallest turbulent fluctuation length-scale, they can be considered to move in a uniform fluid environment, that is, they respond only to the local velocity (and temperature) of the fluid. The Reynolds number of the relative motion to the fluid is normally smaller than one, the density of the droplet is much larger than the density of the surrounding air so that the most relevant forces on the droplet are the Stokes drag and gravity [107]

$$\mathbf{F} = 6\pi\mu r_d(\mathbf{u}_\infty - \mathbf{v}_d) + m\mathbf{g} \quad (6.4)$$

where r_d is the radius of the droplet. Additional forces, that is, added mass, pressure gradient, Faxen term and Basset history have a minor impact since the droplet/air density ratio is of order 10^3 [107], as it was discussed in more detail in the Introduction. Assuming that the contribution of the mass variation is small, that is, the condensation/evaporation is not extremely rapid and the relative velocity $|\mathbf{v}_r|$ is small, the equation for the droplet motion reduces to

$$\frac{d\mathbf{v}_d}{dt} = \frac{\mathbf{u}_\infty - \mathbf{v}_d}{\tau_p} + \mathbf{g} \quad (6.5)$$

where τ_p is the Stokes relaxation time (6.1).

6.2.2 Droplet growth

Immediately following its formation through heterogeneous nucleation, a cloud droplet grows by vapour diffusion and condensation. In this section, we analyze the equation for the growth rate of a single droplet. Let us call r_d the radius of a droplet situated in a vapour field whose density is ρ_v . Since the droplet radius is much smaller than the Kolmogorov microscale and the droplet field is quite diluted, each droplet can be considered in a uniform environment. Moreover, since the Reynolds number of the relative motion of the particle in the surrounding air is small, convection can be neglected and the temperature and vapour density fields are described by the Fourier equations,

$$\rho c_p \frac{\partial T}{\partial t} = \lambda \nabla^2 T \quad (6.6)$$

$$\frac{\partial \rho_v}{\partial t} = \kappa_v \nabla^2 \rho_v, \quad (6.7)$$

where ρ , c_p , and λ are the air density, specific heat at constant pressure and thermal conductivity, respectively, while κ_v is the diffusivity of water vapour in air. The dependence of all these parameters from temperature and vapour concentration has been neglected, since vapour concentration and temperature variations around the droplet are small. Analogously, the temperature in the spherical droplet is given by

$$\rho_L c_L \frac{\partial T}{\partial t} = \lambda_L \nabla^2 T \quad (6.8)$$

where ρ_L , c_L , and λ_L are the liquid water density, specific heat and thermal conductivity, respectively. Due to the spherical symmetry of the problem, all variables depend only on the radial coordinate r and the time t , and $\nabla^2 = \partial_{rr}^2 + (2/r)\partial_r$. The boundary conditions for $r \rightarrow +\infty$, which represent the matching with the surrounding ambient at $r \gg R$, are

$$\begin{aligned} \lim_{r \rightarrow +\infty} T &= T_\infty(t) \\ \lim_{r \rightarrow +\infty} \rho_v &= \rho_{v,\infty}(t) \end{aligned}$$

where the ambient temperature T_∞ and water vapour density $\rho_{v,\infty}$ can change with time. At the droplet-humid air interface, $r = R(t)$, we impose the continuity of temperature and of water mass flow,

$$\frac{dR}{dt} = \frac{\kappa_v}{\rho_L} \frac{\partial \rho_v}{\partial r}(R^+, t), \quad (6.9)$$

$$T(R^-, t) = T(R^+, t). \quad (6.10)$$

Moreover, the enthalpy variation due to condensation or evaporation should be equal to the heat flow, obtaining a Stefan-like condition

$$-\rho_L L \frac{dR}{dt} = -\lambda_L \frac{\partial T}{\partial r}(R^-, t) + \lambda \frac{\partial T}{\partial r}(R^+, t) \quad (6.11)$$

where L is the latent heat of condensation. By inserting (6.9) into (6.11), this last can be rewritten as

$$L\kappa_v \frac{\partial \rho_v}{\partial r}(R^+, t) = \lambda_L \frac{\partial T}{\partial r}(R^-, t) - \lambda \frac{\partial T}{\partial r}(R^+, t).$$

By integrating (6.8) in the droplet volume, using the spherical symmetry, it is possible to express the conductive heat flux at the droplet surface as

$$\lambda_L \frac{\partial T}{\partial r}(R^-, t) = \frac{1}{r_d^2} \int_0^R \rho_L c_L \frac{\partial T}{\partial t} r^2 dr,$$

so that

$$L\kappa_v \frac{\partial \rho_v}{\partial r}(R^+, t) = \frac{1}{r_d^2} \int_0^R \rho_L c_L \frac{\partial T}{\partial t} r^2 dr - \lambda \frac{\partial T}{\partial r}(R^+, t). \quad (6.12)$$

Now, by assuming that the diffusion timescales are much smaller than both the droplet growth timescale and the thermal relaxation timescale, the time derivatives in equations (6.7), (6.6) and (6.8) can be neglected and a quasi-steady solution can be used, that is,

$$\rho_v(r, t) = \rho_{v,\infty} - (\rho_{v,\infty} - \rho_{vs}(\theta_d(t))) \frac{R(t)}{r} \quad (6.13)$$

$$T(r, t) = \begin{cases} \theta_d(t) & \text{if } r \leq R(t) \\ T_\infty - (T_\infty - \theta_d(t)) \frac{R(t)}{r} & \text{if } r \geq R(t) \end{cases} \quad (6.14)$$

where $\theta_d(t)$ is the droplet surface temperature from (6.10). Introducing these solutions into (6.9) and (6.12), the following equations for the time evolution of the droplet radius and droplet temperature are obtained:

$$\frac{dR}{dt} = \frac{\kappa_v}{\rho_L} \frac{\rho_{v,\infty} - \rho_{vs}(\theta_d)}{R} \quad (6.15)$$

$$\frac{d\theta_d}{dt} = \frac{3\lambda}{\rho_L c_L r_d^2} (T_\infty - \theta_d) + \frac{3\kappa_v L}{\rho_L c_L r_d^2} (\rho_{v,\infty} - \rho_{vs}(\theta_d)) \quad (6.16)$$

Last equation can be reformulated in order to explicitly put into evidence the thermal relaxation time (6.2),

$$\frac{d\theta_d}{dt} = \frac{T_\infty - \theta_d}{\tau_\theta} + \frac{L\kappa_v \rho_{v,\infty} - \rho_{vs}(\theta_d)}{\lambda \tau_\theta}$$

The thermal inertia of the droplet is usually neglected [152, 123, 94]. This implies that the left-hand side in (6.16) is neglected and that equation reduces to an instantaneous relation between the temperature θ_d and the saturated vapour density at temperature T_∞ ,

$$\theta_d - T_\infty = \frac{L\kappa_v}{\lambda} (\rho_{v,\infty} - \rho_{vs}(\theta_d)). \quad (6.17)$$

In this way, the droplet temperature and its radius are no more independent variables and a single equation describes both processes. When θ_d is treated as an independent variable which defines state of the droplet, it is not necessary to express $\rho_{vs}(\theta_d)$ in terms of $\rho_{vs}(T_\infty)$. Anyway, the model can be simplified, neglecting the droplet thermal inertia, as in equation , to obtain an expression for $\rho_{vs}(\theta_d)$. Indeed, since it is expected that $(\theta_d - T_\infty)/T_\infty \ll 1$, then $\rho_v(\theta_d)$ can be linearized around T_∞ . By using the perfect gas state equation

$$\rho_{vs}(\theta_d) = \frac{p_{vs}(\theta_d)}{R_v \theta_d}$$

where $R_v = R/M_v$ is the gas constant of vapour, and the Clausius-Clapeyron relation, which, with the usual approximations reduces to

$$\frac{dp_{vs}}{dT} = \frac{L}{T(v_{vs} - v_L)} \simeq \frac{Lp_{vs}}{R_v T^2},$$

a first-order Taylor approximation leads to

$$\rho_{vs}(\theta_d) \simeq \rho_{vs}(T_\infty) + \frac{\rho_{vs}(T_\infty)}{T_\infty} \left(\frac{L}{R_v T_\infty} - 1 \right) (\theta_d - T_\infty).$$

Therefore, the model equations used in [94] are obtained

$$\frac{dR}{dt} = \frac{\kappa_v \rho_{v,\infty} - \rho_{vs}(T_\infty)}{\rho_L} + \frac{\kappa_v \rho_{vs}(T_\infty)}{\rho_L T_\infty} \left(\frac{L}{R_v T_\infty} - 1 \right) \frac{T_\infty - \theta_d}{R} \quad (6.18)$$

$$\begin{aligned} \frac{d\theta_d}{dt} &= \frac{3\lambda}{\rho_L c_L r_d^2} \left[1 - \frac{\kappa_v L \rho_{vs}(T_\infty)}{\lambda T_\infty} \left(\frac{L}{R_v T_\infty} - 1 \right) \right] (T_\infty - \theta_d) \\ &+ \frac{3\kappa_v L}{\rho_L c_L r_d^2} (\rho_{v,\infty} - \rho_{vs}(T_\infty)) \end{aligned} \quad (6.19)$$

Since the air velocity, temperature and vapour density are used into equations (6.5), (6.18) and (6.19), it is assumed that droplets do not interact directly between themselves, except during collisions, but only indirectly through their feedback on the ambient velocity, temperature and vapour fields.

6.2.3 Fluid flow equations

As customary, it is assumed that the flow is described by the Navier-Stokes equations within the Boussinesq approximation for small density variations from a reference ambient state with temperature T_0 , air density ρ_v and vapour density $\rho_{v,0}$, and water vapour is represented as an advected passive scalar. With the inclusion of an external forcing and particles feedback in a two-way coupling regime, the system of equations takes the following form

$$\nabla \cdot \mathbf{u} = 0 \quad (6.20a)$$

$$\frac{\partial \mathbf{u}}{\partial t} + \mathbf{u} \cdot \nabla \mathbf{u} = -\frac{1}{\rho_0} \nabla p + \nu \nabla^2 \mathbf{u} + B \mathbf{g} + \frac{1}{\rho_0} \mathbf{C}_u + \mathbf{f}_u \quad (6.20b)$$

$$\frac{\partial T}{\partial t} + \mathbf{u} \cdot \nabla T = \kappa \nabla^2 T + \frac{1}{\rho_0 c_p} C_T + f_T \quad (6.20c)$$

$$\frac{\partial \rho_v}{\partial t} + \mathbf{u} \cdot \nabla \rho_v = \kappa_v \nabla^2 \rho_v + C_d + f_v \quad (6.20d)$$

where B is the buoyancy, \mathbf{f}_u , f_T and f_v are forcing terms to obtain a statistically steady state, and the source terms \mathbf{C}_u , C_T and C_d are the particle feedback terms, that is the momentum, enthalpy and water vapour transfer per unit volume and time from the droplets to the humid air phase. Contributions from the droplets on the continuity equation are neglected. From equations (6.5), (6.15) and (6.16), the droplet back-reaction on the fluid flow is given by

$$\mathbf{C}_u = \sum_{d=1}^{N_D} m_d \frac{\mathbf{v}_d(t) - \mathbf{u}(\mathbf{x}_d, t)}{\tau_{u,d}} \delta(\mathbf{x} - \mathbf{x}_d), \quad (6.21a)$$

$$C_T = \sum_{d=1}^{N_D} c_L m_d \frac{T_{d,m}(t) - T(\mathbf{x}_d, t)}{\tau_{\theta,d}} \delta(\mathbf{x} - \mathbf{x}_d), \quad (6.21b)$$

$$C_d = \sum_{d=1}^{N_D} 4\pi \kappa_v R_m^2 (\rho_{vs}(T_{d,m}(t)) - \rho_v(\mathbf{x}_d, t)) \delta(\mathbf{x} - \mathbf{x}_d). \quad (6.21c)$$

where $m_d = 4\pi r_d^3/3$ is the mass of the d -th droplet and \mathbf{v}_d its velocity. $B \mathbf{g}$ is the buoyancy force per unit volume, where B is given by

$$B = \frac{T - T_0}{T_0} + \frac{\rho_v - \rho_{v,0}}{\rho_{v,0}}.$$

It should be noted that B does not contain any term associated with the liquid phase (droplets) in this formulation, unlike all published papers on Direct Numerical Simulations of a cloud parcel where gravity is taken into account (e.g. [152, 97, 95, 62]). Actually, the presence of the droplets in the momentum equation (6.20b) is already represented through \mathbf{C}_u . The usual formulation of buoyancy can be

recovered if it is assumed that droplets are falling with their terminal velocity $\mathbf{v}_d = \mathbf{u}(\mathbf{x}_d, t) + \tau_{u,d}\mathbf{g}$: since the liquid water phase (droplet) density is

$$\rho_w = \sum_{d=1}^{N_D} m_d \delta(\mathbf{x} - \mathbf{x}_d)$$

the force per unit mass becomes

$$\mathbf{C}_u = \sum_{d=1}^{N_D} m_d \mathbf{g} \delta(\mathbf{x} - \mathbf{x}_d) = \rho_w(\mathbf{x}, t) \mathbf{g},$$

therefore the acceleration induced on the flow, \mathbf{C}_u/ρ_0 is equal to the gravity multiplied by the liquid water mixing ratio ρ^*/ρ_0 , that is, the missing term with respect to the formulation in [152]. However, even if small Stokes number are considered, the droplet velocity can be expanded as $\mathbf{v}_d = \mathbf{u}(\mathbf{x}_d, t) + \tau_p(\mathbf{g} + D\mathbf{u}/Dt(\mathbf{x}_d, t)) + O(\tau_p^2)$ so that $\mathbf{C}_u = \rho_w(\mathbf{g} + D\mathbf{u}/Dt) + O(\tau_p)$, and the contribution of fluid acceleration is missed even for very small Stokes numbers. Moreover, since horizontal motions of droplets cannot be accounted in a buoyancy term, the presented model, which employs equations (6.20b) and (6.21a) should be able to better represent the momentum exchange between air and droplets.

6.3 Setup of the numerical simulations

Equations (6.20a) and (6.20d) describing the velocity, temperature and vapour density fields are solved using a Fourier-Galerkin pseudo-spectral method, dealiased with the 3/2 rule [23], on a cubic domain with periodic boundary conditions on all sides. The momentum balance equations (6.20b) are solved in rotation form and the Non-Uniform Fast Fourier Transform (NUFFT) is employed for the coupling between the fluid and particle phases. Time integration is carried out using a second order exponential integrator for both the fluid and the particles. Details on the numerical procedure can be found in Chapter 4 and Appendix A.

The forcing terms \mathbf{f}_u , f_T and f_v which represent the external large-scale forcing necessary to achieve a statistically steady state, are defined in wavenumber space as:

$$\hat{\mathbf{f}}_u = \varepsilon \frac{\hat{\mathbf{u}}(\mathbf{k}, t)}{\sum_{\mathbf{k} \in \mathcal{K}} \|\hat{\mathbf{u}}(\mathbf{k}, t)\|^2} \quad (6.22a)$$

$$\hat{f}_T = \chi_T \frac{\hat{T}(\mathbf{k}, t)}{\sum_{\mathbf{k} \in \mathcal{K}} \|\hat{T}(\mathbf{k}, t)\|^2} \quad (6.22b)$$

$$\hat{f}_v = \chi_v \frac{\hat{\rho}_v(\mathbf{k}, t)}{\sum_{\mathbf{k} \in \mathcal{K}} \|\hat{\rho}_v(\mathbf{k}, t)\|^2} \quad (6.22c)$$

Quantity	Symbol	Value	Unit
Latent heat of evaporation	L	$2.5 \cdot 10^6$	J/kg
Reference temperature	T_0	280	K
Air density	ρ	1.06	kg/m ³
Air kinematic viscosity	ν	$1.5 \cdot 10^{-5}$	m ² /s
Air thermal diffusivity	κ	$2.2 \cdot 10^{-5}$	m ² /s
Saturated vapour density	$\rho_{vs}(T_0)$	$7.67 \cdot 10^{-3}$	kg/m ³
Vapour mass diffusivity in air	κ_v	$2.3 \cdot 10^{-5}$	m ² /s
Liquid water density	ρ_L	1000	kg/m ³
Liquid water thermal diffusivity	κ	0.5	m ² /s
Dissipation rate	ε	$5 \cdot 10^{-3}$	m ² /s ³
Taylor microscale Reynolds number	Re_λ	115	
Kolmogorov length scale	η	1	mm
Integral length scale	ℓ	75	mm
R.m.s. velocity	u'	0.1	m/s
Domain size		0.36	m
Number of Fourier modes (3/2 rule)		256^3	
Forced wavenumber	k_f	3	
Kolmogorov time scale	τ_η	0.055	s
Integral time scale	\mathcal{T}	0.8	s
Simulated time interval	T	90	s
Droplet initial volume fraction	ϕ	10^{-6}	
Droplet initial radius	r_0	10, 15, 20	μm
Number of droplets	N_D	11664896, 3456256, 1457920	
Droplet initial Stokes number	St_0	0.03, 0.06, 0.10	
Initial thermal Stokes number	$St_{\theta,0}$	0.11, 0.25, 0.45	

Table 6.1: Main parameters employed in the presented numerical simulations.

where \mathcal{K} is the set of forced wavenumbers, ε , χ_T and χ_v are the imposed turbulent dissipation, temperature and vapour density fluctuation variance, respectively:

$$\varepsilon = \nu \left\langle \frac{\partial u_i}{\partial x_k} \frac{\partial u_i}{\partial x_k} \right\rangle, \quad \chi_T = \kappa \left\langle \frac{\partial T}{\partial x_k} \frac{\partial T}{\partial x_k} \right\rangle, \quad \chi_v = \kappa \left\langle \frac{\partial \rho_v}{\partial x_k} \frac{\partial \rho_v}{\partial x_k} \right\rangle.$$

Additionally, a deterministic forcing scheme that imposes the root mean square of the scalar fields has been employed. Parameters have been set up so that the grid spacing in physical space, after dealiasing, is comparable to the Kolmogorov scale η , while forcing is applied at the largest scales of the simulated flow, that is $\mathcal{K} = \{\mathbf{k} : \|\mathbf{k}\| - k_f < 0.5\}$, with forced wavenumber $k_f = 3$. Forcing is applied to all the air phase fields, velocity, temperature and vapour density, in order to maintain a statistically steady state (with the exception of the slow droplet growth and its

back-reaction on the fluid flow). The mean value of vapour density is set to have a unity mean relative humidity (zero mean supersaturation), so that the droplet size distribution broadens mainly due to humidity fluctuations. Therefore, because collisions are still quite rare events in the range of parameters considered, droplet-droplet collisions and hydrodynamical interactions are ignored. Here we aim to investigate how the thermal inertia of droplets modifies small scale turbulence and affects the broadening of droplet size distribution. We do not consider gravitational settling, even if gravity and stratification are included in the model, so that focus is put on heat exchange while the interplay between turbulence and sedimentation, which has been already considered (e.g. [65]) is left for future investigations.

6.4 Results

In this Section preliminary results from Direct Numerical Simulations of a forced, statistically isotropic turbulent flow are presented. The turbulent air flow advects its temperature and humidity, which are treated as passive scalars, together with the particles. The droplets are initially monodisperse and, due to the turbulent fluctuations, some droplets shrink and other droplets grow, broadening the droplet size distribution. Focus is put on that size broadening and on the interaction between the droplets and the temperature/humidity fields. The main simulation parameters are listed in Table 6.1.

6.4.1 Droplet size distribution

The evolution of initially monodisperse droplets with radius ranging from 10 to 20 μm is investigated, with focus on the effects of the temperature inertia and external forcing. Deterministic large-scale forcing is implemented to maintain a constant average dissipation rate $\epsilon = 5 \cdot 10^{-3} \text{ m}^2/\text{s}^3$. The deterministic also maintains constant energy of the fluctuations of the scalar fields. The mean temperature is 280 K and its root mean square value is 0.06% of the mean value. The mean vapour density is $7.67 \times 10^{-3} \text{ kg}/\text{m}^3$ and its root mean square is 0.6% of the mean value. The stochastic forcing consists of a Wiener process, which variance is tuned in order to reproduce the values imposed by means of the deterministic forcing. The resulting variances of the flow fields forced with the two different methods turned out to be the same, but the flow fields forced with a Wiener process have larger dissipation rates. This aspect should be improved in future works, trying to obtain similar small-scale statistics of the fields forced with the two different methods, in order to better isolate the effect of the forcing scheme. At any rate, in the presented results, differences in the characteristic scales of the flows maintained by deterministic and stochastic forcing do not exceed 10%. The mean vapour density is set equal to the saturated vapour density at the mean temperature so that there is no

mean growth. However, when droplet temperature fluctuations are considered, this condition is not straightforward to realize, since it requires

$$\left\langle \frac{\rho_v(\mathbf{x}_d, t) - \rho_{vs}(\theta_d)}{r_d} \right\rangle = 0 \quad (6.23)$$

and therefore, even when $\langle \rho_v \rangle = \rho_{vs}(T_0)$ variations of the mean droplet radius can still take place, due to independent fluctuations of ρ_v and θ_d .

The standard deviation of the droplet radius square is usually employed to analyze the broadening of the droplet size distribution. Indeed, the equation for the particle radius resembles that of a Ornstein-Uhlenbeck process

$$\frac{dr_d^2}{dt} = 2 \frac{\kappa_v}{\rho_L} (\rho_v(\mathbf{x}_d, t) - \rho_{vs}(\theta_d))$$

if $\rho_v(\mathbf{x}_d, t)$ is assumed to be uncorrelated from the particle dynamics and with Gaussian statistics. A stochastic model for the droplet radius has been developed by [132] emulating the equations for evaporation/condensation based on the Twomey model forced with a Wiener process. The results showed clear diffusive scaling of the standard deviation of the droplet radius squared, $\sigma_{r_d^2} \sim \sqrt{t}$. In this work we aim to understand how much of that net diffusive scaling originates from the external forcing and how much from the spontaneous tendency of the scalar fields to develop Gaussian statistics. Figure 6.2(a) shows the time evolution of the standard deviation of the droplet radius squared for different initial radii r_0 and with deterministic and stochastic forcing. The droplet thermal inertia is considered in those simulations so that the droplet temperature is an independent state variable. As expected, the droplet size distribution broadens with a standard deviation that grows approximately as the square root of time. However, the $\sim \sqrt{t}$ trend is evident when stochastic Gaussian forcing is employed for all the initial radii, while it is clear only for the smallest initial radius ($r_0 = 10\mu\text{m}$) when deterministic forcing is employed. For larger initial radii, with deterministic forcing, the transient before the power law trend can last relatively long (about one minute) and even when the power law trend is established the exponent seems less than the expected 0.5. This aspect will be examined in more detail looking at the PDF of the droplet radius and its rate of change. The results show that, even if forcing is confined at large scales, much larger than the droplet size, it can considerably influence the droplet dynamics quantitatively and qualitatively. This has been observed for the temperature statistics of inertial particles in turbulence [8, 25] since, as the particle thermal response time approaches zero, the particle temperature rate of change is governed by a stochastic forcing term.

Figure 6.2(a) shows time evolution of the standard deviation of the droplet radius squared for different initial radii r_0 including and neglecting the droplet thermal inertia. Deterministic forcing is employed in those simulations. The droplet

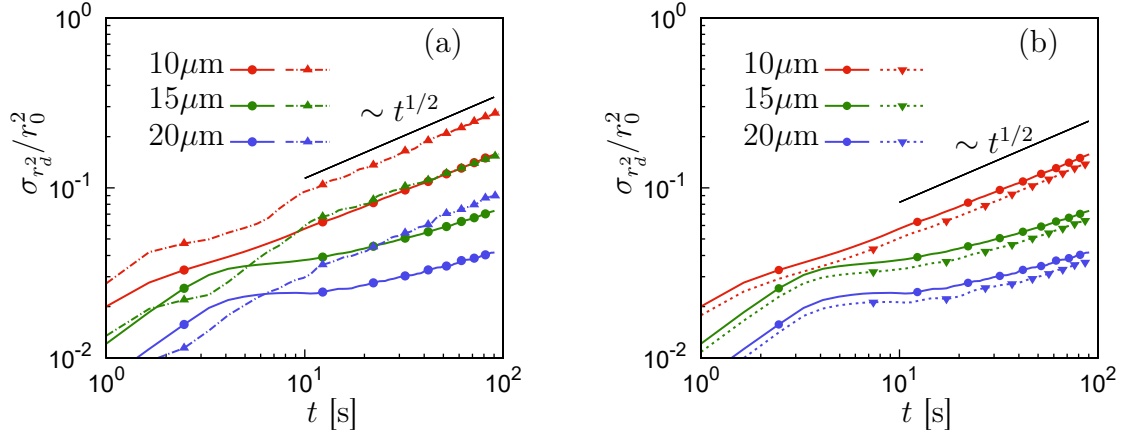


Figure 6.2: Time evolution of the square droplet radius standard deviation for different initial radius r_0 and various simulation setup. (a) Effect of the forcing method. Solid lines refer to simulations with deterministic forcing and dash-dot lines refer to simulations with stochastic forcing, droplet thermal inertia is considered in both the sets of simulations. (b) Effect of the droplet thermal inertia. Solid lines refer to simulations in which droplet thermal inertia is considered (model proposed in this work) and dotted lines refer to simulations in which droplet thermal inertia are not considered (Vaillancourt model), deterministic forcing is employed in both the sets of simulations.

thermal inertia contributes to enhance the droplet size distribution broadening even if its effect is quite small. The variance of the size of the smallest droplets tends to grow faster while larger droplets grow slower since $d_t r_d \sim 1/r_d$. The proposed model, which includes the droplet thermal inertia, always predicts a faster droplet growth than the classic model [152]. The effect of the thermal inertia is relatively large if compared to extremely small temperature fluctuations considered. Indeed the temperature standard deviation is the 0.06% of its mean value that corresponds to approximately 0.17 K. Therefore, the droplet size distribution seems to be very sensitive to droplet temperature fluctuations, which can be relevant in strong mixing regions where larger temperature fluctuations can take place. Moreover, the effect of the thermal inertia is more relevant for larger droplets, which have larger thermal Stokes number, and it can positively contribute to overcome the bottleneck in the droplet growth process, in the transition between condensation-dominated growth to collision-dominated droplet growth.

Figures 6.3(a-c-e) show the probability density function (PDF) of the droplet radius at different times, employing different forcing methods and for various initial radii r_0 . The droplet size distribution of small droplets is slightly negatively skewed, since the radius rate of change increases as the droplet becomes smaller. Therefore, the evaporation of smaller droplets is faster than the growth of larger droplets. The

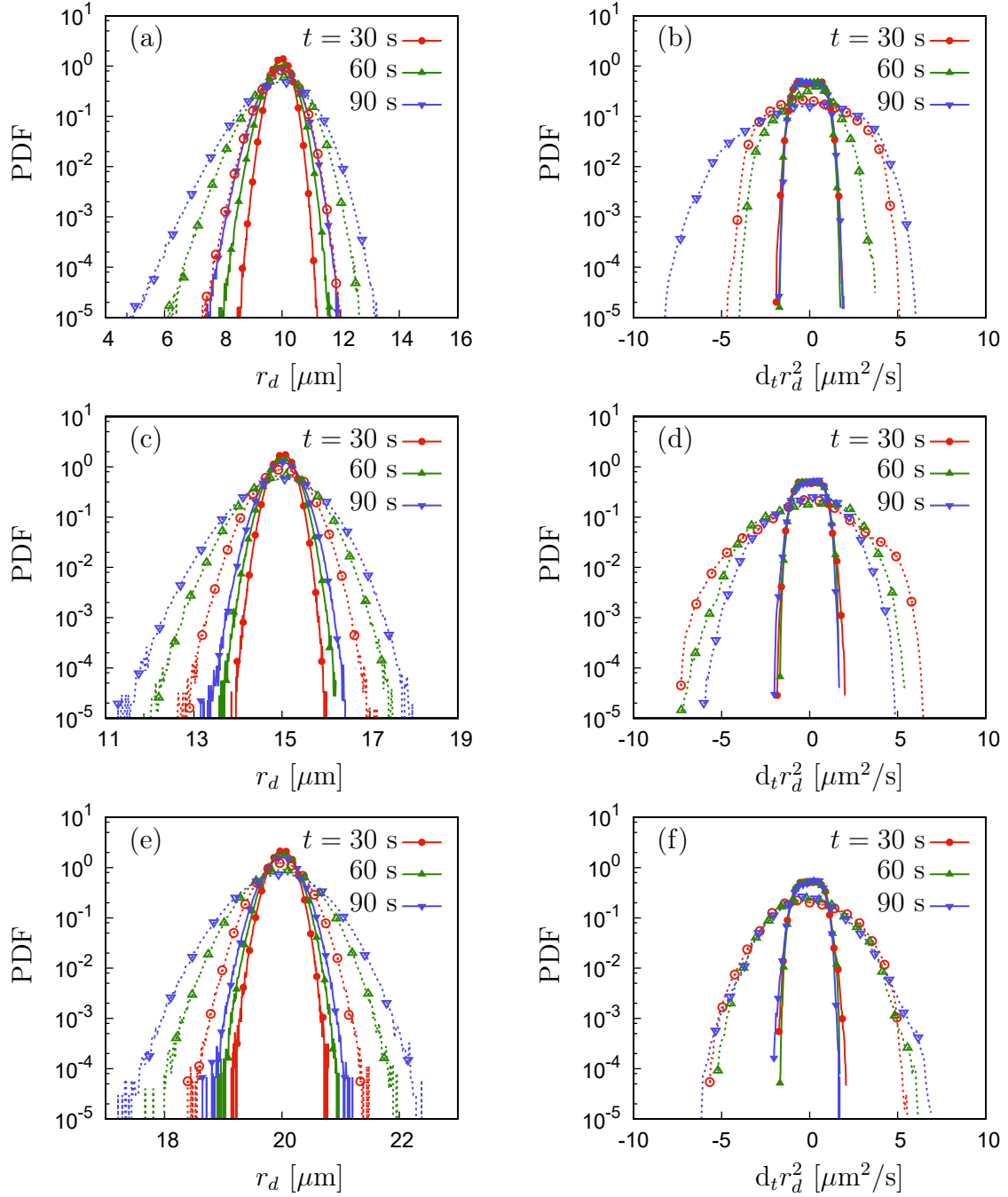


Figure 6.3: Probability Density Function (PDF) of the droplet radii (a-c-e) and (b-d-f) PDF of the rate of change of the droplet radius squared. The PDFs are computed at different times. Solid lines refer to simulations with deterministic forcing which imposes the average kinetic energy dissipation rate and the root mean square of the scalar fields. Dotted lines indicate simulations with stochastic forcing tuned in order to emulate the average dissipation rate and root mean square values imposed by the deterministic forcing.

asymmetry becomes less evident as the initial droplet radius is increased and the distribution approaches a Gaussian shape. Again, the droplet size distribution is closer to Gaussian when stochastic Gaussian forcing is employed.

Figures 6.3(b-d-f) show the PDF of the rate of change of the droplet radius squared, $d_t r_d^2$, for initial radii $r_0 = 10, 15, 20 \mu\text{m}$. This quantity is proportional to the supersaturation $\varphi = \rho_v/\rho_{vs}(\theta_d) - 1$ if fluctuations of the saturated vapour density are neglected. The qualitative difference between the statistics in simulations forced with deterministic and stochastic forcing is evident. When stochastic forcing is employed, the distribution of the rate of change of the particle surface is very close to Gaussian. On the other hand, when the fields are sustained by deterministic forcing the distribution of $d_t r_d^2$ is almost flat around moderate values and decays fast for larger values, displaying markedly sub-Gaussian tails. This sub-Gaussianity of the droplet surface rate of change can explain why $\sigma_{r_d^2}$ tends to grow slower than \sqrt{t} when deterministic forcing is employed to maintain statistically steady flow fields. Those results show that the rate of change of the droplet radius is dominated by a stochastic forcing and that the statistics of the largest scales strongly affect the droplet radius dynamics. Therefore, attention should be paid to the setup of direct numerical simulations in statistically steady turbulence since the small-scale universality hypothesis which seems to be satisfied by the velocity field is not fulfilled by the droplets. Universality issues have been observed also in the small-scale dynamics of passive scalars in turbulence [63].

6.4.2 Droplet temperature distribution

The droplet temperature distribution, at various times, for different initial radii and for deterministic and stochastic forcing schemes is shown in figure 6.4. After the initial transient the droplet temperature distribution remains almost steady, the maximum/minimum temperature being imposed by the energy of the surrounding temperature field. The results for larger particles show how the external forcing affects the distribution of the droplet temperature, that is particularly sensitive to a stochastic forcing [8] since the droplet thermal response time is quite small, $St_\theta < 0.45$ in the presented simulations. If a deterministic forcing is employed, small deviations of the droplet temperature from the mean temperature are very likely while large fluctuations take place rarely, the distribution has sub-Gaussian tails. On the other hand an external Gaussian forcing imposes a temperature distribution which is close to Gaussian. It should be noted that the root mean square values of the flow fields forced with deterministic and stochastic forcing are the same. The effect of the forcing can be enhanced by the relatively low Reynolds number in the presented simulations. A higher Reynolds number would result into a larger inertial range and a wider scale separation between the scales of the droplet phase and the forced scales.

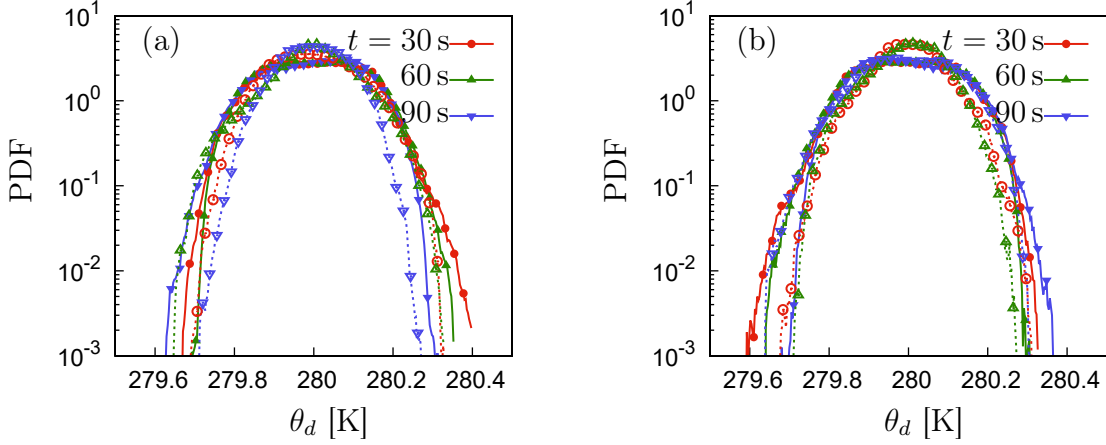


Figure 6.4: Probability Density Function of the droplet temperature for (a) $r_0 = 10\mu\text{m}$ and (b) $r_0 = 20\mu\text{m}$. Solid lines refer to deterministic forcing, dotted lines to stochastic forcing.

6.4.3 Droplet–scalar gradients interaction

Inertial particles in turbulence tend to cluster in correspondence of the sharp gradients of the scalar fields [8]. Therefore, the spatial distribution of cloud droplets, with respect to the temperature and humidity fields gradients, has a strong effect on the droplet growth. Droplets which are located in correspondence of large vapour density gradients can experience very large supersaturation fluctuations along their path. Droplets clustering is characterized by means of the radial distribution function (RDF) shown in figure 6.5. The radial distribution function is defined as

$$g(r) = \frac{1}{n_d} \frac{\delta N_d(r)}{4\pi\delta r^3/3} \quad (6.24)$$

where n_d is the average droplet number density and $\delta N_d(r)$ is the number of particles contained in a spherical shell of volume $4\pi\delta r^3/3$. Since the droplets have different size also the radial mass distribution can be defined

$$g_m(r) = \frac{1}{\rho_L\phi} \frac{\delta M_d(r)}{4\pi\delta r^3/3} \quad (6.25)$$

where M_d is the liquid water mass contained in a spherical shell of volume $4\pi\delta r^3/3$. However, in the range of parameters analyzed in this work, $g_m(r)$ and $g(r)$ are almost indistinguishable. The results for the RDF are in agreement with the results for monodisperse particles [81], therefore, in this range of parameters, the effect of polydispersity on clustering is small. The numerical results overestimate the clustering in real droplets [99] mainly due to the huge difference between the actual Reynolds number in atmospheric clouds and the simulated Reynolds number. The

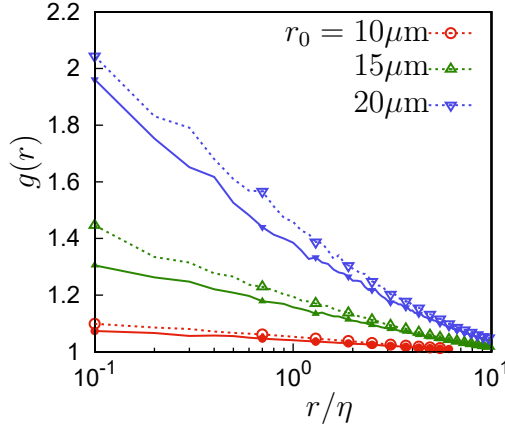


Figure 6.5: Droplet radial distribution (RDF) at $t = 90$ s. Solid lines refer to flow fields sustained by deterministic forcing, dotted lines indicate flow fields sustained by stochastic forcing.

effect of the forcing is moderate and likely due to the differences between the small scale parameters between the two sets of simulations.

The droplets can experience strong vapour density and temperature fluctuations along their path if they can cross the sharp gradients of the scalar fields (which are referred to as fronts). The particle flux across the vapour density fronts is quantified by means of

$$q_0 = \frac{1}{u'} \mathbf{v}_d \cdot \frac{\nabla \rho_v(\mathbf{x}_d, t)}{\|\nabla \rho_v(\mathbf{x}_d, t)\|} \quad (6.26)$$

and conditioned average upon the magnitude of the vapour density gradient, $\|\nabla \rho_v\|$, will be considered. Figure 6.6(a) shows that the particle flux across the surface at constant vapour density decreases as the magnitude of the vapour density gradient increases. The trend is very similar to the trend observed for the same quantity q_0 conditioned on the local temperature gradient [25]. The orientation between the droplet velocity and local vapour density gradient is characterized by

$$\cos \alpha = \frac{\mathbf{v}_d}{\|\mathbf{v}_d\|} \cdot \frac{\nabla \rho_v(\mathbf{x}_d, t)}{\|\nabla \rho_v(\mathbf{x}_d, t)\|} \quad (6.27)$$

and the reduction of the particle flux is caused by statistical misalignment between \mathbf{v}_d and $\nabla \rho_v(\mathbf{x}_d)$ as $\|\rho_v(\mathbf{x}_d)\|$ is increased, as figure 6.6(b) shows.

The interaction between the scalar fields and droplets is investigated by looking at the transport of heat and mass fluxes across the temperature and vapour density fronts. For the temperature field we define

$$q_1^{(T)} = \frac{\mathcal{T}}{r_0^3 T_0 u'} \frac{d}{dt} (r_d^3 \theta_d) \mathbf{v}_d \cdot \frac{\nabla T(\mathbf{x}_d, t)}{\|\nabla T(\mathbf{x}_d, t)\|} \quad (6.28)$$

that is, by using equation (6.16)

$$q_1^{(T)} = \frac{\mathcal{T} r_d^3}{r_0^3 T_0 u'} \frac{T(\mathbf{x}_d, t) - \theta_d}{\tau_\theta} \mathbf{v}_d \cdot \frac{\nabla T(\mathbf{x}_d, t)}{\|\nabla T(\mathbf{x}_d, t)\|} \quad (6.29)$$

where u' and \mathcal{T} are the integral scale velocity and time respectively. This quantities has been employed to study the thermal interaction between the fluid flow and the suspended particles [25] and revealed how, in absence of droplet mass variations and fixed thermal dissipation rate, the particles always smooth out the temperature field. The average of $q_1^{(T)}$ conditioned on $\|\nabla T\|$ is in figure 6.6(c) and it shows that particles tend to smooth the temperature field also when latent heat release/absorption is included. The smoothing effect of the droplets is evident also at in correspondence of the smallest temperature gradients (that is at the largest scales), due to the lack of instantaneous thermal equilibrium between the droplet and the surrounding fluid flow caused by the droplets condensation/evaporation.

In order to characterize the interaction between the droplets and the vapour density field we define

$$q_1^{(\rho_v)} = \frac{\mathcal{T}}{r_0^3 u'} \frac{dr_d^3}{dt} \mathbf{v}_d \cdot \frac{\nabla \rho_v(\mathbf{x}_d, t)}{\|\nabla \rho_v(\mathbf{x}_d, t)\|} \quad (6.30)$$

that is, by using equation (6.15)

$$q_1^{(\rho_v)} = \frac{3\mathcal{T}R k_v}{r_0^3 u' \rho_L} (\rho_v(\mathbf{x}_d, t) - \rho_{vs}(\theta_d)) \mathbf{v}_d \cdot \frac{\nabla \rho_v(\mathbf{x}_d, t)}{\|\nabla \rho_v(\mathbf{x}_d, t)\|}. \quad (6.31)$$

The physical meaning of the defined quantity is as follows. When the particle moves towards a region with higher vapour density ($\mathbf{v}_d \cdot \nabla \rho_v > 0$) and it is growing ($dr_d^3 > 0$) then $q_1^{(\rho_v)} > 0$ and the droplet will absorb mass from the higher ρ_v region, smoothing the vapour density field. Analogously, when the particle moves towards a region with lower vapour density ($\mathbf{v}_d \cdot \nabla \rho_v < 0$) and it is shrinking ($dr_d^3 < 0$) then $q_1^{(\rho_v)} > 0$ and the droplet will release mass into the lower ρ_v region, smoothing the vapour density field. Therefore, $q_1^{(\rho_v)}$ positive corresponds to the particles smoothing out the vapour density field, while $q_1^{(\rho_v)}$ negative corresponds to the particles enhancing the vapour density gradients. $q_1^{(\rho_v)}$ is positive for large vapour density gradients and large droplets. Therefore, large droplets tend to effectively smooth out the vapour density fronts, indirectly reducing their growth rate, which is an additional limitation to further growth of large droplets. However, larger droplets can cross the vapour density fronts more easily because of their inertia, enhancing the vapour density fluctuations experienced along their path. $q_1^{(\rho_v)}$ is negative for $\|\nabla \rho_v\|$ very small indicating that the droplets are shrinking on average. This is due to the condition (6.23) being not exactly satisfied, because of the independent fluctuations of θ_d and ρ_v . This aspect should be improved in future work.

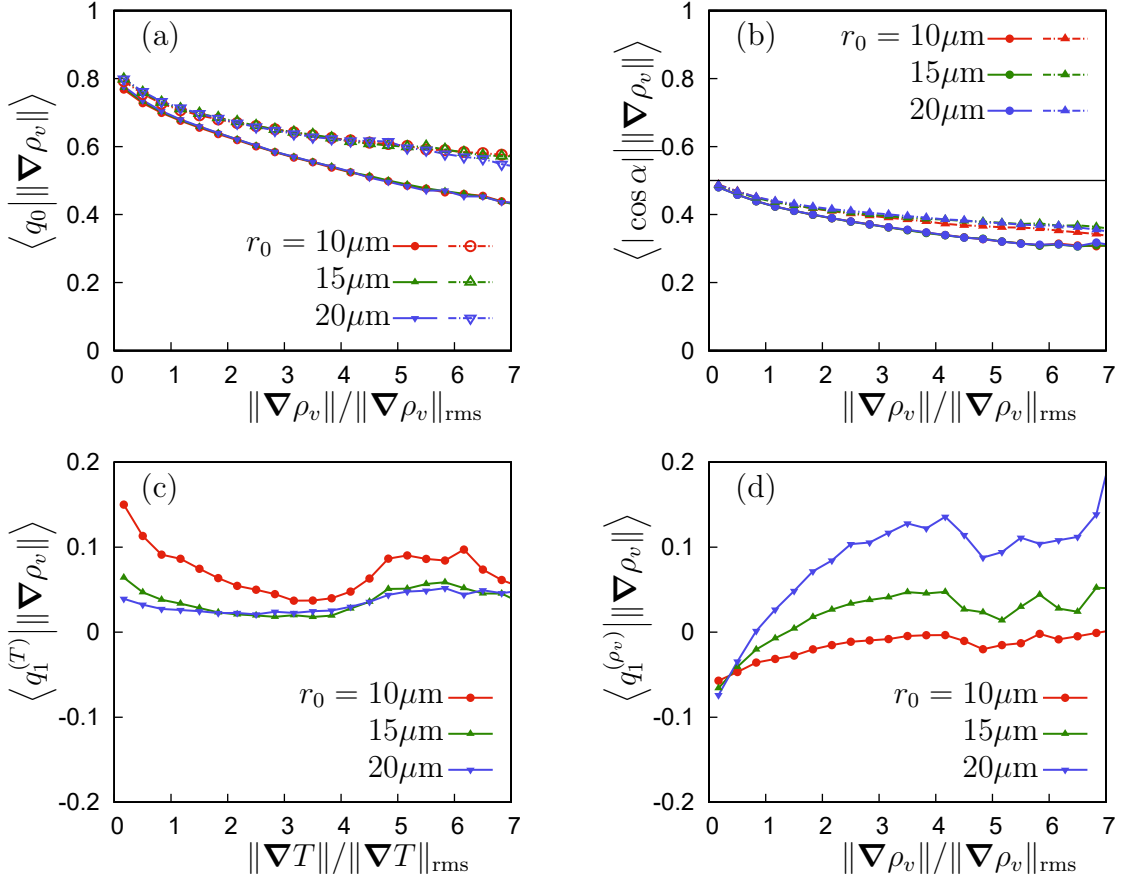


Figure 6.6: Particle flux across the scalar fields at $t = 90\text{s}$. (a) Droplet velocity component along the vapour density gradient at the droplet position. (b) Orientation between the droplet velocity and the vapour density gradient at the droplet position. (c) Thermal diffusive flux due to the particle motion across the temperature field. (d) Water mass flux due to the droplet motion across the vapour density field.

6.5 Conclusions

Water vapour transport by diffusion to or from a water droplet involves a substantial flow of heat as well, owing to the release or absorption of heat during the phase change, which produces a temperature difference between the particle and the local environment. This causes a heat flow by thermal diffusion between the droplet and the surrounding air. When the thermal relaxation time of the droplet is not negligible with respect to the timescales of turbulent fluctuations and temperature fluctuations are relevant, the heat flow between droplets and fluid can enhance the broadening of the droplet size. Also the forcing method turned out to play a significant role in the droplet size distribution, despite the wide scale separation between droplet size and forced scale. A Gaussian forcing produces Gaussian droplet statistics, which result into the diffusive growth of the standard deviation of the droplet surface ($\sigma_{r_d^2} \sim \sqrt{t}$), while a deterministic forcing produces sub-Gaussian distributions, which result into a long transient in the droplet growth before approaching a regime close to ($\sigma_{r_d^2} \sim \sqrt{t}$). The fluxes of heat and mass across the temperature and vapour density fronts due to the droplet inertia show that particles with large inertia can carry heat and mass across the flow, resulting into smoothing of the flow fields. The results showed that the preferential concentration of larger droplets in correspondence of the gradients of the temperature and vapour density fields, together with their capability to cross the scalar fronts, leads to large fluctuations of the scalar fields along the particle path which can enhance further growth of large droplets. This effect can be particularly relevant at very large Reynolds numbers, which is a key feature of atmospheric clouds.

Appendix A

The numerical code

A Fortran-MPI code for the numerical simulation of two-way coupled particle-laden flows has been developed by the candidate during the PhD period. A standard Fourier pseudo-spectral solver for the Navier-Stokes equations has been implemented, together with the Non-Uniform Fast Fourier Transform for the coupling between the fluid flow and the dispersed particles. In this Appendix the main features of the algorithms employed and their parallel implementation are presented. The main modules of the code are reported and briefly described.

A.1 Setup for Fourier Transforms

The Fast Fourier Transforms required for the pseudo-spectral solver and NUFFT's are carried out in parallel by means of the P3DFFT library [118]. Pruned Fourier transforms are employed, that is, the fields in physical space are discretized into a finer grid with respect to the fields in Fourier space. This corresponds to take the discrete FFT of a field and neglect the largest frequencies or, equivalently, to interpolate the field on an oversampled grid by means of the inverse discrete FFT. In particular, physical space fields are discretized into M_x, M_y, M_z grid points and Fourier space fields are discretized into N_x, N_y, N_z wave numbers. Due to the Hermitian symmetry for real fields the Fourier transform can be truncated along one direction and only $N_x/2+1$ wave numbers are employed. The oversampling factor can be chosen, usually $M_x=3*N_x/2$ is employed (the factor is the same along y and z), which is the minimum oversampling factor to ensure de-aliasing of the convolution sums [23]. The grid step Δx is chosen as $\Delta x = 2\pi/M$ while the step in Fourier space is unitary, $\Delta k = 1$. The number of points along the y direction is set as reference, $M=M_y$. The important point for the FFT algorithm is that $\Delta x \Delta k = 2\pi/M$ and any combination of Δx and Δk which satisfy that condition can be chosen. The component of a field in physical space, indicated by `P_u(:, :, i)`, requires $M_x * M_y * M_z$ real numbers of `kind=p3dfft_type` (usually 4 or 8) and its Fourier transform, indicated

by, indicated by $F_u(:, :, i)$, occupies $(N_x/2+1)*N_y*N_z$ **complex** numbers of the same kind. Therefore, physical and Fourier representations are almost of the same size, the Fourier representation being slightly larger.

A.2 Domain parallelization

The domain is divided into pencils and each pencil is assigned to a MPI process. In physical space the coordinates y and z correspond to MPI directions 1 and 2 and are divided into $\text{dims}(1)$ and $\text{dims}(2)$ slices respectively, while direction x is not parallelized. Thus, the domain is divided into $\text{dims}(1)*\text{dims}(2)$ pencils which are managed by $N_{\text{procs}}=\text{dims}(1)*\text{dims}(2)$ processors. Left/right is used to indicate the direction along y while up/down identifies the direction along z . Each pencil has a halo region that is used for interpolation of the fields at the particle position and for the computation of the particle back-reaction on the fluid flow. The size of the halo region depends on the number of grid points used for interpolation, that is, on the degree of the B-spline employed. When N_{stencil} grid points are used for interpolation then, along the y coordinate, $\text{padd1L}=(N_{\text{stencil}}-1)/2+d_{\text{cache}}$ points are added on the left of the pencil and $\text{padd1R}=N_{\text{stencil}}/2+d_{\text{cache}}$ are added on the right (the division between non-negative integers is rounded down). The same padding is employed along the z coordinate and the size of each pencil is then $M_x, (\text{padd1L}+M_y+\text{padd1R})/\text{dims}(1), (\text{padd2L}+M_y+\text{padd2R})/\text{dims}(2)$ which is stored into the array $P_{\text{size}}(1:3)$. The pencil starts at $P_{\text{start}}(:)$ and ends at $P_{\text{end}}(:)$. d_{cache} additional grid points are employed in order to reduce the communications to exchange particles. Due to the CFL condition $u_{\text{max}}\Delta t \leq \Delta x$, then some particles will exit the bounds of the pencil only after d_{cache} time steps. Therefore, if d_{cache} additional grid points are employed, the particles should be sorted among the processors every d_{cache} time steps. The additional halo region acts like a cache for the MPI processes. Increasing that cache size in general speeds up the computation in the one-way coupling regime, however, it has some drawbacks when the physical model is enriched. Indeed, a larger cache region requires to exchange a larger portion of the particle back-reaction fields and, if collisions are included, it also requires to exchange more particles at the boundaries between processors.

In Fourier space, the k_y and k_x wave-numbers correspond to MPI directions 1 and 2 and are divided into $\text{dims}(1)$ and $\text{dims}(2)$ slices respectively, while direction k_z is not parallelized. The size of each pencil is then $N_z, N_y/\text{dims}(1), (N_x+2)/(2*\text{dims}(2))$ which is stored into the array $F_{\text{size}}(1:3)$. The pencil starts at $F_{\text{start}}(:)$ and ends at $F_{\text{end}}(:)$. The pencil domain is not padded in Fourier space. The Fourier space parallelization is important for the P3DFFT library routines and for the Input/Output of the flow fields.

A.3 Navier-Stokes equations pseudo-spectral solver

A.3.1 Time integration

A second order Runge-Kutta exponential integrator is employed [76]. The fields are integrated in Fourier space and the first integration step reads

$$\bar{\mathbf{u}}_{n+1}(\mathbf{k}) \leftarrow \mathbf{u}_n(\mathbf{k}) + \Delta t \phi_1 \mathbf{a}_n[\mathbf{u}_n, (\mathbf{x}_p)_n, (\mathbf{v}_p)_n](\mathbf{k}), \quad (\text{A.1a})$$

$$\phi_1 = \frac{1 - e^{-z}}{z} \quad (\text{A.1b})$$

$$z = \|\mathbf{k}\|^2 \nu \Delta t / \text{Sc} \quad (\text{A.1c})$$

where \mathbf{a}_n includes convection, forcing and particle back-reaction, while the diffusive term is included in the exponential integrator weight. The same steps are performed for the velocity field and the scalar fields and Sc indicates the corresponding Schmidt number. The scheme employed introduces minimal numerical diffusion [76]. Nyquist frequencies are also set to zero during the time-integration, minimizing cache-missing.

```

do j = 1, N_comp
  js = max(1, j-2)
  aux = Sc(js)/nu
  if(proc_id .eq. 0) F_u(1, 1, 1, j) = F_u(1, 1, 1, j) + dt*F_A0(1, 1, 1, j)
do i3 = F_start(3), Nx_Nyq-1
  ex = kexp_x(i3, js)
do i2 = F_start(2), F_end(2)
  if(i2 .ne. Ny_Nyq) then
    exy = ex*kexp_y(i2, js)
do i1 = F_start(1), Nz_Nyq-1
    exyz = exy*kexp_z(i1, js)
    phil = 1_rtype - exyz
    phil = phil*aux*k2(i1, i2, i3)
    F_u(i1, i2, i3, j) = exyz*F_u(i1, i2, i3, j) + phil*F_A0(i1, i2, i3, j)
end do
F_u(Nz_Nyq, i2, i3, j) = imag0
do i1 = Nz_Nyq+1, F_end(1)
    exyz = exy*kexp_z(i1, js)
    phil = 1_rtype - exyz
    phil = phil*aux*k2(i1, i2, i3)
    F_u(i1, i2, i3, j) = exyz*F_u(i1, i2, i3, j) + phil*F_A0(i1, i2, i3, j)
end do
else
  F_u(F_start(1):F_end(1), Ny_Nyq, i3, j) = imag0
end if
end do
end do
end do
if(coords(1) .eq. dims(1) - 1) F_u(F_start(1):F_end(1), :, Nx_Nyq, j) = imag0
end do

```

The second integration step reads

$$\mathbf{u}_{n+1}(\mathbf{k}) \leftarrow \bar{\mathbf{u}}_n(\mathbf{k}) + \Delta t \phi_2 \{ \mathbf{a}_{n+1} [\bar{\mathbf{u}}_{n+1}, (\bar{\mathbf{x}}_p)_{n+1}, (\bar{\mathbf{v}}_p)_{n+1}] (\mathbf{k}) - \mathbf{a}_n [\mathbf{u}_n, (\mathbf{x}_p)_n, (\mathbf{v}_p)_n] (\mathbf{k}) \}, \quad (\text{A.2a})$$

$$\phi_1 = \frac{1 - e^{-z}}{z}, \quad \phi_2 = \frac{1 - \phi_1}{z} \quad (\text{A.2b})$$

$$z = \|\mathbf{k}\|^2 \nu \Delta t / \text{Sc}. \quad (\text{A.2c})$$

The field $\bar{\mathbf{u}}_{n+1}$ is stored into F_u and results from the previous step (A.1).

A.3.2 Convective terms

In the presented version of the code the Navier-Stokes equations are written in rotation form. The gradient part of the convective term is included in the total pressure,

$$\mathbf{a}_{\text{convective}} = \mathbf{u} \times \boldsymbol{\omega} - \nabla \bar{P}^0. \quad (\text{A.3})$$

The pressure is implicitly computed by projecting the Fourier transform of the velocity field onto the plane orthogonal to the wave-vector \mathbf{k} :

$$\hat{\mathbf{u}} \leftarrow \hat{\mathbf{u}} - \mathbf{k} \frac{\hat{\mathbf{u}} \cdot \mathbf{k}}{\|\mathbf{k}\|^2}$$

Therefore, the pressure gradient compensates the divergent contribution of both the convective term and particle back-reaction.

```

subroutine convective(u, A)
use variables, only: P_u, P_omg, P_tmp, F_tmp
implicit none

complex(p3dfft_type), dimension(F_start(1):F_end(1)+padd_c, &
F_start(2):F_end(2), F_start(3):F_end(3), N_comp), intent(in) :: u
complex(p3dfft_type), dimension(F_start(1):F_end(1)+padd_c, &
F_start(2):F_end(2), F_start(3):F_end(3), N_comp), intent(out) :: A
integer :: i1, i2, i3
integer :: j, k

!vorticity in P space
allocate(P_omg(P_start(1):P_end(1), &
P_start(2):P_end(2), &
P_start(3):P_end(3), 3))
!aux in Fourier space
allocate(F_tmp(F_start(1):F_end(1)+padd_c, &
F_start(2):F_end(2), &
F_start(3):F_end(3)))

```

```

!compute vorticity_x
forall(i1=F_start(1):F_end(1), i2=F_start(2):F_end(2), &
      i3=F_start(3):F_end(3))
  F_tmp(i1, i2, i3) = k_y(i2)*u(i1, i2, i3, 3) - k_z(i1)*u(i1, i2, i3, 2)
  F_tmp(i1, i2, i3) = F_tmp(i1, i2, i3)*imagI
end forall
!F to P vorticity_x
call p3dfft_btran_c2r(F_tmp(F_start(1):F_end(1), :, :), &
& P_omg(P_start(1):P_end(1), :, :, 1), 'fff')

!compute vorticity_y
forall(i1=F_start(1):F_end(1), i2=F_start(2):F_end(2), &
      i3=F_start(3):F_end(3))
  F_tmp(i1, i2, i3) = k_z(i1)*u(i1, i2, i3, 1) - k_x(i3)*u(i1, i2, i3, 3)
  F_tmp(i1, i2, i3) = F_tmp(i1, i2, i3)*imagI
end forall
!F to P vorticity_y
call p3dfft_btran_c2r(F_tmp(F_start(1):F_end(1), :, :), &
& P_omg(P_start(1):P_end(1), :, :, 2), 'fff')

!compute vorticity_z
forall(i1=F_start(1):F_end(1), i2=F_start(2):F_end(2), &
      i3=F_start(3):F_end(3))
  F_tmp(i1, i2, i3) = k_x(i3)*u(i1, i2, i3, 2) - k_y(i2)*u(i1, i2, i3, 1)
  F_tmp(i1, i2, i3) = F_tmp(i1, i2, i3)*imagI
end forall
!F to P vorticity_z
call p3dfft_btran_c2r(F_tmp(F_start(1):F_end(1), :, :), &
& P_omg(P_start(1):P_end(1), :, :, 3), 'fff')

!product of fields in P space
allocate(P_tmp(P_start(1):P_end(1), &
& P_start(2):P_end(2), &
& P_start(3):P_end(3), 1))

!F to P the fields
do j = 1, N_comp
  F_tmp(F_start(1):F_end(1), :, :) = u(F_start(1):F_end(1), :, :, j)
  call p3dfft_btran_c2r(F_tmp(F_start(1):F_end(1), :, :), &
& P_tmp(P_start(1):P_end(1), :, :, 1), 'fff')
  P_u(P_start(1):P_end(1), P_start(2):P_end(2), &
      P_start(3):P_end(3), j) = P_tmp(P_start(1):P_end(1), :, :, 1)
end do

deallocate(F_tmp)

!for each scalar field_j compute theta*u_k
do j = 4, N_comp

  do k = 1, 3

```

```

!compute u_k*theta
  forall(i1=P_start(1):P_end(1), i2=P_start(2):P_end(2), &
         i3=P_start(3):P_end(3))
    P_tmp(i1, i2, i3, 1) = P_u(i1, i2, i3, j)*P_u(i1, i2, i3, k)
  end forall
!and go to F space-->A_k
  call p3dfft_ftran_r2c(P_tmp(P_start(1):P_end(1), :, :, 1), &
&                        A(F_start(1):F_end(1), :, :, k), 'fff')
  end do

!compute the divergence of the flux theta*u_k
!put in A_j, it's always j>3
  call k_dot(A(:, :, :, 1:3), A(:, :, :, j))
  forall(i1=F_start(1):F_end(1), i2=F_start(2):F_end(2), &
         i3=F_start(3):F_end(3))
    A(i1, i2, i3, j) = -A(i1, i2, i3, j)*imagI
  end forall

end do

!compute (u cross omega)_x
forall(i1=P_start(1):P_end(1), i2=P_start(2):P_end(2), &
       i3=P_start(3):P_end(3))
  P_tmp(i1, i2, i3, 1) = P_u(i1, i2, i3, 2)*P_omg(i1, i2, i3, 3) - &
&                        P_u(i1, i2, i3, 3)*P_omg(i1, i2, i3, 2)
end forall
call p3dfft_ftran_r2c(P_tmp(P_start(1):P_end(1), :, :, 1), &
&                        A(F_start(1):F_end(1), :, :, 1), 'fff')

!compute (u cross omega)_y
forall(i1=P_start(1):P_end(1), i2=P_start(2):P_end(2), &
       i3=P_start(3):P_end(3))
  P_tmp(i1, i2, i3, 1) = P_u(i1, i2, i3, 3)*P_omg(i1, i2, i3, 1) - &
&                        P_u(i1, i2, i3, 1)*P_omg(i1, i2, i3, 3)
end forall
call p3dfft_ftran_r2c(P_tmp(P_start(1):P_end(1), :, :, 1), &
&                        A(F_start(1):F_end(1), :, :, 2), 'fff')

!compute (u cross omega)_z
forall(i1=P_start(1):P_end(1), i2=P_start(2):P_end(2), &
       i3=P_start(3):P_end(3))
  P_tmp(i1, i2, i3, 1) = P_u(i1, i2, i3, 1)*P_omg(i1, i2, i3, 2) - &
&                        P_u(i1, i2, i3, 2)*P_omg(i1, i2, i3, 1)
end forall
call p3dfft_ftran_r2c(P_tmp(P_start(1):P_end(1), :, :, 1), &
&                        A(F_start(1):F_end(1), :, :, 3), 'fff')

deallocate(P_omg, P_tmp)

!normalize

```

```

forall(i1=F_start(1):F_end(1), i2=F_start(2):F_end(2), &
      i3=F_start(3):F_end(3), j=1:N_comp)
  A(i1, i2, i3, j) = A(i1, i2, i3, j)*fact_xyz
end forall

end subroutine

subroutine projection(v)
use variables, only: F_tmp
implicit none

complex(p3dfft_type), dimension(F_start(1):F_end(1)+padd_c, &
  F_start(2):F_end(2), F_start(3):F_end(3), 3) :: v
real(p3dfft_type) :: kx, ky
integer :: i1, i2, i3

!allocate the divergence in Fourier space
allocate(F_tmp(F_start(1):F_end(1)+padd_c, &
&          F_start(2):F_end(2), F_start(3):F_end(3)))

!compute the divergence of the field
call k_dot(v, F_tmp)
!normalize kk to unit vector
forall(i1=F_start(1):F_end(1), i2=F_start(2):F_end(2), &
      i3=F_start(3):F_end(3))
  F_tmp(i1, i2, i3) = F_tmp(i1, i2, i3)*k2(i1, i2, i3)
end forall
!project the field onto the incompressibility plane
do i3 = F_start(3), F_end(3)
  kx = k_x(i3)
  do i2 = F_start(2), F_end(2)
    do i1 = F_start(1), F_end(1)
      v(i1, i2, i3, 1) = v(i1, i2, i3, 1) - kx*F_tmp(i1, i2, i3)
    end do
  end do
end do
do i3 = F_start(3), F_end(3)
  do i2 = F_start(2), F_end(2)
    ky = k_y(i2)
    do i1 = F_start(1), F_end(1)
      v(i1, i2, i3, 2) = v(i1, i2, i3, 2) - ky*F_tmp(i1, i2, i3)
    end do
  end do
end do
do i3 = F_start(3), F_end(3)
  do i2 = F_start(2), F_end(2)
    do i1 = F_start(1), F_end(1)
      v(i1, i2, i3, 3) = v(i1, i2, i3, 3) - k_z(i1)*F_tmp(i1, i2, i3)
    end do
  end do
end do

```

```

    end do
  end do
end do

deallocate(F_tmp)

end subroutine

subroutine k_dot(v, div)
use p3dfft
use parameters
implicit none

complex(p3dfft_type), dimension(F_start(1):F_end(1)+padd_c, &
F_start(2):F_end(2), F_start(3):F_end(3), 3), intent(in) :: v
complex(p3dfft_type), dimension(F_start(1):F_end(1)+padd_c, &
F_start(2):F_end(2), F_start(3):F_end(3)), intent(out) :: div
real(p3dfft_type) :: ky, kx
integer :: i1, i2, i3

!compute k dot v
do i3 = F_start(3), F_end(3)
  kx = k_x(i3)
  do i2 = F_start(2), F_end(2)
    do i1 = F_start(1), F_end(1)
      div(i1, i2, i3) = kx*v(i1, i2, i3, 1)
    end do
  end do
end do

do i3 = F_start(3), F_end(3)
  do i2 = F_start(2), F_end(2)
    ky = k_y(i2)
    do i1 = F_start(1), F_end(1)
      div(i1, i2, i3) = div(i1, i2, i3) + ky*v(i1, i2, i3, 2)
    end do
  end do
end do

do i3 = F_start(3), F_end(3)
  do i2 = F_start(2), F_end(2)
    do i1 = F_start(1), F_end(1)
      div(i1, i2, i3) = div(i1, i2, i3) + k_z(i1)*v(i1, i2, i3, 3)
    end do
  end do
end do

end subroutine

```

A.3.3 Forcing methods

Stochastic and deterministic forcing schemes are implemented. The forcing acts in Fourier space on a small subset of wavenumbers. In three dimensions, the forcing is applied at low wavenumbers only and energy flows to the smallest scale and the small scale statistics are supposed to be independent of the forcing details.

The stochastic forcing is based on a Wiener process, which increments are obtained by means of the Box-Muller algorithm. The image of the Gaussian distribution is uniformly sampled and the values on the domain follow a normal distribution. The forced wavenumbers and the corresponding forcing term are stored into linked lists.

```

!go through the forced wavenumbers, velocity and scalars
do j = 1, N_comp

  k = 0
  js = max(1, j-2)
  kn => forced_k(js)%p
  do while(associated(kn))
!forced wavenumbers
    i1 = kn%i(1)
    i2 = kn%i(2)
    i3 = kn%i(3)
!unrolled index
    k = k + 1
!Box-Muller: dW is Gaussian, sigma_W: read in input
    uw1 = rand(0)
!sqrt(dt) = std dev later multiplied by dt (add)
    aw = sigma_W(js)*sqrt(-2./dt*log(uw1+1d-15))
    uw2 = twoPI*rand(0)
!Wiener process
    dW = aw*cmplx(cos(uw2), sin(uw2))
!then integrate OU to obtain a continuous forcing
!N_F = number of forced wavenumbers
    force(j)%f(k) = dW
!advance
    kn => kn%next

  end do
end do

```

The average dissipation rate of kinetic/scalar energy is imposed by the linear forcing [94]. This is achieved by defining the forcing term in the form of equation (5.2). The sum over the forced wavenumbers requires a reduction of the energy, which is performed over a small communicator that contains processes that manage small wavenumbers. After that, the same processes add the forcing terms to the time derivative of the fields \mathbf{a} .

```

!energy contained in the forced wavenumbers

```

```

aux = 0d0
!go through the forced wavenumbers, velocity
do j = 1, 3
  k = 0
  kn => forced_k(1)%p
  do while(associated(kn))
!which wavenumbers
    i1 = kn%i(1)
    i2 = kn%i(2)
    i3 = kn%i(3)
!Take into account the Hermitian symmetry
    hsf = min(i3, 2)
!unrolled index
    k = k + 1
!energy = v_i v^i*
    aux = aux + hsf*abs(v(i1, i2, i3, j))**2
    force(j)%f(k) = v(i1, i2, i3, j)
!advance
    kn => kn%next
  end do
end do
den_f(1) = aux

!go through the forced wavenumbers, scalars
do j = 4, N_comp
  aux = 0d0
  js = j - 2
  k = 0
  kn => forced_k(js)%p
  do while(associated(kn))
!which wavenumbers
    i1 = kn%i(1)
    i2 = kn%i(2)
    i3 = kn%i(3)
!H symmetry
    hsf = min(i3, 2)
!unrolled index
    k = k + 1
!energy = theta^2
    aux = aux + hsf*abs(v(i1, i2, i3, j))**2
    force(j)%f(k) = v(i1, i2, i3, j)
!advance
    kn => kn%next
  end do
  den_f(js) = aux

end do

!if proc is involved in forcing then sum up the energy
if(flag_force)then

```



```

    call MPI_Allreduce(den_f, ene_f, 1+N_scal, p3dfft_MPIreal, &
        MPI_SUM, FORCE_COMM, j)
end if

```

A.4 Flow fields Input/Output

The Fourier representation of the flow fields is stored/read into binary files using MPI I/O utilities. The storage required for I/O could be optimized by compressing the output files (for example by means of the HDF5 library) and also by storing only two components of the velocity field and use the continuity equation to recover the third component. However, this direct implementation allows to easily read the output of the simulations and more sophisticated solutions are considered only for very large simulations.

At first, the type, size and offset at which each process should start writing the file are initialized.

```

if(io_kind .eq. 4) MPI_io_kind = MPI_COMPLEX
if(io_kind .eq. 8) MPI_io_kind = MPI_DOUBLE_COMPLEX
!plane zy
call MPI_type_contiguous(F_size(1)*F_size(2), MPI_io_kind, &
    MPI_slice, ierr)
call MPI_type_commit(MPI_slice, ierr)
!planes zy separated by the planes zy of the other processes
stride = F_size(1)*Ny*sizeof(io_tmp)
call MPI_type_hvector(F_size(3), 1, stride, MPI_slice, &
    MPI_F_slice, ierr)
call MPI_type_commit(MPI_F_slice, ierr)
!offset, where the file starts for the process
aux = ( (F_start(3) - 1)*Ny + F_start(2) - 1)*Nz
off_u = int(aux*sizeof(io_tmp), MPI_OFFSET_KIND)

```

Then, the fields can be written/read by means of few MPI calls. An auxiliary buffer is employed in order to read/write files using complex kinds that differ from the kind used for the simulations.

```

subroutine save_u(j0, j1, iter)
use variables
implicit none

!component of the field to store
integer, intent(in) :: j0, j1
integer :: j, fh
integer :: i1, i2, i3, ierr
integer :: stat(mpi_status_size)
integer, intent(in) :: iter

!file names, fields
1 format("u", I1.1, ".", I3.3, ".bin")

```

```

allocate( io_buff(F_start(1):F_end(1), F_start(2):F_end(2), &
&           F_start(3):F_end(3)) )

do j = j0, j1
  write(file_u, 1) j, iter
  forall(i1=F_start(1):F_end(1), i2=F_start(2):F_end(2), &
        i3=F_start(3):F_end(3))
    io_buff(i1, i2, i3) = cmplx(F_u(i1, i2, i3, j), kind = io_kind)
  end forall
  call MPI_file_open(MPI_comm_world, file_u, MPI_mode_create + &
& MPI_mode_wronly, MPI_info_null, fh, ierr)
  call MPI_file_set_view(fh, off_u, MPI_slice, MPI_F_slice, &
& 'native', MPI_info_null, ierr)
  call MPI_file_write_all(fh, io_buff, F_size(3), &
& MPI_slice, stat, ierr)
  call MPI_file_close(fh, ierr)
end do

deallocate(io_buff)

end subroutine

```

A.5 Particle data structure

Particles are stored as a structure of arrays, each array has size three times the maximum allowed number of particles per processor. Therefore, the coordinates of the particle are stored in memory with unitary stride, then the coordinates of the next particle and so on. On the contrary, the particle position, velocity and scalars are stored in memory with a large stride and concurrent accesses to those distinct arrays should be minimized.

```

module particles_variables
use p3dfft
use parameters
use particles_parameters
implicit none

!Particle position, velocity, temperature, radius and index.
type particle
  real(p3dfft_type), dimension(:, :), pointer :: x0      !3, Np
  real(p3dfft_type), dimension(:, :), pointer :: u0      !3, Np
  real(p3dfft_type), dimension(:, :), pointer :: uf0     !3, Np
  real(p3dfft_type), dimension(:, :), pointer :: s0      !3, Np
  real(p3dfft_type), dimension(:, :), pointer :: sf0     !N_scal_part, Np
!DEC$ ATTRIBUTES ALIGN: 64 :: x0
!DEC$ ATTRIBUTES ALIGN: 64 :: u0
!DEC$ ATTRIBUTES ALIGN: 64 :: s0

```

```

!DEC$ ATTRIBUTES ALIGN: 64 :: uf0
!DEC$ ATTRIBUTES ALIGN: 64 :: sf0
  real(p3dfft_type), dimension(:, :), pointer :: x1      !3, Np
  real(p3dfft_type), dimension(:, :), pointer :: u1      !3, Np
  real(p3dfft_type), dimension(:, :), pointer :: uf1     !3, Np
  real(p3dfft_type), dimension(:, :), pointer :: s1      !3, Np
  real(p3dfft_type), dimension(:, :), pointer :: sf1     !N_scal_part, Np
!DEC$ ATTRIBUTES ALIGN: 64 :: x1
!DEC$ ATTRIBUTES ALIGN: 64 :: u1
!DEC$ ATTRIBUTES ALIGN: 64 :: s1
!DEC$ ATTRIBUTES ALIGN: 64 :: uf1
!DEC$ ATTRIBUTES ALIGN: 64 :: sf1
end type
!particles and buffer to send
type(particle), allocatable, dimension(:) :: part, send
!array for sorting among processors
integer(1), allocatable, dimension(:) :: part_id

```

The three components represent spatial coordinates in the `x0` array, velocity components in the `u0` array and radius, temperature, particle index in the `s0` array. The arrays `uf0` and `sf0` contain the fluid velocity and scalars at the particle position and have size number of scalars times the maximum number of particles per processor. Additional `x1`, `v1`, `s1`, `uf1`, `sf1` arrays are allocated for time integration. Runge-Kutta integrators would actually require less memory than that, but all the variables are kept in order to facilitate implementation of the collision detection and to allow for straightforward extensions/modifications of the model employed.

```

N_part_max(i) = nint(N_part(i)*sec_coeff)
allocate(part(i)%x0 (3, N_part_max(i)))
allocate(part(i)%u0 (3, N_part_max(i)))
allocate(part(i)%s0 (3, N_part_max(i)))
allocate(part(i)%uf0 (3, N_part_max(i)))

```

A contiguous MPI type composed by three `p3dfft_MPIreal` is employed to transfer elements of a single particle, that is, its position, velocity and scalars which all have rank three.

```

call MPI_type_contiguous(3, p3dfft_MPIreal, MPI_P, i)
call MPI_type_commit(MPI_P, i)

```

A.6 Particles distribution among MPI processes

In order to exchange the particles a local communicator surrounding each process is created. Only nearest-neighbour communications are allowed, even though the methodology can be easily extended to larger sets of processes. The local communicator involves the process itself and the eight nearest-neighbours, so that particles can migrate from/to a pencil to/from the nearest eight pencils. The coordinates y and z are parallelized in physical space and correspond to MPI directions

1 and 2 respectively. Left/right is used to indicate the direction along y while up/down identifies the direction along z and therefore the receivers are numbered from the top left in clockwise direction while the sources are reversed. Assuming uniform particle number density the weights for the local communications are set based on the size of the ghost regions from/to which particles can migrate. Additionally, the processors are grouped into rows, that is communicators along y at fixed z and columns, that is communicators along z at fixed y . Those Cartesian communicators are employed for Input/Output.

```

subroutine create_communicators
use parameters
implicit none

integer, dimension(8) :: sources, dests
integer, dimension(8) :: comm_weight_s, comm_weight_d
integer :: coo1, coo2
integer :: i, j, k

!define neighborhood to exchange boundaries and particles
k = 0
!3 procs above proc_id
j = -1
do i = -1, 1
  coo1 = mod(coords(1) + i + dims(1), dims(1))
  coo2 = mod(coords(2) + j + dims(2), dims(2))
  k = k + 1
  dests(k) = coo1 + dims(1)*coo2
end do
!2 procs next to proc_id
j = 0
do i = -1, 1, 2
  coo1 = mod(coords(1) + i + dims(1), dims(1))
  coo2 = mod(coords(2) + j + dims(2), dims(2))
  k = k + 1
  dests(k) = coo1 + dims(1)*coo2
end do
!3 procs below proc_id
j = 1
do i = -1, 1
  coo1 = mod(coords(1) + i + dims(1), dims(1))
  coo2 = mod(coords(2) + j + dims(2), dims(2))
  k = k + 1
  dests(k) = coo1 + dims(1)*coo2
end do

!sources for proc_id
sources(8:1:-1) = dests(1:8)
!communication weights sources and dests
comm_weight_s(1) = padd2L *padd2L
comm_weight_s(2) = P_size(2)*padd2L

```

```

comm_weight_s(3) = padd2R *padd2L
comm_weight_s(4) = P_size(3)*padd2L
comm_weight_s(5) = P_size(3)*padd2R
comm_weight_s(6) = padd2L *padd2R
comm_weight_s(7) = P_size(2)*padd2R
comm_weight_s(8) = padd2R *padd2R
comm_weight_s = (comm_weight_s(8:1:-1) + comm_weight_s)/2
comm_weight_d = comm_weight_s

!create local communicator
reorder = .false.
call MPI_dist_graph_create_adjacent(MPI_COMM_WORLD, 8, sources, &
comm_weight_s, 8, dests, comm_weight_d, MPI_INFO_NULL, reorder, &
LOC_COMM, i)

!create column/row communicators
call MPI_Comm_split(MPI_COMM_WORLD, coords(2), coords(1), COMM(1), i)
call MPI_Comm_split(MPI_COMM_WORLD, coords(1), coords(2), COMM(2), i)

end subroutine

```

After this initialization the actual communication of the migrating particles, which is executed at each step of the time integration, consists only of a MPI call. Outgoing particles are sent by the processors to the nearest receivers and incoming particles are received from the nearest sources by means of the local `neighbor_alltoall` utility. In the presented version of the code blocking communications are employed, but non-blocking communications can be easily introduced.

```

subroutine exchange_part(send, recv, req_n, i_St)
use p3dfft
implicit none

real(p3dfft_type), dimension(1:, 1:), intent(in) :: send
real(p3dfft_type), dimension(1:, 1:), intent(out) :: recv
integer, intent(in) :: req_n, i_St
integer :: i

call MPI_neighbor_alltoallv(send, send_count_part(:, i_St), &
displ_s_part(:, i_St), MPI_P, recv, recv_count_part(:, i_St), &
displ_r_part(:, i_St), MPI_P, LOC_COMM, i)

end subroutine

```

The particles that need to be sent/received, the number of particles to send/receive and the address at which the send/receive operation starts is determined based on the particle current position. The index of the neighbour processor corresponding to the particle is determined. After that the number of particles to send is computed and communicated to the receivers. In order to perform the communication, auxiliary buffers to store the particles to send are allocated and the

displacements from the origin of the array to the first particle to send to each neighbouring processor is computed. The neighbouring processor 1 receives particles from 1 to `send_count_part(1, i_St)`, the neighbouring processor 2 receives particles from `send_count_part(1, i_St)+1` to `send_count_part(2, i_St)` and so on.

```

subroutine distribute_part(displ_dx, step, i_St)
use particles_variables
implicit none

real(p3dfft_type), dimension(2) :: x, displ
real(8), intent(in) :: displ_dx
integer :: aux(-4:4)
integer :: i, i_rem, j, k
integer(1) :: ip, i1, i2
integer, intent(in) :: step, i_St
integer :: N_rem, s_size

!particle corresponding processor
allocate(part_id(N_part(i_St)))
!shift the particles (interp + coll detect)
displ = delta_x_part + real(displ_dx, p3dfft_type)
!determine particle processor
do i = 1, N_part(i_St)
!particle position shifted
  x(1:2) = part(i_St)%x1(2:3, i) + displ
!particles index in proc grid proc_size = P_size*dx
  i1 = int( floor(x(1)*div_proc_size(1)) - coords(1), kind = 1)
  i2 = int( floor(x(2)*div_proc_size(2)) - coords(2), kind = 1)
!unrolled index -4, .., 4. 0 is the proc
  part_id(i) = i1 + 3_1*i2
end do

!how many part to send to neighb(j)
aux = 0
do i = 1, N_part(i_St)
  ip = part_id(i)
  aux(ip) = aux(ip) + 1
end do
send_count_part(1:4, i_St) = aux(-4:-1)
send_count_part(5:8, i_St) = aux(1:4)

!tell the 8 neighbours how many particles to exchange
call MPI_neighbor_alltoall(send_count_part(:, i_St), 1, MPI_INTEGER, &
  recv_count_part(:, i_St), 1, MPI_INTEGER, LOC_COMM, i)
!displacements for receiving
displ_r_part(1, i_St) = 0
do i = 1, 7
  displ_r_part(i+1, i_St) = displ_r_part(i, i_St) + recv_count_part(i, i_St)
end do
!displ for sending

```

```

displ_s_part(1, i_St) = 0
do i = 1, 7
  displ_s_part(i+1, i_St) = displ_s_part(i, i_St) + send_count_part(i, i_St)
end do
s_size = displ_s_part(8, i_St) + send_count_part(8, i_St)

!temporary buffer to send/receive
allocate(send(i_St)%x1(3, s_size + 1))
allocate(send(i_St)%s1(3, s_size + 1))
allocate(send(i_St)%u1(3, s_size + 1))

!remaining particles
N_rem = N_part(i_St)
i_rem = N_part(i_St)
k = 0
!send to first four
do j = -4, -1
  do i = N_rem, 1, -1
    if(part_id(i) .eq. j)then
      k = k + 1
      send(i_St)%x1(:, k) = part(i_St)%x1(:, i)
      part(i_St)%x1(:, i) = part(i_St)%x1(:, i_rem)
      send(i_St)%u1(:, k) = part(i_St)%u1(:, i)
      part(i_St)%u1(:, i) = part(i_St)%u1(:, i_rem)
      send(i_St)%s1(:, k) = part(i_St)%s1(:, i)
      part(i_St)%s1(:, i) = part(i_St)%s1(:, i_rem)
      part_id(i) = part_id(i_rem)
      i_rem = i_rem - 1
    end if
  end do
  N_rem = i_rem
end do
!send to last four
do j = 1, 4
  do i = N_rem, 1, -1
    if(part_id(i) .eq. j)then
      k = k + 1
      send(i_St)%x1(:, k) = part(i_St)%x1(:, i)
      part(i_St)%x1(:, i) = part(i_St)%x1(:, i_rem)
      send(i_St)%u1(:, k) = part(i_St)%u1(:, i)
      part(i_St)%u1(:, i) = part(i_St)%u1(:, i_rem)
      send(i_St)%s1(:, k) = part(i_St)%s1(:, i)
      part(i_St)%s1(:, i) = part(i_St)%s1(:, i_rem)
      part_id(i) = part_id(i_rem)
      i_rem = i_rem - 1
    end if
  end do
end do
!remaining particles
N_rem = i_rem
end do

```

```

!send particles
call exchange_part(send(i_St)%x1, &
part(i_St)%x1(:, N_rem+1:N_part_max(i_St)), 1, i_St)
call exchange_part(send(i_St)%u1, &
part(i_St)%u1(:, N_rem+1:N_part_max(i_St)), 2, i_St)
call exchange_part(send(i_St)%s1, &
part(i_St)%s1(:, N_rem+1:N_part_max(i_St)), 3, i_St)
!update the number of particles
N_part(i_St) = N_rem + sum(recv_count_part(:, i_St))
!free memory
deallocate(send(i_St)%x1, send(i_St)%u1, send(i_St)%s1)
deallocate(part_id)

end subroutine

```

A.7 Exchange of fields ghost regions between neighbouring MPI processes

The interpolation of fields at the position of a particle close to the boundary between neighbouring MPI processes requires ghost regions. For example, the processor on the left sends to its right neighbour the field array elements corresponding to a slice of grid point of size `padd1R` along y and `P_size(2)+padd2L+padd2R` along z . The same for up/down processors. The exchange of ghost regions is performed by means of MPI derived data types. The array `type_s_field(1:8)` contains MPI vector types to send fields to neighbouring processes starting from up/left in clockwise direction. The the displacements to send ghost regions `displ_s_field` and to receive ghost regions `displ_r_field` are computed according to the size of the arrays in physical space. The same initialization is carried out for the feedback fields, since ghost regions require to sum the contributions to the feedback on a portion of the domain from the particles located in that portion of the domain and also from the particles located in a ghost region that overlaps with that portion of the domain.

```

subroutine create_types_field
implicit none

integer :: Ps(8, 2:3)

integer(8) :: aux

integer :: stride1, stride2

integer :: i

stride1 = P_b1(1) - P_b0(1) + 1
stride2 = P_b1(2) - P_b0(2) + 1

```



```
!segment @i2,i3 in P space
call MPI_type_contiguous(stride1, p3dfft_mpireal, SEGMENT, i)
call MPI_type_commit(SEGMENT, i)

!block to be sent on diagonal left-up
call MPI_Type_vector(padd2R, padd2R, stride2, SEGMENT, type_s_field(1), i)
call MPI_type_commit(type_s_field(1), i)

!Planes to be sent up
call MPI_Type_vector(padd2R, P_size(2), stride2, SEGMENT, type_s_field(2), i)
call MPI_type_commit(type_s_field(2), i)

!block to be sent on diagonal right-up
call MPI_Type_vector(padd2R, padd2L, stride2, SEGMENT, type_s_field(3), i)
call MPI_type_commit(type_s_field(3), i)

!Planes to be sent left
call MPI_Type_vector(P_size(3), padd2R, stride2, SEGMENT, type_s_field(4), i)
call MPI_type_commit(type_s_field(4), i)

!Planes to be sent right
call MPI_Type_vector(P_size(3), padd2L, stride2, SEGMENT, type_s_field(5), i)
call MPI_type_commit(type_s_field(5), i)

!block to be sent on diagonal left-down
call MPI_Type_vector(padd2L, padd2R, stride2, SEGMENT, type_s_field(6), i)
call MPI_type_commit(type_s_field(6), i)

!Planes to be sent down
call MPI_Type_vector(padd2L, P_size(2), stride2, SEGMENT, type_s_field(7), i)
call MPI_type_commit(type_s_field(7), i)

!block to be sent on diagonal right-down
call MPI_Type_vector(padd2L, padd2L, stride2, SEGMENT, type_s_field(8), i)
call MPI_type_commit(type_s_field(8), i)

!count to send fields
send_count_field = 1

!displacement to send fields
Ps(1, 2) = P_start(2)
Ps(2, 2) = P_start(2)
Ps(3, 2) = P_end(2) - padd2L + 1
Ps(4, 2) = P_start(2)
Ps(5, 2) = P_end(2) - padd2L + 1
Ps(6, 2) = P_start(2)
Ps(7, 2) = P_start(2)
Ps(8, 2) = P_end(2) - padd2L + 1
```

```

Ps(1, 3) = P_start(3)
Ps(2, 3) = P_start(3)
Ps(3, 3) = P_start(3)
Ps(4, 3) = P_start(3)
Ps(5, 3) = P_start(3)
Ps(6, 3) = P_end(3) - padd2L + 1
Ps(7, 3) = P_end(3) - padd2L + 1
Ps(8, 3) = P_end(3) - padd2L + 1

!unroll index
do i = 1, 8

  aux = (Ps(i, 2) - P_b0(2) + &
    (Ps(i, 3) - P_b0(3))*stride2)*stride1*p3dfft_type

  displ_s_field(i) = int(aux, MPI_ADDRESS_KIND)

end do

!to recv fields
type_r_field = type_s_field
recv_count_field = 1

!displacement to recv fields
Ps(8, 2) = P_b0(2)
Ps(7, 2) = P_start(2)
Ps(6, 2) = P_end(2) + 1
Ps(5, 2) = P_b0(2)
Ps(4, 2) = P_end(2) + 1
Ps(3, 2) = P_b0(2)
Ps(2, 2) = P_start(2)
Ps(1, 2) = P_end(2) + 1

Ps(8, 3) = P_b0(3)
Ps(7, 3) = P_b0(3)
Ps(6, 3) = P_b0(3)
Ps(5, 3) = P_start(3)
Ps(4, 3) = P_start(3)
Ps(3, 3) = P_end(3) + 1
Ps(2, 3) = P_end(3) + 1
Ps(1, 3) = P_end(3) + 1

!unroll index
do i = 1, 8

  aux = ( Ps(i, 2) - P_b0(2) + &
    (Ps(i, 3) - P_b0(3))*stride2 ) * stride1 * p3dfft_type

```

```

    displ_r_field(i) = int(aux, MPI_ADDRESS_KIND)

end do

!to send feedb
type_s_feedb(1:8) = type_s_field(8:1:-1)

!displacement to send feedback
Ps(1, 2) = P_b0(2)
Ps(2, 2) = P_start(2)
Ps(3, 2) = P_end(2) + 1
Ps(4, 2) = P_b0(2)
Ps(5, 2) = P_end(2) + 1
Ps(6, 2) = P_b0(2)
Ps(7, 2) = P_start(2)
Ps(8, 2) = P_end(2) + 1

Ps(1, 3) = P_b0(3)
Ps(2, 3) = P_b0(3)
Ps(3, 3) = P_b0(3)
Ps(4, 3) = P_start(3)
Ps(5, 3) = P_start(3)
Ps(6, 3) = P_end(3) + 1
Ps(7, 3) = P_end(3) + 1
Ps(8, 3) = P_end(3) + 1

!unroll index
do i = 1, 8

    aux = ( Ps(i, 2) - P_b0(2) + &
            (Ps(i, 3) - P_b0(3))*stride2 ) * stride1 * p3dfft_type

    displ_s_feedb(i) = int(aux, MPI_ADDRESS_KIND)

end do

!buffer for recv feedback
buff_size_feedb = (padd2L + P_size(2) + padd2R + P_size(3)) * (padd2L + padd2R)
buff_size_feedb = buff_size_feedb * stride1

!type to recv in the buffer, feedback
type_r_feedb(1:8) = SEGMENT

!how many segments to recv, feedback
recv_count_feedb(1) = padd2L * padd2L

```

```

recv_count_feedb(2) = P_size(2)*padd2L
recv_count_feedb(3) = padd2R      *padd2L
recv_count_feedb(4) = P_size(3)*padd2L
recv_count_feedb(5) = P_size(3)*padd2R
recv_count_feedb(6) = padd2L      *padd2R
recv_count_feedb(7) = P_size(2)*padd2R
recv_count_feedb(8) = padd2R      *padd2R

!displ to recv feedb into unrolled buff
displ_r_feedb(1) = 0
do i = 1, 7
  displ_r_feedb(i+1) = displ_r_feedb(i) + recv_count_feedb(i)
end do
displ_r_feedb = int(p3dfft_type*stride1*displ_r_feedb, MPI_ADDRESS_KIND)

end subroutine

```

After this initialization the ghost regions can be exchanged by means of just an MPI call. Ghost regions are put also along the x direction in order to avoid cache missing in the interpolation of fields at particles which x coordinate is close to 0 or 2π .

```

subroutine exchange_field(j)
use variables, only: P_u
implicit none

integer :: i1, i2, i3
integer, intent(in) :: j

do i3 = P_start(3), P_end(3)
  do i2 = P_start(2), P_end(2)
!last part of u into buffer left x
    do i1 = P_b0(1), 0
      P_u(i1, i2, i3, j) = P_u(P_end(1) + i1, i2, i3, j)
    end do
!first part of u into buffer right x
    do i1 = P_end(1) + 1, P_b1(1)
      P_u(i1, i2, i3, j) = P_u(i1 - P_end(1), i2, i3, j)
    end do
  end do
end do

call MPI_neighbor_alltoallw(P_u(P_b0(1), P_b0(2), P_b0(3), j), &
&  send_count_field, displ_s_field, type_s_field, &
&  P_u(P_b0(1), P_b0(2), P_b0(3), j), recv_count_field, &
&  displ_r_field, type_r_field, LOC_COMM, i1)

end subroutine

```

A.8 Flow fields interpolation at the particle position and particle back-reaction

The coefficients for deconvolution in Fourier space, necessary for the B-spline interpolation, are computed at the beginning of the simulation and separation of variables is exploited. The one-dimensional Fourier transform of the B-spline polynomials is

$$\mathcal{F}_x [B_n(x)] (k_x) = \frac{1}{2\pi} (\text{sinc}(k_x \Delta x / 2))^{n+1}, \quad (\text{A.4})$$

and the three-dimensional transform is

$$\begin{aligned} \mathcal{F} [B_n(\mathbf{x})] (\mathbf{k}) &= \mathcal{F}_x \mathcal{F}_y \mathcal{F}_z [B_n(x) B_n(y) B_n(z)] (\mathbf{k}) = \\ &= \frac{1}{(2\pi)^3} (\text{sinc}(k_x \Delta x / 2) \text{sinc}(k_y \Delta x / 2) \text{sinc}(k_z \Delta x / 2))^{n+1}. \end{aligned} \quad (\text{A.5})$$

The one-dimensional transforms along x , $(\mathcal{F}_x [B_n(x)] (k_x))^{-1}$, y and z are stored into the real arrays `F_cx`, `F_cy`, `F_cz`.

```

module particles_interpolate
use particles_parameters
use particles_communications
use parameters
implicit none

real(p3dfft_type), save, allocatable, dimension(:) :: F_cx, F_cy, F_cz
real(p3dfft_type), save, dimension(N_stencil) :: w_interp1
real(p3dfft_type), save, dimension(N_stencil) :: w_interp2
real(p3dfft_type), save, dimension(N_stencil) :: w_interp3
real(p3dfft_type), save :: x
real(p3dfft_type), parameter :: N_stencil_div2 = N_stencil/2d0
integer, save :: xj(3)

contains

subroutine initialize_interp
use parameters
implicit none

real(p3dfft_type) :: aux, zeta, zeta_i
integer :: l, inf, i1, i2, i3

allocate(F_cx(F_start(3):F_end(3)+padd_c), &
          F_cy(F_start(2):F_end(2)+padd_c), &
          F_cz(F_start(1):F_end(1)+padd_c))

!compute the coefficients beforehand
inf = 0
F_cz(F_start(1)) = 1d0

```

```

do i1 = max(2, F_start(1)), F_end(1)
  aux = 0d0
  zeta_i = 0.5d0*k_z(i1)*dx
  do l = -inf, inf
    zeta = zeta_i + l*0.5d0*twoPI
    aux = aux + (dsin(zeta)/zeta)**(2*N_stencil)
  end do
  F_cz(i1) = aux
end do
F_cy(F_start(2)) = 1d0
do i2 = max(2, F_start(2)), F_end(2)
  aux = 0d0
  zeta_i = 0.5d0*k_y(i2)*dx
  do l = -inf, inf
    zeta = zeta_i + l*0.5d0*twoPI
    aux = aux + (dsin(zeta)/zeta)**(2*N_stencil)
  end do
  F_cy(i2) = aux
end do
F_cx(F_start(3)) = 1d0
do i3 = max(2, F_start(3)), F_end(3)
  aux = 0d0
  zeta_i = 0.5d0*k_x(i3)*dx
  do l = -inf, inf
    zeta = zeta_i + l*0.5d0*twoPI
    aux = aux + (dsin(zeta)/zeta)**(2*N_stencil)
  end do
  F_cx(i3) = aux
end do
!coeff c(k)
F_cx = 1d0/dsqrt(1d0*F_cx)
F_cy = 1d0/dsqrt(1d0*F_cy)
F_cz = 1d0/dsqrt(1d0*F_cz)
!Delete Nyquist
if(coords(1) .eq. dims(1) - 1) F_cx(Nx_Nyq) = 0d0
if(coords(2) .eq. dims(2) / 2) F_cy(Ny_Nyq) = 0d0
F_cz(Nz_Nyq) = 0d0

end subroutine

```

When the fields at the particle position are required, the deconvolution is carried out in Fourier space by multiplying the field by the predefined weights, an inverse FFT takes the field in physical space and the ghost regions at the boundary between neighbouring processes are exchanged.

```

subroutine F_to_P_deconv(A, j0, j1)
  use variables, only: P_u, F_tmp
  use parameters
  implicit none

  complex(p3dffft_type), dimension(F_start(1):F_end(1)+padd_c, &

```

```

F_start(2):F_end(2), F_start(3):F_end(3), N_comp), intent(in) :: A

real(p3dfft_type), dimension(P_start(1):P_end(1), &
P_start(2):P_end(2), P_start(3):P_end(3)) :: aux

real(p3dfft_type) :: cx, cxy

integer, intent(in) :: j0, j1

integer :: i1, i2, i3, j

allocate(F_tmp(F_start(1):F_end(1)+padd_c, &
& F_start(2):F_end(2), F_start(3):F_end(3)))

do j = j0, j1

do i3 = F_start(3), F_end(3)
cx = F_cx(i3)
do i2 = F_start(2), F_end(2)
cxy = cx*F_cy(i2)
forall(i1=F_start(1):F_end(1))
F_tmp(i1, i2, i3) = cxy*F_cz(i1)*A(i1, i2, i3, j)
end forall
end do
end do

call p3dfft_btran_c2r(F_tmp(F_start(1):F_end(1), :, :), aux, 'fff')

P_u(P_start(1):P_end(1), P_start(2):P_end(2), P_start(3):P_end(3), j) = aux

call exchange_field(j)

end do

deallocate(F_tmp)

end subroutine

```

Once that the field in physical space is available at all the grid points, the interpolation is carried out as a convolution over N_{stencil}^3 grid points surrounding the particle, for all the particles.

```

subroutine interpolate(xp, j0, j1, interp3)
use variables, only: P_u
implicit none

real(p3dfft_type), dimension(3), intent(in) :: xp
real(p3dfft_type) :: xp1(3), x

real(p3dfft_type) :: interp1(N_stencil, 4)

```

```

real(p3dfft_type) :: interp2(N_stencil, 4)
real(p3dfft_type), intent(out) :: interp3(4)

integer :: i2, i3

integer, intent(in) :: j0, j1
integer :: j_comp, ji

!normalize x:x+dx -> 0:1
xp1 = xp*div_dx

!x of the first node used
xj = ceiling(xp1 - N_stencil_div2)

x = xj(1) - xp1(1)
call comp_spline(x, w_interp1)

x = xj(2) - xp1(2)
call comp_spline(x, w_interp2)

x = xj(3) - xp1(3)
call comp_spline(x, w_interp3)

do j_comp = j0, j1
  ji = j_comp - j0 + 1

  do i3 = 1, N_stencil

!contraction on i1 for each i2, i3
    forall(i2=1:N_stencil)
      interp1(i2, ji) = dot_product(w_interp1, &
        P_u(xj(1)+1:xj(1)+N_stencil, xj(2)+i2, xj(3)+i3, j_comp))
    end forall

!contraction on i2 for each i3
    interp2(i3, ji) = dot_product(w_interp2, interp1(:, ji))

  end do

!contraction on i3
  interp3(ji) = dot_product(w_interp3, interp2(:, ji))

end do

end subroutine

```

At the same time, if feedback on fields is required, the particle force (and/or heat flux) exerted on the fluid flow is computed and projected onto the equispaced

Cartesian grid by using the B-spline interpolation weights already computed for the interpolation. This is achieved by performing the steps for the interpolation in reversed order for each particle.

```

subroutine feedback_part_fields(j0 , j1 , interp3)
use variables , only: P_tmp
implicit none

real(p3dfft_type) , intent(in) :: interp3(4)
real(p3dfft_type) :: aux1 , aux2

integer :: i1 , i2 , i3

integer , intent(in) :: j0 , j1
integer :: j_comp , ji

do j_comp = j0 , j1

    ji = j_comp - j0 + 1

    !expand on i3
    do i3 = 1 , N_stencil

        aux2 = w_interp3(i3)*interp3(ji)

    !expand on i2 for each i3
    do i2 = 1 , N_stencil

        aux1 = w_interp2(i2)*aux2

    !expand on i1 for each i2 , i3
    forall(i1=1:N_stencil)
        P_tmp(xj(1)+i1 , xj(2)+i2 , xj(3)+i3 , j_comp) = &
        P_tmp(xj(1)+i1 , xj(2)+i2 , xj(3)+i3 , j_comp) + &
        w_interp1(i1)*aux1
    end forall

    end do
end do
end do

end subroutine

```

The projection of the forces exerted by particles is then taken to Fourier space where the deconvolution is carried out.

```

subroutine P_to_F_deconv(j0 , j1)
use variables , only: P_tmp , F_tmp , F_feedb
use parameters
implicit none

```

```

real(p3dfft_type), dimension(P_start(1):P_end(1), &
P_start(2):P_end(2), P_start(3):P_end(3)) :: aux

real(p3dfft_type) :: cx, cxy
integer :: i1, i2, i3

integer, intent(in) :: j0, j1
integer :: j

call wait_for_feedb(j0, j1)

!take the feedback to Fourier space
do j = j0, j1

  aux = P_tmp(P_start(1):P_end(1), P_start(2):P_end(2), P_start(3):P_end(3), j)

  call p3dfft_ftran_r2c(aux, F_feedb(F_start(1):F_end(1), :, :, j), 'fff')

!and remove the previous convolution
do i3 = F_start(3), F_end(3)
  cx = F_cx(i3)
  do i2 = F_start(2), F_end(2)
    cxy = cx*F_cy(i2)
    forall(i1=F_start(1):F_end(1))
      F_feedb(i1, i2, i3, j) = F_feedb(i1, i2, i3, j)*cxy*F_cz(i1)
    end forall
  end do
end do

end do

end subroutine

Convolutions in physical space are carried out using B-spline polynomials of order
up to 4 (that is N_stencil=5) written in the Horner form to minimize the float-
ing point operations necessary to compute evaluate the polynomial. Notice that
the select case is removed by the compiler since N_stencil is a parameter (compiler
directives can be employed as well to define N_stencil).

subroutine comp_spline(x, w)
use p3dfft
use parameters
implicit none

real(p3dfft_type), intent(in) :: x
real(p3dfft_type), intent(out) :: w(N_stencil)

real(p3dfft_type), parameter :: div6 = 1d0/6d0
real(p3dfft_type), parameter :: div24 = 1d0/24d0

#ifdef PARTICLES

```

```

select case(N_stencil)

case(1)
w(1) = 1d0

case(2)
w(1) = x + 1d0
w(2) = - x

case(3)
w(1) = 0.5d0*x*(x + 3d0) + 1.125d0
w(2) = -x*(x + 2d0) - 0.25d0
w(3) = 0.5d0*x*(x + 1d0) + 0.125d0

case(4)
w(1) = x*(x*(x + 6d0) + 12d0) + 8d0
w(2) = -3d0*x*(x*(x + 5d0) + 7d0) - 5d0
w(3) = 3d0*x*(x*(x + 4d0) + 4d0) + 4d0
w(4) = -x*(x*(x + 3d0) + 3d0) - 1d0
w = w*div6

case(5)
w(1) = x*(x*(x*(x + 10d0) + 37.5d0) + 62.5d0) + 39.0625d0
w(2) = -4d0*x*(x*(x*(x + 9d0) + 28.5d0) + 35.25d0) - 45.25d0
w(3) = 6d0*x*(x*(x*(x + 8d0) + 21.5d0) + 22d0) + 50.375d0
w(4) = -4d0*x*(x*(x*(x + 7d0) + 16.5d0) + 16.75d0) - 25.25d0
w(5) = x*(x*(x*(x + 6d0) + 13.5d0) + 13.5d0) + 5.0625d0
w = w*div24

end select

#endif

end subroutine

```

A.9 Particles collision detection

The particles are grouped into small boxes according to their position and then only couples of particles contained in each box are checked for collision. For each box a linked list with the addresses of the contained particles is created. For N_P particles and N_B boxes the whole collision detection process takes approximately $O(N_P^2/N_B)$, neglecting the time to access memory. The time spent on memory accesses and to create the linked list can be significant for large N_B . Therefore a good compromise on N_B should be found.

```

module particles_collisions
use parameters

```

```

use particles_parameters
use particles_variables
use particles_distribute
implicit none

type :: p_node
integer :: i
type(p_node), pointer :: next
end type
type(p_node), pointer :: node_a, node_b

type :: ptr
type(p_node), pointer :: p
end type
type(ptr), allocatable, dimension(:, :, :) :: list

real(p3dfft_type), dimension(3, N_St_max) :: B_size
integer, dimension(3, N_St_max) :: N_B
real(p3dfft_type) :: div_B_size(3)
character(32) :: file_coll

contains

subroutine init_coll
implicit none

real(8) :: aux
integer :: i_St, N_part_per_box=4

do i_St = 1, N_St

!N_B^3 boxes
N_B(1:3, i_St) = nint((1d0*N_part(i_St)/N_part_per_box)**(1d0/3d0))
N_B(1, i_St) = max(N_B(1, i_St), dims(1))
N_B(2, i_St) = max(N_B(2, i_St), dims(1))
N_B(3, i_St) = max(N_B(3, i_St), dims(2))
N_B(1, i_St) = N_B(1, i_St)/dims(1)*dims(1)
N_B(2, i_St) = N_B(2, i_St)/dims(1)*dims(1)
N_B(3, i_St) = N_B(3, i_St)/dims(2)*dims(2)
!box size
B_size(1:3, i_St) = twoPI*AR(1:3)/N_B(1:3, i_St)
!parallel y,z
N_B(2:3, i_St) = N_B(2:3, i_St)/dims(1:2)

end do

end subroutine

```

```
subroutine search_for_coll(i_St)
implicit none

real(p3dfft_type) :: shift , x1(3)
integer :: i, j, ierr
integer , intent(in) :: i_St

!lists of particles inside boxes
allocate(list(0:N_B(1, i_St)-1, 0:N_B(2, i_St)-1, 0:N_B(3, i_St)-1))

!distribute particles according to x1
call distribute_part(0d0, 0, i_St)
do i = 1, N_part(i_St)
  x1 = mod(part(i_St)%x1(:, i)+delta_x_part+twoPI*AR, twoPI*AR) - delta_x_part
  part(i_St)%x0(:, i) = part(i_St)%x0(:, i) + x1 - part(i_St)%x1(:, i)
  part(i_St)%x1(:, i) = x1
end do
!search for collision without shifting
call group_part(0d0, i_St)
call detect_coll(i_St)
call deallocate_lists(i_St)

!shift along x,y,z
shift = 3d0*init_radius(i_St)
forall(i = 1:N_part(i_St))
  part(i_St)%x1(:, i) = part(i_St)%x1(:, i) + shift
  part(i_St)%x0(:, i) = part(i_St)%x0(:, i) + shift
end forall
call distribute_part(0d0, 0, i_St)
do i = 1, N_part(i_St)
  x1 = mod(part(i_St)%x1(:, i)+delta_x_part+twoPI*AR, twoPI*AR) - delta_x_part
  part(i_St)%x0(:, i) = part(i_St)%x0(:, i) + x1 - part(i_St)%x1(:, i)
  part(i_St)%x1(:, i) = x1
end do
!search in shifted config
call group_part(0d0, i_St)
call detect_coll(i_St)
call deallocate_lists(i_St)

!shift back
forall(i = 1:N_part(i_St))
  part(i_St)%x1(:, i) = part(i_St)%x1(:, i) - shift
end forall

deallocate(list)

end subroutine
```

```

subroutine group_part(displ_dx, i_St)
implicit none

real(p3dfft_type), intent(in) :: displ_dx
real(p3dfft_type) :: displ(3), x(3)

integer, intent(in) :: i_St
integer :: i, i1, i2, i3

do i3 = 0, N_B(3, i_St)-1
do i2 = 0, N_B(2, i_St)-1
do i1 = 0, N_B(1, i_St)-1
    nullify(list(i1, i2, i3)%p)
end do
end do
end do

div_B_size = 1d0/B_size(:, i_St)
!displ = displ_dx
displ = delta_x_part + displ_dx

do i = 1, N_part(i_St)

!particle position shifted
x = part(i_St)%x1(:, i) + displ

i1 = mod(floor(x(1)*div_B_size(1)) + N_B(1, i_St), N_B(1, i_St))
i2 = mod(floor(x(2)*div_B_size(2)) + N_B(2, i_St), N_B(2, i_St))
i3 = mod(floor(x(3)*div_B_size(3)) + N_B(3, i_St), N_B(3, i_St))

allocate(node_a)
node_a%i = i
node_a%next => list(i1, i2, i3)%p
list(i1, i2, i3)%p => node_a

end do

end subroutine

```

A.9.1 Interpolation of the particle path

The numerical simulation provides the state variables and their time derivatives at time t_0 and $t_1 = t_0 + \Delta t$. The time resolution Δt is small compared to the smallest temporal scale of the flow but may be quite large compared to temporal scale of the particles since the particle radius is much smaller than the smallest scale of the flow. The state variables are known only at time t_0 and t_1 but the collision

generally occurs at $t_0 < t_c \leq t_1$, as a consequence the particle path has to be traced for each time $t \in (t_0, t_1]$. For simplicity let:

$$\begin{aligned} t_0 &= 0 \\ t_1 &= 1. \end{aligned}$$

A zero order interpolation scheme may lead to $\mathbf{v}(t_1) \cdot \Delta \mathbf{x}(t_1) > 0$, that is, the particles are separating at the time of the collision! On the other hand, an accurate interpolation of the particle trajectory is useless if the order of that interpolation is higher than the order of the time integration.

Here we provide a general scheme for particle trajectory reconstruction. For each particle we define the vector of the degrees of freedom as:

$$\tilde{\mathbf{q}} = [\mathbf{x}(t_0), \mathbf{x}(t_1), \mathbf{v}(t_0), \mathbf{v}(t_1)]^T$$

and the relative position and velocity between the particles α and β as:

$$\begin{aligned} \Delta \mathbf{x} &= \mathbf{x}^{(\alpha)} - \mathbf{x}^{(\beta)} \\ \Delta \mathbf{v} &= \mathbf{v}^{(\alpha)} - \mathbf{v}^{(\beta)} \end{aligned}$$

hence $\mathbf{q} = \tilde{\mathbf{q}}^{(\alpha)} - \tilde{\mathbf{q}}^{(\beta)}$ reads:

$$\mathbf{q} = [\Delta \mathbf{x}(t_0), \Delta \mathbf{x}(t_1), \Delta \mathbf{v}(t_0), \Delta \mathbf{v}(t_1)]^T.$$

When the particle size changes in time we define the vector of the radius and its derivative as:

$$\tilde{\mathbf{R}} = \left[r(t_0), r(t_1), \frac{dr}{dt}(t_0), \frac{dr}{dt}(t_1) \right]^T$$

then, the sum of $\tilde{\mathbf{R}}$ for the particles α and β is:

$$\mathbf{R} = \left[r^{(\alpha)}(t_0) + r^{(\beta)}(t_0), r^{(\alpha)}(t_1) + r^{(\beta)}(t_1), \frac{dr^{(\alpha)}}{dt}(t_0) + \frac{dr^{(\beta)}}{dt}(t_0), \frac{dr^{(\alpha)}}{dt}(t_1) + \frac{dr^{(\beta)}}{dt}(t_1) \right]^T$$

The collision criterion employed is that at the time of the collision the distance between the center of mass of the particles equals the sum of the radii of the particles and it reads

$$\left\| \mathbf{x}^{(\alpha)}(t_c) - \mathbf{x}^{(\beta)}(t_c) \right\| = r^{(\alpha)}(t_c) + r^{(\beta)}(t_c). \quad (\text{A.6})$$

Each degree of freedom of the particle is interpolated in time using the generic interpolating functions $H^i(t)$. Then the collision criterion becomes

$$\left\| H^i(t) \mathbf{q}_i \right\| = H^i(t) R_i, \quad (\text{A.7})$$

in which repeated upper and lower indexes imply summation. Squaring both sides one obtains,

$$H^i(t)H^j(t)(\mathbf{q}_i \cdot \mathbf{q}_j - R_i R_j) = 0 \quad (\text{A.8})$$

The generic interpolating polynomial of order M can be written as $H^i(t) = A_k^i t^k$, where the upper index i refers to the degree of freedom and t^k actually means t to the k power. Defining the quantity Z :

$$Z_{ij} = (\mathbf{q}_i \cdot \mathbf{q}_j - R_i R_j) \quad (\text{A.9})$$

the expression of the distance between two particles finally reads.

$$D(t) = Z_{ij} A_m^i A_n^j t^m t^n. \quad (\text{A.10})$$

Hence $D(t) = a_p t^p$ is a polynomial of degree $2M$ with coefficients:

$$a_p = \sum_{m+n=p} Z_{ij} A_m^i A_n^j, \quad p = 0, \dots, 2M \quad (\text{A.11})$$

At the collision time it happens that $D(t_c) = 0$. Since the degree of the polynomial $D(t)$ is higher than one then t_c is not unique in general. We suppose that previous collisions have already been detected, so the minimum time $t_c \in (0,1]$ such that $D(t_c) = 0$ is the quantity of interest. Therefore, the collision detection problem reads

$$t_c = \min \{ t \in \mathbb{R} : t \in (0,1] \text{ and } Z_{ij} A_m^i A_n^j t^m t^n = 0 \}.$$

The procedure sketched above is implemented in the code using polynomials of degree one to reconstruct the particle path. This is justified since in the presented simulations $\Delta t/\tau_p$ is small.

```

subroutine detect_coll(i_St)
implicit none

real(p3dfft_type), dimension(3) :: dx0, dx1
real(p3dfft_type), dimension(3) :: rel_x, xa, xb
real(p3dfft_type) :: dist_coll

real(p3dfft_type), dimension(3) :: va, vb, rel_v
real(p3dfft_type) :: Ta, ra, Tb, rb
real(p3dfft_type) :: R0, R1
real(p3dfft_type) :: r3, vel_coll, delta_v(3)

real(p3dfft_type) :: Z00, Z01, Z11
real(p3dfft_type) :: delta, a1, a2, div_a2
real(p3dfft_type) :: sol(3), tc, L0, L1
real(p3dfft_type) :: div_dist_coll
    
```



```

integer , intent(in) :: i_St

integer :: i1 , i2 , i3
integer :: ia , ib , j_ncoll

R0 = 2d0*init_radius(i_St) !part(i_St)%s0(2, ib) + part(i_St)%s0(2, ia)
R1 = 2d0*init_radius(i_St) !part(i_St)%s1(2, ib) + part(i_St)%s1(2, ia)

do i3 = 0, N_B(3, i_St)-1
do i2 = 0, N_B(2, i_St)-1
do i1 = 0, N_B(1, i_St)-1

node_a => list(i1, i2, i3)%p
do while(associated(node_a))
ia = node_a%i

node_b => node_a%next
do while(associated(node_b))
ib = node_b%i

!particles a and b at t0 and t1
dx0 = part(i_St)%x0(:, ib) - part(i_St)%x0(:, ia)
dx1 = part(i_St)%x1(:, ib) - part(i_St)%x1(:, ia)

!metric of the collision
Z00 = dot_product(dx0, dx0) - R0*R0
Z01 = dot_product(dx0, dx1) - R0*R1
Z11 = dot_product(dx1, dx1) - R1*R1
!determinant condition
delta = Z01*Z01 - Z00*Z11
determinant: if(delta .ge. 0d0)then
!approaching cond
approaching: if((norm2(dx1)-norm2(dx0)).lt.0d0)then

sol = 3d0
a2 = Z00 - 2d0*Z01 + Z11

delta = sqrt(delta)

!degree 2
if(a2 .ne. 0d0)then

div_a2 = 1d0/a2
a1 = Z01 - Z00
tc = (-a1 - delta)*div_a2
if(tc*tc .le. tc) sol(1) = tc
tc = (-a1 + delta)*div_a2
if(tc*tc .le. tc) sol(2) = tc

!degree 1

```

```

else

    a1 = 2d0*(Z01 - Z00)
    if(a1 .ne. 0d0)then
        tc = -Z00/a1
        if(tc*tc .le. tc) sol(3) = tc
    end if

end if

tc = minval(sol(1:3))
found: if(tc*tc .le. tc)then

!Lagrange in time
    L1 = tc
    L0 = 1d0 - tc

!variables at coll, not the actual velocity
    xa = L0*part(i_St)%x0(:, ia) + L1*part(i_St)%x1(:, ia)
    va = (part(i_St)%x1(:, ia) - part(i_St)%x0(:, ia))/dt
    Ta = L0*part(i_St)%s0(1, ia) + L1*part(i_St)%s1(1, ia)
    ra = init_radius(i_St)
    !L0*part0(i_St)%r(1, ia) + L1*part1(i_St)%r(1, ia)

    xb = L0*part(i_St)%x0(:, ib) + L1*part(i_St)%x1(:, ib)
    vb = (part(i_St)%x1(:, ib) - part(i_St)%x0(:, ib))/dt
    Tb = L0*part(i_St)%s0(1, ib) + L1*part(i_St)%s1(1, ib)
    rb = init_radius(i_St)
    !L0*part0(i_St)%r(2, ib) + L1*part1(i_St)%r(1, ib)

    rel_x = xb - xa
    dist_coll = norm2(rel_x)

    rel_x = rel_x/dist_coll
    rel_v = vb - va
    vel_coll = dot_product(rel_x, rel_v)

    delta_v = vel_coll*rel_x
    part(i_St)%u1(:, ia) = va + delta_v
    part(i_St)%x1(:, ia) = xa + part(i_St)%u1(:, ia)*L0*dt
    part(i_St)%u1(:, ib) = vb - delta_v
    part(i_St)%x1(:, ib) = xb + part(i_St)%u1(:, ib)*L0*dt

end if found

end if approaching
end if determinant

node_b => node_b%next

```

```
end do!list b

node_a => node_a%next

end do!list a

end do
end do
end do!coordinates of the cell

end subroutine
```

A.10 Particles sorting

In order to avoid cache missing in the interpolation of the flow fields at the particles positions and in the particle back-reaction computation the particles are sorted based on their position. Indeed, the fields are stored in memory varying the x coordinates first, then y and then z . Therefore, particles should be stored from the smallest to the largest z_p , from the smallest to the largest y_p and from the smallest to the largest x_p in order to minimize cache-missing when the patch of field is uploaded in memory to perform the direct/reverse interpolation. Since the cache (especially L2 and L3 levels) have a relatively large size, cache missing can be avoided even if the particles are not ordered strictly. The most important particle ordering criterion is based on the z_p coordinate, since a stride in z different from one implies skipping $x - y$ planes in memory, while a non-unitary stride in y implies skipping only x segments. The classical merge-sort algorithm is employed and the routine is called seldom, only when the particles are stored, since it is quite time-consuming. In order to optimize the procedure pointers are employed, avoiding actual copying operations.

```
module particles_sorting
use parameters
use particles_parameters
use particles_variables
implicit none

integer(sort_kind), dimension(:), pointer :: id_ms0, id_ms1

contains

subroutine merge_sort_part(i_St)
implicit none

integer :: i, i1, i2
```

```

integer :: N_p, N_p2, N_mstep
integer :: we, width, width2
integer, intent(in) :: i_St

allocate( id_ms0(N_part(i_St) + 1), id_ms1(N_part(i_St) + 1) )
id_ms0(N_part(i_St) + 1) = 0
id_ms1(N_part(i_St) + 1) = 0

do i = 1, N_part(i_St)
  id_ms1(i) = floor(part(i_St)%x1(1, i)*div_dxS(1))
  id_ms1(i) = id_ms1(i) + floor(part(i_St)%x1(2, i)*div_dxS(2))*P_size1
  id_ms1(i) = id_ms1(i) + floor(part(i_St)%x1(3, i)*div_dxS(3))*P_size2
end do

N_p = N_part(i_St)
N_mstep = ceiling( dlog(1d0*N_part(i_St))/dlog(2d0) )
width = 1
do we = 1, N_mstep
  width2 = 2*width
  N_p2 = N_p - mod(N_p, width2)
  do i = 1, N_p2, width2
    i1 = i + width
    i2 = i + width2
    call merge_sub(i, i1, i2, i_St)
  end do
  i = min(N_p2 + width, N_p)
  call merge_sub(N_p2+1, i+1, N_p+1, i_St)
  call swap_part(i_St)
  call swap_part_id
  width = width2
end do

deallocate(id_ms0, id_ms1)

end subroutine

subroutine merge_sub(left, center, right, i_St)
implicit none

integer, intent(in) :: i_St
integer, intent(in) :: left, center, right
integer :: i, j, k
integer :: ii

i = left
j = center
k = left

```

```

if( id_ms1(center-1) .gt. id_ms1(center) ) then
do while(i .lt. center .and. j .lt. right)
  if( id_ms1(i) .le. id_ms1(j) ) then
    call copy_part(k, i, i_St)
    id_ms0(k) = id_ms1(i)
    i = i + 1
  else
    call copy_part(k, j, i_St)
    id_ms0(k) = id_ms1(j)
    j = j + 1
  end if
  k = k + 1
end do
end if
do ii = i, center - 1
  call copy_part(k, ii, i_St)
  id_ms0(k) = id_ms1(ii)
  k = k + 1
end do
do ii = j, right - 1
  call copy_part(k, ii, i_St)
  id_ms0(k) = id_ms1(ii)
  k = k + 1
end do

end subroutine

```

```

subroutine copy_part(id, is, i_St)
implicit none

```

```

integer, intent(in) :: i_St, id, is

```

```

part(i_St)%x0(:, id) = part(i_St)%x1(:, is)
part(i_St)%u0(:, id) = part(i_St)%u1(:, is)
part(i_St)%s0(:, id) = part(i_St)%s1(:, is)

```

```

end subroutine

```

```

subroutine swap_part(i_St)
implicit none

```

```

real(p3dfft_type), dimension(:, :), pointer :: part_tmp => null()
integer, intent(in) :: i_St

```

```

!swap particle pointers
part_tmp      => part(i_St)%x1

```

```

part(i_St)%x1 => part(i_St)%x0
part(i_St)%x0 => part_tmp
part_tmp      => part(i_St)%u1
part(i_St)%u1 => part(i_St)%u0
part(i_St)%u0 => part_tmp
part_tmp      => part(i_St)%s1
part(i_St)%s1 => part(i_St)%s0
part(i_St)%s0 => part_tmp
part_tmp      => null()

```

```
end subroutine
```

```

subroutine swap_part_id
implicit none

```

```
integer(sort_kind), dimension(:), pointer :: id_tmp => null()
```

```
!swap position index pointers
```

```

id_tmp => id_ms1
id_ms1 => id_ms0
id_ms0 => id_tmp
id_tmp => null()

```

```
end subroutine
```

```
end module
```

A.11 Particles Input/Output

Particles following the domain parallelization to allow a quick restart of the simulation. An offset file `part_off` is stored, which contains the index of the first particle belonging to the process and the number of particles in that process, for each MPI process. Here we report the subroutines used to read the particles files. The arrays particle position `part_x`, velocity `part_u` and scalars `part_s` are stored in separate binary files, which are concurrently written by all the processes by means of MPI I/O utilities. The MPI process searches into the offset file for the addresses of the particles corresponding to its portion of domain and then calls the subroutines for parallel file reading.

```

subroutine read_part(iter, i_St)
implicit none

```

```
integer, intent(in) :: i_St, iter
```

```
integer(kind = MPI_OFFSET_KIND) :: off
```

```

integer :: Np

integer :: old_coords(2), old_proc_id
integer :: i_read, j_read
integer :: i, j

if(proc_id .eq. 0) print*, "Reading_file_part", iter

1 format("part_off", I1.1, ".", I3.3, ".bin")
2 format("part_x",   I1.1, ".", I3.3, ".bin")
3 format("part_u",   I1.1, ".", I3.3, ".bin")
4 format("part_s",   I1.1, ".", I3.3, ".bin")

j = 0
!how many times new coords are in old coords
do j_read = 0, (old_dims(2) - 1)/dims(2)

!coordinates of the same domain in the old decomposition
old_coords(2) = old_dims(2)*coords(2)/dims(2) + j_read

do i_read = 0, (old_dims(1) - 1)/dims(1)

old_coords(1) = old_dims(1)*coords(1)/dims(1) + i_read

!number of the processor in old decomposition
old_proc_id = old_coords(1) + old_dims(1)*old_coords(2)

!offset and number of part from old proc grid
write(file_part, 1) i_St, iter
call read_part_off(old_proc_id)

off = int(off_vect(1), MPI_OFFSET_KIND) !offset (Bytes)
Np  = int(off_vect(2), kind(1)) !N_part

allocate(buff_io(3, Np))

!read x0
write(file_part, 2) i_St, iter
call read_part_comp(off, Np)
part(i_St)%x0(:, j+1:j+Np) = real(buff_io, p3dfft_type)

!read u0
write(file_part, 3) i_St, iter
call read_part_comp(off, Np)
part(i_St)%u0(:, j+1:j+Np) = real(buff_io, p3dfft_type)

!read s0
write(file_part, 4) i_St, iter
call read_part_comp(off, Np)
part(i_St)%s0(:, j+1:j+Np) = real(buff_io, p3dfft_type)

```

```

!update number of particles
  j = j + Np

  deallocate(buff_io)

  end do
end do

N_part(i_St) = j

!the first step may require p0 and p1
do j = 1, N_part(i_St)

  part(i_St)%x1(:, j) = part(i_St)%x0(:, j)
  part(i_St)%u1(:, j) = part(i_St)%u0(:, j)
  part(i_St)%s1(:, j) = part(i_St)%s0(:, j)

end do

!compute and display tot number of particles
call MPI_reduce(int(N_part(i_St), 8), N_part_tot(i_St), &
1, MPI_INTEGER8, MPI_SUM, 0, MPI_COMM_WORLD, i)

if(proc_id .eq. 0) print*, "Read", N_part_tot(i_St), "particles"

end subroutine

subroutine read_part_off(id)
implicit none

integer(kind = MPI_OFFSET_KIND) :: off
integer :: Np
integer :: fh, ierr
integer, intent(in) :: id

!off for the file of the offsets
off = int(16*id, MPI_OFFSET_KIND)
Np = 2

fh = 0
ierr = 0
call MPI_FILE_OPEN(MPI_COMM_WORLD, file_part, &
& MPI_MODE_RDONLY, MPI_INFO_NULL, fh, ierr)

call MPI_File_set_view(fh, off, MPI_DOUBLE, MPI_DOUBLE, &
& "native", MPI_INFO_NULL, ierr)

```



```
call MPI_FILE_READ_ALL(fh, off_vect, &
Np, MPI_DOUBLE, MPI_STATUS_IGNORE, ierr)

call MPI_FILE_CLOSE(fh, ierr)

end subroutine

subroutine read_part_comp(off, Np)
implicit none

integer, intent(in) :: Np
integer(kind = MPI_OFFSET_KIND), intent(in) :: off
integer :: fh, ierr

fh = 0
ierr = 0
call MPI_FILE_OPEN(MPI_COMM_WORLD, file_part, &
& MPI_MODE_RDONLY, MPI_INFO_NULL, fh, ierr)

call MPI_File_set_view(fh, off, MPI_io_kind, MPI_io_kind, &
& "native", MPI_INFO_NULL, ierr)

call MPI_FILE_READ_ALL(fh, buff_io, &
3*Np, MPI_io_kind, MPI_STATUS_IGNORE, ierr)

call MPI_FILE_CLOSE(fh, ierr)

end subroutine
```


Bibliography

- [1] G. Alfonsi. “On Direct Numerical Simulation of Turbulent Flows”. In: ASME. Applied Mechanics Reviews 64 (2 2011), pp. 020802–020802-33. doi: [10.1115/1.4005282](https://doi.org/10.1115/1.4005282).
- [2] M. Andrejczuk et al. “Numerical simulation of cloud-clear air interfacial mixing: effects on cloud microphysics”. In: Journal of the Atmospheric Sciences 63 (2006), pp. 3204–3225.
- [3] V.I. Arnold. Geometrical Methods in the Theory of Ordinary Differential Equations. Springer-Verlag New York, 1988.
- [4] W. T. Ashurst et al. “Alignment of vorticity and scalar gradient with strain rate in simulated Navier–Stokes turbulence”. In: The Physics of Fluids 30.8 (1987), pp. 2343–2353. doi: [10.1063/1.866513](https://doi.org/10.1063/1.866513).
- [5] T. R. Auton. “The lift force on a spherical body in a rotational flow”. In: Journal of Fluid Mechanics 183 (1987), pp. 199–218. doi: [10.1017/S002211208700260X](https://doi.org/10.1017/S002211208700260X).
- [6] J. G. Ballouz and N. T. Ouellette. “Tensor geometry in the turbulent cascade”. In: Journal of Fluid Mechanics 835 (2018), pp. 1048–1064. doi: [10.1017/jfm.2017.802](https://doi.org/10.1017/jfm.2017.802).
- [7] A. B. Basset. Treatise on Hydrodynamics. Deighton Bell, 1888.
- [8] J. Béc, H. Homann, and G. Krstulovic. “Clustering, Fronts, and Heat Transfer in Turbulent Suspensions of Heavy Particles”. In: Physical Review Letters 112 (23 2014), p. 234503. doi: [10.1103/PhysRevLett.112.234503](https://doi.org/10.1103/PhysRevLett.112.234503).
- [9] J. Bec et al. “Heavy Particle Concentration in Turbulence at Dissipative and Inertial Scales”. In: Physical Review Letters 98 (8 2007), p. 084502. doi: [10.1103/PhysRevLett.98.084502](https://doi.org/10.1103/PhysRevLett.98.084502).
- [10] R. Betchov. “An inequality concerning the production of vorticity in isotropic turbulence”. In: Journal of Fluid Mechanics 1.5 (1956), pp. 497–504. doi: [10.1017/S0022112056000317](https://doi.org/10.1017/S0022112056000317).
- [11] G. Beylkin. “On the Fast Fourier Transform of Functions with Singularities”. In: Applied and Computational Harmonic Analysis 2.4 (1995), pp. 363–381. doi: <https://doi.org/10.1006/acha.1995.1026>.

- [12] G. Boffetta et al. “The Eulerian description of dilute collisionless suspension”. In: *Europhysics Letters* 78.1 (2007), p. 14001.
- [13] M. Boivin, O. Simonin, and K. D. Squires. “Direct numerical simulation of turbulence modulation by particles in isotropic turbulence”. In: *Journal of Fluid Mechanics* 375 (1998), pp. 235–263. doi: [10.1017/S0022112098002821](https://doi.org/10.1017/S0022112098002821).
- [14] V. Borue and S. A. Orszag. “Local energy flux and subgrid-scale statistics in three-dimensional turbulence”. In: *Journal of Fluid Mechanics* 366 (1998), pp. 1–31.
- [15] L. Botto and A. Prosperetti. “A fully resolved numerical simulation of turbulent flow past one or several spherical particles”. In: *Physics of Fluids* 24.1 (2012), p. 013303. doi: [10.1063/1.3678336](https://doi.org/10.1063/1.3678336).
- [16] A. D. Bragg, P. J. Ireland, and L. R. Collins. “Mechanisms for the clustering of inertial particles in the inertial range of isotropic turbulence”. In: *Physical Review E* 92 (2 2015), p. 023029. doi: [10.1103/PhysRevE.92.023029](https://doi.org/10.1103/PhysRevE.92.023029).
- [17] A. D. Bragg, P. J. Ireland, and L. R. Collins. “On the relationship between the non-local clustering mechanism and preferential concentration”. In: *Journal of Fluid Mechanics* 780 (2015), pp. 327–343. doi: [10.1017/jfm.2015.474](https://doi.org/10.1017/jfm.2015.474).
- [18] A.D. Bragg and L.R. Collins. “New insights from comparing statistical theories for inertial particles in turbulence: I. Spatial distribution of particles.” In: *New Journal of Physics* 16 (2014), p. 055013.
- [19] A.D. Bragg and L.R. Collins. “New insights from comparing statistical theories for inertial particles in turbulence: II. Relative velocities of particles.” In: *New Journal of Physics* 16 (2014), p. 055014.
- [20] D. Buaria et al. “Extreme velocity gradients in turbulent flows”. In: *New Journal of Physics* 21.4 (2019), p. 043004. doi: [10.1088/1367-2630/ab0756](https://doi.org/10.1088/1367-2630/ab0756).
- [21] Y. A. Buevich. “Motion resistance of a particle suspended in a turbulent medium”. In: *Fluid Dynamics* 1.6 (1966), pp. 119–119. doi: [10.1007/BF01022298](https://doi.org/10.1007/BF01022298).
- [22] B. J. Cantwell. “Exact solution of a restricted Euler equation for the velocity gradient tensor”. In: *Physics of Fluids A: Fluid Dynamics* 4.4 (1992), pp. 782–793. doi: [10.1063/1.858295](https://doi.org/10.1063/1.858295).
- [23] C. Canuto et al. *Spectral Methods in Fluid Dynamics*. Springer, 1988.
- [24] M. Carbone and A. D. Bragg. “Is vortex stretching the main cause of the turbulent energy cascade?” In: *Journal of Fluid Mechanics* 883 (2020), R2. doi: [10.1017/jfm.2019.923](https://doi.org/10.1017/jfm.2019.923).
- [25] M. Carbone, A. D. Bragg, and M. Iovieno. “Multiscale fluid–particle thermal interaction in isotropic turbulence”. In: *Journal of Fluid Mechanics* 881 (2019), pp. 679–721. doi: [10.1017/jfm.2019.773](https://doi.org/10.1017/jfm.2019.773).

- [26] M. Carbone, A.D. Bragg, and M. Iovieno. “Modulation of fluid temperature fluctuations by inertial particles in turbulence”. In: Springer Proceedings in Physics 226 (2019), pp. 247–252. doi: [10.1007/978-3-030-22196-6_39](https://doi.org/10.1007/978-3-030-22196-6_39).
- [27] M. Carbone and M. Iovieno. “Accurate Direct Numerical Simulation of two-way coupled particle-laden flows through the Nonuniform Fast Fourier Transform”. In: International Journal of Safety and Security Engineering, in press (2020).
- [28] M. Carbone and M. Iovieno. “Application of the Non-Uniform Fast Fourier Transform to the Direct Numerical Simulation of two-way coupled Turbulent Flows”. In: Advances in Fluid Mechanics XII. Vol. 120. 2018, pp. 237–248.
- [29] M. Carbone, M. Iovieno, and A. D. Bragg. “Gauge symmetry and dimensionality reduction of the anisotropic pressure Hessian”. In: Submitted to the Journal of Fluid Mechanics (2020). arXiv: [1911.08652v1](https://arxiv.org/abs/1911.08652v1).
- [30] A. Celani et al. “Universality and Saturation of Intermittency in Passive Scalar Turbulence”. In: Physical Review Letters 84 (11 2000), pp. 2385–2388. doi: [10.1103/PhysRevLett.84.2385](https://doi.org/10.1103/PhysRevLett.84.2385).
- [31] S. Chen, K. R. Sreenivasan, and M. Nelkin. “Inertial Range Scalings of Dissipation and Enstrophy in Isotropic Turbulence”. In: Physical Review Letters 79 (7 1997), pp. 1253–1256. doi: [10.1103/PhysRevLett.79.1253](https://doi.org/10.1103/PhysRevLett.79.1253).
- [32] M. Chertkov, A. Pumir, and B. I. Shraiman. “Lagrangian tetrad dynamics and the phenomenology of turbulence”. In: Physics of Fluids 11.8 (1999), pp. 2394–2410. doi: [10.1063/1.870101](https://doi.org/10.1063/1.870101).
- [33] L. Chevillard and C. Meneveau. “Lagrangian Dynamics and Statistical Geometric Structure of Turbulence”. In: Physical Review Letters 97 (17 2006), p. 174501. doi: [10.1103/PhysRevLett.97.174501](https://doi.org/10.1103/PhysRevLett.97.174501).
- [34] L. Chevillard et al. “Modeling the pressure Hessian and viscous Laplacian in turbulence: Comparisons with direct numerical simulation and implications on velocity gradient dynamics”. In: Physics of Fluids 20.10 (2008), p. 101504. doi: [10.1063/1.3005832](https://doi.org/10.1063/1.3005832).
- [35] J. Chun et al. “Clustering of aerosol particles in isotropic turbulence”. In: Journal of Fluid Mechanics 536 (2005), pp. 219–251.
- [36] J. D. Cole. “On a quasi-linear parabolic equation occurring in aerodynamics”. In: Quarterly of Applied Mathematics 9 (1951), pp. 225–236. doi: [10.1017/jfm.2016.630](https://doi.org/10.1017/jfm.2016.630).
- [37] S. Corrsin and J. Lumley. “On the equation of motion for a particle in turbulent fluid”. In: Applied Scientific Research, Section A 6.2 (1956), pp. 114–116. doi: [10.1007/BF03185030](https://doi.org/10.1007/BF03185030).

- [38] Y. Cui et al. “On Constitutive Models for the Momentum Transfer to Particles in Fluid-Dominated Two-Phase Flows”. In: *Advances in Mechanics of Materials and Structural Analysis: In Honor of Reinhold Kienzler*. Springer International Publishing, 2018, pp. 1–25. doi: [10.1007/978-3-319-70563-7_1](https://doi.org/10.1007/978-3-319-70563-7_1).
- [39] Y. Cui et al. “Towards a unified shear-induced lift model for prolate spheroidal particles moving in arbitrary non-uniform flow”. In: *Computers & Fluids* 196 (2020), p. 104323. doi: <https://doi.org/10.1016/j.compfluid.2019.104323>.
- [40] M. Danish and C. Meneveau. “Multiscale analysis of the invariants of the velocity gradient tensor in isotropic turbulence”. In: *Physical Review Fluids* 3 (4 2018), p. 044604. doi: [10.1103/PhysRevFluids.3.044604](https://doi.org/10.1103/PhysRevFluids.3.044604).
- [41] S. K. Das, S. U. S. Choi, and H. E. Patel. “Heat transfer in nanofluids - A review”. In: *Heat Transfer Engineering* 27.10 (2006), pp. 3–19.
- [42] P. A. Davidson. *Turbulence: an introduction for scientists and engineers*. Oxford, 2004.
- [43] T. de Karman and L. Howarth. “On the Statistical Theory of Isotropic Turbulence”. In: *Proceedings of the Royal Society of London. Series A - Mathematical and Physical Sciences* 164.917 (1938), pp. 192–215. doi: [10.1098/rspa.1938.0013](https://doi.org/10.1098/rspa.1938.0013).
- [44] F. De Lillo et al. “Turbulent Fluid Acceleration Generates Clusters of Gyrotactic Microorganisms”. In: *Physical Review Letters* 112 (4 2014), p. 044502. doi: [10.1103/PhysRevLett.112.044502](https://doi.org/10.1103/PhysRevLett.112.044502).
- [45] B. J. Devenish et al. “Droplet growth in warm turbulent clouds”. In: *Quarterly Journal of the Royal Meteorological Society* 138 (2012), pp. 1401–1429.
- [46] R. Dhariwal and S. L. Rani. “Effects of deterministic and stochastic forcing schemes on the relative motion of inertial particles in DNS of isotropic turbulence”. In: *Powder Technology* 339 (2018), pp. 46–69. doi: <https://doi.org/10.1016/j.powtec.2018.07.058>.
- [47] Rohit Dhariwal and A. D. Bragg. “Small-scale dynamics of settling, bidisperse particles in turbulence”. In: *Journal of Fluid Mechanics* 839 (2018), pp. 594–620.
- [48] N. A. K. Doan et al. “Scale locality of the energy cascade using real space quantities”. In: *Physical Review Fluids* 3 (8 2018), p. 084601. doi: [10.1103/PhysRevFluids.3.084601](https://doi.org/10.1103/PhysRevFluids.3.084601).
- [49] D. A. Donzis, P. K. Yeung, and K. R. Sreenivasan. “Dissipation and enstrophy in isotropic turbulence: Resolution effects and scaling in direct numerical simulations”. In: *Physics of Fluids* 20.4 (2008), p. 045108. doi: [10.1063/1.2907227](https://doi.org/10.1063/1.2907227).

- [50] E. Dresselhaus and M. Tabor. “The kinematics of stretching and alignment of material elements in general flow fields”. In: *Journal of Fluid Mechanics* 236 (1992), pp. 415–444. doi: [10.1017/S0022112092001460](https://doi.org/10.1017/S0022112092001460).
- [51] A. Dutt and V. Rokhlin. “Fast Fourier Transforms for Nonequispaced Data”. In: *SIAM Journal on Scientific Computing* 14.6 (1993), pp. 1368–1393. doi: [10.1137/0914081](https://doi.org/10.1137/0914081).
- [52] H. Eggers, T. Knopp, and D. Potts. “Field inhomogeneity correction based on gridding reconstruction for magnetic resonance imaging”. In: *IEEE Transactions on Medical Imaging* 26.3 (2007), pp. 374–384.
- [53] S. Elghobashi. “On predicting particle-laden turbulent flows”. In: *Applied Scientific Research* 52.4 (1994), pp. 309–329. doi: [10.1007/BF00936835](https://doi.org/10.1007/BF00936835).
- [54] S. Elghobashi. “Particle-laden turbulent flows: direct simulation and closure models”. In: *Applied Scientific Research* 48.3 (1991), pp. 301–314. doi: [10.1007/BF02008202](https://doi.org/10.1007/BF02008202).
- [55] G. L. Eyink. “Cascade of circulations in fluid turbulence”. In: *Physical Review E* 74 (6 2006), p. 066302. doi: [10.1103/PhysRevE.74.066302](https://doi.org/10.1103/PhysRevE.74.066302).
- [56] G. L. Eyink. “Multi-scale gradient expansion of the turbulent stress tensor”. In: *Journal of Fluid Mechanics* 549 (2006), pp. 159–190. doi: [10.1017/S0022112005007895](https://doi.org/10.1017/S0022112005007895).
- [57] G. Falkovich. “Symmetries of the turbulent state”. In: *Journal of Physics A: Mathematical and Theoretical* 42 (2009), p. 123001.
- [58] G. Falkovich and K. Gawędzki. “Turbulence on Hyperbolic Plane: The Fate of Inverse Cascade”. In: *Journal of Statistical Physics* 156.1 (2014), pp. 10–54. doi: [10.1007/s10955-014-0995-x](https://doi.org/10.1007/s10955-014-0995-x).
- [59] H. Faxén. “Der Widerstand gegen die Bewegung einer starren Kugel in einer zähen Flüssigkeit, die zwischen zwei parallelen ebenen Wänden eingeschlossen ist”. In: *Annalen der Physik* 373.10 (1922), pp. 89–119. doi: [10.1002/andp.19223731003](https://doi.org/10.1002/andp.19223731003).
- [60] U. Frisch. *Turbulence: The Legacy of A. N. Kolmogorov*. Cambridge University Press, 1995.
- [61] S. S. Girimaji and S. B. Pope. “A diffusion model for velocity gradients in turbulence”. In: *Physics of Fluids A: Fluid Dynamics* 2.2 (1990), pp. 242–256. doi: [10.1063/1.857773](https://doi.org/10.1063/1.857773).
- [62] T. Gotoh, T. Suchito, and I. Saito. “Continuous growth of cloud droplets in continuous cloud”. In: *New Journal of Physics* 19 (2016), p. 043042. doi: [10.1088/1367-2630/4/043042](https://doi.org/10.1088/1367-2630/4/043042).

- [63] T. Gotoh and T. Watanabe. “Power and Nonpower Laws of Passive Scalar Moments Convected by Isotropic Turbulence”. In: *Physical Review Letters* 115 (11 2015), p. 114502. doi: [10.1103/PhysRevLett.115.114502](https://doi.org/10.1103/PhysRevLett.115.114502).
- [64] P. Götzfried et al. “Droplet dynamics and fine-scale structure in a shearless turbulent mixing layer with phase changes”. In: *Journal of Fluid Mechanics* 814 (2017), pp. 452–483. doi: [10.1017/jfm.2017.23](https://doi.org/10.1017/jfm.2017.23).
- [65] W. W. Grabowski and L.P. Wang. “Growth of Cloud Droplets in a Turbulent Environment”. In: *Annual Review of Fluid Mechanics* 45.1 (2013), pp. 293–324. doi: [10.1146/annurev-fluid-011212-140750](https://doi.org/10.1146/annurev-fluid-011212-140750).
- [66] L. Greengard. *The Rapid Evaluation of Potential Fields in Particle Systems*. MIT Press, 1988.
- [67] L. Greengard and J. Lee. “Accelerating the Nonuniform Fast Fourier Transform”. In: *SIAM Review* 46.3 (2004), pp. 443–454. doi: [10.1137/S003614450343200X](https://doi.org/10.1137/S003614450343200X).
- [68] P. Gualtieri et al. “Clustering and turbulence modulation in particle-laden shear flows”. In: *Journal of Fluid Mechanics* 715 (2013), pp. 134–162. doi: [10.1017/jfm.2012.503](https://doi.org/10.1017/jfm.2012.503).
- [69] P. Gualtieri et al. “Exact regularized point particle method for multiphase flows in the two-way coupling regime”. In: *Journal of Fluid Mechanics* 773 (2015), pp. 520–561. doi: [10.1017/jfm.2015.258](https://doi.org/10.1017/jfm.2015.258).
- [70] G. Gulitski et al. “Velocity and temperature derivatives in high-Reynolds-number turbulent flows in the atmospheric surface layer. Part 1. Facilities, methods and some general results”. In: *Journal of Fluid Mechanics* 589 (2007), pp. 57–81.
- [71] K. Gustavsson and B. Mehlig. “Ergodic and non-ergodic clustering of inertial particles”. In: *Europhysics Letters* 96 (2011), p. 60012.
- [72] K. Gustavsson and B. Mehlig. “Statistical models for spatial patterns of heavy particles in turbulence”. In: *Advances in Physics* 65.1 (2016), pp. 1–57. doi: [10.1080/00018732.2016.1164490](https://doi.org/10.1080/00018732.2016.1164490).
- [73] R. J. Hill. “Equations relating structure functions of all order”. In: *Journal of Fluid Mechanics* 434 (2001), pp. 379–388.
- [74] Reginald J. Hill. “Applicability of Kolmogorov’s and Monin’s equations of turbulence”. In: *Journal of Fluid Mechanics* 353 (1997), pp. 67–81. doi: [10.1017/S0022112097007362](https://doi.org/10.1017/S0022112097007362).
- [75] M.A.T. Hinsberg, van et al. “On the efficiency and accuracy of interpolation methods for spectral codes”. In: *SIAM Journal on Scientific Computing* 34.4 (2012), B479–B498. doi: [10.1137/110849018](https://doi.org/10.1137/110849018).
- [76] M. Hochbruck and A. Ostermann. “Exponential integrators”. In: *Acta Numerica* 19 (2010), pp. 209–286.

- [77] M. Holzer and E. D. Siggia. “Turbulent mixing of a passive scalar”. In: *Physics of Fluids* 6.5 (1994), pp. 1820–1837. doi: [10.1063/1.868243](https://doi.org/10.1063/1.868243).
- [78] E. Hopf. “The partial differential equation $u_t + uu_x = \mu_{xx}$ ”. In: *Communications on Pure and Applied Mathematics* 3.3 (1950), pp. 201–230. doi: [10.1002/cpa.3160030302](https://doi.org/10.1002/cpa.3160030302).
- [79] J.A.K. Horwitz and A. Mani. “Accurate calculation of Stokes drag for point-particle tracking in two-way coupled flows”. In: *Journal of Computational Physics* 318 (2016), pp. 85–109. doi: <https://doi.org/10.1016/j.jcp.2016.04.034>.
- [80] M. Iovieno and M. Carbone. “On the condensational growth of droplets in isotropic turbulence”. In: *Springer Proceedings in Physics* 226 (2019), pp. 265–270. doi: [10.1007/978-3-030-22196-6_42](https://doi.org/10.1007/978-3-030-22196-6_42).
- [81] P. J. Ireland, A. D. Bragg, and L. R. Collins. “The effect of Reynolds number on inertial particle dynamics in isotropic turbulence. Part 1. Simulations without gravitational effects”. In: *Journal of Fluid Mechanics* 796 (2016), pp. 617–658. doi: [10.1017/jfm.2016.238](https://doi.org/10.1017/jfm.2016.238).
- [82] P. J. Ireland, A. D. Bragg, and L. R. Collins. “The effect of Reynolds number on inertial particle dynamics in isotropic turbulence. Part 2. Simulations with gravitational effects”. In: *Journal of Fluid Mechanics* 796 (2016), pp. 659–711. doi: [10.1017/jfm.2016.227](https://doi.org/10.1017/jfm.2016.227).
- [83] P. J. Ireland et al. “Highly parallel particle-laden flow solver for turbulence research”. In: *Computers & Fluids* 76 (2013), pp. 170–177. doi: [10.1016/j.compfluid.2013.01.020](https://doi.org/10.1016/j.compfluid.2013.01.020).
- [84] A. Jaczewski and S. P. Malinowski. “Spatial distribution of cloud droplets in a turbulent cloud-chamber flow”. In: *Quarterly Journal of the Royal Meteorological Society* 131 (2005), pp. 2047–2062. doi: [10.1256/qj.04.65](https://doi.org/10.1256/qj.04.65).
- [85] H. Jeffreys. *Cartesian Tensors*. Cambridge University Press, 1931.
- [86] P. L. Johnson and C. Meneveau. “A closure for Lagrangian velocity gradient evolution in turbulence using recent-deformation mapping of initially Gaussian fields”. In: *Journal of Fluid Mechanics* 804 (2016), pp. 387–419. doi: [10.1017/jfm.2016.551](https://doi.org/10.1017/jfm.2016.551).
- [87] P. L. Johnson and C. Meneveau. “Turbulence intermittency in a multiple-time-scale Navier-Stokes-based reduced model”. In: *Physical Review Fluids* 2 (7 2017), p. 072601. doi: [10.1103/PhysRevFluids.2.072601](https://doi.org/10.1103/PhysRevFluids.2.072601).
- [88] E. A. Kearsley and J. T. Fong. “Linearly Independent Sets of Isotropic Cartesian Tensors of Ranks up to Eight”. In: *Journal Of Research of the National Bureau of Standards - B. Mathematical Sciences* 79B.1-2 (1975), pp. 49–58. doi: https://nvlpubs.nist.gov/nistpubs/jres/79b/jresv79bn1-2p49_a1b.pdf.

- [89] A. P. Khain et al. “Representation of microphysical processes in cloud-resolving models: spectral(bin) microphysics versus bulk parametrization”. In: *Review of Geophysics* 53 (2015), pp. 247–322. doi: [10.1002/2014RG000468](https://doi.org/10.1002/2014RG000468).
- [90] A. N. Kolmogorov. “The local structure of turbulence in an incompressible viscous fluid for very large Reynolds numbers”. In: *Doklady Akademii Nauk SSSR* 30 (1941), pp. 299–303.
- [91] A. B. Kostinski. “Simple approximations for condensational growth”. In: *Environmental Research Letters* 4 (2009), p. 015005. doi: [10.1088/1748-9326/4/1/015005](https://doi.org/10.1088/1748-9326/4/1/015005).
- [92] R. H. Kraichnan. “Anomalous scaling of a randomly advected passive scalar”. In: *Physical Review Letters* 72 (7 1994), pp. 1016–1019. doi: [10.1103/PhysRevLett.72.1016](https://doi.org/10.1103/PhysRevLett.72.1016).
- [93] J. G. M. Kuerten, C. W. M. van der Geld, and B. J. Geurts. “Turbulence modification and heat transfer enhancement by inertial particles in turbulent channel flow”. In: *Physics of Fluids* 23.12 (2011), p. 123301. doi: [10.1063/1.3663308](https://doi.org/10.1063/1.3663308).
- [94] B. Kumar, J. Schumacher, and R. A. Shaw. “Cloud microphysical effects of turbulent mixing and entrainment”. In: *Theoretical and Computational Fluid Dynamics* 27.3 (2013), pp. 361–376.
- [95] B. Kumar, J. Schumacher, and R. A. Shaw. “Lagrangian Mixing Dynamics at the Cloudy–Clear Air Interface”. In: *Journal of the Atmospheric Sciences* 71.7 (2014), pp. 2564–2580. doi: [10.1175/JAS-D-13-0294.1](https://doi.org/10.1175/JAS-D-13-0294.1).
- [96] B. Kumar et al. “Cloud-edge mixing: direct numerical simulation and observation in Indian monsoon clouds”. In: *Journal of Advances in Modeling Earth Systems* 9 (2017), pp. 332–353. doi: [10.1002/2016MS000731](https://doi.org/10.1002/2016MS000731).
- [97] B. Kumar et al. “Extreme responses of a coupled scalar-particle system during turbulent mixing”. In: *New Journal of Physics* 14, 115020 (2012).
- [98] A. S. Lanotte, A. Seminara, and F. Toschi. “Cloud Droplet Growth by Condensation in Homogeneous Isotropic Turbulence”. In: *Journal of the Atmospheric Sciences* 66.6 (2009), pp. 1685–1697. doi: [10.1175/2008JAS2864.1](https://doi.org/10.1175/2008JAS2864.1).
- [99] M. L. Larsen et al. “Fine-Scale Droplet Clustering in Atmospheric Clouds: 3D Radial Distribution Function from Airborne Digital Holography”. In: *Physical Review Letters* 121 (20 2018), p. 204501. doi: [10.1103/PhysRevLett.121.204501](https://doi.org/10.1103/PhysRevLett.121.204501).
- [100] J. M. Lawson and J. R. Dawson. “On velocity gradient dynamics and turbulent structure”. In: *Journal of Fluid Mechanics* 780 (2015), pp. 60–98. doi: [10.1017/jfm.2015.452](https://doi.org/10.1017/jfm.2015.452).

- [101] D. Lindbo and A. K. Tornberg. “Spectral accuracy in fast Ewald-based methods for particle simulations”. In: *Journal of Computational Physics* 230.24 (2011), pp. 8744–8761. doi: <https://doi.org/10.1016/j.jcp.2011.08.022>.
- [102] E. Lindborg. “A note on Kolmogorov’s third-order structure-function law, the local isotropy hypothesis and the pressure–velocity correlation”. In: *Journal of Fluid Mechanics* 326 (1996), pp. 343–356. doi: [10.1017/S0022112096008348](https://doi.org/10.1017/S0022112096008348).
- [103] J. G. M. Kuerten. “Point-Particle DNS and LES of Particle-Laden Turbulent flow—a state-of-the-art review”. In: *Flow, Turbulence and Combustion* 97.3 (2016), pp. 689–713. doi: [10.1007/s10494-016-9765-y](https://doi.org/10.1007/s10494-016-9765-y).
- [104] T. Ma et al. “Progress in the second-moment closure for bubbly flow based on direct numerical simulation data”. In: *Journal of Fluid Mechanics* 883 (2020), A9. doi: [10.1017/jfm.2019.851](https://doi.org/10.1017/jfm.2019.851).
- [105] A. J. Majda and A. L. Bertozzi. *Vorticity and Incompressible Flow*. 2001. doi: [10.1017/CBO9780511613203](https://doi.org/10.1017/CBO9780511613203).
- [106] M. R. Maxey. “The gravitational settling of aerosol particles in homogeneous turbulence and random flow fields”. In: *Journal of Fluid Mechanics* 174 (1987), pp. 441–465. doi: [10.1017/S0022112087000193](https://doi.org/10.1017/S0022112087000193).
- [107] M. R. Maxey and J. J. Riley. “Equation of motion for a small rigid sphere in a nonuniform flow”. In: *Physics of Fluids* 26.4 (1983), pp. 883–889. doi: [10.1063/1.864230](https://doi.org/10.1063/1.864230).
- [108] C. Meneveau. “Lagrangian Dynamics and Models of the Velocity Gradient Tensor in Turbulent Flows”. In: *Annual Review of Fluid Mechanics* 43.1 (2011), pp. 219–245. doi: [10.1146/annurev-fluid-122109-160708](https://doi.org/10.1146/annurev-fluid-122109-160708).
- [109] P. Moin and K. Mahesh. “Direct Numerical Simulation: A Tool in Turbulence Research”. In: *Annual Review of Fluid Mechanics* 30 (1998), pp. 539–578.
- [110] M.R. Momenifar et al. “Effect of lubricating oil on flow boiling characteristics of R-600a/oil inside a horizontal smooth tube”. In: *Applied Thermal Engineering* 91 (2015), pp. 62–72. doi: <https://doi.org/10.1016/j.applthermaleng.2015.08.003>.
- [111] A. S. Monin, A. M. Yaglom, and J. L. Lumley. *Statistical Fluid Mechanics: Mechanics of Turbulence*, Vol. 2. The MIT Press, 1975.
- [112] A. Naso and A. Pumir. “Scale dependence of the coarse-grained velocity derivative tensor structure in turbulence”. In: *Physical Review E* 72 (5 2005), p. 056318. doi: [10.1103/PhysRevE.72.056318](https://doi.org/10.1103/PhysRevE.72.056318).
- [113] K. K. Nomura and G. K. Post. “The structure and dynamics of vorticity and rate of strain in incompressible homogeneous turbulence”. In: *Journal of Fluid Mechanics* 377 (1998), pp. 65–97. doi: [10.1017/S0022112098003024](https://doi.org/10.1017/S0022112098003024).

- [114] K. Ohkitani. “Eigenvalue problems in three-dimensional Euler flows”. In: *Physics of Fluids A: Fluid Dynamics* 5.10 (1993), pp. 2570–2572. doi: [10.1063/1.858772](https://doi.org/10.1063/1.858772).
- [115] R. Onishi, K. Takahashi, and J. C. Vassilicos. “An efficient parallel simulation of interacting inertial particles in homogeneous isotropic turbulence”. In: *Journal of Computational Physics* 242 (2013), pp. 809–827. doi: <https://doi.org/10.1016/j.jcp.2013.02.027>.
- [116] M. R. Overholt and S. B. Pope. “Direct numerical simulation of a passive scalar with imposed mean gradient in isotropic turbulence”. In: *Physics of Fluids* 8.11 (1996), pp. 3128–3148. doi: [10.1063/1.869099](https://doi.org/10.1063/1.869099).
- [117] Y. Pan and S. Banerjee. “Numerical simulation of particle interactions with wall turbulence”. In: *Physics of Fluids* 8.10 (1996), pp. 2733–2755. doi: [10.1063/1.869059](https://doi.org/10.1063/1.869059).
- [118] D. Pekurovsky. “P3DFFT: A Framework for Parallel Computations of Fourier Transforms in Three Dimensions”. In: *SIAM Journal on Scientific Computing* 34.4 (2012), pp. C192–C209. doi: [10.1137/11082748X](https://doi.org/10.1137/11082748X).
- [119] V. E. Perrin and H. J. Jonker. “Lagrangian droplet dynamics in the subsiding shell of a cloud using direct numerical simulations”. In: *Journal of the Atmospheric Sciences* 72 (2015), pp. 4015–4028. doi: [10.1175/JAS-D-15-0045.1](https://doi.org/10.1175/JAS-D-15-0045.1).
- [120] M. Pippig and D. Potts. “Parallel Three-Dimensional Nonequispaced Fast Fourier Transforms and Their Application to Particle Simulation”. In: *SIAM Journal on Scientific Computing* 35.4 (2013), pp. C411–C437. doi: [10.1137/120888478](https://doi.org/10.1137/120888478).
- [121] S. B. Pope. *Turbulent Flows*. New York: Cambridge University Press, 2000.
- [122] R. Prasher et al. “Effect of aggregation on thermal conduction in colloidal nanofluids”. In: *Applied Physics Letters* 89.14 (2006), p. 143119. doi: [10.1063/1.2360229](https://doi.org/10.1063/1.2360229).
- [123] H. R. Pruppacher and J. D. Klett. *Microphysics of Clouds and Precipitation*. 2nd ed. Springer, 2010.
- [124] J. Ravnik, C. Marchioli, and A. Soldati. “Application limits of Jeffery’s theory for elongated particle torques in turbulence: a DNS assessment”. In: *Acta Mechanica* 229.2 (2018), pp. 827–839. doi: [10.1007/s00707-017-2002-5](https://doi.org/10.1007/s00707-017-2002-5).
- [125] L. F. Richardson. *Weather Prediction by Numerical Process*. New York: Cambridge University Press, 1922.
- [126] H. P. Robertson. “The invariant theory of isotropic turbulence”. In: *Mathematical Proceedings of the Cambridge Philosophical Society* 36.2 (1940), pp. 209–223. doi: [10.1017/S0305004100017199](https://doi.org/10.1017/S0305004100017199).

-
- [127] P. G. Saffman. “The lift on a small sphere in a slow shear flow”. In: *Journal of Fluid Mechanics* 22.2 (1965), pp. 385–400. doi: [10.1017/S0022112065000824](https://doi.org/10.1017/S0022112065000824).
- [128] P. G. Saffmann and J. S. Turner. “On the collision of drops in turbulent clouds”. In: *Journal of Fluid Mechanics* 1 (1955), pp. 16–30.
- [129] P. Sagaut and C. Cambon. *Homogeneous Turbulence Dynamics*. Springer International Publishing, 2018.
- [130] I. Saito and T. Gotoh. “Turbulence and cloud droplets in cumulus clouds”. In: *New Journal of Physics* 20.2 (2018), p. 023001.
- [131] J. P. L. C. Salazar and L. R. Collins. “Inertial particle relative velocity statistics in homogeneous isotropic turbulence”. In: *Journal of Fluid Mechanics* 696 (2012), pp. 45–66.
- [132] G. Sardina et al. “Continuous Growth of Droplet Size Variance due to Condensation in Turbulent Clouds”. In: *Physical Review Letters* 115 (18 2015), p. 184501. doi: [10.1103/PhysRevLett.115.184501](https://doi.org/10.1103/PhysRevLett.115.184501).
- [133] Y. S. Sedunov. *Physics of Drop Formation in the Atmosphere*. Wiley, 1974.
- [134] G. Segré and A. Silberberg. “Behaviour of macroscopic rigid spheres in Poiseuille flow Part 1. Determination of local concentration by statistical analysis of particle passages through crossed light beams”. In: *Journal of Fluid Mechanics* 14.1 (1962), pp. 115–135. doi: [10.1017/S002211206200110X](https://doi.org/10.1017/S002211206200110X).
- [135] B. I. Shraiman and E. D. Siggia. “Scalar turbulence”. In: *Nature* 405 (2000), p. 639.
- [136] L. M. Smith and S. L. Woodruff. “Renormalization-Group Analysis of Turbulence”. In: *Annual Review of Fluid Mechanics* 30.1 (1998), pp. 275–310. doi: [10.1146/annurev.fluid.30.1.275](https://doi.org/10.1146/annurev.fluid.30.1.275).
- [137] K. R. Sreenivasan. “The passive scalar spectrum and the Obukhov–Corrsin constant”. In: *Physics of Fluids* 8.1 (1996), pp. 189–196. doi: [10.1063/1.868826](https://doi.org/10.1063/1.868826).
- [138] H. A. Stone. “Philip Saffman and viscous flow theory”. In: *Journal of Fluid Mechanics* 409 (2000), pp. 165–183. doi: [10.1017/S0022112099007697](https://doi.org/10.1017/S0022112099007697).
- [139] S. Sundaram and L. R. Collins. “Numerical Considerations in Simulating a Turbulent Suspension of Finite-Volume Particles”. In: *Journal of Computational Physics* 124.2 (1996), pp. 337–350. doi: <https://doi.org/10.1006/jcph.1996.0064>.
- [140] T. Takeuchi and D. N. C. Lin. “Radial Flow of Dust Particles in Accretion Disks”. In: *The Astrophysical Journal* 581.2 (2002), p. 1344.
- [141] G. I. Taylor. “Diffusion by Continuous Movements”. In: *Proceedings of the London Mathematical Society* s2-20.1 (1922), pp. 196–212. doi: [10.1112/plms/s2-20.1.196](https://doi.org/10.1112/plms/s2-20.1.196).

-
- [142] G. I. Taylor. “Production and dissipation of vorticity in a turbulent fluid”. In: *Proceedings of the Royal Society of London A: Mathematical, Physical and Engineering Sciences* 164.916 (1938), pp. 15–23.
- [143] G. I. Taylor. “The transport of vorticity and heat through fluids in turbulent motion”. In: *Proceedings of the Royal Society of London A: Mathematical, Physical and Engineering Sciences* 135.828 (1932), pp. 685–702. doi: [10.1098/rspa.1932.0061](https://doi.org/10.1098/rspa.1932.0061).
- [144] C. H. Tchen. *Mean Value and Correlation Problems connected with the Motion of Small Particles suspended in a turbulent fluid*. Springer Netherlands, 1947.
- [145] H. Tennekes and J. L. Lumley. *A first course in turbulence*. Cambridge: MIT Press, 1972.
- [146] W. T. Thomson. “Equations of motion for the variable mass system”. In: *AIAA Journal* 4 (4 1966), pp. 766–768.
- [147] F. Toschi and E. Bodenschatz. “Lagrangian Properties of Particles in Turbulence”. In: *Annual Review of Fluid Mechanics* 41.1 (2009), pp. 375–404. doi: [10.1146/annurev.fluid.010908.165210](https://doi.org/10.1146/annurev.fluid.010908.165210).
- [148] Abdalnour Y. Toukmaji and John A. Board. “Ewald summation techniques in perspective: a survey”. In: *Computer Physics Communications* 95.2 (1996), pp. 73–92. doi: [https://doi.org/10.1016/0010-4655\(96\)00016-1](https://doi.org/10.1016/0010-4655(96)00016-1).
- [149] J. Towns et al. “XSEDE: Accelerating Scientific Discovery”. In: *Computing in Science & Engineering* 16.5 (2014), pp. 62–74. doi: [10.1109/MCSE.2014.80](https://doi.org/10.1109/MCSE.2014.80).
- [150] A. Tsinober. *An informal introduction to turbulence*. Kluwer Academic Publishers, 2001.
- [151] S. Twomey. “The nuclei of natural cloud formation. Part II: The supersaturation in natural clouds and the variation of cloud droplet concentration”. In: *Pure And Applied Geophysics* 43 (1959), pp. 243–249.
- [152] P. A. Vaillancourt, M. K. Yau, and W. W. Grabonski. “Microscopic approach to cloud droplet growth. Part I: Model description and results without turbulence”. In: *Journal of the Atmospheric Sciences* 58 (2001), pp. 1945–1964. doi: [10.1175/1520-0469\(2003\)060<0103:CEOAL>2.0.CO;2](https://doi.org/10.1175/1520-0469(2003)060<0103:CEOAL>2.0.CO;2).
- [153] P. A. Vaillancourt et al. “Microscopic Approach to Cloud Droplet Growth by Condensation. Part II: Turbulence, Clustering, and Condensational Growth”. In: *Journal of the Atmospheric Sciences* 59 (2002), pp. 3421–3435. doi: [10.1175/1520-0469\(2002\)059<3421:MATCDG>2.0.CO;2](https://doi.org/10.1175/1520-0469(2002)059<3421:MATCDG>2.0.CO;2).
- [154] M. A. T. van Hinsberg et al. “Optimal interpolation schemes for particle tracking in turbulence”. In: *Physical Review E* 87 (4 2013), p. 043307. doi: [10.1103/PhysRevE.87.043307](https://doi.org/10.1103/PhysRevE.87.043307).

-
- [155] P. Vieillefosse. “Internal motion of a small element of fluid in an inviscid flow”. In: *Physica A: Statistical Mechanics and its Applications* 125.1 (1984), pp. 150–162. doi: [https://doi.org/10.1016/0378-4371\(84\)90008-6](https://doi.org/10.1016/0378-4371(84)90008-6).
- [156] P. Vieillefosse. “Local interaction between vorticity and shear in a perfect incompressible fluid”. In: *Journal de Physique France* 43.6 (1982), pp. 837–842. doi: <https://doi.org/10.1051/jphys:01982004306083700>.
- [157] D. G. Vlaykov and M. Wilczek. “On the small-scale structure of turbulence and its impact on the pressure field”. In: *Journal of Fluid Mechanics* 861 (2019), pp. 422–446. doi: [10.1017/jfm.2018.857](https://doi.org/10.1017/jfm.2018.857).
- [158] M. Voßkuhle et al. “Prevalence of the sling effect for enhancing collision rates in turbulent suspensions”. In: *Journal of Fluid Mechanics* 749 (2014), pp. 841–852. doi: [10.1017/jfm.2014.259](https://doi.org/10.1017/jfm.2014.259).
- [159] A. W. Vreman. “Particle-resolved direct numerical simulation of homogeneous isotropic turbulence modified by small fixed spheres”. In: *Journal of Fluid Mechanics* 796 (2016), pp. 40–85. doi: [10.1017/jfm.2016.228](https://doi.org/10.1017/jfm.2016.228).
- [160] L. P. Wang and M. R. Maxey. “Settling velocity and concentration distribution of heavy particles in homogeneous isotropic turbulence”. In: *Journal of Fluid Mechanics* 256 (1993), pp. 27–68.
- [161] Z. Warhaft. “Passive Scalars in Turbulent Flows”. In: *Annual Review of Fluid Mechanics* 32.1 (2000), pp. 203–240. doi: [10.1146/annurev.fluid.32.1.203](https://doi.org/10.1146/annurev.fluid.32.1.203).
- [162] T. Watanabe and T. Gotoh. “Statistics of a passive scalar in homogeneous turbulence”. In: *New Journal of Physics* 6.1 (2004), p. 40.
- [163] H. Weyl. *The Classical Groups*. Princeton University Press, 1939.
- [164] M. Wilczek and C. Meneveau. “Pressure Hessian and viscous contributions to velocity gradient statistics based on Gaussian random fields”. In: *Journal of Fluid Mechanics* 756 (2014), pp. 191–225. doi: [10.1017/jfm.2014.367](https://doi.org/10.1017/jfm.2014.367).
- [165] M. Wilkinson and B. Mehlig. “Caustics in turbulent aerosols”. In: *Europhysics Letters* 71.2 (2005), pp. 186–192.
- [166] V. Yakhot and S. A. Orszag. “Renormalization group analysis of turbulence. I. Basic theory”. In: *Journal of Scientific Computing* 1.3 (1986), pp. 3–51. doi: <https://doi.org/10.1007/BF01061452>.
- [167] P. K. Yeung, D. A. Donzis, and K. R. Sreenivasan. “Dissipation, enstrophy and pressure statistics in turbulence simulations at high Reynolds numbers”. In: *Journal of Fluid Mechanics* 700 (2012), pp. 5–15. doi: [10.1017/jfm.2012.5](https://doi.org/10.1017/jfm.2012.5).
- [168] L. I. Zaichik, O. Simonin, and V. M. Alipchenkov. “Two statistical models for predicting collision rates of inertial particles in homogeneous isotropic turbulence”. In: *Physics of Fluids* 15.10 (2003), pp. 2995–3005. doi: [10.1063/1.1608014](https://doi.org/10.1063/1.1608014).

BIBLIOGRAPHY

- [169] L. Zaichik, V. M. Alipchenkov, and E. G. Sinaiski. *Particles in Turbulent Flows*. Vol. 84. Wiley-VCH Verlag GmbH & Co. KGaA, 2009.
- [170] R. Zamansky et al. “Radiation induces turbulence in particle-laden fluids”. In: *Physics of Fluids* 26.7 (2014).
- [171] R. Zamansky et al. “Turbulent thermal convection driven by heated inertial particles”. In: *Journal of Fluid Mechanics* 809 (2016), pp. 390–437. doi: [10.1017/jfm.2016.630](https://doi.org/10.1017/jfm.2016.630).
- [172] F. Zonta, C. Marchioli, and A. Soldati. “Direct numerical simulation of turbulent heat transfer modulation in micro-dispersed channel flow”. In: *Acta Mechanica* 195.1–4 (2008), pp. 305–326.
- [173] E. Zorzetto, A. D. Bragg, and G. Katul. “Extremes, intermittency, and time directionality of atmospheric turbulence at the crossover from production to inertial scales”. In: *Physical Review Fluids* 3 (9 2018), p. 094604. doi: [10.1103/PhysRevFluids.3.094604](https://doi.org/10.1103/PhysRevFluids.3.094604).

This Ph.D. thesis has been typeset by means of the T_EX-system facilities. The typesetting engine was pdfL^AT_EX. The document class was toptesi, by Claudio Beccari, with option tipotesi =scudo. This class is available in every up-to-date and complete T_EX-system installation.